# Development of a low-cost graphene-based impedance biosensor

By **Sinziana Mirela Popescu**

School of Engineering

Mechanical and Systems Engineering Department

Newcastle University, United Kingdom

Thesis submitted to the Faculty of Science, Agriculture and Engineering for the degree of Doctor of Philosophy (PhD)

*January 2018*

## Acknowledgments

I would like to express my sincere gratitude to my supervisors: Dr John Hedley, Dr Neil Keegan and Mr Richard Burnett for their support and guidance throughout my research work. Overcoming project challenges, I had the chance to develop valuable professional and personal abilities. I am also grateful to the School of Mechanical and Systems Engineering for the awarded PhD scholarship and the given opportunity to work on such an intriguing multidisciplinary project.

A big thank you to experienced researchers and colleagues for constructive discussions, their help and shared lessons learnt: Julia Spoors, Dr Carl Dale, Dr Sami Ramadan, Dr Anders Barlow, Prof Biswajit Ghosh, Prof Ian Fletcher, Prof Stephen Foti, Dr Harriet Grigg, Dr Jose Portoles, Dr Naoko Sano, Dr Billy Murdoch, Dr Isabel Arce-Garcia, Dr Sabrina Tardio, Dr Monica Florescu, Dr Konstantin Vasilevskiy, Dr Peter King, Srinivas Ganti, and Philip Emanuel. It was a pleasure and an inspiring research experience to meet Prof Richard Kaner and his team at the University of California Los Angeles. I am also thankful to Michael Foster, Stephen Moore, Paul Harrison and Frank Atkinson for the provided technical support.

During my PhD, I truly learned the power of friends and family. As coffee breaks and friendly chats have been a must during my PhD, a heartfelt thank you to all my colleagues in the MEMS & Sensors, Bioengineering, ICM and Clean Room, and especially to Hannah Swinburne, Dr Ana Marina Ferreira-Duarte, Dr Steve Akande and Zeyad Al-Shibaany. Ildiko, Maria and Ciprian, thanks for keeping me strong and entertained!

Finally, I would like to express my deepest gratitude to my family, for their love, support and patience. I feel blessed to have you all in my life and I hope to make up for all the “grumpy” days! Radu, thank you for taking care of me (listening, advising, cooking, cleaning, cheering me up) in all this time and for always encouraging me to pursue my dreams.

## Abstract

The current applicability and accuracy of point-of-care devices is limited, with the need of future technologies to simultaneously target multiple analytes in complex human samples. Graphene's discovery has provided a valuable opportunity towards the development of high performance biosensors. The quality and surface properties of graphene devices are critical for biosensing applications with a preferred low contact resistance interface between metal and graphene. However, each graphene production method currently results in inconsistent properties, quality and defects thus limiting its application towards mass production. Also, post-production processing, patterning and conventional lithography-based contact deposition negatively impact graphene properties due to chemical contamination.

The work of this thesis focuses on the development of fully-functional, label-free graphene-based biosensors and a proof-of-concept was established for the detection of prostate specific antigen (PSA) in aqueous solution using graphene platforms. Extensive work was carried out to characterize different graphene family nanomaterials in order to understand their potential for biosensing applications. Two graphene materials, obtained via a laser reduction process, were selected for further investigations: reduced graphene oxide (rGO) and laser induced graphene from polyimide (LIG). Electrically conductive, porous and chemically active to an extent, these materials offer the advantage of simultaneous production and patterning as capacitive biosensing structures, i.e. interdigitated electrode arrays (IDE). Aiming to enhance the sensitivity of these biosensors, a novel, radio-frequency (RF) detection method was investigated and compared with conventional electrochemical impedance spectroscopy (EIS) on a well-known biocompatible material: gold (standard). It was shown that the RF detection methods require careful design and testing setup, with conventional EIS performing better in the given conditions. The method was further used on rGO and LIG IDE devices for the electrochemical impedance detection of PSA to assess the feasibility of the graphene based materials as biosensors.

The graphene-based materials were successfully functionalized via the available carboxylic groups, using the EDC-NHS chemistry. Despite the difficulty of producing reproducible graphene-based electrodes, highly required for biosensor development, extensive testing was carried out to understand their feasibility. The calibration curves obtained via successive PSA addition showed a moderate-to-high

sensitivity of both rGO and LIG IDE. However, further adsorption and drift testing underlined some major limitations in the case of LIG, due to its complex morphology and large porosity. To enable low contact resistance to these biosensors, the electroless nickel coating process is shown to be compatible with various graphene-based materials. This was demonstrated by tuning the chemical nickel bath and method conditions for pristine graphene and rGO for nickel contacts deposition.

## List of publications

**Sinziana M. Popescu**, Carl Dale, Neil Keegan, Biswajit Ghosh, Richard Kaner, John Hedley, “Rapid prototyping of a low-cost graphene-based impedimetric biosensor”, *Procedia Technology*, Apr 2017, vol. 27, pp 274-276

**Sinziana M. Popescu**, Anders J. Barlow, Sami Ramadan, Srinivas Ganti, Biswajit Ghosh, John Hedley, “Electroless Nickel Deposition: An Alternative for Graphene Contacting”, *ACS Applied Materials and Interfaces*, Oct 2016, vol. 8 (45), pp 31359–31367

Anders J. Barlow, **Sinziana Popescu**, Kateryna Artyushkova, Oliver Scott, Naoko Sano, John Hedley, Peter J. Cumpson, “Chemically specific identification of carbon in XPS imaging using Multivariate Auger Feature Imaging (MAFI)”, *Carbon*, May 2016, vol. 107, pp 190-197

## Abbreviations

| | |
|---|---|
| AFM | Atomic force microscopy |
| BLG | Bilayer graphene |
| BSA | Bovine serum albumin |
| CNT | Carbon nanotubes |
| CMOS | Complementary metal-oxide-semiconductor |
| CrGO | Chemically reduced graphene oxide |
| CVD | Chemical vapour deposition |
| DTSP | 3,3′-Dithiodipropionic acid di(N-hydroxysuccinimide ester |
| EDC | N-(3-Dimethylaminopropyl)-N′-ethylcarbodiimide |
| EG | Epitaxially grown graphene |
| EIS | Electrochemical impedance spectroscopy |
| ErGO | Electrochemically reduced graphene oxide |
| ESEM | Environmental scanning electron microscope |
| FEA | Finite element analysis |
| FET | Field-effect transistor |
| FLG | Few-layer graphene |
| GFET | Graphene FET |
| GO | Graphene oxide |
| HIM | Helium ion microscopy |
| IC | Integrated circuit |
| IDE | Interdigitated electrode array |
| LIG | Laser induced graphene |
| LoC | Lab-on-Chip |
| MEMS | Micro-electro-mechanical systems |
| MLG | Multi-layer graphene |
| NanoGO | Nano-size layers graphene oxide |
| NHS | N-hydroxysulfosuccinimide |
| NP | Nanoparticles |
| PBS | Phosphate buffered saline |
| PCB | Printed circuit board |
| PI | Polyimide |
| PoC | Point of Care system |
| PSA | Prostate specific antigen |

| | |
|---|---|
| QD | Quantum dots |
| RF | Radio frequency |
| rGO | Reduced graphene oxide |
| SEM | Scanning electron microscopy |
| SLG | Single-layer graphene |
| SNR | Signal to noise ratio |
| SUT | Sample under test |
| VNA | Vector network analyzer |
| XPS | X-ray photoelectron spectroscopy |
| XRD | X-ray powder diffraction |

## Contents

## List of Figures

## List of Tables

# Chapter 1. Introduction

## 1.1. Background and motivation

Healthcare systems, patients and their families are facing more than 200 types of cancer worldwide. As we all know, the consequences are dramatic and sometimes irreversible: 8.2 million people died because of cancer in 2012. In the research race for single molecule detection, graphene has been identified as one of the most promising biosensor candidates, with a bright potential to accelerate medical diagnostics.

"*Life exists in the universe only because the carbon atom possesses certain exceptional properties*" - James Jeans, physicist and mathematician (1877-1946).

Carbon is one of the most abundant elements in the universe, being the main component of organic structures and the backbone of life on earth. With the increasing interest in nanotechnology, over the last three decades, carbon allotropes have become the main research focus in engineering, science and medicine.

While the exceptional properties of graphene are theoretically addressed, several limitations of graphene have been identified in practical applications. Firstly, the properties of graphene are highly dependent on its production method. The processing conditions and techniques for graphene integration into devices further impact material properties and performance. Secondly, graphene sensing devices require metal contacts for measurements and / or connection to other components. The current conventional metal deposition techniques are not yet fully transferable and compatible with 2D materials.

The anticipation of graphene revolutionising the 21$^{st}$ century has encouraged its exploration as an alternative to current biosensing technologies and beyond. The attempt to overcome application-specific challenges led to further important discoveries, with the continuous expansion of the graphene nanomaterials family.
But the question remains: can graphene make it under so much research pressure?

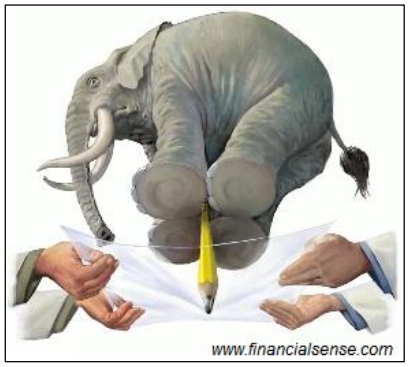

## 1.2. Thesis overview

This research project investigates the feasibility of low-cost graphene based materials for biosensing applications. With inconsistent research results available on graphene sensors, the thesis addresses several critical aspects of graphene, from large-scale production and patterning to the delivery of a generic, fully functional device. Therefore, the main objectives of this work are:

- The low-cost, reproducible synthesis of graphene and the understanding of different properties for a variety of graphene based materials.
- The investigation of rapid fabrication techniques for graphene integration in capacitive biosensing structures.
- The chemical surface modification i.e. functionalization of graphene.
- The evaluation of the proposed graphene based biosensors, with proof of concept on prostate specific antigen (PSA) detection.

Chapter 2 provides a literature review relevant to this research work. It starts with an overview of biosensors and their application in Point of Care (PoC) technologies, being focused on more detailed aspects of graphene and biomolecules detection methods - conventional and novel approaches. This section also articulates research trends and opportunities for graphene, impedance and radio frequency (RF) based detection mechanism for the progress of future biosensors and PoC systems.

Chapter 3 compares different graphene based materials and their suitability for biosensing applications. Various qualitative and quantitative factors, such as graphene “purity”, electrical properties, production cost, technology accessibility and ease of patterning are considered. High-resolution microscopy is used to reveal graphene based materials with a rich morphology and porosity. The outcome of this chapter is the selection of graphene material(s) fit as biosensing platforms.

Chapter 4 looks into the potential of the RF biosensing and principles for the detection of molecular interactions at the electrode surface. Firstly, electrical circuit simulations are used to compare the performance of conventional low frequency, electrochemical impedance spectroscopy (EIS) and the high frequency RF approach using capacitive biosensors. The theoretical hypothesis is also tested in practice by employing commercially available gold interdigitated electrode arrays (IDE) for PSA detection. The output of this chapter enables the decision of the detection mode for graphene biosensors.

Chapter 5 presents the fabrication, characterisation and analysis of the graphene based IDE devices for PSA antibody-antigen detection. Spectroscopic

measurements are performed to understand the induced chemical surface changes. Systematic experimental studies are performed to comprehend the feasibility of the graphene materials for the development of generic biosensor platforms. The outcome of this chapter is a thorough investigation into the potential of porous, 3D graphene materials as biosensors.

Chapter 6 reports a novel coating approach on graphene. The electroless nickel deposition method allows for low-cost, fast and accessible metal contacting. The technique is demonstrated on pristine single-layer graphene, as well as “defective” graphene (reduced graphene oxide), with the extraction of contact resistance. The output of this chapter serves as research guidance towards the accessible and rapid prototyping of fully functional graphene sensors.

Chapter 7 enunciates the general conclusions based on the main research work presented in this thesis. It also provides some recommendations for further research activities related to the production of graphene materials and their integration for improved performance and compact biosensing devices.

# Chapter 2. Literature review

## 2.1. Point-of-Care testing

The healthcare diagnostics market has seen a steady progress in the development of Point of Care (PoC) testing systems for over four decades [1]. Before 1990s, the research focus was placed on the understanding of biomolecules and methods of immobilization at the electrode surfaces. Optical / fluorescence biosensors have been developed for the detection of various molecules by 2000. In early 2000s, the miniaturisation technology trend influenced biosensing technologies towards Lab-on-Chip (downsized PoC test systems) and portable medical devices. Later, driven by the need to improve the signal-to-noise ratio (SNR) and sensitivity, nanomaterials (including hybrids) and integration solutions have been explored. The last few years have seen a technological boom in user-friendly health monitoring devices and smartphone applications. Future discoveries are expected to target disease prevention by real-time vitals monitoring and personalised medicine for improved quality of life. Figure 2.1 presents some significant events in the development of PoC systems and medical devices [2][3][4].

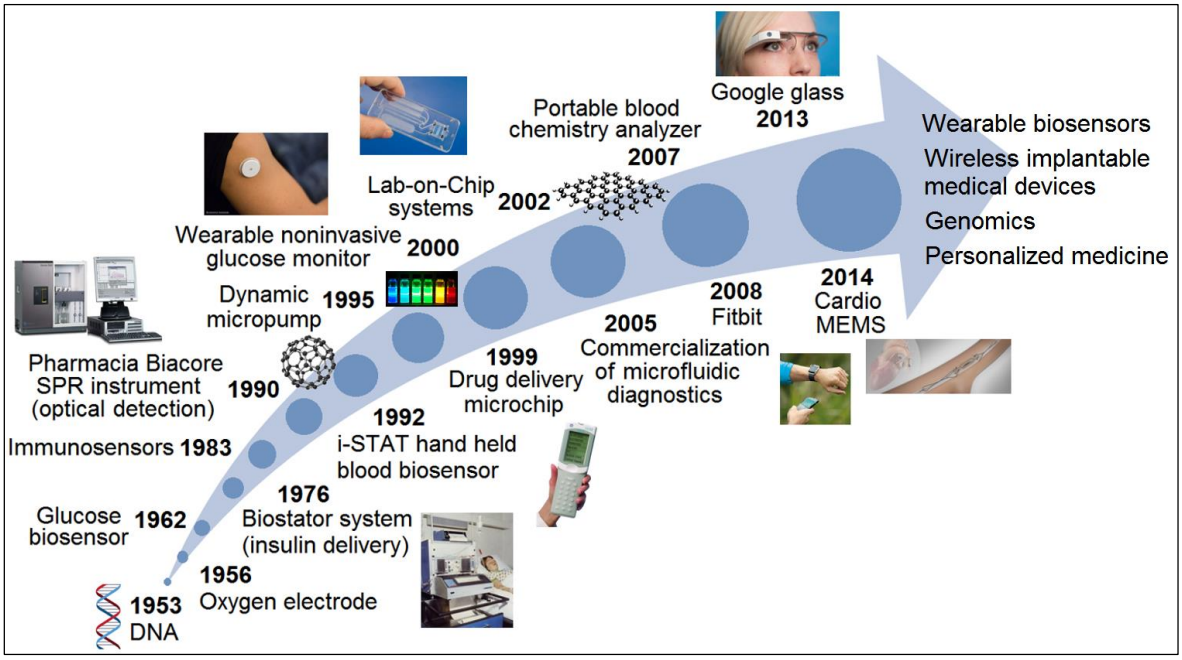


Figure 2.1. A timeline of biosensors and medical technologies.

PoC systems are the result of technological efforts for advanced patient care. PoC integrates the biosensing platform, the measurement instrumentation and the microfluidics module to deliver rapid diagnostic or prognostic test performed near the patient [5], in clinical or non-clinical environments. The robust and user-friendly

interface with consumer electronics allows for simplified biosensor results reading / interpretation, with no need for specialist personnel. PoC testing systems vary from simple, lateral flow-based, such as the pregnancy test, to more complex, blood analysis-based e.g. portable glucose test. A “sample-to-answer” PoC system is shown in Figure 2.2.

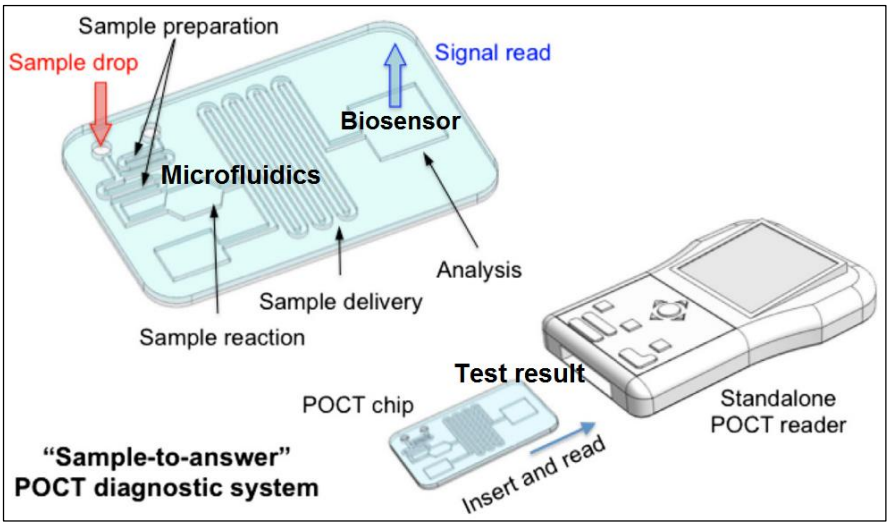


Figure 2.2. Example of a PoC diagnostic system, adapted from [16].

The development of such integrated systems require a complex and multi-disciplinary approach. An example in this respect is the work reported by Ahn et al. [6] for the development and manufacturing of a disposable lab-on-chip system using electrochemical detection of several blood parameters (oxygen partial pressure, lactate and glucose).

While PoC diagnostics offer advantages like: simpler sample collection and smaller sample volume, ease of handling, faster test results and increased patient satisfaction, their accuracy is still limited compared to conventional laboratory tests and usually comes at a higher cost and the loss of patient test data [7]. In order to improve their accuracy and precision, PoC requires more evidence-based data and thorough quality control and assessment [8]. Nowadays, modern countries focus on disease prevention, but the PoC technology is essential in developing countries [9][10], where infectious diseases represent a major public health concern, and the access to basic wellbeing and healthcare resources is restricted.

## 2.2. Biosensors

Biosensors are a key player in the technological and scientific progress in healthcare, as tackling disease diagnostics and health monitoring. A biosensor consists of a biorecognition element and a sensing element, being presented in Figure

2.3. By integrating the two elements, an analytical device is obtained, with the triggered response (in the form of a discrete or continuous electrical signal) based on the interaction between the biologically active substrate and test analyte [11]. Depending on the operating environment, biosensors are classified: in-vivo (inside a real biological system) and in-vitro (external, using sample collected from the biological system) [12]. Further biosensors categories are based on the recognition layer and detection mechanism (see Figure 2.3).

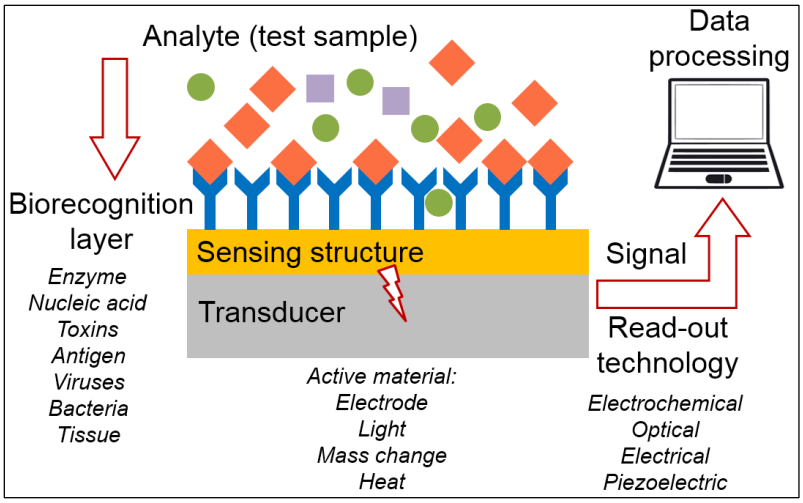


Figure 2.3. The configuration of a biosensor.

The first biosensor, employed for glucose detection (enzyme-based), was reported and documented in 1962 by Leland C. Clark Jr [13]. Since then, three generations of enzyme biosensors have evolved towards what we know at present as an integrated biosensor (the biorecognition element became part of the transducer), briefly presented in Figure 2.4.

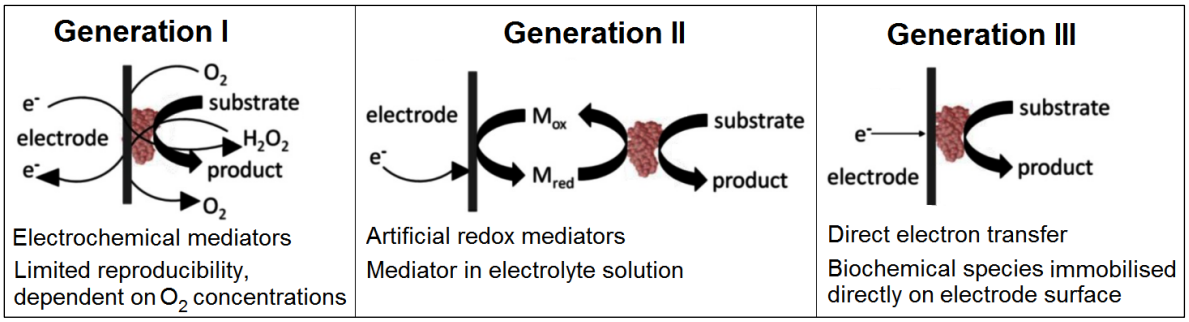


Figure 2.4. The evolution of enzymatic biosensors from first to third generation, adapted from [14][15].

The construction of a successful biosensor is a complex process, balancing the practical performance and its development cost. The most important attributes of a biosensor are captured in Figure 2.5 and discussed in the following paragraphs.

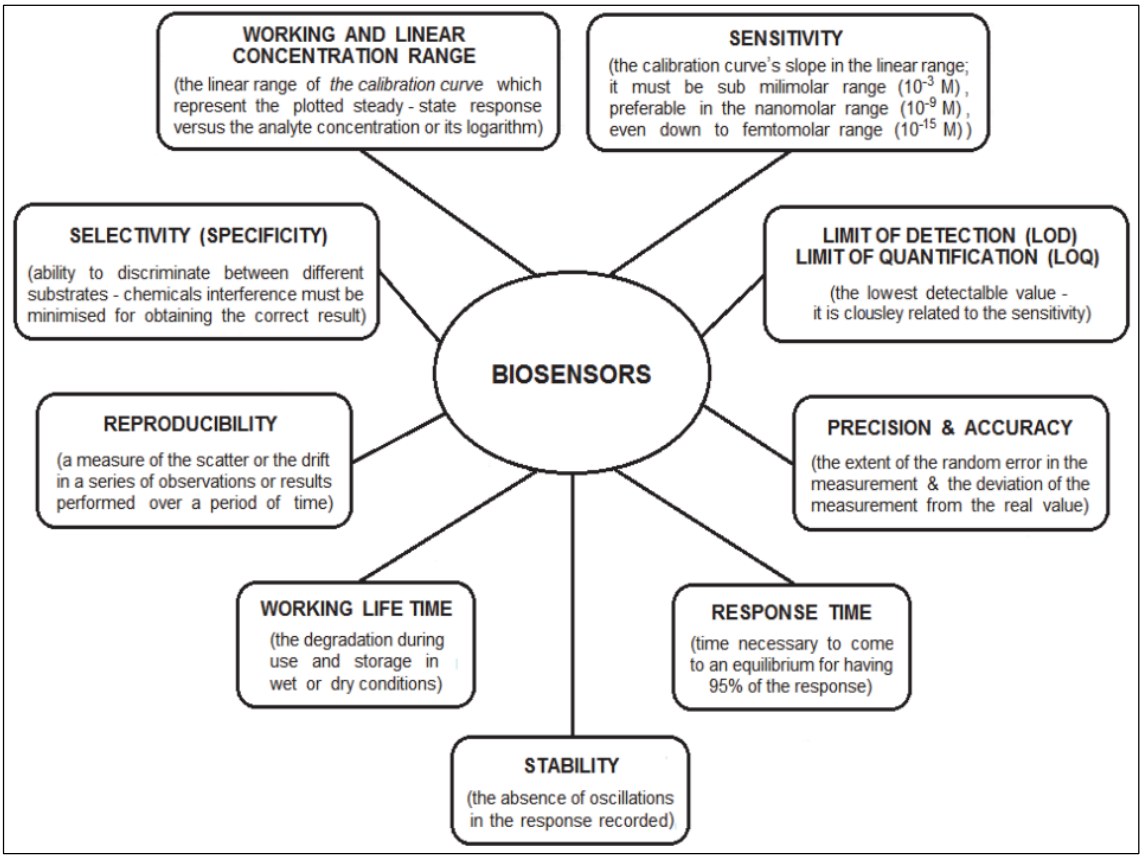


Figure 2.5. Essential attributes of a reliable biosensor [16].

Firstly, the biosensor response must be measurable and repeatable. This is usually verified by comparing the "blank" (in the absence of the analyte) and analyte measurements. The biosensor's response must be specific and triggered by the target analyte only. This requires the optimisation of the immobilization protocol for the biorecognition layer in order to maximise the surface coverage and tailoring to minimise or even eliminate the attachment of non-targeted biomolecules, referred as non-specific adsorption.

The measured response must be proportional to the analyte concentration. This is usually demonstrated by the construction of calibration curves, fitted by a first or second order polynomial [17] or one-side binding curve [18]. Blank response corrections / normalisation can be performed prior to constructing the calibration curve. The quality of the fitting ($R^2$) is an indicator of biosensor's sensitivity and its linear range constitutes the working range of the biosensor. The signal difference, as Δ or % change in signal, can be used to build the calibration curve, with the formula:

$$\Delta\,(\%) = \frac{S_i - S_0}{S_0} \qquad (2\text{-}1)$$

where: $S_0$ is the reference measurement (initial or the "blank" prior to detection) and $S_i$ is the measured signal upon functionalization and / or detection.

The minimum amount of analyte detectable by the biosensor is referred as the limit of detection (LoD), defined as: $\mathrm{LOB} + 1.645\sigma_{\mathrm{Blank}}$ [19], where LOB is the limit of blank. The limit of quantitation (LoQ) accounts for the lowest measurable limit of detection, in case of poor repeatability and errors [19]; this can be the same as LoD or slightly higher. The biosensor response must be stable to external disturbances and available within a time frame: the quicker, the better. Last but not least, the reproducibility of biosensor measurements and response is also a confirmation of the employed protocol efficiency, as well as the reliability of the sensing platform e.g. part-to-part variation.

The sensor design plays an essential role in biosensor performance and SNR, but this is sometimes restricted by the fabrication techniques and capability. This is also valid for the sensing platform material, reason for which these aspects are carefully considered (including numerical simulations) prior to geometry and detection mode selection. Further biosensor development must also address manufacturing, sample size and delivery aspects. This varies from “immersion” based electrochemical biosensors [20] to micro and nanofluidics [21] module attachment for compact biosensors. Rackus et al. [22] addressed in their literature review the integration of conventional measurement techniques and fluidics for biosensing applications. Also, one must consider the storage conditions for the biosensor, depending on the nature of the material and biomolecular layer, if present.

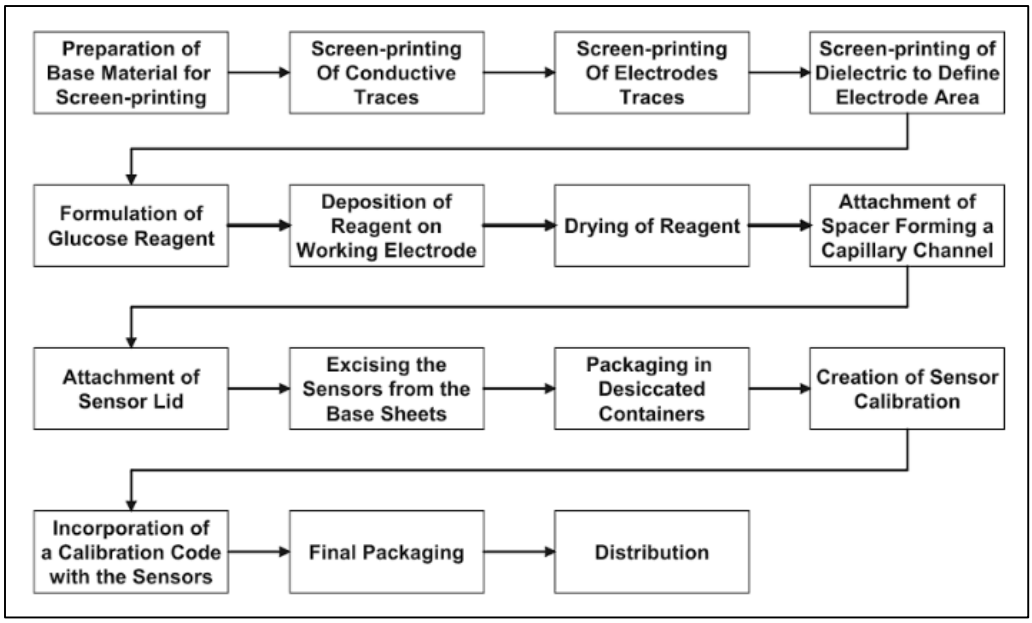


Figure 2.6. The manufacturing process for disposable glucose biosensors [23].

Several challenges arise for the large-scale manufacturing of biosensing platforms. In order to exemplify the complexity of biosensor fabrication, Figure 2.6

presents the manufacturing process for screen-printed disposable glucose biosensors, with the note that screen-printing is already a well-established technology, being first time employed in electrochemical sensing in 1981 [24]. In the case of novel materials, extensive validation efforts are needed, from concept to sensing platform integration within functional devices.

## 2.3. Graphene

As stated by A.K. Geim, graphene inventor: “Graphene is a wonder material with many superlatives to its name. It is the thinnest known material in the universe and the strongest ever measured. Graphene can sustain current densities six orders of magnitude higher than that of copper, shows record thermal conductivity and stiffness, is impermeable to gases, and reconciles such conflicting qualities as brittleness and ductility” [25].

### 2.3.1 *Fabrication, properties and applications*

Since its physical discovery using the scotch-tape method in 2004 [26] at Manchester University, graphene, the “miracle material”, has received huge research attention. The first experimental realisation of graphite, the most common source material for graphene synthesis, was reported back in 1859, with a later attempt to chemically reduce graphite in 1962 [27]. Daniel R. Dreyer et al. [28] gathered evidence in terms of graphene hypothetical reference dating back to 1986, revealing a remarkable description i.e. polycyclic aromatic hydrocarbon origin and a single carbon layer. The discovery of fullerenes and CNT in early 1990s retriggered the interest for graphite and graphene.

Graphene is a stable two-dimensional stable crystal and it represents the basic structural element of graphite, CNT and fullerenes (see Figure 2.7a). Being a single atom thick (≈ 0.3 nm), its nomenclature originates from “graphite and alkene” (double carbon bond) [29] as graphene has the carbon atoms densely packed in a $sp^2$-bonded hexagonal structure, which can be regarded as two intercalated triangular lattices [30] (see Figure 2.7b).

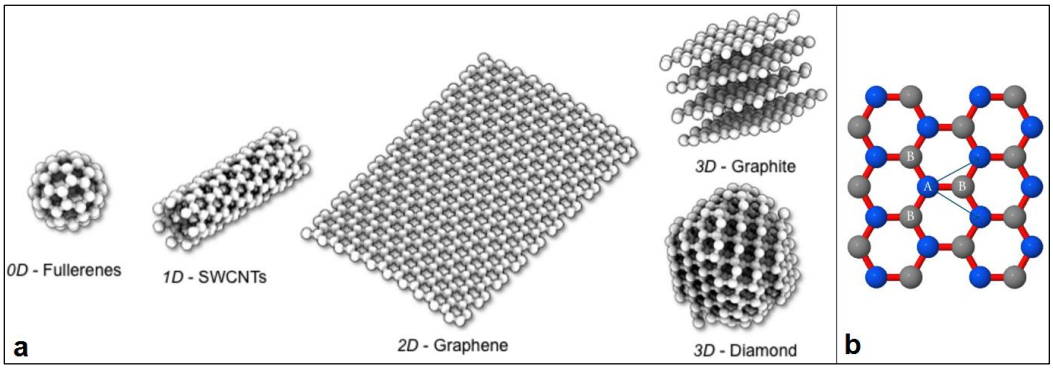


Figure 2.7. (a) The atomic structure of carbon nanomaterials [96]; (b) intercalated carbon sub-lattices arrangement in graphene [95].

Some of graphene's extraordinary properties are captured in Table 2-1, selected from a review conducted by Copper et al. [30]. In addition to its large surface area [31], graphene is a better electrical conductor than copper, harder than diamond, whilst transparent, flexible and impermeable.

Table 2-1. Experimentally determined properties of graphene [30].

| **Properties** | **Graphene values** |
|---|---|
| Young's modulus | ~ 1 TPa |
| Fracture strength | 130 GPa |
| Thermal conductivity | ~ 5000 $W \cdot m^{-1} \cdot K^{-1}$ |
| Thermal resistance | ~ 4 x $10^{-8}$ $K \cdot m^2 \cdot W^{-1}$ |
| Specific surface area | 2,630 $m^2 \cdot g^{-1}$ |
| Optical transmittance | ~ 97.7% |
| Sheet resistance | 1.3 x $10^4$ – 5.1 x $10^4$ $\Omega \cdot sq^{-1}$ |
| Mobility (typical) | 15,000 $cm^2 \cdot V^{-1} \cdot s^{-1}$ |
| Mobility (intrinsic) | 200,000 $cm^2 \cdot V^{-1} \cdot s^{-1}$ |
| Current density | $10^8$ $A \cdot cm^{-2}$ |
| Fermi velocity | c/300 = 1,000,000 $m \cdot s^{-1}$ |

While graphene is suitable for a variety of applications, as presented in Figure 2.8, its properties are highly dependent on the production method [30]. The graphene synthesis method and processing conditions should be considered based on the purpose of the experiment and targeted practical applications. However, this leads to variations in the graphene structure, further addressed in section 2.2.

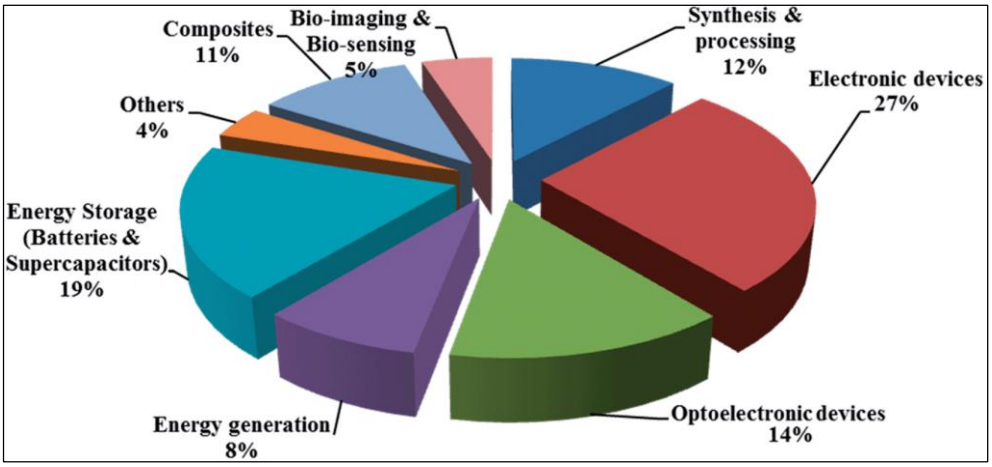


Figure 2.8. Graphene applications and corresponding research focus [29].

The production methods can be classified in two main categories: top-down and bottom-up [32]. The first approach is generally more cost effective and suitable for high-volume production, but it fails to provide consistent properties and quality e.g. micro-mechanical cleavage of graphite. The bottom-up synthesis methods, such as chemical vapour deposition (CVD), offer the advantage of thickness and number of layers' control, but at a much higher cost [29][33]; this growth-based approach requires post-production processing / handling. The most common synthesis methods are captured in Table 2-2; other methods have been reported, such as the chemical reduction of graphene oxide via sugar [34] or green tea [35], laser reduction and patterning of graphene oxide [36][37], and even detonation of carbon-containing compounds for graphene mass production [38].

Table 2-2. Common graphene synthesis methods, properties and applications, from [39].

| Method | Crystallite size (μm) | Sample size (mm) | Applications |
|---|---|---|---|
| Mechanical exfoliation | >1,000 | >1 | Research |
| Chemical exfoliation | ≤0.1 | Infinite as a layer of overlapping flakes | Coatings, paint/ink, composites, transparent conductive layers, energy storage, bioapplications |
| Chemical exfoliation via graphene oxide | ~100 | Infinite as a layer of overlapping flakes | Coatings, paint/ink, composites, transparent conductive layers, energy storage, bioapplications |
| CVD | 1,000 | ~1,000 | Photonics, nanoelectronics, transparent conductive layers, sensors, bioapplications |
| SiC | 50 | 100 | High-frequency transistors and other electronic devices |

The reduced graphene oxide (rGO) is a remarkable graphene based material. The reduction of graphene oxide leads to the synthesis of "defective graphene" [40][41]. Graphene oxide (GO) can be obtained from oxidized graphite, which is further exfoliated to single-layer flakes via sonication. The graphite oxidation was reported with various oxidizing agents and strong acids, the most common being Hummers'

method which employs potassium permanganate [42]. Once the oxygen functionalities are introduced, the graphene planes are spaced and the individual sheets can be separated from the initial structure as they are held together by van der Waals forces [43]. Graphene oxide reduction can be achieved in-solution or on as-deposited GO films via: chemical (hydrazine [44][45], organic solvents such as ethanol or DMF [45], vitamin C [46]), electrochemical (cyclic voltammetry [47], potential cycling [48]) thermal (annealing in vacuum [49], Ar/$H_2$ [50], $N_2$ [51]), photo-thermal (camera flash [52], laser [53], UV [54]). The reduction process is schematically presented below in Figure 2.9.

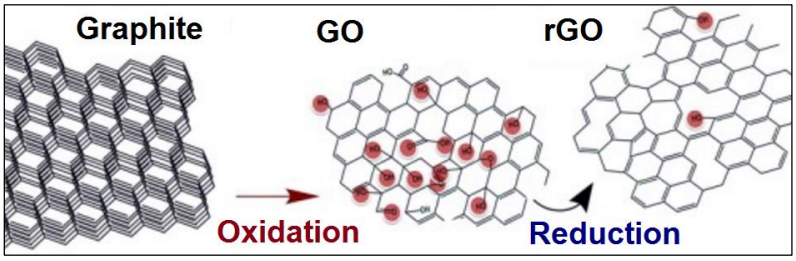


Figure 2.9. Graphene oxide reduction process for reduced graphene oxide (rGO) synthesis [55].

According to the efficiency of the reduction process, the functional groups are removed from the graphitic backbone, from the basal plane and edges. This method presents many advantages, among which fast graphene production, reduced complexity (improved safety), low-cost and flexibility in terms of substrate and reduction approach. While single layer production via GO reduction is possible [56], the oxidation process is not fully reversible and the electrical properties are significantly inferior compared to pristine graphene. The accessible LightScribe DVD engraving technique was successfully adopted for the GO photo-thermal reduction. The porous, stacked structure of multi-layer rGO with a surface area of 1520 $m^2/g$ [57] showed high electrical conductivity and suitability for electrochemical capacitors.

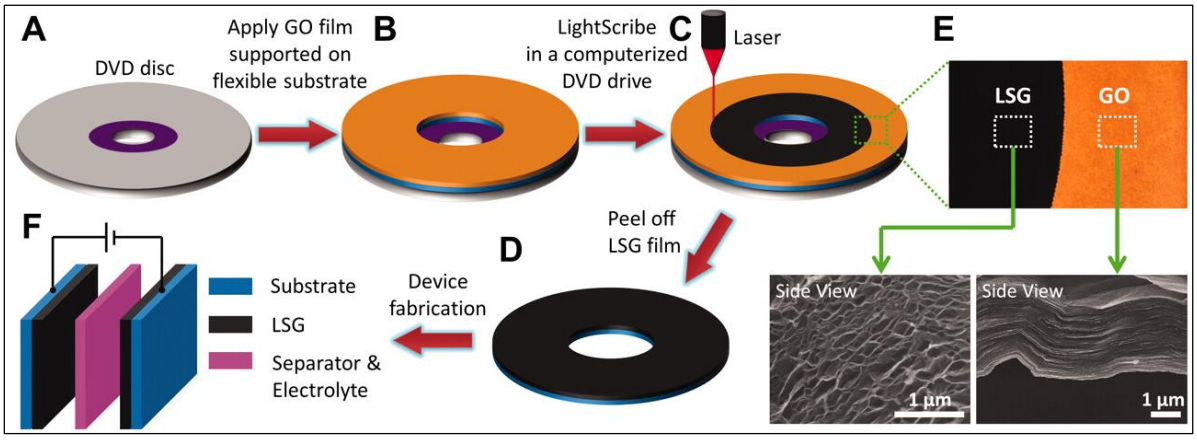


Figure 2.10. GO reduction to obtain rGO via LightScribe method [57].

### 2.3.2 *Graphene nanomaterials family*

The intense research focus on graphene led to its production using a variety of methods, as well as the generalisation of the term “graphene” in the literature which can be misleading. In this respect, Bianco et al. [58] proposed a set of criteria (structure, lateral dimension, nanoscience terminology) to distinguish between different graphene based materials, as presented in Figure 2.11. Later, the graphene “family” demarcation criteria was developed by Wick et al. [59], adding another major player in the material definition: carbon composition and purity.

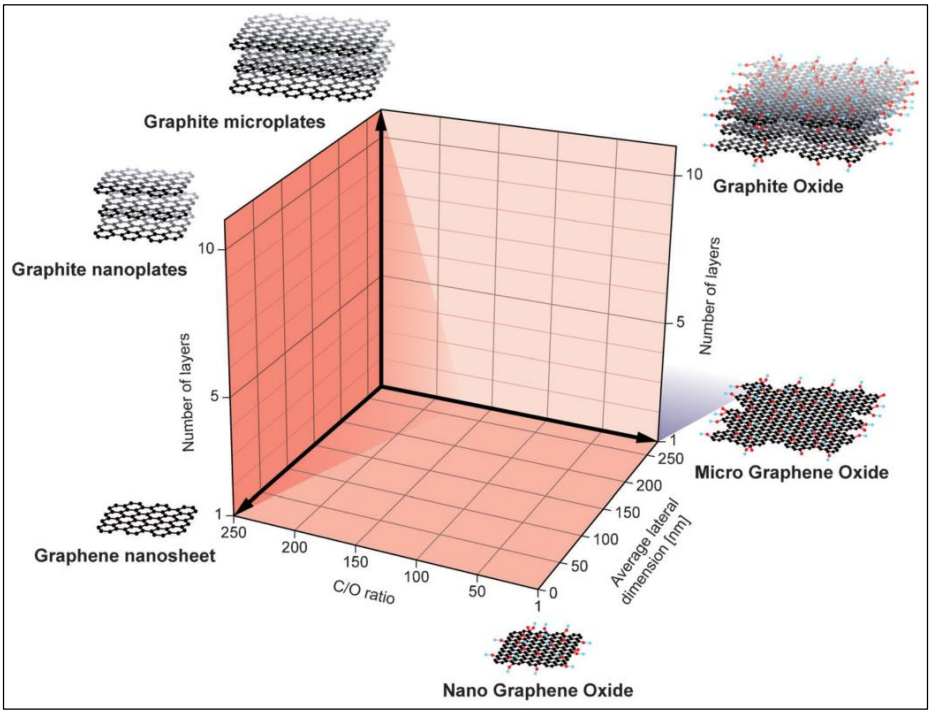


Figure 2.11. A proposed classification of graphene family members [59].

The properties of graphene based materials are highly dependent on the carbon composition, chemical properties and number of layers of [60]. For example, the toxicity of graphene family nanomaterials is under debate and substantial research progress depends on the fabrication process control and reproducibility. Overall, pristine graphene is the most toxic, while GO exhibited improved biocompatibility via surface modifications [61]. Variations in graphene properties according to the number of layers are shown in Figure 2.12.

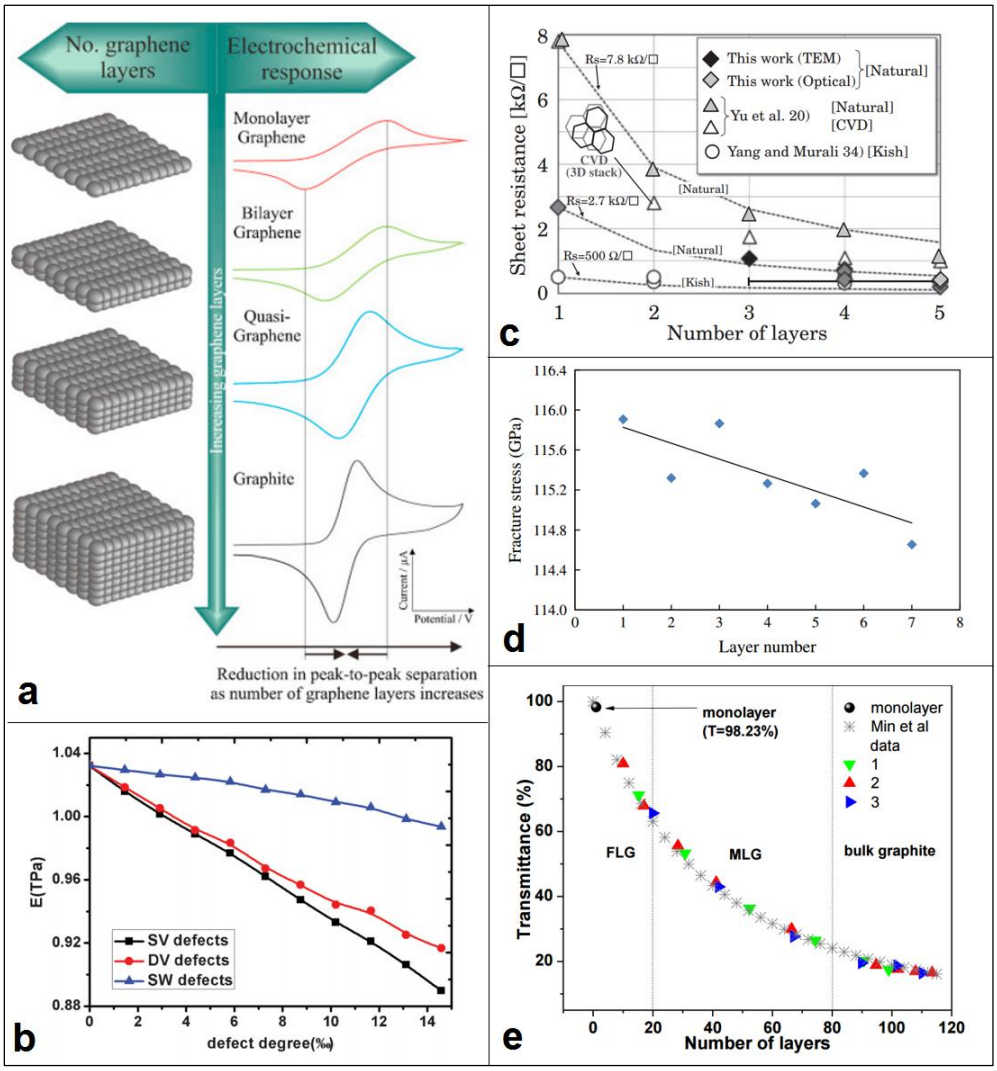


Figure 2.12. Variation in graphene properties as induced by the number of layers and defects presence: (a) electrochemical properties [62]; (b) Young's modulus, where: SV- single vacancy; DV - double vacancy and SW - Stone-Wales defects [63]; (c) sheet resistance [64]; (d) fracture stress [65]; (e) optical transmittance [66].

### 2.3.3 *Graphene characterisation techniques*

Conventional microscopy (AFM, HR-TEM/SEM) and spectroscopy (XPS, FTIR, Raman) techniques can be utilized to study the structure, quality and properties of graphene. The variety of graphene family members require careful analysis; subtle differences, as in the case of monolayer and few-layer CVD grown graphene, can have a decisive impact on material performance as employed in practice. Also, one must understand the sample background (substrate and synthesis method), as well as the employed analytical methodology. Several methods are usually combined for the accurate characterisation and validation of the carbon nanomaterial.

#### *2.3.3.1 X-ray photoelectron spectroscopy (XPS): a graphene review*

XPS is used to analyse the surface chemistry of the material, being essential to understand material's suitability for particular applications [67]. The technique has been widely used by researchers in order to determine a sample's "closeness to graphene".

The general target for graphene is a maximum carbon content with minimum oxygen content which is related to the amount of structural defects. However, this approach is rather superficial as the sampling depth plays an important role and the equipment is vertically limited to 5-10 nm [67], significantly above the thickness of the pristine graphene i.e. ≈ 0.35 nm [68]. For this reason, high resolution elemental spectrum analysis is required: by curve fitting the XPS carbon C 1s spectrum, one can identify corresponding chemical bonds (functional groups) based on the position of the peaks i.e. binding energies. XPS databases [69][70] and relevant literature are available in this respect. Figure 2.13 shows the XPS carbon C 1s spectrum of a pristine graphene sample, presenting an asymmetric profile and dominated by a single peak at 284.5 eV [71].

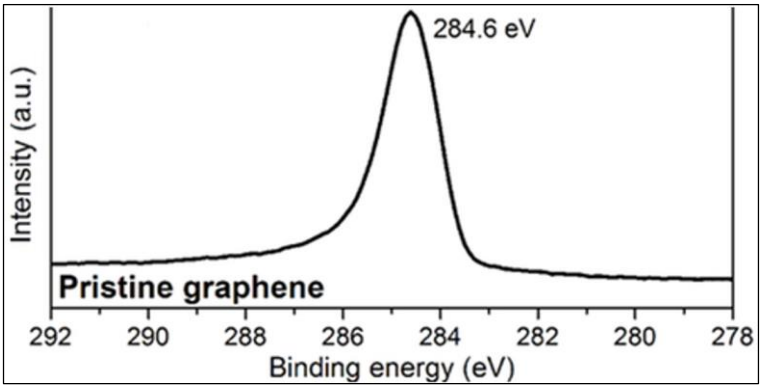


Figure 2.13. XPS high resolution C 1s spectrum of pristine graphene [72].

Moreover, the Auger C KLL spectrum can provide additional information regarding the concentration of $sp^2$ (graphite) and $sp^3$ (amorphous, defective) carbon hybridisation states. Materials with a high concentration of $sp^2$ carbon were reported to exhibit an asymmetric tail towards higher binding energy [73], linked to their high electrical conductivity, while $sp^3$ based elements e.g. diamond, exhibit a symmetrical C 1s band. The D-parameter is used to quantify the width of the C KLL profile (= $peak_{max}$ - $peak_{min}$) and it is correlated with the $sp^2/sp^3$ ratio. Specific values are associated with the pure $sp^3$ domain: 13 eV, respectively pure $sp^2$: 21 eV [73]. Hence, the D-parameter for the graphene based materials is expected to be in the top range ≈ 19-20 eV.

In a remarkable paper, Kaciulis et al. [73] conducted a comparative spectroscopic study of various carbon allotropes, with a focus on XPS and Auger spectrum i.e. D-parameter. The study highlighted possible confusions with regards to C 1s spectrum of the carbon allotropes (including highly oriented pyrolytic graphite and single wall carbon nanotubes) and it recommended a detailed knowledge of sample's history. Moreover, when analysing carbon based nanomaterials, the surface contaminants (carbon-based) can dramatically affect the survey results.

Low O:C ratios are expected for CVD grown graphene, with typical values around 0.1 [74], but post-processing techniques like graphene transfer to $Si/SiO_2$ substrate or device integration leads to an increase in defects' density [75]. For a reliable and direct comparison between various graphene based samples, one should refer to the atomic concentration of the identified chemical elements as per survey spectrum. This eliminates the XPS survey peak variation linked to equipment capability and operation mode, as well as post-data processing (noise or background removal, smoothing techniques, etc.). Table 2-3 collates reported peak positions and carbon-to-oxygen ratios for different graphene based materials.

Table 2-3. XPS carbon peak positions and C:O ratio for graphene materials.

| **Sample** / **eV** | **$sp^2$** | **$sp^3$** | **Covalent** | **Hydroxyl** | **Carbonyl** | **Carboxyl** | **C:O** |
|---|---|---|---|---|---|---|---|
| | **C=C** | **C-C** | **C-O** | **-OH** | **C=O** | **-COOH** | **at [%]** |
| Aliphatic carbon [67] | 284.4 | 285.2 | - | 286.3 | 287.7 | 289.4 | - |
| Graphite oxide [73] | - | 284.5 | 285.8 | - | 287.1 | 288.5 | 5.25 |
| Graphene oxide [76] | 284.7 | | 286.7 | | 287.4 | 288.8 | 1.13 |
| Graphene oxide [77] | 285.5 | | - | 285.9 | 287.8 | 289.3 | - |
| Graphene oxide [78] | - | 284.6 | 286.5 | - | 288.7 | - | 0.905 |
| CrGO - sulphur [76] | 284.7 | 285.5 | 286.5 | | 287.9 | 289.1 | 8.55 |
| CrGO - hydrazine [79] | 284.3 | 284.9 | - | 286.2 | 287.5 | 288.9 | 15.9 |
| CVD SLG [74] | 284.8 | - | 286.6 | - | 287.9 | - | 19 |
| CVD MLG [74] | 284.6 | 285.7 | | | 286.9 | - | 13.2 |
| Thermal rGO [77] | 285 | | - | 286.5 | 287.5 | 289 | 6.3 |
| Bacteria rGO [76] | 284.3 | 284.9 | - | 286.3 | 287.8 | 289 | 8.1 |
| Photo-thermal rGO [80] | 284.9 | - | 285.9 | - | 287.8 | 290 | 40 |

Reduced graphene oxide (rGO) has received considerable attention due to its scalability and low-cost production. XPS analysis is extremely useful in confirming the level of reduction, as well as the quality of the precursor material [81]. As highlighted in section 2.3.1, significant variation is expected based on the synthesis method. The transition from graphite to graphene should be evident, as GO exhibits two main peaks, separated by 2-3 eV, a main carbon peak at 284.5 eV and oxygenated functional groups at 287 eV. The O:C ratio substantially decreases as a result of the reduction process and it shifts towards lower binding energies. Also, the $sp^2$ graphitic component with the peak at 284.5 eV significantly diminishes, confirming the development of a more homogenous chemical environment and ordered structure. The FWHM was reported as 1.4 eV for GO and 0.8-1.1 eV for rGO [46]. Figure 2.14 presents a comparative carbon and oxygen XPS spectra for the chemically reduced graphene oxide, with a clear decrease in density of the surface attached functional groups.

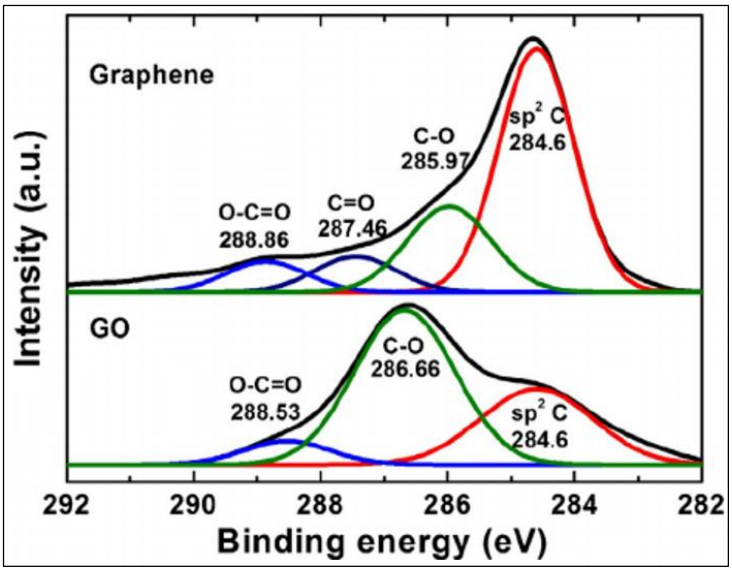


Figure 2.14. C 1s spectra of GO and graphene obtained by in-solution chemical reduction [82].

An interesting comparative study of graphene synthesis via different reduction methods was carried out by Boutchich et al. [76]. A shift towards lower energies in C 1s peak (≈283.8 eV) was reported for the most efficient GO reduction, using hydrazine ($N_2H_4$). Moreover, Meng and Park [83] characterised graphene nanosheets by chemically reducing the graphite oxide using sodium borohydride ($NaBH_4$). The XPS results suggested a partial reduction of GO, with the O:C ratio reduced by a factor of 6.3. In an experimental approach trying to find an alternative for hazardous reducing agents such as hydrazine, W. Chen et al. [79] assessed less hazardous sulphur compounds, such as sodium sulphite ($Na_2SO_3$) or thionyl chloride ($SOCl_2$). The XPS survey confirmed the successful reduction of the GO; based on the chemical

compound used and concentration, the reduction factor varied between 6.4 and 7.8 for sodium bisulfite ($NaHSO_3$), significantly lower than hydrazine i.e. 11.4.

Dai et al. [84] reported superior electrical properties compared to previous published results for single layer rGO, obtained via thermal reduction at 1000°C in $Ar/H_2$ gas, followed by carbon source decomposition which introduced additional carbon radicals. This additional step was aimed to repair reduction-induced rGO defects and it was confirmed by the improved C1 spectrum, with a 9% increase in graphitic carbon (C-C bonds). Thermally reduced GO showed substantial variation depending on the annealing temperature and gas environment, with O:C ratio as high as 0.25 [85].

Furthermore, the XPS data at low binding energy levels can provide information on the valence band spectrum. Akhavan et al. [77] estimated the electron density of valence band compared to the Fermi level, located at 0 eV. As a result of the thermal reduction of GO, the valence peak downshifted from approximately 6 eV to -0.5 eV (see Figure 2.15), indicative of material change from electrically insulating to conductive. A similar trend was reported by Vadahanambi et al. [81], however, in this case, the valence peak was completely absent for prior to microwave irradiation (≈1.8 eV).

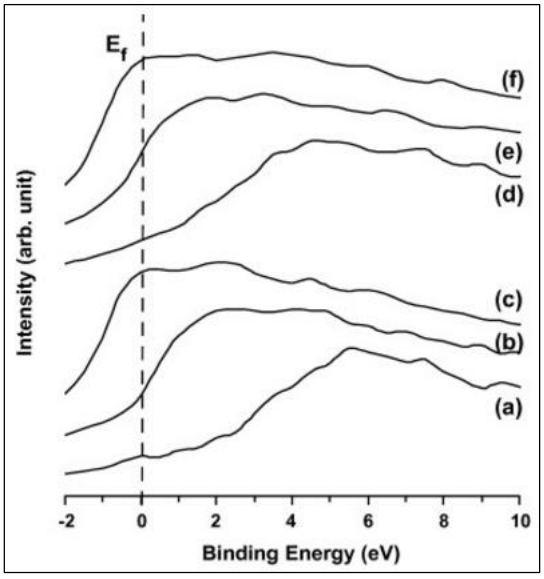


Figure 2.15. XPS valence spectra for: GO (a,d); rGO obtained by one step thermal treatment of GO (b,c); two-step thermal treatment of GO (e,f) [77].

Finally, XPS data analysis requires some level of experience and subsequent data processing is essential for correct results interpretation. The study of the high-resolution oxygen spectrum O 1s can supplement graphene C 1s spectrum

analysis [8]. The complete disappearance of other peaks and bumps and formation of the single peak at 533 eV (C-OH) is indicative of oxygen loss [85].

#### *2.3.3.2 Raman spectroscopy: a graphene review*

Raman spectroscopy is widely used to determine subtle changes in molecular chemistry and structure of various nanomaterials, being the most popular graphene characterisation technique. Ferrari et al. [86] performed the first in-depth Raman study of graphene, identifying its specific features: the G band at ≈ 1580 $cm^{-1}$, corresponding to in-plane vibration of graphitic $sp^2$ carbon atoms and the 2D (or G') peak at ≈ 2700 $cm^{-1}$, explained by two phonon resonance process [30]. The Raman spectra for graphite and graphene is presented in Figure 2.16.

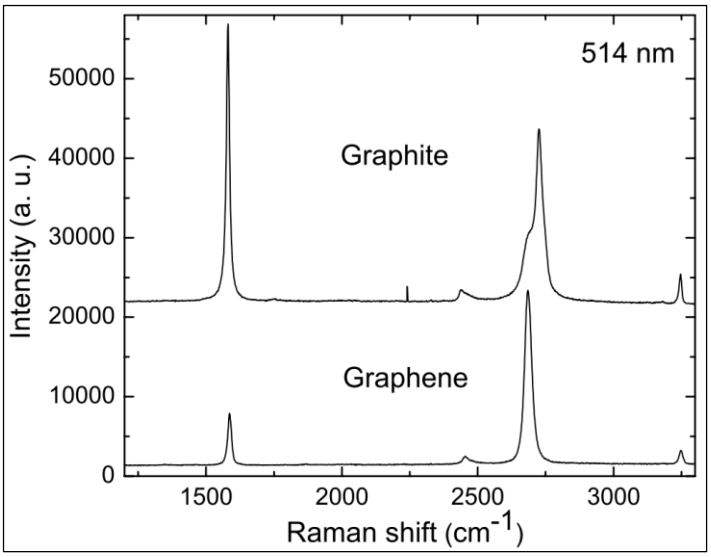


Figure 2.16. Comparative Raman spectra of graphite and graphene [86].

These characteristics are prominent for pristine graphene, however, most of (non-pristine) graphene materials - e.g. few-layer, rGO - exhibit an additional disorder induced D peak at 1350 $cm^{-1}$ [30]. This band is caused by graphene edges and defects [87]. Table 2-4 compiles some literature reported results for some graphene-based samples. A direct comparison between different samples should be cautiously approached as exposure to different Raman energy leads to data variation [88].

Moreover, Raman spectroscopy can aid in distinguishing between $sp^3$ type (functional groups attached to the carbon rings) and vacancy-type defects [89]; an increased number of structural disorders triggers the appearance of a G peak right-shoulder, also named D' peak (≈ 1650 $cm^{-1}$), being more intense for changes in carbon-hybridization [89]. Examples in this respect are oxidation, doping and functionalization.

Table 2-4. Literature reported D-to-G ($I_D/I_G$) band intensity ratio for graphene based materials.

| Material | Synthesis method | $I_D/I_G$ |
|---|---|---|
| SLG [90] | Mechanically exfoliated from graphite | 0.001 |
| SLG [91] | Epitaxial graphene on SiC | 0.05 |
| BLG [92] | CVD grown on Nickel | 0.1 |
| FLG [93] | PMMA decomposition on Silicon | 0.008 |
| FLG [94] | Electrochemical exfoliation of graphite foil | 0.29 |
| FLG [95] | CVD grown on Copper tape | 0.16 |
| rGO [76] | Hydrazine reduced GO; initial GO ratio: 1.4 | 1.9 |
| rGO SLG [96] | GO paper reduced as dispersed in hydrazine | 1.1 |
| rGO MLG [97] | Thermally reduced GO; initial GO ratio: 2.11 | 2.01 |

Ferrari et al. [98] showed that the number of fitted Lorentzian components of the 2D band is indicative of the number of graphene layers. While pristine monolayer graphene presents a sharp and single-curve fitted 2D peak, the number of fitted components increases to four for bilayer graphene [99]. Figure 2.17 illustrates Raman spectra differences for different graphene samples, obtained via mechanical cleavage. Significant deviations were found for up to 5 layers, while higher number of layers showed a graphite-like 2D profile [86][98]. Also, the 2D peak was reported to upshift for increasing number of layers [99]. Variations in the $I_{2D}/I_G$ ratio can be monitored in order to identify further material changes such as doping [100].

Vibrational spectroscopy is highly sensitive, and so, different forms of the graphene based materials, such as graphene nanosheets and graphene nanoribbons exhibit measurable differences in their Raman spectrum. These samples usually exhibit higher D-band peak area and peak intensity [101], which is related to the increased number of defects and edges. Also, the defects' distribution in GO and rGO lead to discontinuity in their hexagonal crystal symmetry, affecting the resonance [102] and hence diminishing the 2D peak. However, for pristine graphene, the $I_D/I_G$ ratio should be close to 0, with $I_{2D}/I_G$ as high as 3 [95].

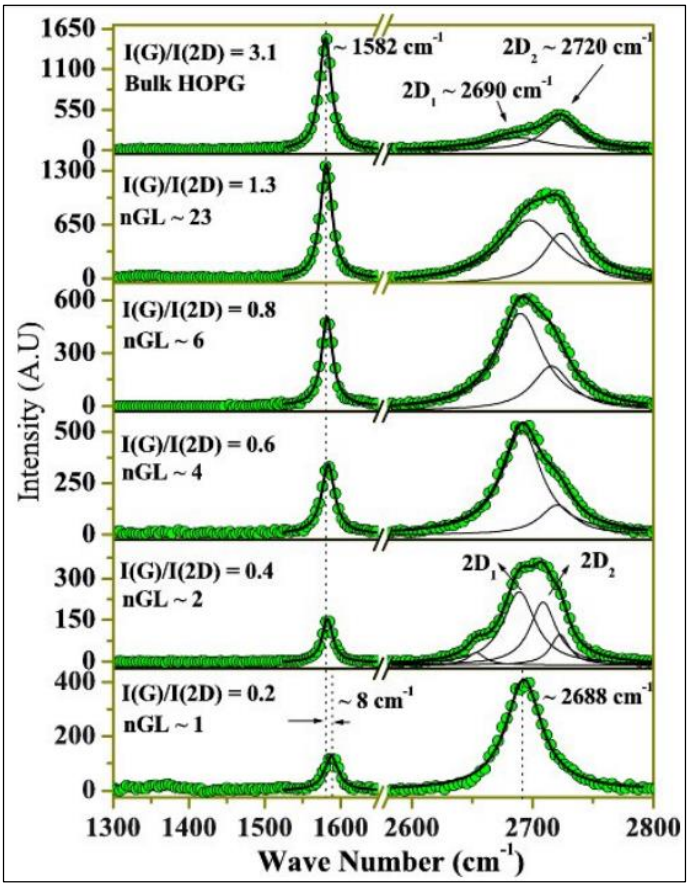


Figure 2.17. Comparative Raman spectra for graphite (HOPG) and graphene with various number of layers (marked as nGL) [88].

With regards to defective graphene based materials such as rGO, Raman spectroscopy is recommended to be performed before and after reduction. The changes in D, G and 2D bands should be evident and representative for the level of reduction. GO exhibits a broader and higher D band due to its abundance of disordered carbon atoms, shown in Figure 2.18. Chen et al. reported a slight blue shift (towards lower frequencies) in both D and G bands upon reduction [79].

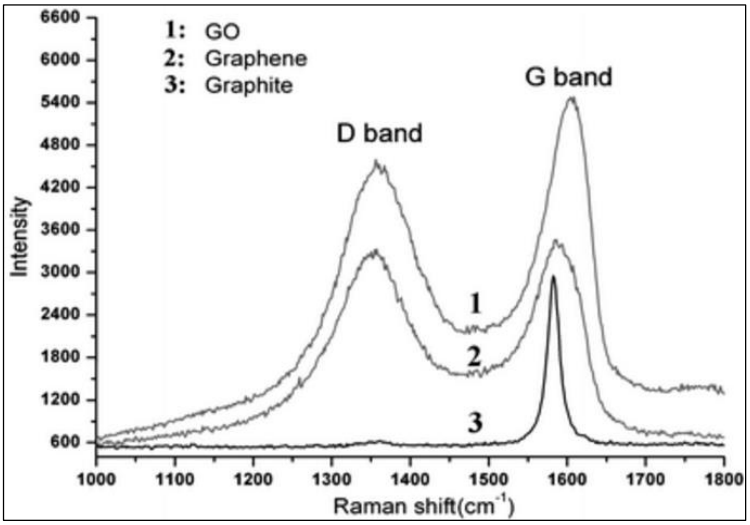


Figure 2.18. Comparative Raman spectra of graphite, GO and rGO [103].

However, as a result of the reduction process, an increase in the $I_D/I_G$ ratio is mostly reported in the literature; this is due to GO's initial defective structure, as no structural repairing takes place. The decrease in the crystallite average size occurs simultaneously with an increase in the number of $sp^2$ domains [41]. The 2D band is weak for both GO and rGO and its interpretation is not as straightforward as for pristine SLG or FLG; additional humps can be noticed at both lower and higher frequency shifts [104]. The intensity of the 2D band for defective graphene structures is associated with the level of disorder, hence, by increasing the level of disorder, the 2D band can be entirely supressed, as in the case GO [105]. The level of oxidation of graphite oxide / GO, as well the exfoliation and reduction processes certainly impact the properties of the obtained graphene materials, further reflected in the Raman spectrum.

More challenges arise for the comparison of different graphene samples. Wang et al. [106] performed Raman measurements on graphene samples as deposited on different substrates and observed upshifts in G and 2D bands by up to 32 $cm^{-1}$. In contrast, epitaxially grown graphene on SiC (EG) showed a significant downshift, which was associated with a strain effect as bonds were formed between the grown graphene and the carbide substrate. Moreover, the Raman laser penetration depth varies with the excitation wavelength e.g. 300 nm depth for 514.5 nm wavelength, 5 nm depth for 351 nm wavelength [107]. The effect of charged impurities received special attention in the work of Casiraghi et al. [108] which demonstrated a large variation in $I_{2D}/I_G$ ratio of identically produced graphene samples. This was associated with effects due to sample substrate, adsorbents and surface residues. Also, the Raman spectra of suspended graphene exhibited broader and more intense G and 2D bands [109].

Overall, Raman spectroscopy is one of the most effective characterisation techniques of graphene based materials. The specific D, G and 2D bands represent the key elements in the interpretation of Raman spectra for graphene samples.

## 2.4. Graphene based biosensing platforms

Based on its high surface area, electrical conductivity, robustness and thermal stability, graphene shows a promising potential in bio/sensing applications [110]. The synthesis-induced properties of graphene and its derivatives enabled the employment of various detection mechanisms for biomolecules detection. In order to satisfy the requirements of a high performance biosensor, graphene requires an optimum

compromise between the amount of “defects” (chemical activity) and its electrical conductivity (purity). According to Liu et al. [111], pristine graphene substrates (e.g. CVD grown, graphite mechanical exfoliation) are desirable for electrical and electronic sensors, while defective graphene materials such as rGO are recommended for (electro)chemical detection, while GO is suitable for labelled optical biosensing platforms. Therefore, the development of a graphene based biosensor requires careful optimization and tuning, and graphene captured researchers’ imagination in this respect.

Zhu et al. [112] exploited graphene’s versatility by proposing a multimodal (electrical, mechanical and optical) biosensor for the detection of immunoglobin G (Ig G) using CVD-grown graphene (see Figure 2.19a). Also, Labroo and Cui [113] successfully detected multiple metabolites (glucose, lactate, xanthine, cholesterol) using a graphene-enzyme ink sensing platform on a microfluidic paper, presented in Figure 2.19b.

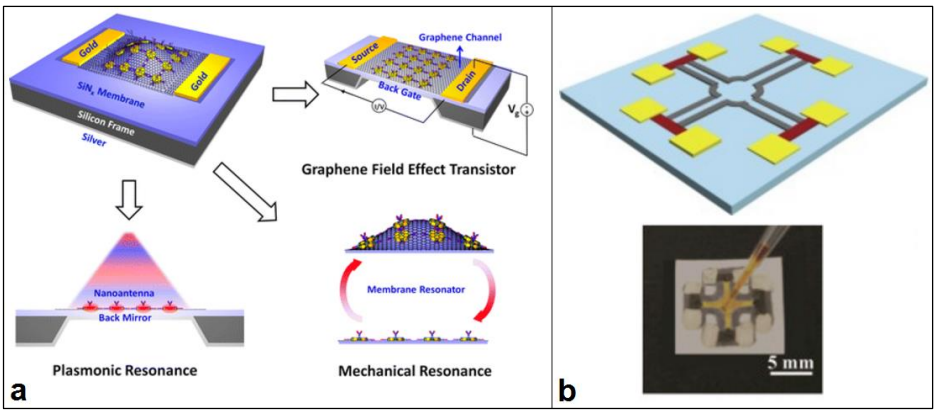


Figure 2.19. (a) Multi-modal graphene based biosensor [112]; (b) graphene based enzyme biosensor printed on microfluidic paper [113].

Pristine (mechanically exfoliated) graphene was shown to be highly sensitive to pH changes, measured as function of change in a simple two-point resistance setup [114]. One of the early reports on graphene FET (GFET) demonstrated its high sensitivity to electrolyte pH and protein presence, even without substrate functionalization [115]. Figure 2.20 shows the biosensor setup and reported response in the presence of bovine serum albumin (BSA). A later work by Soikkeli et al. [116] looked into the utilisation of fusion proteins on GFET to improve graphene based biosensor specificity.

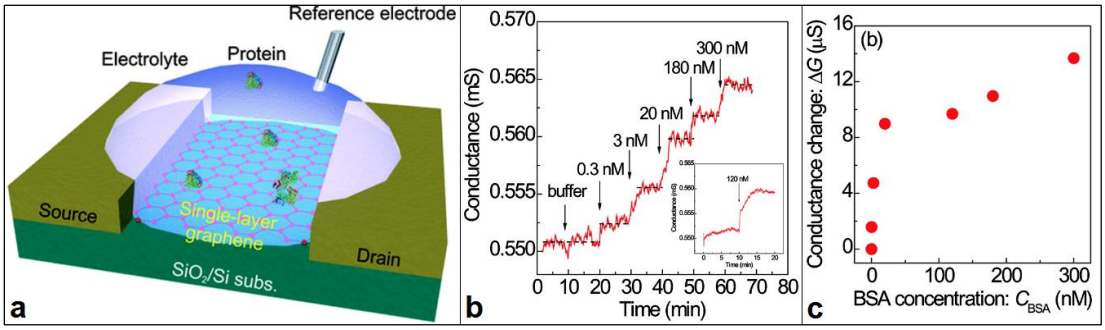


Figure 2.20. Electrolyte gated GFET for electrolyte pH and protein detection: (a) sensor representation and design; (b) conductance changes vs time as per the addition of BSA at various concentrations; (c) quantified conductance change vs BSA concentration [93].

rGO presents edge plane-like defective structures, providing anchoring sites for biomolecules attachment, facilitated via the oxygen containing groups [117]. Bonanni et al. [118] compared the electrochemical activity of rGO materials obtained via different reduction routes for the detection of DNA hybridization and polymorphism events. In this study, electrochemically reduced GO (ErGO) outperformed the chemically reduced GO (CrGO), GO and its graphite oxide precursor. Another comparative study was reported by Zhou et al. [119] who showed an improved electrochemical behaviour of chemically reduced GO via hydrazine. Yang et al. [120] reported rGO potential for multi-analyte (dopamine, ascorbic acid, uric acid) electrocatalytic detection. Moreover, a porous, defective graphene material was recently produced by the laser engraving of polyimide (Kapton) tape [121]. Tehrani and Bavarian [122] put the laser induced graphene (LIG) in practice for the electrochemical detection of glucose, with the sensor response shown in Figure 2.21.

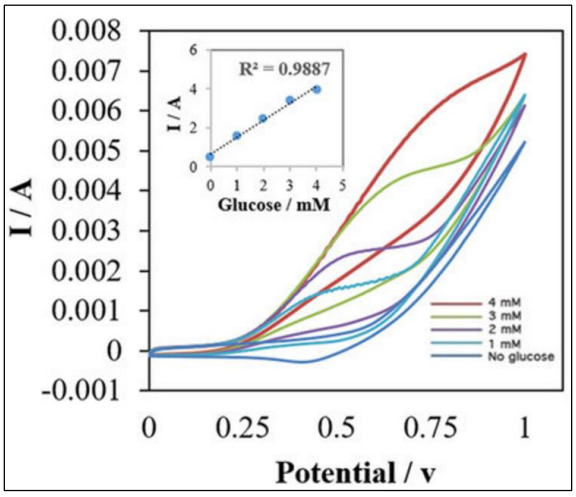


Figure 2.21. Cyclic voltammograms of a LIG-based electrode for increasing glucose concentration (1-5 mM) [122].

Furthermore, an interesting result was reported by Kumar et al. [123] who fabricated an rGO-based paper electrode for cancer biomarker (carcinoembryonic

antigen) electrochemical detection. The incorporation of rGO into the conducting filter paper led to increased surface area and faster electron transfer kinetics. Other rGO-based electrochemical sensors were reported for the detection of glucose [119], tyrosine [123], nicotinamide adenine dinucleotide (NADH) and hydrogen peroxide [124], as well as immunoglobin G (IgG) [125]. As rGO is electrically conductive, it was also integrated in FET biosensing platforms [126][127]. Recent literature reviews in this respect were conducted by Reiner-Rozman et al. [128] and Andronescu and Schuhmann [129].

GO provides ease of dispersibility and an abundance of functional groups on both its edges and basal planes. Additionally, GO exhibits fluorescence over a broad range of wavelengths and its suitability for optical biosensors has been thoroughly discussed in the literature [130]. Wang et al. [131] used pyrene fluorescent die-GO complex for breast cancer cells detection / real-time imaging. Quantum dot conjugated GO was also shown to be effective in optical “turn-on/off” biosensing applications [132][133]. In spite of GO being a poor electrical conductor, Roy et al. [134] reported similar electrochemical properties of GO and hydrazine reduced GO (rGO) coated glassy carbon electrode (GCE) for IgG-AntiRabbit IgG interactions. This is believed to be due to a complete reduction of GO, with no remaining functional groups for functionalization and protein attachment.

Ultimately, significant achievements have been made in the field of graphene based biosensors. A proof in this sense is the progress made towards the commercialization of graphene and graphene oxide based surface plasmon resonance (SPR) biosensor chips [135], shown in Figure 2.22. SPR is a reliable, well-established biosensing technology and these graphene chips are in the process of proving to be a reliable replacement of the current gold-based sensing platforms.

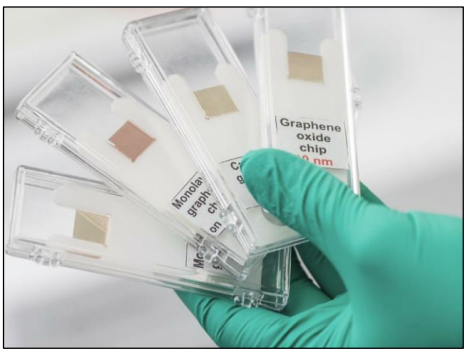


Figure 2.22. Graphene based SPR chips [136].

### 2.4.1 *Graphene functionalization*

Pristine graphene is inert with zero band gap, but chemical surface treatments enable the application-oriented tuning of graphene properties [137][138]. Figure 2.23 presents the two main surface functionalization approaches on graphene: covalent, based on covalent bond formation and non-covalent, associated with hydrophobic, Wan der Waals electrostatic forces [139].

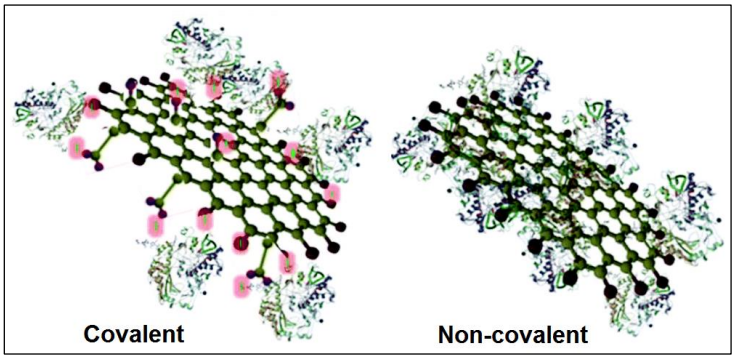


Figure 2.23. Biomolecules immobilization methods on graphene, adapted from [140].

In spite of being effective, the covalent functionalization route leads to structural changes, with a negative impact on graphene's electrical properties. Reliable chemical reactions occur at the edges and / or defective sites of graphene. Hence, it is a common approach to pre-treat the pristine graphene substrate by plasma etching [141][142] to introduce oxygen functional groups, to be used as anchoring points for molecules immobilization. Mohanty and Berry [143] reported the electrical detection of a single bacterium (Bacillus cereus) on plasma-modified graphene-amine.

The EDC-NHS chemistry is commonly employed for the covalent functionalization of carbon materials by activating the carboxyl-reactive groups. An example of this approach is the work carried out by Srivastava et al. [144] who used multilayer graphene for urea detection using covalent urease immobilization. The electrochemical biosensor had a LoD of 39 µg/mL and a 10-second response time, being superior to other GCE and Au-based biosensors reported in the literature. Similar functionalization approaches have been also reported for the detection of food toxin ($AFB_1$) on rGO [145], cancer biomarker α-fetoprotein (AFP) on single graphene sheets [146] and miRNA on CNT/rGO [147]. A different functionalization approach targets reactive intermediates and this path is well addressed in the review conducted by Park et Yan [148]. Diazonium chemistry relies on the grafting of aryl groups (via aromatic nitro groups) to the graphene surface and it was successfully reported on CVD graphene for ovalbumin detection [149], on graphene-modified screen printed carbon

electrodes for milk allergen β-lactoglobulin immunosensor [150], as well as on multi-layer epitaxial graphene for cancer risk biomarker 8-OHdG [140].

On the other hand, the non-covalent functionalization of graphene is adsorption-driven and it preserves graphene's intrinsic structure, but it relies on weak interactions between graphene and the target molecules. Zhou et al. [151] used single-layer CVD graphene for the label-free electrical detection of the carcinoembryonic antigen. The non-covalent functionalization was performed by incubation in dimethylformamide (DMF) and 1-pyrenebutanoic acid succinimidyl ester (PYR-NHS) via π-stacking. The reported LOD (<100 pg/mL) was one order of magnitude lower than the positive clinical value. Lei et al. [152] adopted a similar functionalization method of the epitaxial graphene substrate. Moreover, a rGO FET sensing platform was reported by Stine et al. [153] for real-time DNA detection. A thin layer of graphene oxide was initially deposited on the sensor chips and further reduced in exposure to hydrazine vapour. The chemical modification of the rGO was realized by incubation with glutaraldehyde, facilitating the covalent immobilization of the DNA sequence.

Moreover, graphene and metallic nanoparticles hybrid sensing platforms are of interest due to their increased surface area and sensitivity. With regards to non-covalent surface modification, gold nanoparticles were deposited on CVD graphene by rapid immersion for the electrical DNA hybridization detection [154] or after the SAM-like functionalization of the graphene substrate with thiol (-SH) groups for the electrochemical detection of hydrogen peroxide [155]. Claussen et al. [156] used the covalent functionalization approach for the electrochemical deposition of Pt nanoparticles. The attachment of metal nanoparticles (Au, Ag, Pt) onto graphene materials, led to amplified signals, lower detection limits and higher hole mobility [157] and, implicitly, improved device performance.

Simultaneous or "one pot" functionalization and reduction / exfoliation methods of GO were also reported in the literature [140][158]. Flexible and chemically active rGO sheets were obtained by adding 1-pyrenebutyrate (PB) to the GO solution prior to reduction with hydrazine [159]. This approach is preferred for graphene composites and hybrid materials and it was reported for the covalent [160], as well as non-covalent [161] chemical modification of graphene.

## 2.5. Impedimetric biosensors

### 2.5.1 *The concept of electrical impedance*

The concept of electrical impedance was first introduced by Oliver Heaviside in the 1880s, being further developed by A.E. Kennelly and C.P. Steinmetz [162]. The electrical impedance can be described as a more general, frequency dependent equivalent of the Ohm's law of resistance: $\mathrm{R} = \mathrm{V}/\mathrm{I}$, characteristic for resistors, as well as capacitors and inductors. The electrical impedance quantifies the circuit opposition to a current when a voltage is applied, in either direct current (DC) or alternating current (AC) regime. The electrical impedance expression is characteristic for each electrical component in a circuit:

$$\mathrm{Z_R} = \mathrm{R} \qquad \mathrm{Z_L} = \mathrm{j}\omega\mathrm{L} \qquad Z_C = \frac{1}{j\omega C} \tag{2-2}$$

for angular frequency $\omega = 2\pi\mathrm{f}$, *f* is the measurement frequency. Therefore, the impedance is a complex entity: $\mathrm{Z} = \mathrm{Re(Z)} + \mathrm{j\ Im(Z)}$. The relationship between the current and voltage is presented in the vector diagram in Figure 2.24.

$$\mathrm{Z_{mag}} = |\mathrm{Z}| = \sqrt{\mathrm{Re(Z)}^2 + \mathrm{Im(Z)}^2} \qquad \theta = \arctan\frac{\mathrm{Im(Z)}}{\mathrm{Re(Z)}} \tag{2-3}$$

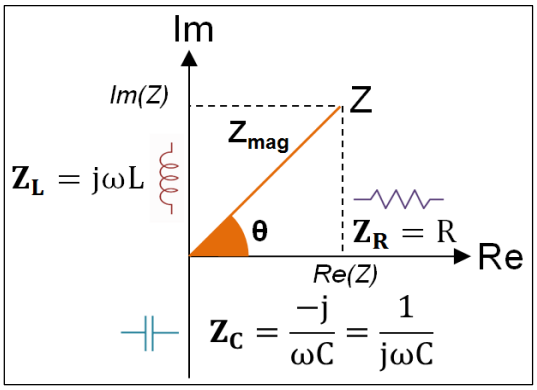


Figure 2.24. Vector impedance diagram for a series RLC circuit.

### 2.5.2 *Electrochemical impedance spectroscopy (EIS)*

Electrochemical impedance spectroscopy (EIS) is an analytical, non-destructive technique that uses impedance measurements in order to evaluate the electro-chemical behaviour at an electrode and/or electrolyte surface [163]. The measurements are usually performed using a potentiostat or an impedance analyzer, as a small excitation AC voltage signal *V*, of small amplitude $V_A$ is applied to the electrochemical system, across a wide frequency range:

$$\mathrm{V(t)} = \mathrm{V_A}\sin(2\pi\mathrm{ft}) = \mathrm{V_A}\sin(\omega\mathrm{t}) \tag{2-4}$$

In a linear or pseudo-linear system, the current response to the sinusoidal input voltage will be a sinusoid of a different amplitude $I_A$ and shifted in phase by θ:

$$I(t) = I_A \sin(\omega t + \theta) \quad (2\text{-}5)$$

The voltage-current relationship is further used to calculate the complex impedance of the circuit:

$$Z = \frac{V(t)}{I(t)} = \frac{V_A \sin(\omega t)}{I_A \sin(\omega t+\theta)} = Z_A \frac{\sin(\omega t)}{\sin(\omega t+\theta)} \quad (2\text{-}6)$$

$$Z = Z_A \frac{\sin(\omega t)}{\sin(\omega t+\theta)} = Z_A e^{j\Phi} = Z_A(\cos\theta + j\sin\theta) = Re(Z) + j\,Im(Z) \quad (2\text{-}7)$$

According to Barsukov and Macdonald [164], the voltage excitation signal should be lower than 25 mV and applied to the system under test (SUT) while in steady state, so that the recorded impedance reflects only the excited system response. By using EIS, one can associate the electrical effects to their chemical counterpart at the electrode / electrolyte surface and identify behaviour changes. Based on the theoretical understanding of the SUT, one can estimate an equivalent circuit of the electrode. The EIS data is analysed by fitting it in the complex plane via Nyquist: *Re(Z) vs Im(Z)* or Bode plots: *frequency vs* $Z_{mag}$ *and* $\theta$ to the equivalent circuit model. The relationship for impedances' combination in series and parallel in a complex circuit is similar to resistors. Once an equivalent circuit is identified, the physico-chemical properties can be correlated with circuit elements and quantify changes. The EIS modelling is a sequential and iterative process, as illustrated in Figure 2.25.

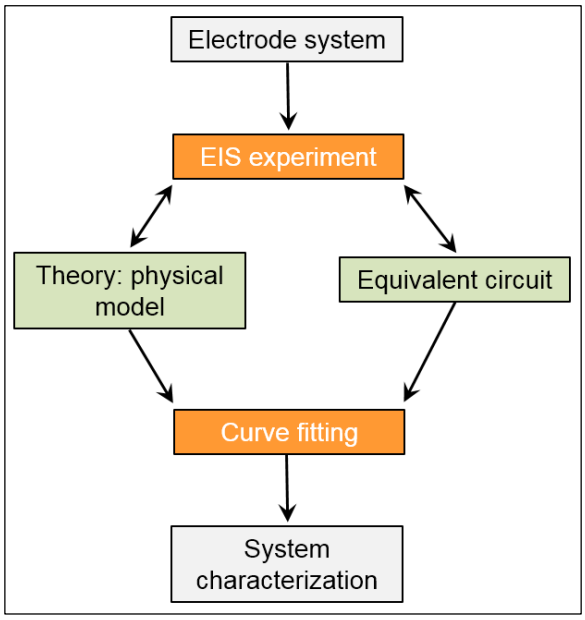


Figure 2.25. Flow diagram of EIS-based system characterisation, adapted from [163].

EIS is applied in a broad range of applications, such as corrosion studies [165], coatings [166][167], batteries [168][169] and (bio)sensors [170]. EIS is a highly sensitive analytical tool, but it requires user experience as there are potential ambiguities in interpretation due to the high (infinite) number of possible equivalent circuits for one system. This can be overcome by iterative comparison between practical and theoretical expectations [162]. The basic electrical components used in equivalent circuit modelling and fitting in EIS applications are presented in Table 2-5.

Table 2-5. Equivalent circuit elements as usually encountered in EIS circuits.

| Circuit component | Significance |
|---|---|
| $R_s$ | Solution resistance due to electrolyte immersion and its related finite conductivity. |
| $C_{dl}$ | Double-layer capacitance formed at the interface between electrode and its surrounding electrolyte. |
| CPE | Constant phase element for non-ideal capacitive behaviour $$Z_{CPE} = \frac{1}{(j\omega)^{\alpha}T} \quad (2\text{-}8)$$ where ω is the angular frequency ($2\pi f$) and for a perfect capacitor, T is the related to the electrode capacitance and α is the constant phase exponent, α=1 for ideal capacitor [171]. |
| $R_{ct}$ | Charge or electron transfer resistance originating from the transfer between a redox couple at the electrode surface. |
| $Z_W$ | Warburg element accounting for mass-transfer impedance, based on the diffusion of electrolyte to the electrode surface (45° phase shift and slope on the Nyquist plot) $$Z_W = \sigma\omega^{-0.5}(1 - j) \quad (2\text{-}9)$$ where $\sigma$ is the Warburg coefficient, ω is the angular frequency. $$\sigma = \frac{RT}{n^2F^2A\sqrt{2}}\left(\frac{1}{C^{*ox}\sqrt{D_{ox}}} + \frac{1}{C^{*red}\sqrt{D_{red}}}\right) \quad (2\text{-}10)$$ where $D_{ox}$ and $D_{red}$ are the diffusion coefficients of the oxidant and reductant, $C^*$ is the bulk concentration of the diffusing species, A is the surface area of the electrode and n is the number of electrons transferred [172]. |

### 2.5.3 *EIS in biosensing applications*

In biosensing applications, EIS is employed as a label-free characterisation tool, allowing for the detection and the analysis of bio-recognition events at modified electrode surfaces. The interfacial changes are thus induced by electrode conductivity

and surface potential changes, and they can be associated with the overall system electrical impedance [173].

Based on the detection method and electrolyte solution, EIS can be classified in two main categories: faradaic and non-faradaic, with representative Nyquist plots and equivalent circuits shown in Figure 2.26. Faradaic current flow implies charge transfer across the electrode interface caused by an electrochemical redox reaction. This triggers a joint effect of resistance (charge transfer) and capacitance (interface layer) at the electrode surface. The semi-circular portion at higher frequencies (Figure 2.26a) corresponds to the faradaic electron transfer process, while the low frequency behaviour provides information about the diffusion process of transport of redox species in the electrolyte to electrode surface [174]. The equivalent circuit is known as a Randles circuit and it is usually employed as a starting point for the equivalent circuit modelling. The circuit components are: solution resistance ($R_s$), double-layer capacitance ($C_{dl}$), charge transfer resistance ($R_{ct}$) and Warburg element ($Z_W$).

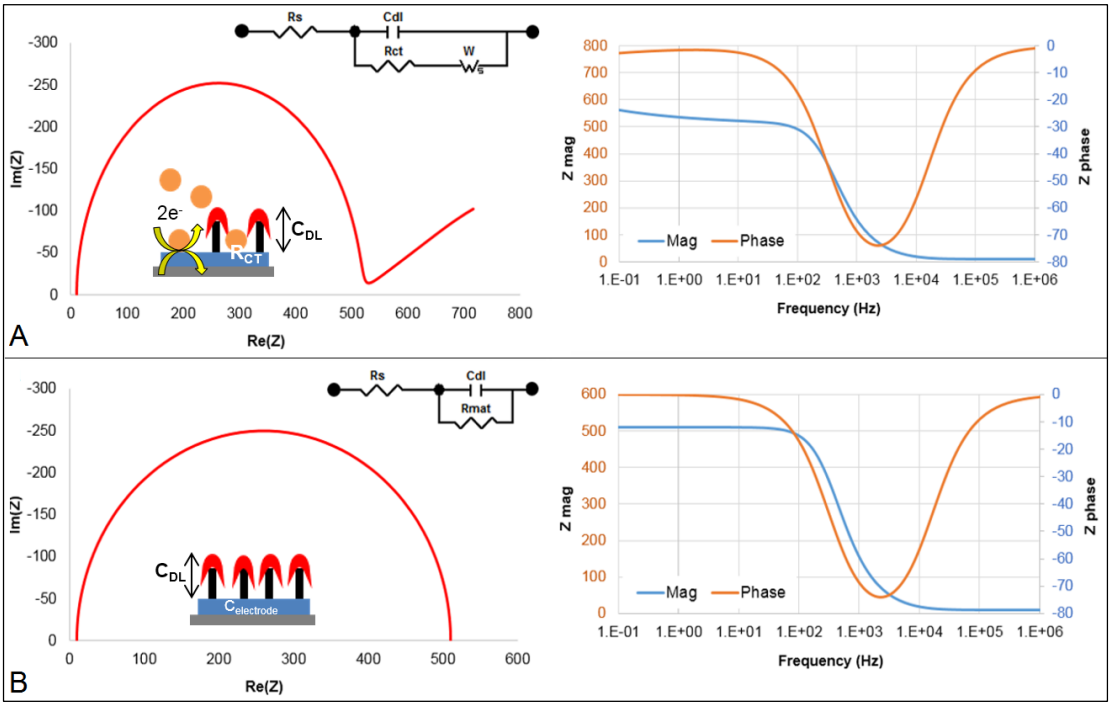


Figure 2.26. Representative Nyquist and Bode plots for: (a) faradaic; (b) non-faradaic impedance, inset shows: equivalent Randles circuit for faradaic EIS and RC circuit for non-faradaic EIS.

On the other hand, non-faradaic impedance spectroscopy targets the electrode properties and surface deposited chemical layers, usually referred as double-layer capacitance ($C_{dl}$) [173]. In non-faradaic detection mode, surface dielectric and charge distribution of local conductance accounts for impedimetric changes [175]. Moreover, the contribution of the electrolyte to the overall system's impedance response is expressed by a resistive ($R_{sol}$) and / or capacitive element ($C_{sol}$). The non-faradaic

charge is associated only with the physico-chemical processes such as adsorption and desorption at the electrode-electrolyte interface, reflected by the double-layer or interface capacitance in the equivalent circuit (Figure 2.26b). Other elements to can be taken into account are the geometric capacitance of the electrode, the contact resistance and the substrate-induced parasitic impedance (resistance and capacitance).

In the work reported by Braiek et al. [176], the electron transfer was considerably reduced during functionalization, as being blocked by the deposited bilayer (self-assembled monolayer formation) and the subsequently attached antibody layer, shown in Figure 2.27. By modelling the impedance response using a modified Randles circuit, the resistive changes were quantified and fitted by a linear trend with a sensitivity of 127 Ω/decade (for increasing S. aureus concentration).

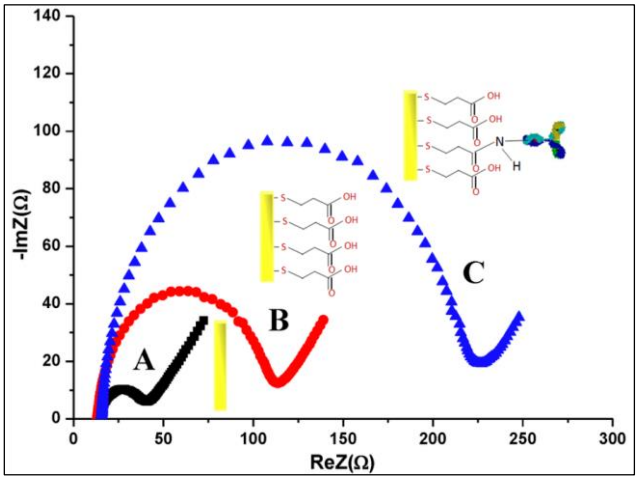


Figure 2.27. Faradaic ($Fe(CN_6)^{3-/4-}$) EIS response for: (A) bare gold electrode; (B) functionalized gold using 3-Mercaptopropionic acid; (C) upon *Staphylococcus aureus* antibody binding, adapted from [176].

Similar $R_{ct}$ data trends have been also reported for the detection of C. difficile toxin using a conventional gold electrode [177], allergen Der f2 on gold coated GCE [178], thrombin on MWCNT modified GCE [179], cholesterol on sol-gel silica/chitosan/MWCNT [180].

However, the EIS detection principle relies on impedance changes, with no one-solution-fits-all. A gold-based immunosensor for E. coli O157:H7 detection [181] showed an inversely proportional trend for impedance with increasing bacteria concentration. The charge of the biomolecule plays an essential role in the either impedance increasing or decreasing trend [182]. Also, Berdat et al. [183] used platinum microelectrodes to faradaically monitor and detect DNA from Salmonella choleraesuis in a three-electrode cell setup, reporting a minimum limit of detection of 1 nM. In this

paper, $R_{ct}$ was reported to decrease for higher DNA concentrations due to the increase of electrical charge carriers in presence of oligonucleotides.

Moreover, Figure 2.28 presents the faradaic impedance response of dengue virus as captured on a nanoporous alumina electrode functionalized with specific immunoglobin G antibody 3H5 [184]. The equivalent circuit accounted for porosity via a parallel RC circuit and did not include a Warburg element, and the sensor performance was described as a linear relationship between the channel resistance and virus concentration.

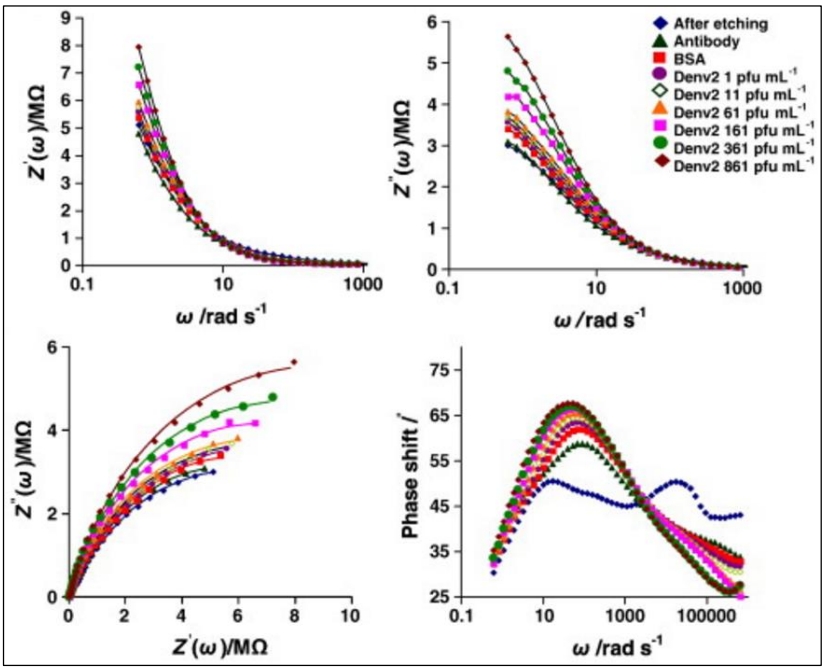


Figure 2.28. Faradaic measurements representation of Re(Z), Im(Z), Nyquist and phase plots as function of the angular frequency, modified from [184].

The literature available on non-faradaic impedance detection of biomolecular interactions is significantly limited compared to faradaic biosensors, employing capacitive sensing platforms. Higher frequencies might be required for the observation of low value capacitive effects ($C_{dl}$) [185], more sensitive to noise. For this reason, single (at most sensitive) frequency measurements are employed for capacitive sensing platforms [186][187].

Lin et al. [188] compared the performance of different membrane-based biosensors using C-reactive protein and myeloperoxidase detection in testing buffer and serum, achieving a LoD of 1 pg/mL. Quantified changes in impedance were monitored, based on the electrical double layer (EDL) variation, reflected by an increase in $C_{dl}$ for antibody and protein doses. In another study, Assaifan et al. [189] targeted changes in phase and capacitance as triggered by the pp65 antigen of the

human cytomegalovirus on the pp65-antibody functionalized ZnO substrate. In this case, the capacitance decreased after biosensor incubation with the antigen, with a sensitivity of 0.07 μF/ln (ng/mL). Bacher et al. [190] used an Ag wire as working electrode in a two-electrode setup for aflatoxin M1 detection in milk. The antibody-antigen interaction led to an overall increase in impedance, whilst showing a decrease in $C_{dl}$.

Last but not least, some charge effects can also be present in non-faradaic impedance testing systems, such as in the case of film electrode modification with more electrochemically active materials, such as CNT [191]. Munje et al. [192] detected troponin-T in fg/mL range (LoD of 10 fg/mL) and showed that the electrical double layer was perturbed due to antibody-antigen binding activity, as the layer was altering the surface dielectric permittivity. The inversely proportional impedance trend for increasing troponin-T concentrations can be explained by the changes in the surface-solution conductivity with the accumulation of the biomolecular double layer.

Luo et al. [193] had a different approach for insulin detection in neat blood serum. As the variation in the magnitude of impedance was limited, the calibration curve was built using the phase changes for different analyte concentration. While the resistor phase is 0°, the phase shift can be attributed to the double layer capacitance of the electrode interface. Moreover, one can control the impedance response (and its fitted equivalent circuit) of the electrode by using an applied DC potential [194]. This was determined by the double layer alignment with the electrode surface [195]. Sharma et al. [196] correlated the impedance phase change with interleukin-8 concentration for detection in serum. By applying a 200 mV DC potential in the non-faradaic employed setup, the authors induced a leaky capacitor behaviour at the surface double-layer. In another study, Qureshi et al. [184] activated gold electrodes with CNT prior to C-reactive protein (CRP) specific RNA aptamer (cRNA) immobilization. The non-faradaic capacitance was extracted at 200 MHz to build the calibration curve (see Figure 2.29) and the sensor exhibited a detection range within normal clinical levels.

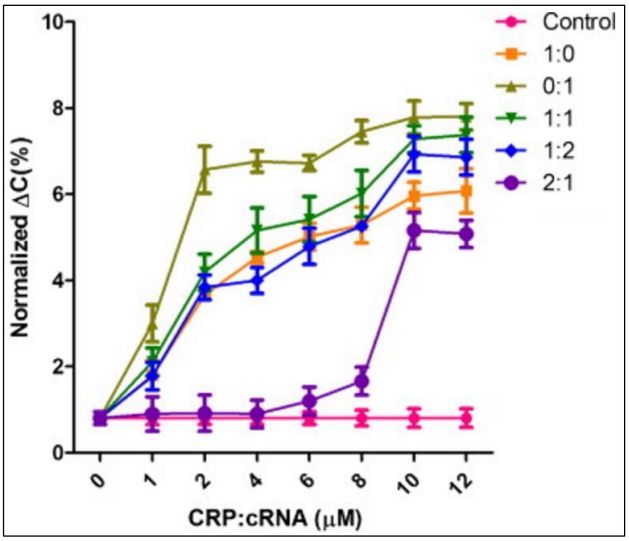


Figure 2.29. Change in capacitive responses dependent on CRP:cRNA concentration ratio [184].

Overall, the redox probe presence can be interpreted as an impedimetric signal amplifier compared to its non-faradaic counterpart [178]. Perfect and continuous monolayers e.g. thiols on gold are expected to cause an increase in impedance [197], as passivating the electrode surface. However, one can argue that the redox probes utilisation in faradaic EIS make this technique non-label-free compared to its non-faradaic counterpart, where the impedimetric response is acquired in testing buffer only.

### 2.5.4 *Graphene materials as impedance biosensors*

The literature review conducted by Bonanni et al. [198] addressed graphene compatibility and suitability for impedance detection, taking into account its high electrical conductivity and large surface area. As discussed in 2.4, graphene properties are highly dependent on the fabrication method, and chemical activation is essential for biosensing applications. Figure 2.30 presents some graphene based materials and structures that were employed in practice as impedance biosensors.

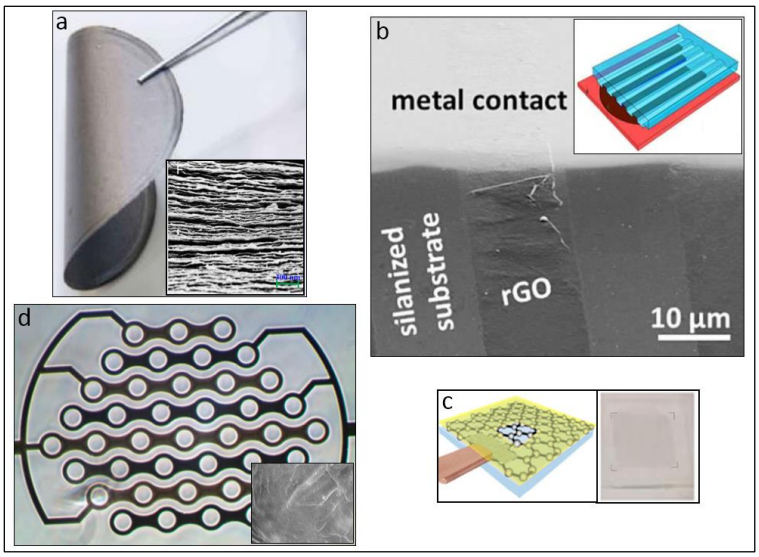


Figure 2.30. Examples of graphene based impedimetric biosensing platforms: (a) graphene paper with inset: SEM cross-sectional view [199]; (b) PDMS stamp for GO deposition followed by thermal reduction [200]; (c) CVD graphene sensor schematic [149]; (d) rGO deposited on a interchain IDE structure [201].

Loo et al. [202] compared the performance of different graphene based materials (graphite oxide, graphene oxide, thermally reduced GO and electrochemically reduced GO) for IgG impedance detection. Disposable printed electrodes were coated with the graphene materials and non-covalently modified with anti-IgG. Faradaic EIS was used to characterise the surface chemistry at each step, targeting $R_{ct}$ changes; thermally reduced GO exhibited the largest impedance variation among all graphene materials and it showed an increasing $R_{ct}$ trend for higher IgG concentrations, in the range 0.01 µg/mL to 10 µg/mL. The suitability of thermally reduced GO (rGO) as electrochemical sensing platform can be explained by its superior electrical conductivity. Also, porous graphene, obtained via a freeze-drying method, was used for faradaic impedance detection of cardiac troponin-I (cTnL) [203]. Delle et al. [200] used a thermally reduced GO multi-linear array sensing platform for histamine (his) detection. Upon anti-his physisorption onto rGO, the magnitude of impedance showed a linear dependence on analyte concentration. The calibration curve was constructed based on the impedance measurements extracted at 10 Hz; in spite of the expected resistive response (phase 0°), discontinuities in the rGO flakes across the linear patterns and further dielectric changes triggered by biomolecules attachment, induced a small capacitive reactance.

Glassy carbon electrodes (GCE) have been coated with graphene based materials and conventionally employed in conventional two or three-electrode cell setup. Lian et al. [204] functionalized CVD-grown graphene in solution using

tryptophan for the electrochemical (DPV) simultaneous detection of ascorbic acid, dopamine and uric acid. The functionalized graphene showed decreased electroactivity compared with GCE or graphene coated GCE, due to its edge defects and increase in $sp^3$ domains. Gong et al. [205] coated a GCE electrode with a composite based on electro-thermally reduced GO. The modified electrode was further incubated with ssDNA capture probe (non-covalent immobilization), preparing the surface for hybridization reaction (dsDNA) with HIV1 gene. The obtained composite film exhibited a layered structure with parallel graphene and Nafion fibrils, facilitating a high density of ssDNA occupied sites. The change in the extracted charge-transfer resistance ($\Delta R_{ct}$) was correlated with HIV1 gene concentration. Regarding its specificity, the interference effect with mismatched DNA varied between 17% and 45%.

Commercially available carbon screen printed electrodes have been also coated with graphene-12HC Ab and settled via a chitosan hydrogel for fibrinogen detection [206]. Using faradaic EIS, the authors quantified $R_{ct}$ changes for different fibrinogen concentrations in an aqueous matrix, human serum and human whole blood samples. A consistent increasing trend for $R_{ct}$ was explained by the increasing density of occupied sites on the electrode surface upon fibrinogen capture, hindering the redox-electrode charge transfer process. In human serum, the graphene based electrodes response indicated a slight decrease in solution resistance and increase in $R_{ct}$. The results are briefly presented in Figure 2.31.

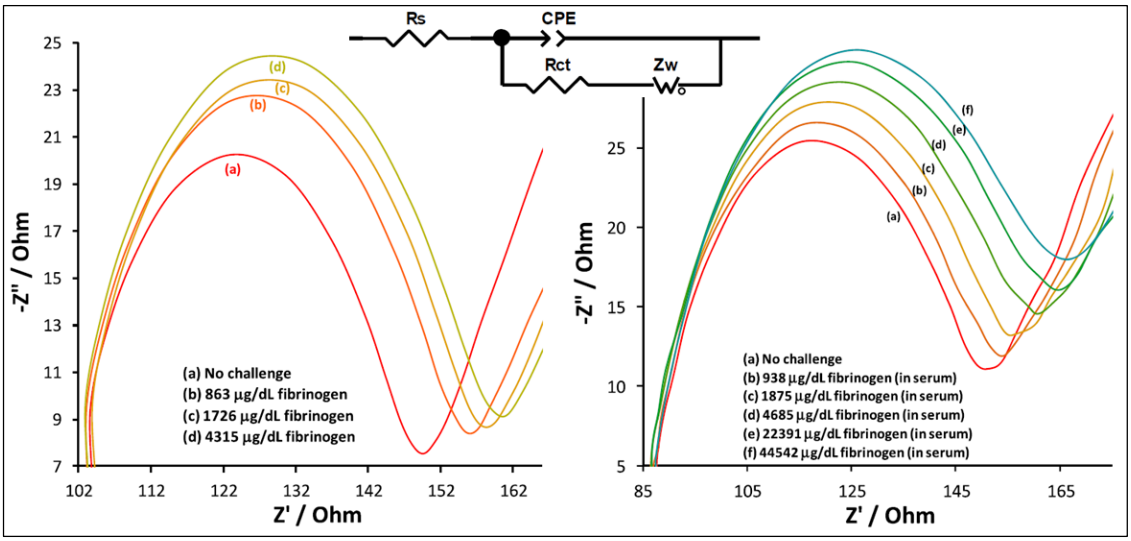


Figure 2.31. EIS Nyquist plots and equivalent circuit of antibody immobilized graphene for fibrinogen detection [206].

Furthermore, Teixeira et al. [207] proposed an immunosensor for pregnancy detection (human chorionic gonadotropin, hCG) based on commercial graphene screen printed electrodes. In order to activate the graphene surface, the authors

performed an oxidation step prior to the electrodeposition of chitosan-gold nanoparticles. The surface changes were monitored via EIS (with 0.1 V applied potential), with the insulating layer formation confirmed by CV. $R_{ct}$ showed a linear increase during graphene functionalization and with increasing hCG concentration in synthetic and real urine samples.

In order to improve bioreceptor immobilization, graphene based materials have been decorated with gold nanoparticles. rGO and Au nanoparticles (NP) were co-electrodeposited onto the surface of indium tin-oxide (ITO) electrode array and covalently functionalized with anti-CRP antibody via EDC/NHS for C-reactive protein (CRP) detection [208]. The rGO hybrid biosensor was EIS tested in a two-electrode configuration, using standard ferri/ferrocyanide redox probe. The rGO-Au NP deposition showed an increase in the surface area of the electrode and $R_{ct}$ significantly decreased upon the electro-coating step, based on the improvement of the charge transfer rate due to conductive gold. The impedance change was proportional to CRP concentration, being most sensitive at low frequencies up to 10 Hz.

CVD graphene was also reported as biosensing platform. Gutés et al. [209] decorated CVD graphene with Au NPs for faradaic impedimetric detection of health hazardous polybrominated diphenyl ethers (DBDEs, flame retardant). The graphene-Au NPs electrode showed a nearly fourfold increase in $R_{ct}$ in the presence of peptide, whereas the change was negligible for plain graphene, with the surface events being extracted and quantified using a Randles circuit equivalent. In another study, Eissa et al. [149] electrografted CVD grown single-layer graphene (transferred to glass) with diazonium salts, prior to covalent immobilization of the ovalbumin antibody (OVA-Ab). Faradaic EIS was used to investigate graphene surface and structural changes. The carboxyphenyl surface modification induced a charge transfer dominant behaviour at the graphene electrode surface, with increasing $R_{ct}$ for subsequent CV electrografting cycles. The covalent immobilization of OVA-Ab was reflected by a drop in impedance and $R_{ct}$, followed by a subsequent increase upon BSA attachment. It should be noted that the impedance was still lower compared with aryl functionalized graphene electrode, but overall, the impedance change was linear with increasing protein concentration.

Yagati et al. [201] proposed an electrochemically rGO interdigitated chain electrode modified for insulin detection. The non-faradaic impedance response was dominated by dielectric capacitance at high frequencies, solution resistance at intermediate frequencies and interfacial capacitance at low frequencies. The

calibration curve was built at a testing frequency of 4.7 kHz. Figure 2.32 shows that during the chemical modification steps, the capacitive reactance dropped due to the formation of dielectric layer, with the electrode resistance presenting an opposite trend.

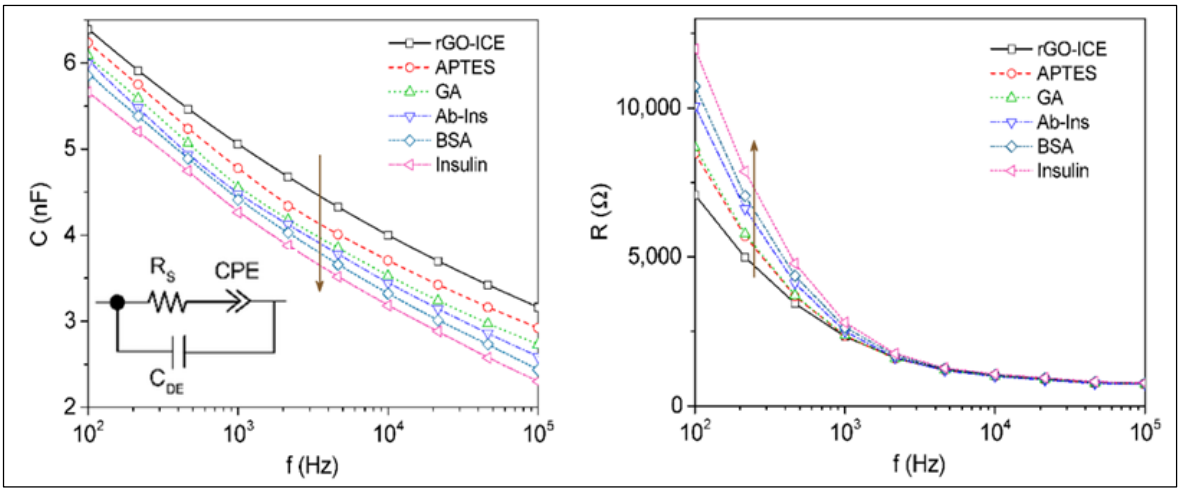


Figure 2.32. rGO chain IDE extracted capacitive and resistance response based on non-faradaic EIS, modified from [201].

Zhang et al. [210] also used pi-stacking to activate hydrazine reduced GO with tryptamine (TRA) for hepatitis B virus detection using DNA hybridization events and faradaic impedance measurements. The Nyquist semicircle diameter ($R_{ct}$) steadily increased during the functionalization steps, as well as for higher cDNA concentrations, due to the restrained electron transfer / electrostatic repulsion of the negatively charged DNA (phosphoric acid groups).

Rich in functional groups which are dependent on the synthesis method, graphene oxide represents a suitable alternative as chemical sensor and biosensor [211]. GO is known as a poor electrical conductor [212], but, interestingly, some reported impedance performance is comparable with graphene. Erdem et al. [213] used a chitosan-GO composite functionalized with amino-linked DNA aptamer for lysozyme (LYS, protein) detection. The electrode behaviour was fitted with a conventional Randles circuit and EIS was used to optimize the GO and APT concentrations to detect LYS by targeting $R_{ct}$ changes. The sensor exhibited good selectivity over interfering species such as BSA. Another study employed an Au-GO composite for DNA detection [214]. A linear decrease in $R_{ct}$, as well as an increase in the capacitive reactance $X_c$, was observed during hybridization and for increasing concentrations of the target DNA. As the GCE electrode was coated with GO and dried under an infrared lamp, a reduction process might have been initiated, explaining the electrode's reported high surface roughness and good electrochemical performance.

Other studies reported GO and related nanocomposites as biosensing platform for the detection of: aflatoxin B1 [215], DNA [216] and tlh gene [217].

### 2.5.5 *The EIS behaviour of coatings and porous electrodes*

The electrochemical impedance behaviour of composites and novel porous materials is more complex compared to thin metallic films. Its understanding is essential for the progress of impedimetric sensors using novel materials. Figure 2.33 presents some standard equivalent circuits for coatings and porous electrodes.

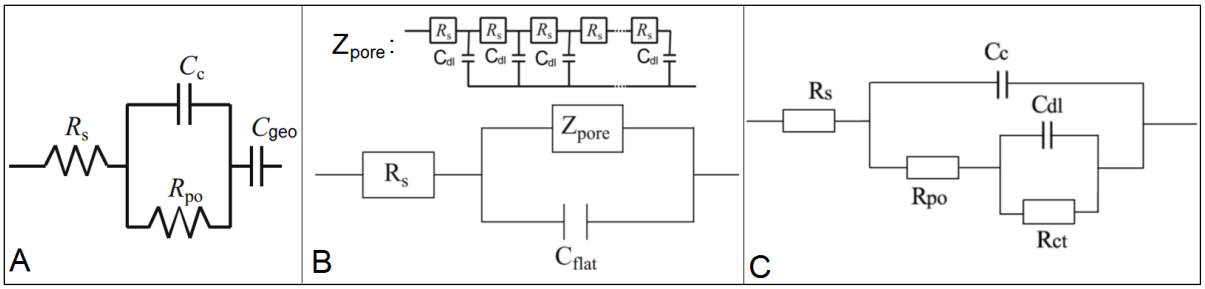


Figure 2.33. Equivalent EIS-based circuit for: (A) coating without corrosion; (B) electrode containing flat and porous part, with identical, parallel and identical pores; (C) damaged organic coating, adapted from [245][246][218], where: $C_c$ – coating capacitance; $Z_{pore}$ – porous layer impedance.

Depending on the electrode surface events and material roughness, the capacitive element can be replaced by a constant phase element (CPE, see Table 2-5) in the case of an unevenly distributed double-layer electric field [219]. Moreover, Franco et al. [220] introduced a series inductance component in the electrochemical impedance for metallic oxide at high frequency to compensate for the disordered movement of charge carriers at complex morphology structures. It has been also shown that the geometry of the pores impacts interface impedance, as presented in Figure 2.34.

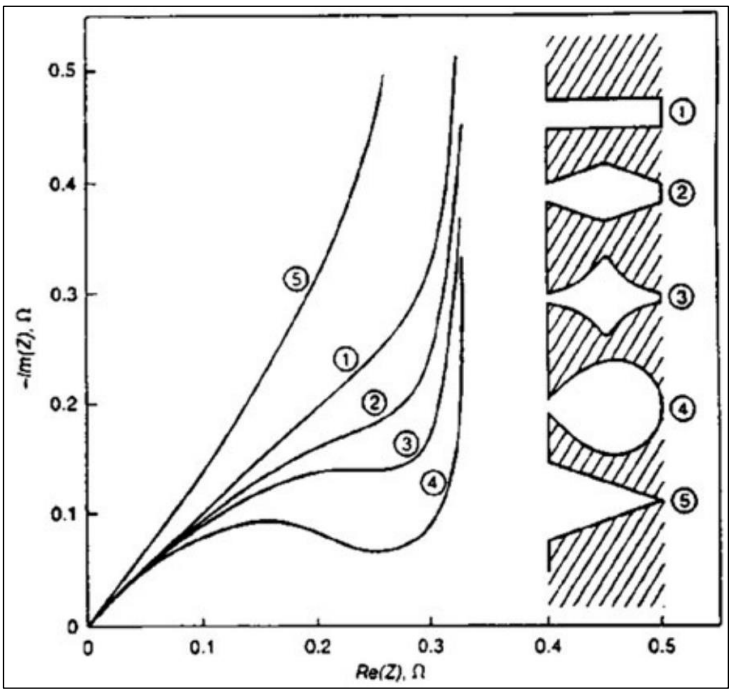


Figure 2.34. EIS Nyquist plot for different pore shapes [221].

While the impedance behaviour of conventional electrodes can be fitted by a Randles circuit (see Figure 2.26), the characterisation of the electrochemical behaviour of novel materials require the adjustment and combination of standard circuits, according to the surface phenomena. Most EIS investigations using porous carbon materials and graphene composites focused on supercapacitors and batteries, with some literature reported circuits captured in Figure 2.35. If in some cases, different material layers can be separated in corresponding parallel R-CPE circuits (Figure 2.35A), the capacitive-related behaviour might be needed to be specifically defined to account for electrode geometry / roughness, reaction areas of the electrode (double-layer), diffusion inside the composite (diffusion layer) and surface adsorption as presented (see Figure 2.35D and Figure 2.35E). In other cases, at low frequencies, the diffusion events were represented by Warburg impedance (see Figure 2.35F).

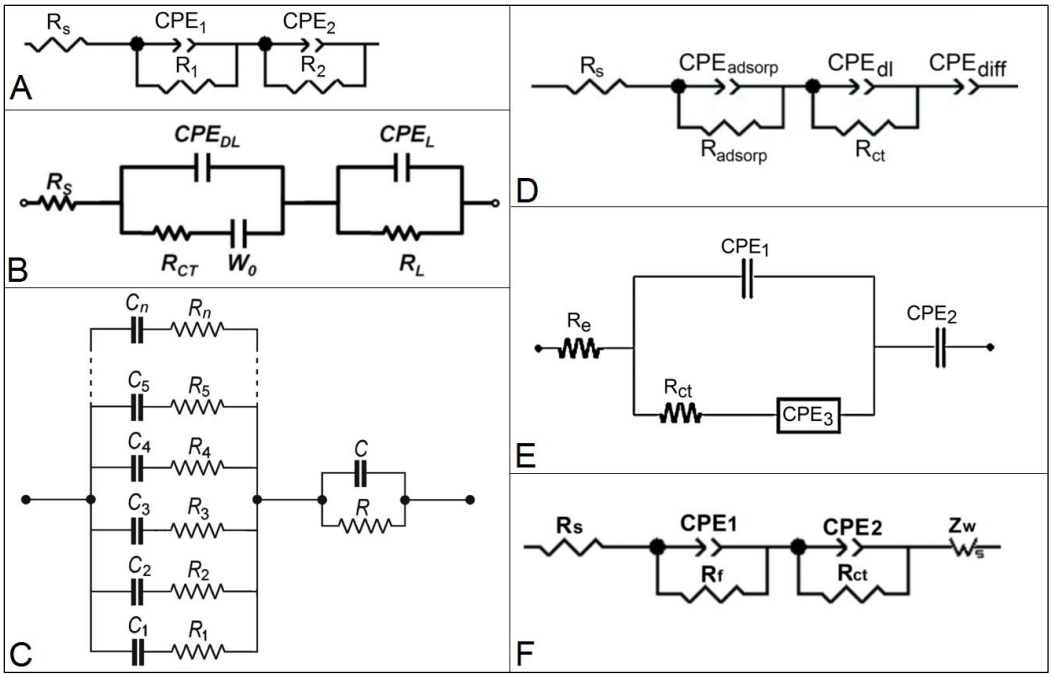


Figure 2.35. Examples of reported equivalent circuits of: (A) conductive polymer and MWCNT nanocomposite film in acidic solution [222]; (B) ruthenium oxide ($RuO_2$) anchored graphene and CNT hybrid foam (RGM) supercapacitor [223]; (C) universal equivalent circuit for a symmetric carbon-based supercapacitor [224]; (D) Ag–$MnO_2$/graphene composite [225]; (E) carbon fiber/PAni composites [226]; (F) Si/CNT/C electrode [227].

## 2.6. High-frequency (bio)sensors

### 2.6.1 *Scattering parameters (s-parameters) concept*

Due to the difficulty in measuring voltages and currents at RF and microwave frequencies, scattering parameters (s-parameters) are used to describe the power flow in the measurement network [228]. The concept of the s-parameters is associated with wave propagation and can be expressed at any frequency [229] for frequency-dependent circuits. The measurement of the s-parameters require the utilisation of a network analyzer; this instrument outsources a voltage wave into the system under test (SUT) and measures the reflected and transmitted voltage to compute the s-parameter(s). The simplified measurement principle is presented in Figure 2.36. A part of the signal gets transmitted into the circuit, while some is reflected back to the source.

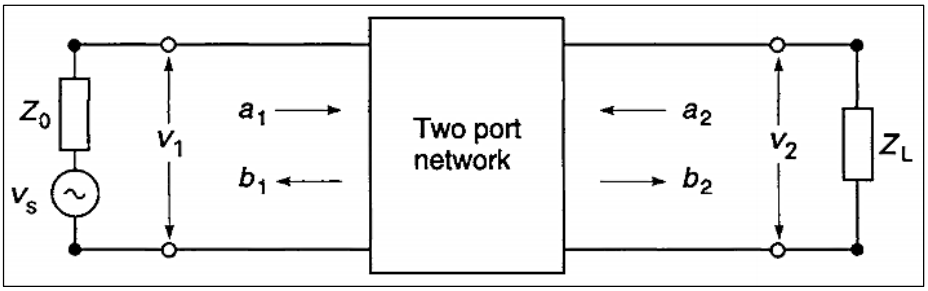


Figure 2.36. Two port scattering network with source and load [286].

The s-parameters describe the reflection and transmission coefficients of the device under test relative to the reference / source impedance and they are mathematically related to the impedance of the load [230]. Analog circuit elements and antennas require one-port, while transmission lines and filters necessitate a two-port connection; the number of ports correspond to the input-output interface of the SUT. For example, for one-port devices $S_{11}$ is defined:

$$S_{11} = \frac{Z - Z_0}{Z + Z_0} \quad (2\text{-}11)$$

where: Z is the impedance of the DUT and $Z_0$ is the reference impedance. The s-parameter for two-port devices extends as a 2 x 2 matrix:

$$S = \begin{bmatrix} S_{11} & S_{12} \\ S_{21} & S_{22} \end{bmatrix} \quad (2\text{-}12)$$

where: $S_{11}$ and $S_{22}$ are the reflection parameters for each port and $S_{12}$ and $S_{21}$ are the transmission parameters forward and backward gain respectively.

### 2.6.2 *Source impedance matching*

The concept of impedance matching is related to antenna transmitter-receiver, and it implicates that by matching the impedance of the source (transmitter) with the load (receiver), maximum power is transferred between the two parts [231][232]. Figure 2.37 shows the relationship between power transfer and efficiency, being maximum 50% in source-load impedance matching conditions [233].

$$Z_{OUT} = R_{out} + jX_{out} \quad (2\text{-}13)$$

$$Z_{IN} = R_{in} + jX_{in} \quad (2\text{-}14)$$

$$Z_{OUT} = Z_{IN} \overset{\text{if}}{\leftrightarrow} R_{in} = R_{out} \wedge X_{in} = -X_{out} \overset{\text{then}}{\Longrightarrow} P_{max} = \frac{V^2}{Z_{IN}} \quad (2\text{-}15)$$

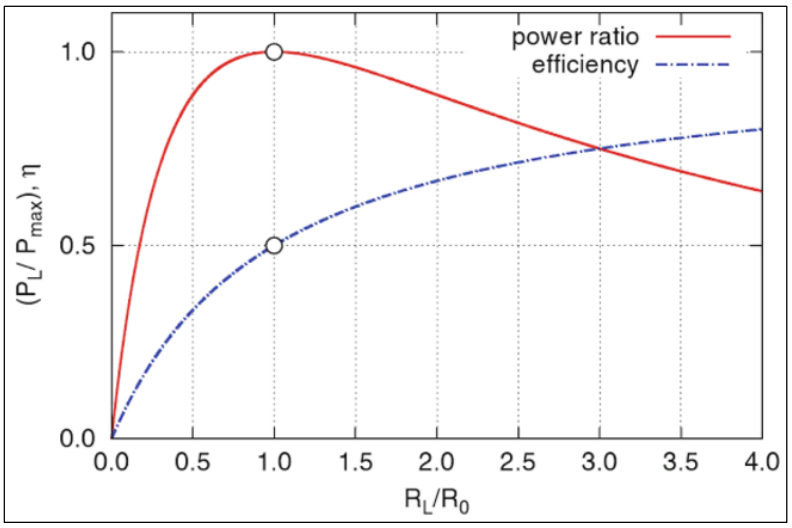


Figure 2.37. Power transfer and power efficiency, where: $P_L$ - maximum power dissipated in the load (when $R_L = R_0$), $R_L$ - load resistance and $R_0$ - reference or source resistance and $\eta$ - power transfer efficiency [234].

Figure 2.38 presents the impedance matching concept: the load impedance becomes equal to the source impedance by using an additional circuit. There are several methodologies to achieve impedance matching, but in terms of lumped elements: two (L-matching) or three-element (T-matching, Π-matching) networks are used. While the first one relies on LC additional circuit, the latter one also allows for Q-factor tuning for the matching circuit by using a third component.

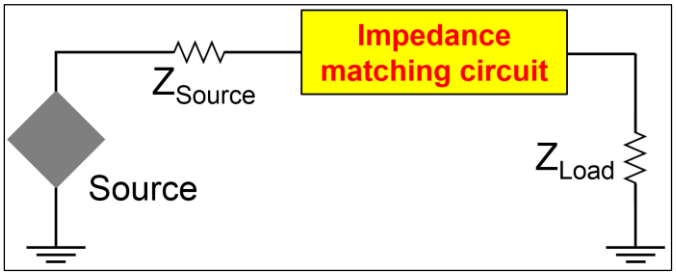


Figure 2.38. Matching circuit concept (black box).

Specific LC arrangements are employed in the case of purely resistive loads, depending on the load value compared to the source resistance. When dealing with complex loads, the additional elements must absorb any stray reactance (shunt capacitors, series inductors) and resonate them with an equal and opposite reactance (capacitive element for inductor and vice versa) at the frequency of interest [235].

Moreover, the Smith chart is a popular RF tool, built from constant resistance and constant reactance circles. The centre of the chart represents the impedance matching point and the load is directed towards by using two arc “movements”: clockwise for inductive element and anticlockwise for capacitive element. Figure 2.39 exemplifies the LC source-load matching network solutions on the Smith chart.

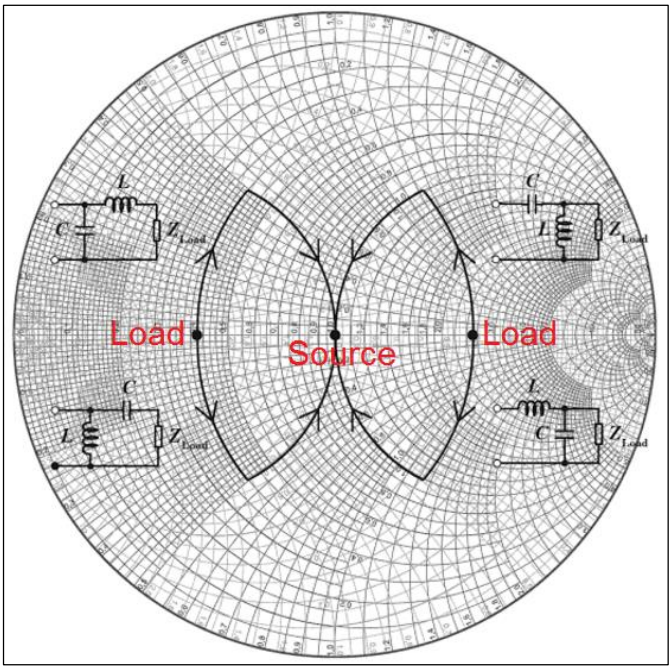


Figure 2.39. Smith chart representation of solutions using L-matching networks to match the load impedance to the 50 Ω source impedance [236].

### 2.6.3 *Electrical and high-frequency (bio)sensors*

Dielectric spectroscopy dominates the high-frequency domain for biological investigations. The main advantages of this technique are its capability for label-free detection and its compatibility with various substrates and sample media, either conductive or insulating. However, the interpretation of the results requires a complex multi-disciplinary approach, with difficulties arising from isolating and identifying different mechanisms triggered by the interaction between electromagnetic waves and biological matter. However, the potential of microwave technology for cancer diagnosis was reported back in 1980 [237], and recent progress led to a simplified approach via s-parameter monitoring [238].

Afroz et al. [239] proposed an in-vivo SiC antenna sensor for continuous glucose monitoring. The reflection parameter ($S_{11}$) steadily downshifted for increasing glucose concentrations and a pig blood sample was used as proof of concept, with a variation of 62 kHz shift per 1 mg/dL change in concentration. Park et al. [240] also looked into mediator-free glucose detection using a ground-signal-ground (GSG) gold (500 nm) pattern, based on a transmission line 2-port design. The glucose sample was placed at the gap between the two ports. The resonant dip at 3.76 GHz for $S_{11}$ decreased and downshifted for increasing glucose concentration, while $S_{21}$ exhibited an increase in amplitude. Based on the equivalent circuit, the authors extracted the

parameters of interest, notable the electrical impedance, which decreased by 5 kΩ per each mM (corresponding to 18 mg/dL [240]) change in glucose concentration.

Lee et al. [241] designed a planar split-ring resonator for prostate specific antigen (PSA) and cortisol detection. The gold sensing area, described by an equivalent RLC circuit, was functionalized with a cysteine-based specific antibody and $S_{21}$ was quantified during functionalization and PSA detection. The average resonant frequency of the bare sensor was 10.5 GHz, having a Q-factor of 50. The biosensor successfully detected 0.1 ng/mL of PSA which triggered a 4 MHz downshift in the transmission parameter $S_{21}$ dip.

Moreover, Alvarez et al. [242] investigated changes in the molecular composition for sandwiched-protein attachment on gold. The reflection parameter ($S_{11}$) presented multiple peaks at microwave frequencies above 8 GHz. Significant amplitude and frequency shifts were reported, with the appearance of a second peak at 9.2 GHz in the presence of streptavidin conjugated with horseradish peroxidase (SA-HRP).

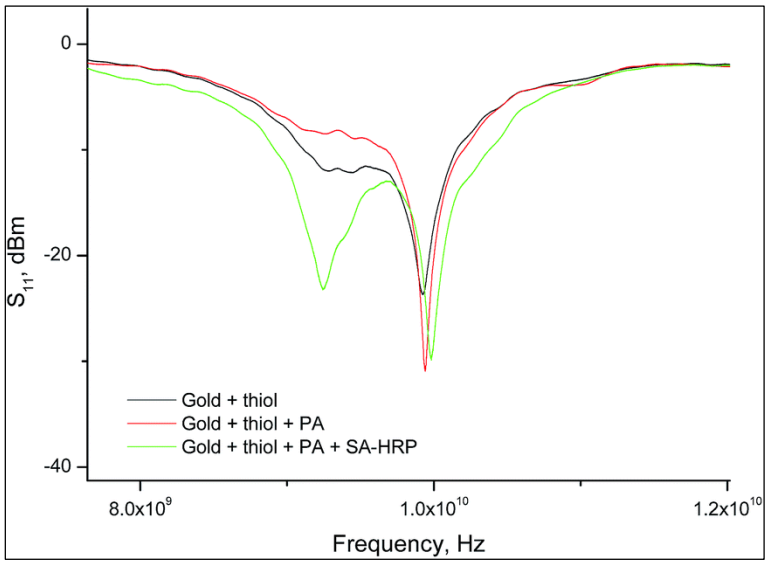


Figure 2.40. $S_{11}$ peak variation for a gold-modified electrode [242].

Therefore, apart from its EIS functionality, the network analyzer can offer a backward approach to the equivalent circuit modelling, while allowing for sufficiently high frequencies in order to isolate the capacitive components. Casares et al. [243] showed that the equivalent capacitance value of an IDE can be determined as a function of the reflected power parameter ($S_{11}$). Additional circuitry or simple IDE design variations can be used to further tune the sensitivity of the biosensing platform.

For example, an interdigitated electrode (IDE) design has been adapted to serve as RF passive device by Lee et al. [244]. The device acted as a resonator at its

self-resonance frequency. The authors correlated a remarkable femto-farad range variation in capacitance with $S_{11}$ (at 10-11 GHz) as triggered by streptavidin-biotin interaction on the CNT coated electrodes. The reflection parameter dip decreased by approximately 20 dB (to -50 dB) for biotin and further by 30 dB (to -60 dB) for streptavidin binding compared to initial IDE $S_{11}$ minimum (at -30 dB). Chang et al. [245] proposed the utilisation of composite metamaterial in order to downsize the antenna dimensions. Using an IDE-microstrip arrangement, different methanol concentrations were tested, reporting a positive correlation trend in terms of frequency shift and reflection parameter.

A valuable example in the field is the work conducted by Kim et al. [246], who developed an electrical resonator biosensor for glucose detection by coupling an intertwined spiral inductor with a standard IDE structure. Two-port measurements have been used in order to fully characterise biosensor electrical properties, found to exhibit a sensitivity of 199 MHz/mg/dL [246], with the reported results shown in Figure 2.41.

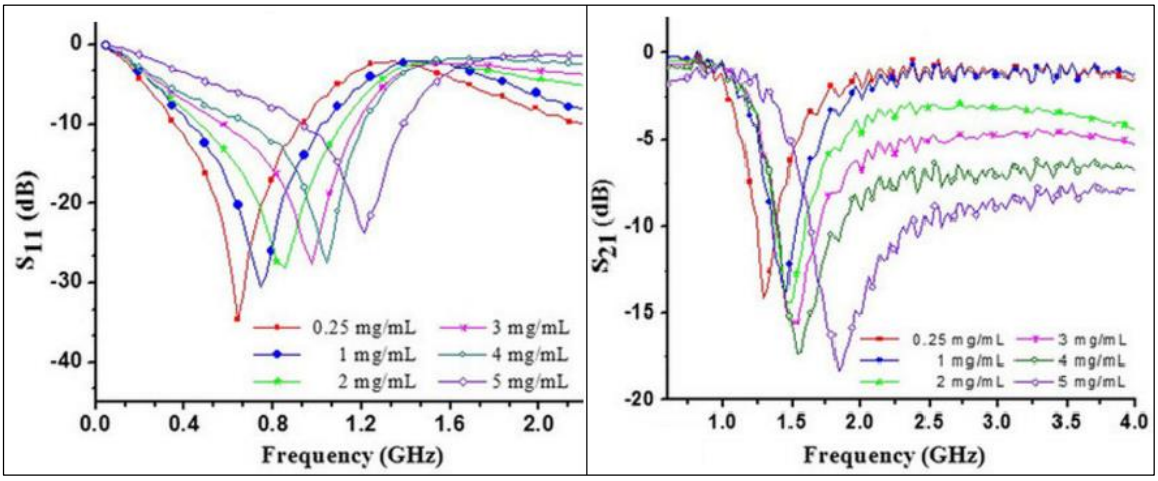


Figure 2.41. RF sensor response to different glucose concentrations (aqueous samples) [246].

### 2.6.4 *Graphene in high-frequency and RF-based (bio)sensing*

The outstanding electrical properties of graphene makes it a suitable candidate for high-frequency (up to THz) circuits and applications. Graphene based materials and nanocomposites were reported to have a good microwave absorption capacity [247]. Figure 2.42 shows some high frequency graphene based devices as reported in the literature for high-frequency (> 1 MHz) sensing.

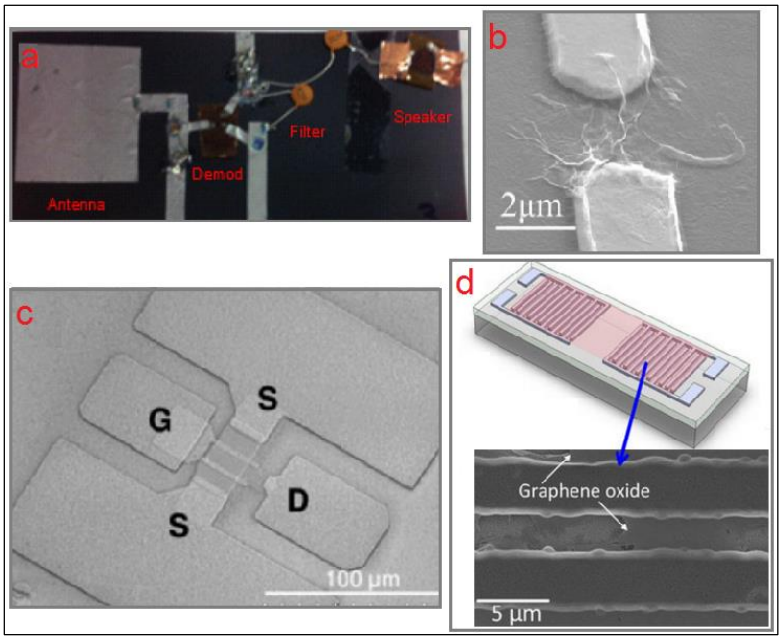


Figure 2.42. Examples of graphene based materials and devices employed as high frequency sensors: (a) flexible graphene antenna on polyimide substrate [248]; (b) RF biosensor based on rGO interconnector between two signal electrodes [249]; (c) GFET fabricated on microbial cellulose substrate [250]; (d) surface acoustic wave humidity sensor with graphene oxide sensing layer [251].

A remarkable result was reported by Mannoor et al. [252] who provided a fully bio-interfaced graphene based wireless sensing platform for highly sensitive bacteria detection. The sensor combines wireless, powerless resonant design and a simple resistive detection approach. The passive telemetry device was designed based on a gold inductive coil for transmission and an IDE gold-graphene resistive sensor for a minimum reflection parameter of ≈ -28 dB at 330 MHz. Using silk bioresorption, the gold-graphene sensor was efficiently transferred onto the tooth surface. The single layer graphene covering the IDE-sensing area of the device was functionalized with antimicrobial peptides which shows activity towards different bacteria (E.coli, H. pylori and S. aureus). The resonant frequency, bandwidth of the sensor and graphene resistance change were monitored for increasing bacteria concentration. The reported result of a limit of detection of ≈ 100 cells in real time (< 10 min) is notable, representing a great progress towards specific single-cell detection.

Interestingly, in a recent work by Park et al. [249] thermally reduced graphene oxide was functionalized with phenylbutyric acid (PBA) linker for glucose detection at frequencies above 2 GHz. The rGO was carefully placed on the gold-defined signal lines via dielectrophoresis. $S_{11}$ and $S_{21}$ showed significant changes with the addition of increasing concentrations of glucose (see Figure 2.43), however, the biosensor performance was assessed based on the equivalent circuit elements, already known

from the sensor design. Notably, the electrical resistance showed the most linear behaviour ($R^2$ = 0.954) and the reported LoD of the biosensor was 3 x $10^{-5}$ mol/L.

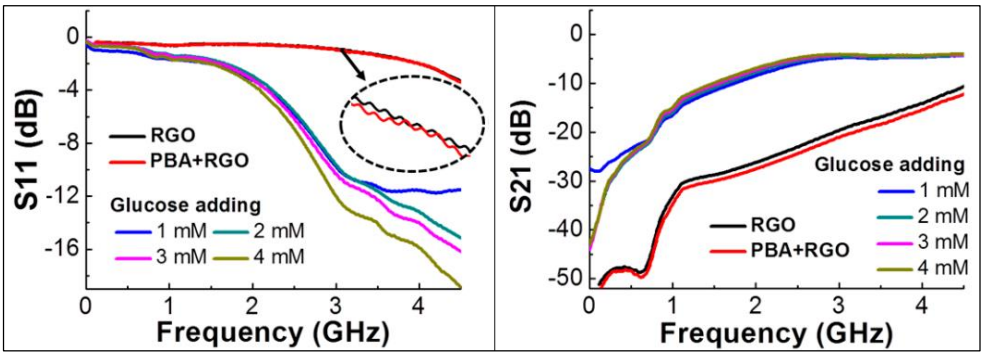


Figure 2.43. S-parameters measurements upon glucose addition on functionalized rGO [249].

Furthermore, graphene-silver nanowire electrode hybrid structures were integrated in a flexible antenna for environmental gas monitoring and detection [253]. Its functionality was demonstrated exposing the sensor to dimethyl methylphosphonate (DMMP) and $S_{11}$ measurements at 400 MHz operating frequency. The magnitude of the reflection parameter increased as per DMMP density by 0.2 dB between 5 ppm and 15 ppm. The work was further extended to demonstrate the real-time potential and technology suitability on various flexible substrates [254]. Another flexible wireless sensor based on platinum-decorated reduced graphene oxide (via hydrazine) was employed for hydrogen measurements after 2-minute gas exposure, with the obtained $S_{11}$ results presented in Figure 2.44.

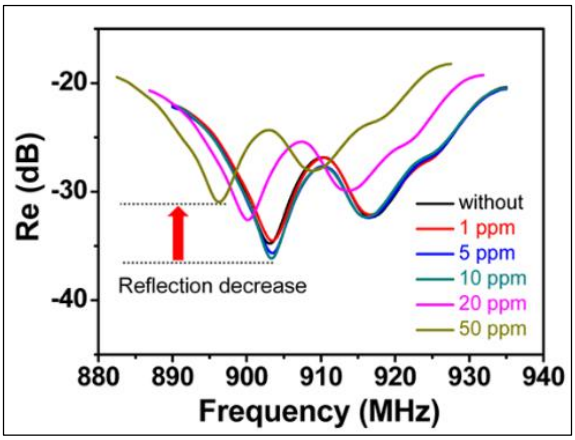


Figure 2.44. Change in reflection parameter for different hydrogen gas concentrations on graphene-Pt based RFID fabricated on a flexible substrate [254].

## 2.7. Ohmic contacts on graphene

The contact between semiconductor and metal plays a crucial role in electrical and electronic devices performance. The ohmic nature of the contact ensures current conduction from metal to semiconductor and vice versa in a linear current-voltage

characteristic as per Ohm's law: $V = IR$. Upon the ohmic contact formation, the Fermi level in the semiconductor ($E_F$) aligns with that of the metal ($E_{FM}$) as shown in Figure 2.45A. However, this requires stable electrical characteristics, as well as low and reproducible contact resistance.

The measured resistance across a structure is defined as:

$$R_T = R_{semi} + 2R_C \qquad (2\text{-}16)$$

where: $R_T$ is the total resistance, $R_{semi}$ is the semiconductor or film resistance, $R_C$ is the contact resistance being a combined result of metal resistance and associated metal-semiconductor interface.

When quantifying semiconductor resistance changes in applications such as (bio)chemical sensors, it is important to distinguish between the two components i.e. actual substrate resistance and contact resistance. Figure 2.45B presents the equivalent circuit of metal-semiconductor interface.

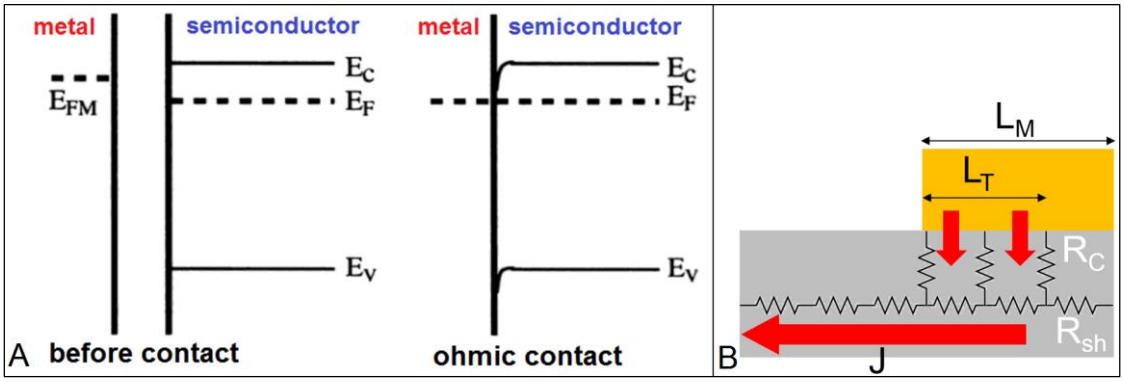


Figure 2.45. (A) Energy bands and transformation in an ohmic contact, modified from [313]; (B) schematic representation of the metal-substrate and notations for properties of interest.

The transmission line method (TLM) is the most popular method for the extraction of contact resistance. It uses an array of contact patterns deposited at various lengths on the material of interest. This allows for the measured resistance to be plotted as a function of the inter-contact distance. The slope of the linearly fitted plot and the y-axis intercept are used to determine sheet resistivity and contact resistance [255], as illustrated in Figure 2.46.

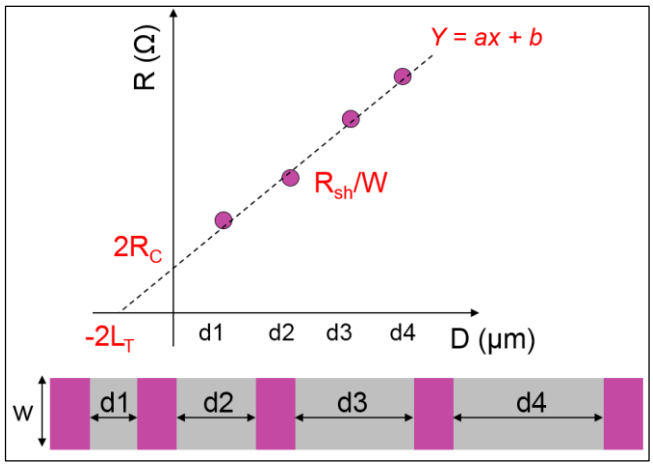


Figure 2.46. TLM method and parameter extraction.

Hence, the above equation expressing total measured resistance can be re-written:

$$R_T = \frac{R_{sh}}{w} \cdot d + 2\frac{\rho_C}{L_T w} \qquad (2\text{-}17)$$

where: $R_{sh}$, w, $\rho_C$, $L_T$ are the sheet resistance, contact width, specific contact resistivity and transfer length respectively. Based on the TLM method, the specific contact resistivity $\rho_C$ can be calculated from the formula:

$$\rho_C = R_{sh} \cdot {L_T}^2 \qquad (2\text{-}18)$$

Novel nanomaterials pose a challenge to existing contact deposition techniques, due to inefficient carrier injection in material transition from 3D (contact) to 2D (substrate or “bulk”). The associated contact resistance represents a major drawback in high-performance electronics applications [256] such as FETs.

With respect to graphene, metal deposition is possible using conventional techniques (Figure 2.47), but the contact resistance is limiting the performance of graphene devices. The deposition of conventional top contacts onto pristine graphene substrates relies on gap-based van der Waals interface bonding (physical adsorption) [257]; this gap behaves as a tunnel barrier, reducing the charge induction from metal and therefore leading to higher contact resistance. Metal chemisorption onto the graphene substrate is possible for “defected” graphene, creating a stronger interaction with the metal, but it significantly alters the structure of graphene [258]. Similarly to semiconductors, contacts on graphene are usually formed by using an intermediate metal layer to serve as adhesive (5-20 nm).

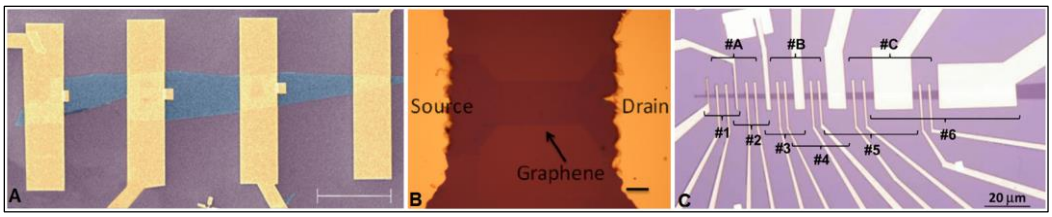


Figure 2.47. Literature-reported optical images for metal contacts on graphene: (A) Ti/Au on micromechanically exfoliated graphene [259]; (B) Au on patterned CVD graphene [260]; (C) Ni on micromechanically exfoliated graphene [261].

The reproducibility of contact deposition on graphene substrates is acknowledged as a major challenge [262][263], also amplified by the variation across graphene samples: production method, quality, number of layers. Pristine graphene has zero energy band gap and exhibits a semi-metallic behaviour [30], with the consequences of its unusual properties shown in Figure 2.48.

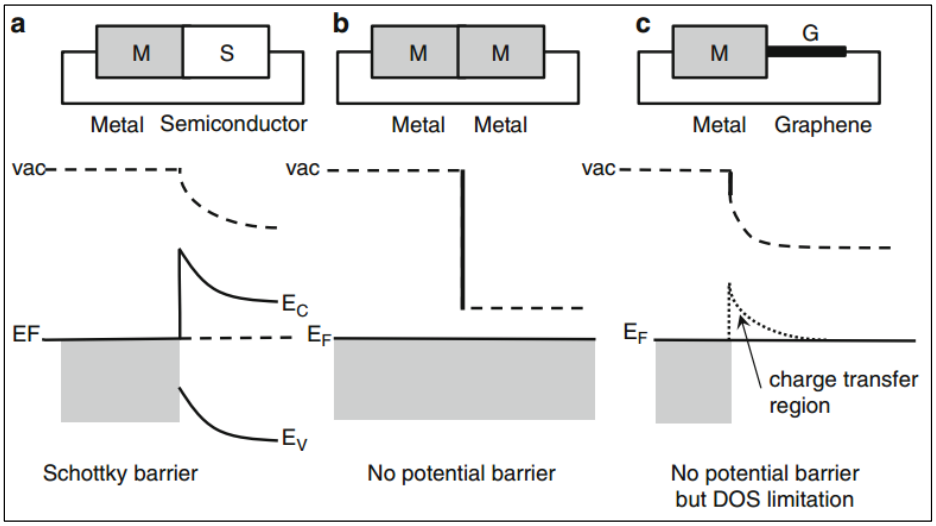


Figure 2.48. Energy band diagram for contacting different materials [264].

Different methods have been employed in order to reduce and control the contact resistance on graphene, such as improved surface cleanliness [265], controlled introduction of graphene edges [266][267] and high purity controlled metal deposition [268]. Contact arrangement and interface engineering have also been attempted for graphene-metal interface improvement [269][270]. Contact resistances on graphene have previously been reported in the range 294 Ω·µm [271] – 12 kΩ·µm [270] using conventional (thermal and e-beam) evaporation techniques. The reported values are highly dependent on the type of graphene, fabrication, contact arrangement and metal used, with some reported results captured in Table 2-6.

Table 2-6. Comparison of literature reported contact resistance on graphene.

| $R_C$ [Ω·μm] | $R_C$ improved [Ω·μm] | Metal type | Intermediate layer | Metallization technique | Improvement method |
|---|---|---|---|---|---|
| 529 | 457<br>*-13%* | Pd | Ti/Pd/Au | E-beam evaporation | Patterning/cuts in contact area [266] |
| 800 | <250<br>*-68%* | Au | Ti | E-beam evaporation | Varying pressure during evaporation [262] |
| 294 | 100<br>*-65%* | Ni | Ni | Thermal evaporation | Zigzag graphene edges [271] |
| 2,000-2,500 | 200-500<br>*-85%* | Au | Ti/Pd | E-beam evaporation | Sacrificial Al layer [263] |
| 715 | 320<br>*-55%* | Au | Ti/Pd | E-beam evaporation | Double contact [272] |
| 1,400 | 83<br>*-94%* | Au | Ti | E-beam evaporation | N-doping and contact edge patterning [269] |
| 6,350 | 1,690<br>*-73%* | Au | Cr | E-beam evaporation | $CO_2$ cluster cleaning [265] |
| 12,000 | 1250<br>*-89.5%* | Pd | - | E-beam evaporation | Metal-on-bottom architecture [270] |
| ≈ 8,000 | >4,000<br>*-50%* | Cu | - | Thermal evaporation | Intermediate graphene layer CVD [273] |

## 2.8. A mini-review on planar interdigitated electrode array (IDE) for chemical and biological sensing

Interdigitated electrode arrays, also referred to as interdigital or multi-electrode array devices (IDE, IDA) are capacitive structures with a comb-like structure consisting of a repeated parallel electrode structure. In this setup, one can engage the conductive (electrodes), dielectric (inter-electrode area) or the entire IDE surface as the biosensing platform. By connecting the electrode sides to the source voltage (DC or AC), a uniform electric field is distributed across the electrodes. The electric field is altered in the presence of biomolecules and at the interface with the analyte [274].

Employed in various sensing applications, IDE structures present significant advantages, such as design simplicity (symmetry), high equivalent capacitance, compatibility with standard CMOS technology, and rapid response allowing for the

detection of capacitive, conductivity and permittivity changes [274][275]. For electro/chemical sensing purposes, the above-mentioned changes in electrical properties are correlated with the concentration of the analyte. Application-specific, IDE devices allow for the exploration of various nanomaterials and designs for improved sensitivity and biocompatibility. Allowing for label-free detection, IDE devices can be easily integrated with additional circuit packages for an improved SNR [276] and do not require post-processing.

It is acknowledged that the full potential of the IDE has not yet been reached [277], due to limited and unsynchronised research activity across the world; however, the number of articles on biosensing IDE has continuously increased over the last decade, as shown in Figure 2.49. IDE devices can be employed as an impedimetric sensing platform, targeting the dielectric and conductive properties of biological test sample. Based on fabrication at large scale, ease of integration and high sensitivity, the IDE represents a valuable alternative to conventional macro-electrodes.

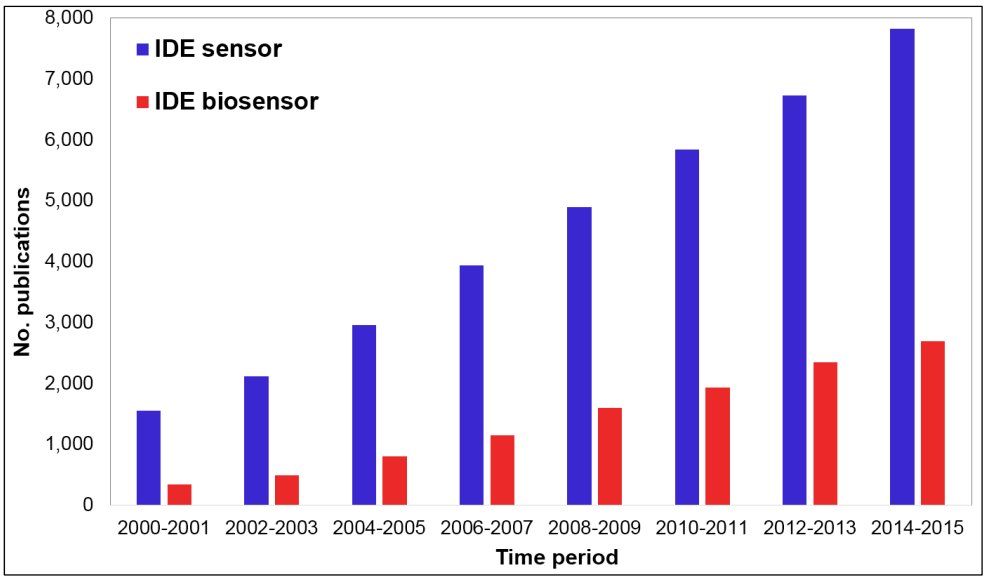


Figure 2.49. The number of journal publications on IDE biosensors according to Google Scholar.

The IDE development process for specific sensing applications involves predictive analysis, design, fabrication and testing, as presented in Figure 2.50 and discussed in the following sections.

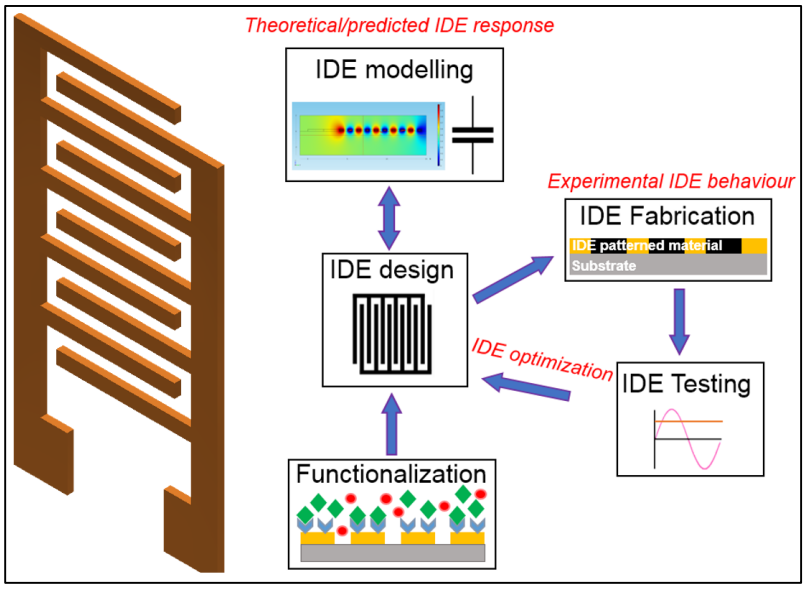


Figure 2.50. IDE development process for biosensing applications.

### 2.8.1 *Analytical and numerical analysis to predict and model the IDE behaviour*

The potential of IDE structures in sensing applications can be fully reached in conditions of optimum design, requiring a compromise between the IDE dimensions and targeted sensitivity.

The IDE characterisation starts with an estimation of its equivalent capacitance. Den Otter [278] provided a theoretical approximation developed from the energy conservation theorem, and the formula shows that one can obtain a high IDE equivalent capacitance value in conditions of maximum electrode width and length, whilst maintaining a minimum inter-electrode gap. With the challenge of ultra-thin films and 2D nanomaterials, this formula can be used to initially predict the equivalent capacitance of the IDE. A later theoretical formulation was based on conformal mapping techniques in conditions of multiple surface layers [279][280]. This is highly applicable in biosensing applications, requiring multiple chemical modification steps in order to define surface specificity.

Finite element analysis (FEA) allows for a priori IDE characterisation, with the input of material properties and geometry of the biosensor. Some authors prefer to perform a full predictive analysis of the IDE; this is exemplified by the work undertaken by Igreja and Dias [279] who validated their analytical estimation in practice using a gold IDE measured at 1 kHz and a finite element model, reporting an error of just 1.4%. Besides the design aspects of the IDE, Vakilian and Majlis [281] highlighted the impact of the dielectric constant permittivity differences between the sensing substrate and

the analyte. In conditions of a lower dielectric constant of the substrate, a higher surface area is required in order to compensate for the corresponding lower capacitance value. To maximise the SNR, the IDE biosensor for bacteria detection required a significantly larger inter-electrode spacing compared to bacteria dimensions [282], ensuring maximum changes in relative permittivity. Ibrahim et al. [283] reported the geometric optimization of an IDE using a dynamic analysis model over the frequency range 100 Hz-10 MHz. The geometry was initially optimized for the dominant capacitive behaviour. The FE model simulated the impedimetric behaviour of an 8-electrode Pt IDE on a glass substrate, including the properties of the electrode-electrolyte and blood medium layers. The cut-off frequency was shifted towards lower values in conditions of a higher electrically conductive medium, and was further optimised at an s/w ratio of 0.66. Notably, a linear increase in sensitivity with the number of electrodes up to a threshold of 16 was reported, but with negligible improvement for higher n values.

FE models facilitate the exploration of novel materials. S. MacKay et al. [284] investigated a micrometre-range gold conventional IDE decorated with gold nanoparticles (NP) for electrochemical applications. The nanoparticles facilitated a more uniform electric field distribution across the whole conductive surface, but at the same time NP can decrease the electric field magnitude in the inter-electrode spacing area. Narrower width and gaps can further decrease system impedance.

In general, one should aim for a large number of long electrodes (n,L) [285] while considering a width-to-spacing ratio (w/s) significantly above unity [283] and lower thickness (t) compared to the width and/or spacing (w,s) [279], i.e. aspect ratio.

### 2.8.2 *IDE fabrication*

The main aspects of interest in IDE fabrication are the quality of the conductive material and practical resolution. PoC system portability, low-cost and reusability requirements led to the exploration of a significant number of manufacturing methods of IDE devices.

Screen printing has been adopted for electrode patterning using materials such as carbon and silver ink, due to its speed, low-cost and repeatability [286]. This method has been widely reported for simple disk-shape microelectrode arrays [287], but the major drawback of screen printing is its limited resolution. In addition, material viscosity control for optimum surface texture is problematic for more complex structures such as IDE devices. In a comparative study conducted by Brischwein et al. [288], the

sputtered thin platinum film (200-300 nm) IDE structures exhibited a 10-fold lower electrical impedance compared to the 9 μm thick screen printed IDE with an identical layout.

The most prevalent IDE patterning method relies on microfabrication techniques, such as photolithography, metallization and lift-off [289][290], which easily allow for μm-range accuracy (see Figure 2.51). Problems can be encountered after the lift-off step, as remaining metal traces can shortcircuit some of the electrodes [285] or lead to uneven surfaces [291]. In this respect, Dimaki at al. [292] included an under-cut fabrication step using hydrofluoric acid in order to eliminate the risen sharp edges of the IDE structure, i.e. “lift-off ears”.

Downsizing towards nm resolution is possible via electron beam lithography [293], which also facilitates the accurate patterning of large numbers of electrode pairs. For example, Hayashi et al. [294] employed e-beam lithography to manufacture IDE structures with 1000 electrodes of only 250 nm width each, and by increasing the aspect ratio by a factor of 8 (reduced electrode width), the adrenaline biosensor sensitivity improved by 60%. An improved patterning technique allowing for <140 nm resolution for the inter-electrode gap was obtained by growing an additional oxide layer, with subsequent wet etching steps [295]. The etching process had a further spacing shrinking effect by approximately 40%, allowing for higher width-to-gap ratios which subsequently improved IDE sensing performance.

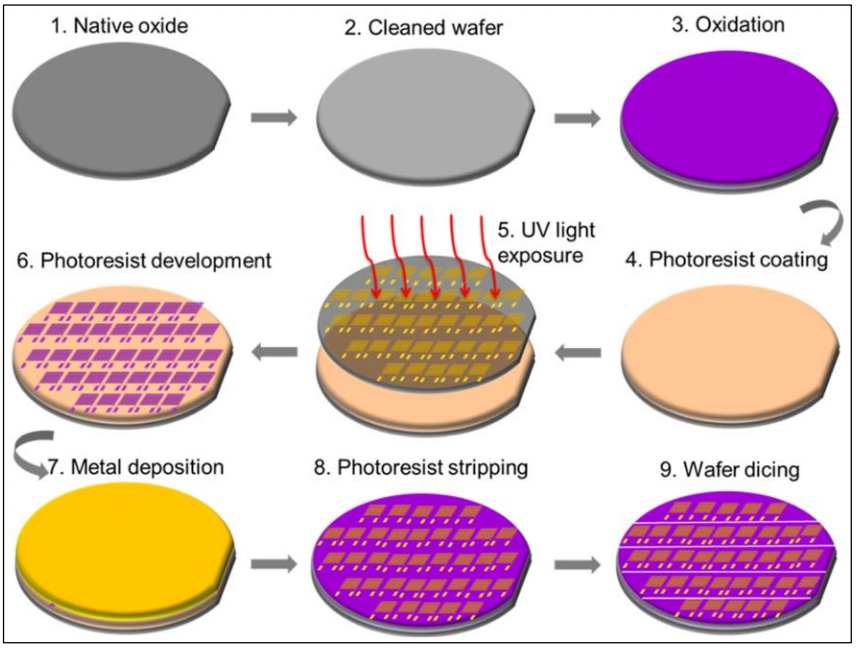


Figure 2.51. Microfabrication techniques involved in the fabrication of IDE devices [296].

Other routes include electroplating [297] and hard mask approach for selective metal deposition in IDE configuration, reported for microporous materials [298]. IDE

pattern transfer using a stamping method has been recently reported by Chou and Lee [299]. The achieved electrode width was 30 μm, with a height of just over 1 μm. Inkjet printing has been lately explored for electrode fabrication purposes [300]. This method allows for rapid, large-scale and low-cost μm resolution manufacturing and material deposition onto a variety of substrates, including paper [301].

### 2.8.3 *IDE testing and performance*

Multimeter measurements are straightforward and can quickly provide an indication of the IDE changes. An example in this respect is the work reported by Kitsara et al. [276], who used an LCR meter to directly quantify surface changes induced by humidity and common alcohols. The directly measured capacitance of 93 pF was correlated with the real part of the corresponding capacitive reactance, associated with dielectric property changes caused by vapour absorption onto the polymer film. This approach relied solely on the estimation of the capacitive behaviour of the IDE, neglecting some resistive and inductive effects. These multi-metric, fixed frequency measurements are limited in terms of accuracy and results interpretation.

Classical electrochemistry techniques can be employed to characterise IDE sensor performance. Cyclic voltammetry (CV) has been used to confirm the cleaning quality of an IDE device [302] as presented in Figure 2.52, but also to assist in the design optimization of the IDE in the presence of a redox probe for signal amplification purposes [303]. CV characterisation also enabled DNA concentration optimization for thin layer formation on chitosan/CNT of composite coated Pt IDE [304]. IDE designs can be employed for efficient electrochemical biosensors, as one electrode array can serve as the anode for oxidation and the other as the cathode for reduction [20]. Samarao et al. [305] used this setup for P-Aminophenol amperometric detection onto gold IDE, giving as low as pM-range detection.

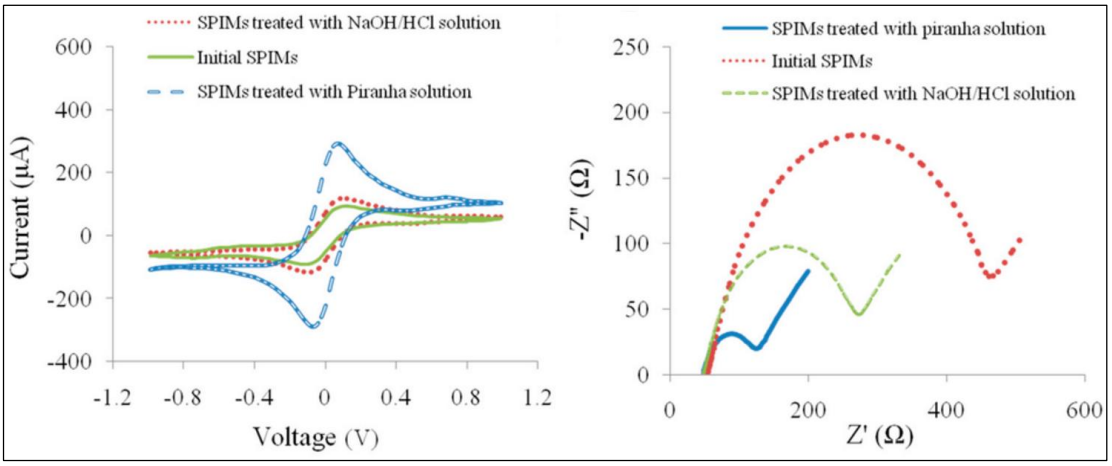


Figure 2.52. CV and EIS plots for cleaning quality of IDE devices [302].

Zou et al. [306] used an integrated Lab-on-Chip gold nano-IDE for non-faradaic impedance detection of immunoglobin (IgG). Three operation regions were identified: low frequencies – conductive surface phenomena; intermediate frequencies – electrolyte effect; and high frequencies – dielectric behaviour. Mouse anti-rabbit IgG protein binding was confirmed by surface properties changes, with an increase in linear impedance in the range of 4-20% [306].

Moreover, in a faradaic EIS study, Ohno et al. [307] employed 20 µm wide gold multi-electrode arrays for human immunoglobin A (IgA) detection, targeting charge transfer resistance variation for various IgA concentrations. The immunosensor was highly sensitive, exhibiting a minimum detection limit of 0.1 ng/mL. A similar approach was used by Arya et al. [308] for cortisol detection on the IDE surface. A different study targeted *pseudomonas aeruginosa* PAO1 detection usng Au and Pt micro-IDE [309]. The devices showed a decrease of approximately 11% for double layer capacitance in the presence of bacterial film.

The EIS characterisation technique has lately been transferred from conventional potentiostat systems to high-frequency / RF technology, allowing for higher frequency electrical and electrochemical testing. For example, a vector network analyser (VNA, introduced in section 2.6.1) can be employed on its own or as an extension of impedance spectroscopy studies by simply targeting load impedance measurements. Further conversions may be required for impedance determination. For example, Quershi et al. [310] showed that multi-analyte detection (CRP, IL6, TNFα) is possible on 40 µm wide Au IDE, over a frequency range of 50 MHz-1 GHz. The impedance data was correlated with corresponding changes in dielectric properties. The biosensor response was found to be consistent in the range of 150-173 MHz, with

an amplified SNR for an equimolar mixture of three antibody types compared to the traditional one-at-a-time approach.

## 2.9. Biosensors for prostate specific antigen (PSA) detection

Cancer is one of the leading causes of premature mortality across the world. Over 1 million men worldwide were diagnosed with prostate cancer in 2012 (World Cancer Research Fund International), being the second most common cancer in the UK in 2014 (Cancer Research). A PSA concentration above 2.5 ng/mL in the circulatory system is indicative of prostate cancerous tumour [311], but lower limits of detection in pg/mL range are rather desirable in case of recurrent tumours and early diagnostics. Biosensors play an essential role for early and fast cancer detection, increasing the survival rate while improving the available treatment solutions as testing their efficiency.

Some remarkable results have been reported using impedimetric immunosensors for PSA detection. In an attempt to provide a lateral flow assay for PSA detection, Fernández-Sánchez et al. [312] used polymer coated screen-printed carbon electrodes for impedance measurements in conjunction with a proof of concept immunostrip testing. The polymer degradation caused the formation of a capacitive double layer in parallel with IDE geometric capacitance. $C_{measured}/C_{initial}$ ratio was quantified at 20 kHz, showing a direct correlation with the PSA concentration. Using a similar sensing platform, Ching et al. [313] non-covalently immobilized PSA antibody on the carbon electrodes. The measurements were performed in the range 6.25 – 400 ng/mL PSA and they showed a good linearity in terms of $Z_{mag}$ at low frequency, around 25 Hz.

Also, gold IDE structures have been used for faradaic EIS detection of PSA. A remarkable detection limit of 1 pg/mL in 5 mM $Fe(CN)_6^{3-/4}$ was reported by Choronkur et al. [314] who modified the gold surface with DTSP for covalent PSA-Ab binding, tested in diluted human plasma as well. A similar immunosensor performance was reported via EDC-NHS chemistry on gold IDE [315], with the reported results shown in Figure 2.53. Chiriacò et al. [316] detected free and total prostate specific antigen on asingle, microfluidic integrated microchip with IDE-based sensing area. The increasing charge transfer resistance $R_{ct}$ was clearly correlated with PSA concentration.

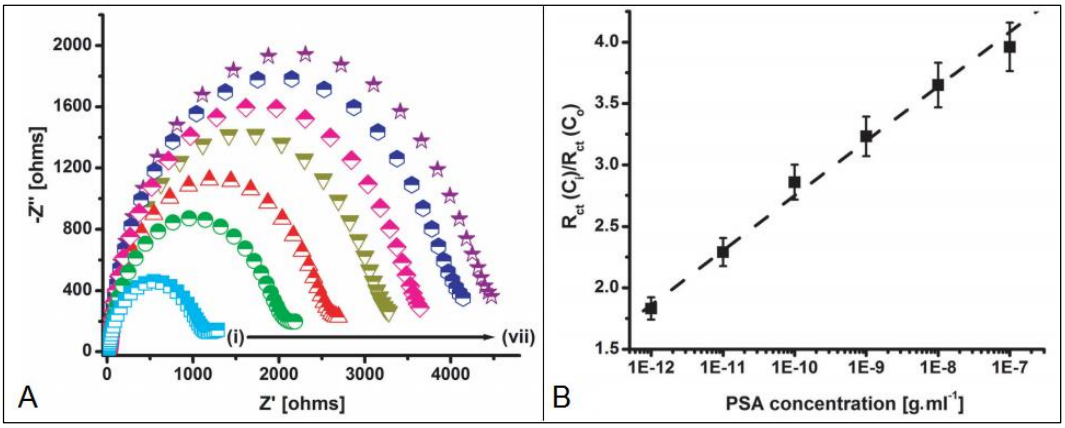


Figure 2.53. (A) Nyquist plot for gold IDE with PSA-Ab in redox buffer (i) and for increasing PSA concentration from (i) 1 pg/mL to (vi) 100 ng/mL; (B) normalized data curve for $R_{ct}$ for various PSA concentrations [315].

Arya et al. [317] fabricated an aptasensor for PSA detection, tested in a three-electrode redox setup with a gold disk as the working electrode. $R_{ct}$ decreased constantly with protein concentration due to the screening of DNA charges, but the biosensor showed very low levels of interference with non-specific molecules.

Other approaches for PSA detection include quantum-dots labelling of the secondary antibody [318] for signal amplification during square-wave voltammetry measurements. Ertürk et al. [319] fabricated PSA imprinted capacitive biosensors; by attaching an automated flow-injection system, the authors performed real-time measurements using the current pulse method. The determined biosensor capacitance showed an inversely proportional trend with antigen concentration.

Lee et al. [320] employed a RF biosensing approach; using a split-ring resonator, microwave transmission measurements >10 GHz were taken at different functionalization steps and for PSA detection. The presence of biomolecular layers triggered a change in the load of the resonator. A frequency downshift of the $S_{21}$ peak was identified for increasing PSA concentration, however, the shift trend was not linear.

Novel graphene based nanomaterials have been also adopted as immunosensors for PSA detection. Ueno et al. [321] managed to simultaneously detect thrombin, PSA and hemagglutinin on a GO-based chip. The sensor showed good specificity but it relied on labelling as using dye-conjugated aptamer for proteins capture. Also, a FET biosensor based on reduced graphene oxide (rGO) [322] showed a clear correlation between the minimum conductivity points and PSA concentration (see Figure 2.54) with a limit of detection of 100 fg/mL.

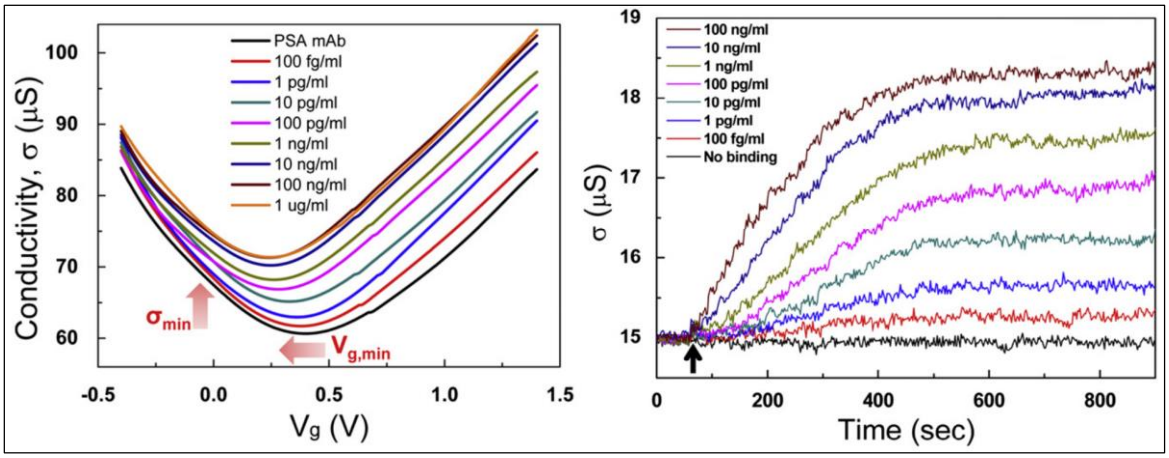


Figure 2.54. Relationship between conductivity, Vg and time for various PSA concentrations as immobilized and detected on the rGO FET channel [323].

rGO was also used as electrochemical platform for PSA detection [323]. The rGO was obtained by reduction in solution formed of graphene oxide and silk peptide which provided an abundance of active groups, hence facilitating PSA antibody immobilization. The peak current of the redox probes decreased linearly for increasing protein concentrations and preliminary results reported for serum samples look encouraging.

## 2.10. Research directions and opportunities

Chin et al. [324] conducted an outstanding review of current PoC technologies form a commercial perspective. In order to progress their reliability and accessibility, a coordination of research efforts on fully integrated biosensor / microfluidics / data processing is required. Future biosensors for cancer diagnosis should address chip-scale devices suitable for multiple analyte detection [325], ideally with in-vivo monitoring option. High sensitivity and signal amplification are two basic requirements for cancer detection [326]. The challenge is to develop existing concepts and apply them to superior materials for efficient, reliable analyte detection in human samples. It was already shown that conventional CMOS technology can be successfully adapted to PoC requirements, whilst facilitating real-time wireless communication and minimum discomfort via patch-like wearable biosensors [327].

Another focus of the current and future research is the fabrication of multifunctional in-vivo devices for biosensing and controlled drug delivery [328][329], and carbon nanomaterials are expected to drive the progress in this field [330]. This was recently proven by Lee et al. [331] who integrated a graphene-gold hybrid biosensor in a sweat-sensitive wearable patch for diabetes monitoring, medication feedback and delivery via bio-resorbable polymeric micro-needles (see Figure 2.55).

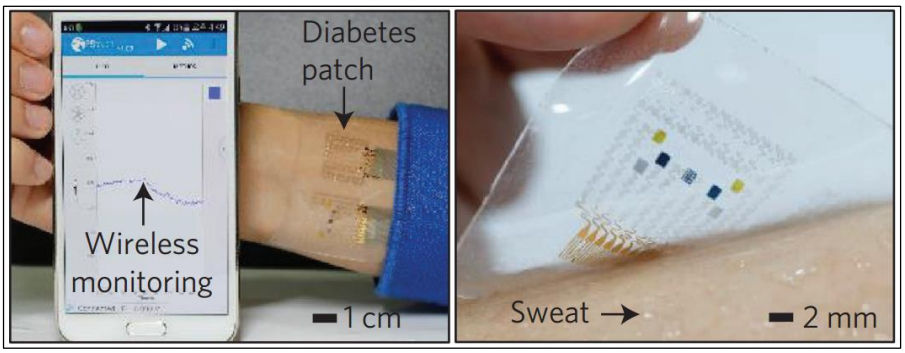


Figure 2.55. Wearable diabetes monitoring and in vivo therapy system [38].

Moreover, it has been recently attempted to integrate reliable biosensing platforms with currently available consumer technologies, such as smartphones. Preechaburana et al. [332] physically interfaced SPR chips with smartphones via a disposable PDMS optical coupler for angle-resolved SPR detection using the smartphone screen illumination and camera. Sun et al. [333] developed an external module, powered by a smartphone and compatible with commercially available screen printed electrodes for electrochemical detection.

The need for cost effective PoC testing systems is driving the development of membrane and paper-based disposable biosensors, while adapting printing technologies to nanomaterials and electrically conductive inks [334][335]. The discovery of graphene and the development of hybrid materials allow for the further exploration of biosensing platforms with improved sensitivity [336]. A remarkable aspect of pristine graphene discovery was the applicability and potential of “imperfect” graphene based materials [337]. Hence, graphene material selection is a compromise between its pristine nature and mechanical, chemical, optical and electrical properties. As outlined in the subsection 2.3.3, graphene materials suited for biosensing applications should satisfy the following requirements:

- Allow for pattern definition with at least µm-range resolution – this is to ensure the electrode design comparable with literature reported results
- $I_D/I_G$ < 1 and the existence of the 2D band – this will confirm the “graphene” nature of the material
- Well defined G band at ≈ 1580 $cm^{-1}$ – characteristic of graphene materials with no structural defects
- Asymmetric XPS $sp^2$ specific peak, with 3 to 5 fitted components of the C1 s spectrum – high nano-carbon quality material, with edge defects and oxygen functionalities
- C:O ratio > 8 – this is of high importance, especially for rGO materials
- Tunable surface chemistry – functional groups are required .

However, further efforts are needed to reduce graphene contamination and properties damage during handling and integration into devices using clean-room technqiues. rGO is a key player in biosensing applications, and the adaptation of inkjet printing [338] and laser-reduction methods [339] allow for low-cost and large scale manufacturing of sensing platforms. Hybrid and nanocomposite materials based on graphene are envisaged to outperform single-material biosensing platforms [340]. An example in this sense is the reduced graphene oxide decorated with polyaniline nanowires for DNA detection [341].

The IDE sensing structures allow for a high SNR and further improvements in signal amplification have been reported for metallic nanoparticle decoration [342]. Ueno et al. [343] used an rGO-gold layered IDE for cortisol detection, showing improved electrode reactivity compared to a conventional gold IDE. Low-cost, laser-induced graphene materials [344] and their applicability for biosensing platforms and electrical circuits [345] is still at an early stage, but the available results strongly justify further work in the field.

With regards to impedance biosensors, the research community has mostly focused on faradaic EIS due to its straightforward approach and more quantifiable changes, while non-faradaic EIS requires an in-depth understanding of the electrode and electrolyte processes. This was highlighted by Qureshi et al. [346] in their review on biosensors for heart disease monitoring and detection. While faradaic detection is more sensitive compared to non-faradaic EIS, it requires a careful construction of the bioreceptor layer [347]. In general, step-by-step chemical modification trigger impedance variations based on the substrate, surface activation layer (methodology) and electrolyte. However, in a recent study, Vogt et al. [348] showed that the redox ions can damage the gold electrode surface. Inconstant, time variable $R_{ct}$ values were reported for the adsorption of the thiol-modified ssDNA onto the gold surface.

Hence, non-faradaic detection is preferred, being simpler in terms of the experimental setup and more compatible with PoC (point-of-care) applications [349]. However, the identification of the dominant element in the equivalent circuit requires thorough studies. The testing cell setup (two or three electrode) must take into account the sensing structure design and application [350]. It is desirable to have an integrated sensing platform and reference electrode to improve the detection accuracy. The scale fabrication of such sensing platforms should ideally include the reference electrode on the same sensing platform. The EIS limitations include signal alteration by

environmental conditions e.g. pH, so the method may not suit weakly charged biomolecules, therefore amplification techniques are desirable [351].

It has been shown that the electrochemical activity of graphene based materials is highly dependent on their properties (e.g. C:O ratio, electrical conductivity, number of layers, morphology) [352]. Taking into account the size of graphene nanomaterials family, it is essential to accurately characterise and identify carbon nanomaterials. King et al. [353] attempted to define new graphene Raman characteristic features aiming to improve the qualitative assessment of graphene based materials. The presence of edge-plane defective sites in graphene based materials like rGO were found to enhance graphene's electrochemical activity [117]. Also, thick, 3D based sensing structures are of interest due to their increased surface area as offering multiple reaction sites, but this comes at the cost of the aspect ratio. For instance, a redox amplification effect was obtained in practice by using 3D carbon IDE structures [354]. However, the step-by-step chemical characterisation of graphene based materials is highly limited.

Label-free EIS biosensing studies have reached a level where they can further assist in the development of point-of-care diagnostics systems using novel materials and sensor designs. An example in this sense is the user-friendly at home INR (prothrombin) testing / blood clot detection technology, presented in Figure 2.56.


Figure 2.56. Alere INR monitoring system, http://www.alere.com/

While biocompatibility is of high interest, less invasive, flexible materials are required for in-vivo sensing applications. Further developments should target simultaneous, multiple analyte diagnosis, with higher specificity in analysing complex human samples [355]. In terms of microfluidics, droplet-based biosensors are favoured due to reduced sample quantity and simplistic design. Moreover, it was suggested that the biosensor stability and sensitivity can be improved by allowing the droplet containing the analyte to evaporate, albeit depending on the nature of the analyte as their properties might degrade [356].

The biosensor design is essential for its static and dynamic performance. The utilisation of low-cost materials would justify the utilisation of disposable biosensing devices. The development of novel materials and improved detection techniques can eventually relax the dimensional requirements and fabrication costs while still providing highly sensitive IDE biosensors e.g. screen printed IDE devices can be fabricated for less than $1 [302]. An example in this respect is the work conducted by Kiilerich-Pedersen et al. [357], who manufactured a fully functional, integrated 4-layer conductive polymer (PEDOT:Tosylate) IDE for the detection of infectious agents in human cell culture. The device exhibited the highest sensitivity at 2 Hz, and it represents a remarkable starting point for the development of fully integrated IDE-based sensing systems. Also, the planar IDE design can be easily tuned in LC resonating sensors, with applications in RF biosensors.

Moreover, impedance-based sensing at high-frequencies is also of interest as high dielectric changes are expected upon biomolecules presence and interaction. This will potentially allow for improved biosensor performance i.e. sensitivity, but SNR and electrical interference remains a problem for portable and easily accessible PoC systems operating at high frequencies. A possible solution in this sense is the application of impedance matching on conventional biosensing structures. Electrical engineering research efforts have focused in the direction of adaptive control of the load impedance ensuring maximum output power, transfer efficiency and receiver sensitivity [358][359]. These approaches can be integrated in RF design in order to maximise biosensor's performance towards single molecule detection.

Graphene based materials can be integrated in passive wireless RF sensing platforms, which do not require continuous power source and can function through wave scattering principles for label-free biomolecule detection. Fabrication efforts are still needed to preserve graphene properties for fabrication of high-frequency (GHz) operating integrated circuits [360], as well as repeatability [361] and low-cost fabrication [362]. While the integration of novel nanomaterials such as graphene allows for simpler circuit designs than in conventional electronics [363], more work is required to improve the robustness and downsize RF biosensors and biochips [364]. Hu et al. [254] used a 10 wt% graphene ink to screen print RF passive components (coplanar transmission line, resonator and antenna) on flexible substrates for wearable electronics, with a potential for mass production. Graphene was also integrated as wireless sensing platform using RF identification (RFID) tag for bacteria monitoring in the hospital environment (see Figure 2.57).

Figure 2.57. Graphene wireless sensor for S. Aureus bacteria detection attached on an intravenous bag [365].

Last but not least, remarkable biosensing results using microwave technology have been reported based solely on the properties (e.g. viscosity) of the SUT, such as the work reported by Kim et al. [246]. With no chemical modification of the surface, specific analyte detection is not reliable, as the human serum contains an abundance of molecules. However, this work represents a great starting point for analyte targeted investigation. Further in-depth studies could possibly lead to the identification of molecular fingerprints and development of an analyte database.

Finally, the research field of biosensors has reached a remarkable level of flexibility in terms of manufacturing, nanomaterials and detection methods. The ability to tune the properties of graphene-family members, applications specific, clearly provides new opportunities to improve biosensor performance. The remaining challenges are the controlled, large-scale graphene synthesis, its integration into biosensing devices and efficient functionalization. While user-friendly PoC systems should provide a simplified and straightforward measurement setup (such as a simple LCR meter) with improved accuracy, wearable biosensing technologies have received increasing attention. PoC testing systems are attempted to be simplified for improved performance, efficient component integration, ease of manufacture and robustness. Scheller et al. [366] correlated this trend with the development of a fourth generation of self-sustained, autonomous and non-invasive biosensors, presented in Figure 2.58.

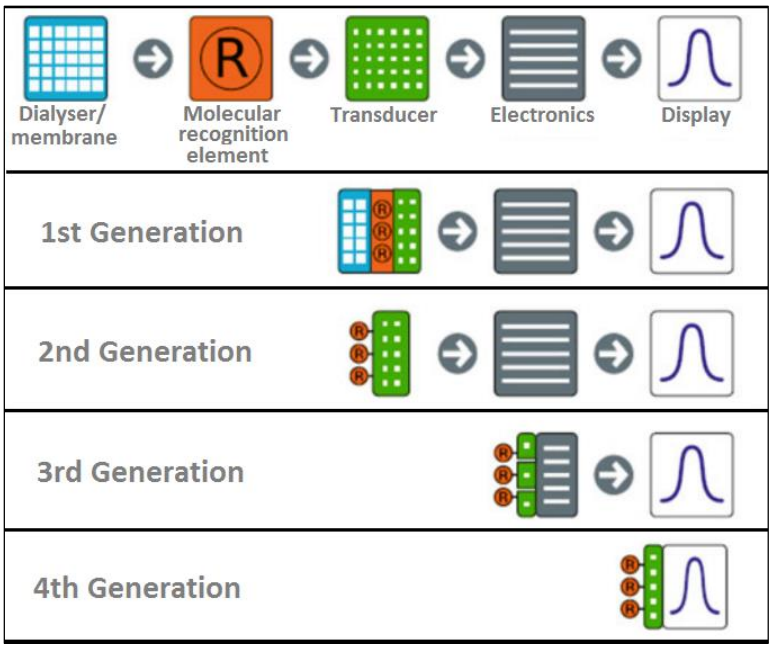


Figure 2.58. Biosensors evolution based on sensing mechanism and components integration [40].

# Chapter 3. The selection of graphene materials for impedance biosensing applications

The selection criteria for graphene materials for biosensing applications were firstly defined by consulting the specialty literature summarised in section 2.3. Various graphene materials were then analysed using XPS, Raman spectroscopy, optical and surface microscopy and electrical measurements. Pristine graphene samples were used as baseline in the assessment of the synthesised graphene based materials. Reduced graphene oxide (rGO) via LightScribe and laser induced graphene (LIG) from polyimide (PI) film showed a good potential towards electro-chemical biosensing applications based on the presence of surface functional groups and complex morphology.

## 3.1. Methodology

### 3.1.1 *Materials*

Ultra-highly concentrated single layer graphene oxide (0.5-5 μm flake size, 6.2 g/L), nano-graphene oxide (90 ±15 nm flake size, 1 g/L), few-layer CVD graphene on $SiO_2$ and $Si/SiO_2$ (90 nm oxide thickness) wafers were purchased from Graphene Supermarket, US. Single-layer CVD-grown graphene transferred onto $SiO_2$ was bought from Graphenea, Spain. Collaborators from University of California Los Angeles, US, provided aqueous graphene oxide solutions (2-3 g/L). Epitaxially grown bi-layer graphene on SiC (EG) was provided by the School of Electronics and Electrical Engineering, Newcastle University. Polyimide (PI) adhesive film was purchased from Farnell, UK. Acetone ($CH_3COCH_3$, 99.5%), 2-propanol ($(CH_3)_2CHOH$, > 99.5%) and l-Ascorbic acid ($C_6H_8O_6$, 99%) were purchased from Sigma-Aldrich, UK. Dilutions of graphene oxide solutions were obtained in deionised (DI) water with a resistivity of 18.8 MΩ·cm at 21 °C.

PET foil (transparent, 100 μm thick, Office Depot brand) was purchased from Viking, UK. 3M repositionable adhesive spray and conductive silver paint for contacting were acquired from RS Components, UK.

### 3.1.2 *Fabrication of graphene materials*

The analysed graphene based samples are shown in Figure 3.1 and the synthesis methods are detailed in the following paragraphs.

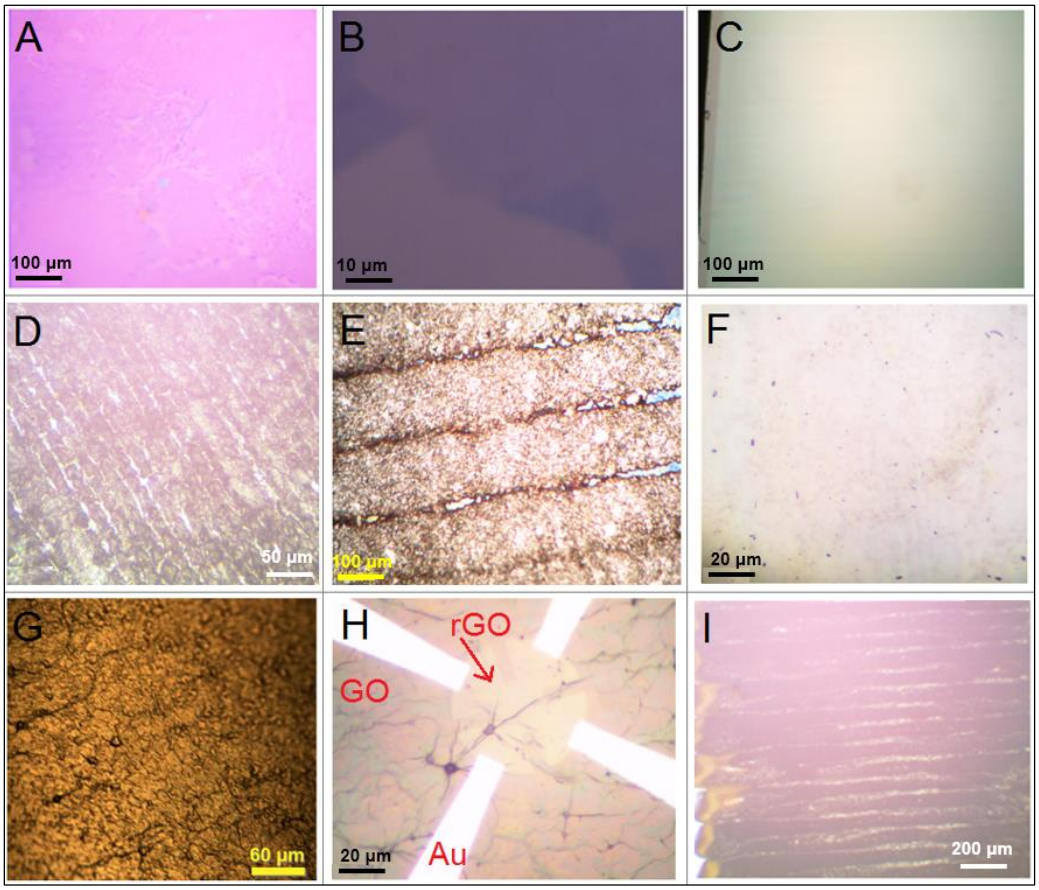


Figure 3.1. Optical images of graphene based materials: (A) multi-layer CVD graphene; (B) single layer CVD graphene; (C) epitaxial graphene; (D) LightScribe reduced graphene oxide; (E) $CO_2$ laser reduced graphene oxide; (F) $CO_2$ laser reduced nanographene oxide; (G) UV reduced graphene oxide; (H) e-beam reduced graphene oxide pattern (Van der Pauw) with gold tracks; (I) $CO_2$ laser induced graphene from polyimide.

#### *3.1.2.1 LightScribe reduced graphene oxide*

This method relies on the graphene oxide (GO) reduction and patterning using a LightScribe DVD drive [57], with a representative sample shown in Figure 3.1D. An initial study was undertaken to look into varying the GO concentration as the available literature states from 0.4 g/L for sensing applications and highly conductive rGO [367][368] and up 10 g/L in composites [369] and lubricants [370] as aiming for good mechanical properties. Based on a qualitative assessment of the ease of reduction i.e. number of engraving cycles, material colour transformation and pattern continuity, the concentration of 2 g/L was selected for further experiments.

Prior to reduction, the GO was sonicated for 1.5 hours at room temperature to ensure a good solution dispersion. PET foil was cut to DVD size using a laser cutter (HPC LS6040, settings: 70% speed, 15% power) and attached to the LightScribe enabled DVD disc (Verbatim 16x DVD-R LightScribe) using the surface mount spray glue. The GO solution was dropcasted on the acetate substrate (15 mL per disc) and

dried overnight at room temperature. The desired design was uploaded in LightScribe Template Labeler software as .bmp file. Once dried, the disc was loaded into the LightScribe burner (LG GP08LU11 8x External DDRW) and the engraving cycle was run for 6 consecutive times. If the reduction and pattern definition were not completed, the design was run for extra couple of times (up to 10 times).

#### *3.1.2.2 $CO_2$ laser reduced graphene oxide and laser induced graphene from polyimide*

The $CO_2$ laser (HPC LS6040) was used to reduce GO and polyimide (PI) tape for rGO and LIG synthesis, shown in Figure 3.1E and Figure 3.1I. The method was developed based on the work reported by Lin et al. [121] and Ghadim et al. [37].

The PI tape was carefully attached to a pre-cleaned acetate substrate, trying to avoid air bubbles and wrinkles. Prior to irradiation, the PI was briefly wiped with IPA. An initial study was conducted to adjust the laser power setting for LIG synthesis. Aiming to preserve the optimum equipment resolution, it was opted for the standard laser-bed distance i.e. 30 mm. While 25% power, corresponding to 10 W, was insufficient to reduce the material, settings above 40% (16 W) were found to locally burn the polyimide (PI) tape and disrupt the patterns. Surprisingly, the laser power did not exhibit a clear correlation with $R_{sheet}$, but very close results were obtained in the power range of 12-16 W: 26-35.9 Ω/sq. Some level of variability could be attributed to operator e.g. silver contact area and sample handling when placing the probe needles of the measurement station. 30% laser power was further selected for LIG synthesis.

The $CO_2$ laser was also used for GO reduction, to produce rGO. The GO aqueous solution (Graphene Supermarket and UCLA) was sonicated for 1.5 hours at room temperature. The $Si/SiO_2$ substrates were cleaned using acetone and isopropanol. The GO was dropcasted onto the substrates and allowed to dry overnight. Following a similar approach to LIG, a qualitative assessment was performed to determine suitable laser power settings for GO on acetate and $Si/SiO_2$ substrates.

The customized patterns (.bmp or .jpeg files) were uploaded on the HPC LS6040 system using the provided Professional Lasercut software. The samples were irradiated using the $CO_2$ laser cutter (HPC LS6040) in engrave mode, with the settings: maximum speed and an average power of 13% for GO deposited on acetate, 27% for GO on silicon dioxide substrate (rGO) and 30% for PI (LIG). These settings ensured patterned, graphene based material synthesis and substrate integrity post-exposure.

#### *3.1.2.3 E-beam reduced graphene oxide*

In an attempt to reduce pattern rGO structures down to few nm, e-beam lithography was used to reduce GO. The samples were prepared in the clean room at Exeter University and an example is shown in Figure 3.1H. This experiment was motivated by the reduction approach of Kwon et al. [371].

Preparatory brief experiments using their equipment confirmed nm-range resolution on GO using e-beam lithography. The GO (2 g/L) was deposited $Si/SiO_2$ substrates cleaned in piranha solution (70% sulfuric acid $H_2SO_4$: 30% hydrogen peroxide $H_2O_2$) and subsequently in oxygen plasma for 5 minutes. Patterns to be reduced and for gold contacting were defined on GO using photolithography. PMMA photoresist (spun at 4,000 rpm for 50 seconds) was coated on GO and dried on a hot plate (160-170 °C) for 10 minutes. After photoresist development in IPA:MIBK:MEK (isopropanol, methyl iso bethyl ketone, methyl ethyl ketone) solution, the alignment marks were defined. The samples were loaded in the e-beam equipment and the patterns on GO were obtained using a 400 nA current and a surface charge density of 100 $C/m^2$. Finally, using the same photoresist deposition and development procedure as described above, contacting tracks were defined on the sample. A 35 nm layer of gold were evaporated on a 50 nm chromium adhesive layer, followed by a lift-off step in acetone.

#### *3.1.2.4 UV-reduced graphene oxide*

rGO was also obtained via GO reduction using UV irradiation, presented in Figure 3.1G. The method was inspired from the work of Guardia et al. [54]. The GO solution was dropcasted on the pre-cleaned $Si/SiO_2$ substrates and the samples were exposed to the UV lamp (100 W UV 365 nm, B-100 series, UVP), at a distance of approximately 25 mm from the light bulb for 18 hours. Also, UV reduction of graphene oxide was attempted in solution (2 g/L), by exposure in a Petri dish for 6 hours.

#### *3.1.2.5 Hydrazine reduced graphene oxide*

2 g/L GO solution was sonicated for 1.5 hours at room temperature and then drop casted onto cleaned $Si/SiO_2$ substrate and allowed to dry overnight. The GO film reduction via hydrazine vapour was conducted with the support from School of Chemistry, Newcastle University. The GO was reduced by exposure to hydrazine monohydrate ($N_2H_4$) vapour for 6 hours, at 74 °C. The hydrazine reduction method is commonly reported in the literature [371].

#### *3.1.2.6 Vitamin C-reduced graphene oxide*

The chemical, in-solution reduction of the GO was also attempted using vitamin C instead of the hazardous hydrazine [46]. Prior to reduction, the GO solution was sonicated for 1.5 hours at room temperature. A quantity of 2.1 mg of l-ascorbic acid was added to the 0.7 g/L GO aqueous solution in a total volume of 10 mL. The pH was increased from 6 to 10 using ammonium hydroxide ($NH_3$) and the solution was heated under stirring to 90 °C ± 2°C on a hot plate (IKA C-Mag), controlled by using a thermometer and allowed to react for 3.5 minutes. The obtained rGO solution became black from initial light brown, and it was pipetted on a pre-cleaned $Si/SiO_2$ substrate and then dried in the oven (Carbolite 300), set at 65 °C for 5 hours.

### 3.1.3 *Measurements*

X-ray photoelectron spectroscopy (XPS) analysis, using a K-Alpha XPS (Thermo Scientific, East Grinstead), and helium ion microscopy (HIM, Zeiss Orion NanoFab HIM) were performed at NEXUS (National EPSRC XPS User's Service), Newcastle University. The Raman spectra was acquired using a Horiba Jobin Yvon HR800 spectrometer with a 514 nm excitation laser, using 10% laser power, 2 data points and 5 seconds acquisition time. The Raman system was calibrated prior to measurements using Silicon peak position definition (521 nm). The electrical measurements (I-V and sheet resistance) were performed using a four-probe Agilent B1500 system in Characterisation Lab, School of Electrical and Electronics Engineering, Newcastle University. Scanning Electron Microscopy (SEM, Tescan Vega 3LMU) and gold sputtering was performed by the Electron Microscopy Research Services at Newcastle University. Surface roughness measurements were taken using a Zygo New View 5000 non-contact white light interferometry system.

CasaXPS and LabSpec software were used to process XPS and Raman spectroscopy data. For the XPS analysis, the binding energies were measured with respect to C1 (s). In comparative graphs, the data was normalized using the maximum value – for presentation purposes. Available specialty literature and XPS databases [69][70] were used for peak identification.

## 3.2. Results and discussion

### 3.2.1 *XPS analysis*

Firstly, the outsourced pristine graphene samples were analysed, with their comparative XPS survey presented in Figure 3.2. The carbon C 1s and oxygen O 1s

peaks are the main qualitative indicators of the graphene based materials. It can be observed that the EG exhibits a more dominating C 1 s peak compared to SLG, but this is due to the carbide presence in the substrate, confirmed by the presence of a stonger silicon peak. Additional peaks can be observed for few-layer graphene, with possibly remaining photoresist residues due to graphene transfer onto $Si/SiO_2$.

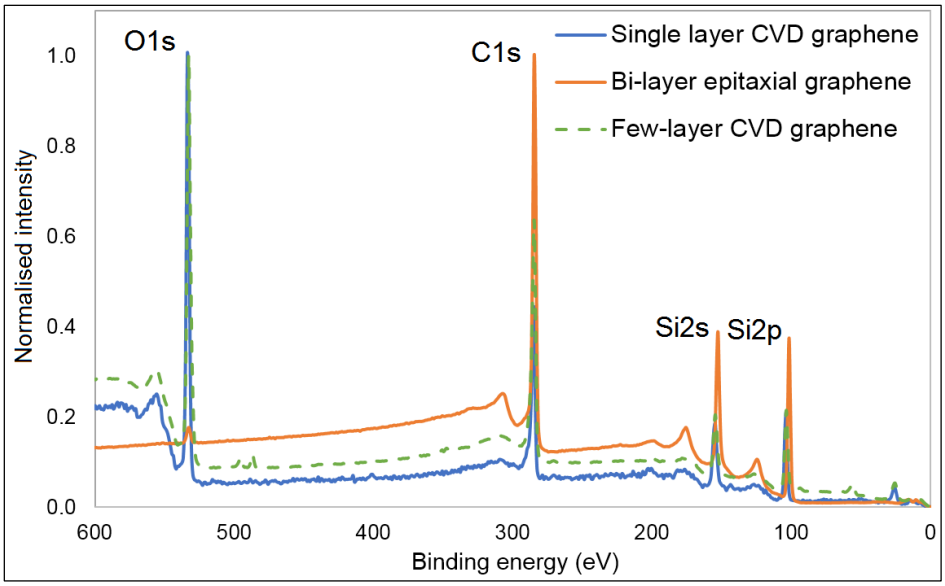


Figure 3.2. Normalised XPS survey of pristine graphene materials: CVD grown single (SLG) and few-layer graphene (FLG) and epitaxial graphene on silicon carbide (EG).

With regards to photo-thermally reduced graphene oxide materials, C 1s was found to dominate the XPS survey among various synthesised rGO materials, as illustrated in Figure 3.3. The PI tape used to produce the laser induced graphene (LIG) has nitrogen in its composition and the increased silicon content is explained by diffusion from its adhesive layer upon carbonization. Part of this study implied the exploitation of e-beam lithography high resolution pattern nm-size structures of graphene. Interestingly, all rGO-based samples showed a dominating carbon composition, except for the rGO obtained using the e-beam reduction method. The structure produced by e-beam reduction (see Figure 3.1H) had a 40 µm diameter, while the minimum XPS probe size is an ellipse with the dimensions 30 µm x 50 µm. Due to the spatial limitation, it is believed that there was an overlap between GO and rGO areas during measurements. Additionally, the GO flake size varies between 0.5 and 5 µm and the flakes must be completely reduced for consistency across the defined pattern. In order to improve this aspect, it was attempted to use nano-GO (100 nm flake size), but the coating peeled off during PMMA drying step on the hot plate. It should be mentioned that conventional microfabrication techniques, such as

photolithography and lift-off posed a problem for the GO layer, which was found to easily delaminate from the Si/$SiO_2$ substrate.

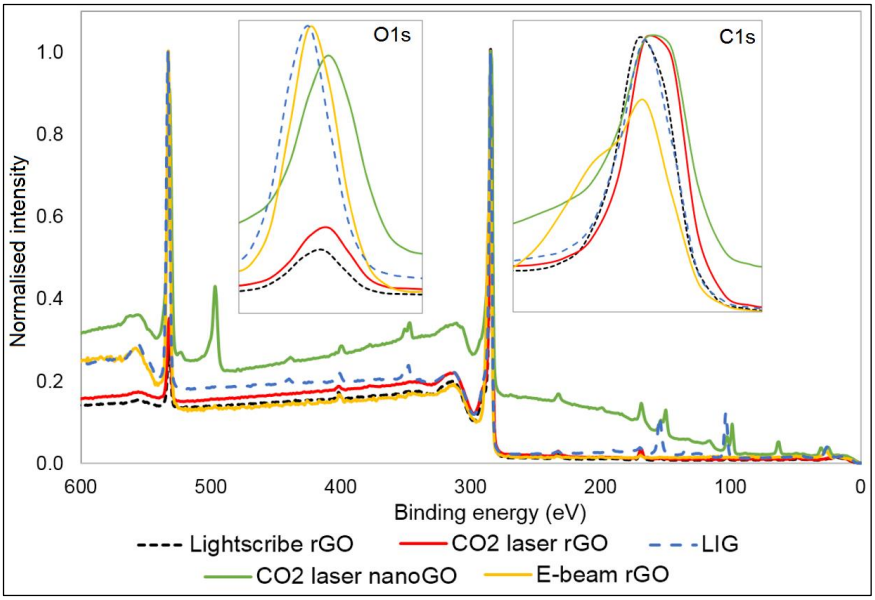


Figure 3.3. Normalised XPS survey for reduced graphene (rGO) materials: LightScribe, $CO_2$ laser and e-beam.

As discussed in section 2.3.3.1, a high reduction factor confirms the efficient structural evolution of rGO in terms of carbon $sp^2$ fractions, hence its transformation towards graphene. Table 3-1 summarises the XPS findings for the analysed samples. Please note that the silicon composition (Si % at) was included for pristine single and few-layer graphene materials in order to compensate for equipment limited depth resolution in order of few µm compared to nm-range graphene, hence Total C at% = Si at% + C at%. Due to significant substrate interference, not all results are representative of the graphene quality (greyed out). The distance between the laser head and sample bed on the $CO_2$ laser was controlled to 30 mm, varying the speed and power parameters of the equipment. The adjustment of the $CO_2$ HPC laser parameters for GO irradiation was rather challenging, as its minimum power setting of 4.4 W was found to completely burn the GO in acetate substrate. 10 W power was the optimum achievable for GO coating on Si/$SiO_2$. A qualitative assessment of the laser power was satisfactory in these conditions as the material transformation was visible from light brown (GO) to black (rGO). The surface chemical properties of LightScribe rGO, obtained using the DVD burner laser diode of 35 mW, are similar with the results obtained for $CO_2$ laser rGO.

Overall, the experimental values from Table 3-1 are comparable with the literature review results presented in Table 2-3, where the C:O ratio of rGO materials varies between 8.55 and 15.9. Moreover, Strong et al. [344] highlighted that graphene

based materials produced in ambient conditions present a higher oxygen content, partially explained by a static interaction between the expanded graphene layers and the oxygen found in the environment.

Table 3-1. C:O ratio extracted from calibrated XPS surveys (at %) for different graphene based materials; grey rows: significant substrate interference results.

| **Material / Synthesis method / Substrate** | **C:O ratio** |
|---|---|
| Single-layer graphene (CVD, $SiO_2$) | 2.2 |
| Bilayer graphene (sublimation, SiC) | 94.7 |
| Few-layer graphene (CVD, $SiO_2$) | 1.76 |
| Graphene oxide (2g/L) | 2.3 |
| rGO (LightScribe, acetate) | 17.9 |
| rGO ($CO_2$ laser, $SiO_2$) | 14.2 |
| Nano rGO ($CO_2$ laser, $SiO_2$) | 3.3 |
| rGO (e-beam, $SiO_2$) | 2.9 |
| rGO (UV, $SiO_2$) | 3.4 |
| rGO (l-ascorbic acid) | 2.8 |
| Polyimide (on acetate) | 2.5 |
| LIG ($CO_2$ laser, PI/acetate) | 3.2 |

Furthermore, the material transformation upon reduction is highlighted in Figure 3.4 by comparing the source material i.e. graphene oxide (GO) and PI tape and its reduced form upon irradiation. The carbon peak increases by nearly 50%, while there is a 70% reduction in the oxygen peak intensity.

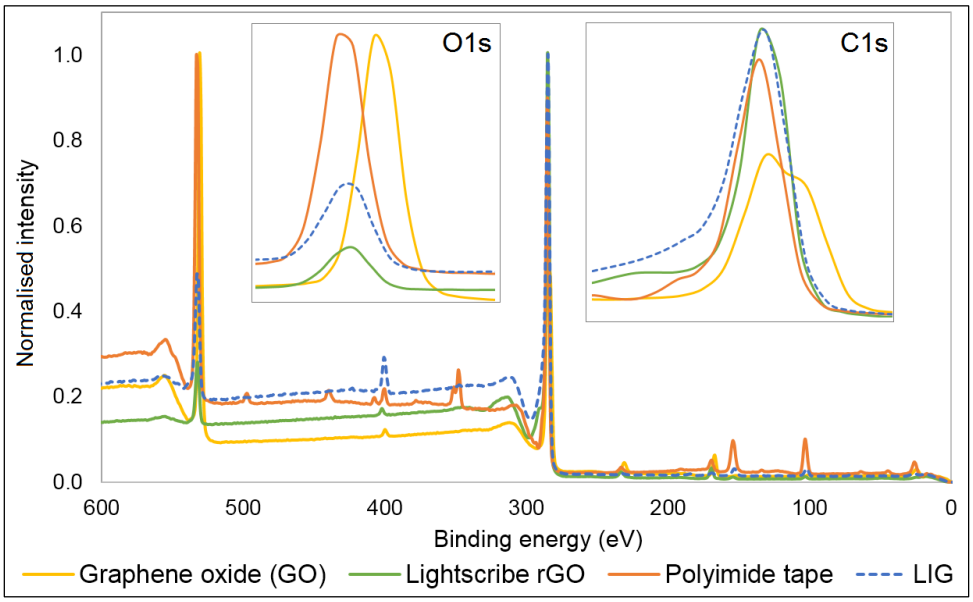


Figure 3.4. Comparative normalised XPS survey showing: GO vs rGO and PI vs LIG.

Curve fitting of the C 1s spectra was performed on various graphene samples using a Gaussian-Lorentzian peak shape. The spectrum for single-layer CVD grown graphene shows a graphene-typical asymmetric peak (see Figure 3.5). Ideally, the spectrum should be fitted by an asymmetric, single $sp^2$ carbon C-C peak. Oxygen functional groups are present due to photoresist contamination and introduced defects [372], with best fit peaks at 285.6 eV and 288 eV.

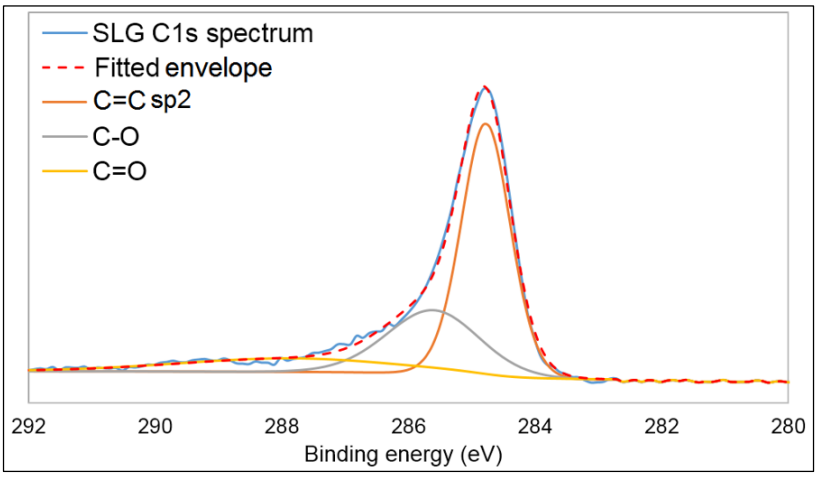


Figure 3.5. High resolution XPS and fitted spectra of C 1s peak for CVD-grown SLG, with corresponding functional groups.

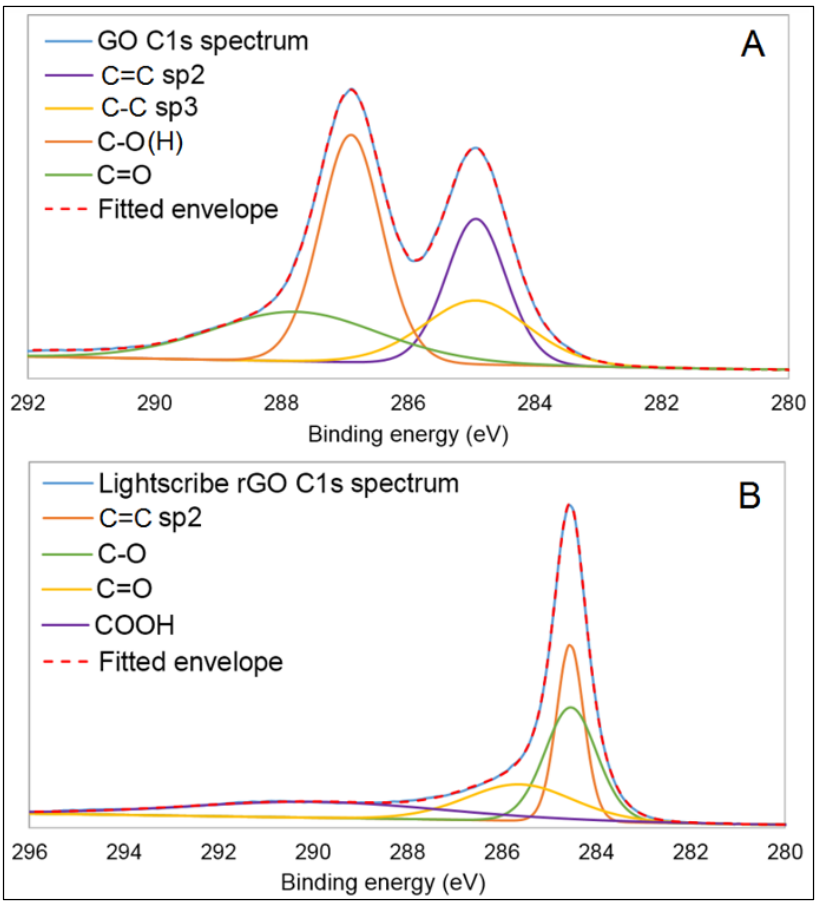


Figure 3.6. High resolution XPS C1 s spectra of (A) GO and (B) rGO obtained via LightScribe engraving method.

By comparing GO and LightScribe-obtained rGO, one can distinguish between $sp^2$ and $sp^3$ hybridization states, as presented shown in Figure 3.6. Upon irradiation, defective features, such as carbonyl, are reduced under irradiation, hence increasing the $sp^2$ carbon contents [373]. In GO, the presence of carboxyl groups is not always evident as they can overlap with hydroxyl species, however, they are not readily reduced / preserved upon irradiation process, with -COOH group specific peak identified at 289.9 eV.

Laser induced graphene (LIG) obtained via $CO_2$ laser irradiation PI tape has been referred in the specialty literature as “defective” graphene due to the edge presence of pentagonal and heptagonal rings, exhibiting interesting properties, as reported by Lin et al. [121]. Some nitrogen content is expected based on PI composition, with the chemical formula: $(C_{22}H_{10}N_2O_5)_n$. Figure 3.7 presents the high resolution C 1s fitted spectrum before and after PI irradiation. The peak at 288.3 eV for PI is associated with polymeric C-N bonds, but it downshifts to 287.6 eV upon carbonization. Si-O-C bonds on LIG were previously reported at binding energies around 285.5 eV [121].

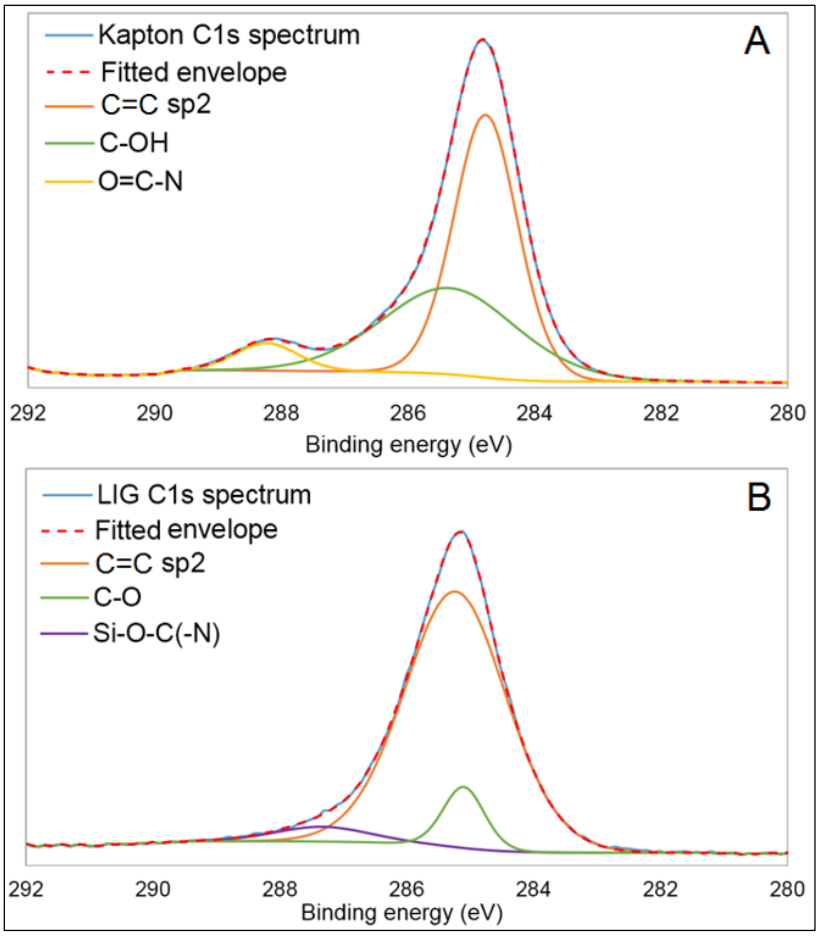


Figure 3.7. High resolution XPS C 1s spectra of (A) PI and (B) LIG obtained via CO2 laser engraving method.

In the case of UV exposed and solution-reduced GO using l-ascorbic acid, the degree of reduction was highly limited. This was reflected in their high resolution C 1s spectra shown in Figure 3.8, with a triple-peak presence, similar to GO before reduction. The solution colour changes upon the UV exposure were visible with the naked eye, with the material becoming darker and rougher. In the case of vitC-rGO, issues with GO layer dispersibility led to a decrease in the reaction time by nearly a half, hence interrupting the reduction process. However, the rGO solution was nearly black after the reduction process, similar to reports by Li and Kaner [374]. With a higher density of structural defects and the presence of a clear additional peak at 289 eV, one can find similarities between UV rGO and vitamin rGO with XPS characteristics of unzipped CNT for graphene nanoribbons formation [374].

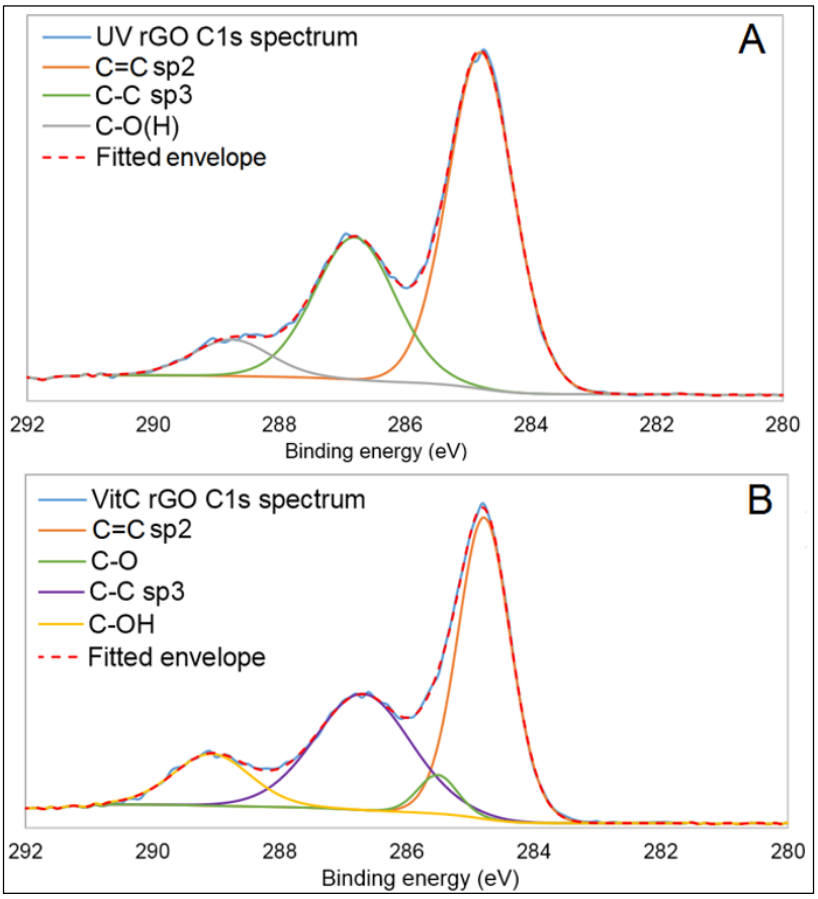


Figure 3.8. High resolution XPS C 1s spectra of (A) UV rGO and (B) l-ascorbic acid rGO.

Last but not least, the D-parameter can be extracted from the Auger (CKL) spectrum in order to identify materials containing various $sp^2$-sp3 hybridized network [373], discussed in 2.3.3.1 . Figure 3.9 presents the parameter extraction method as recommended by NEXUS [375]: based on the carbon Auger C KLL acquired spectra (initial CKL spectra), any noise in the signal and background is removed

(replacing envelope). This is followed by Auger signal range calculation using the minimum (min) and maximum (max) points.

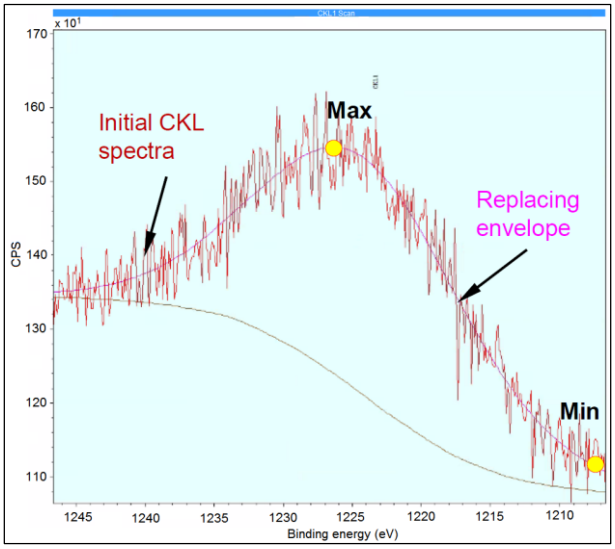


Figure 3.9. D-parameter extraction method from Auger (CKL) spectrum, CASA XPS.

D-parameter values for different types of materials of varying $sp^2/sp^3$ ranges between 13 eV for pure $sp^3$ domain (diamond) and 21 eV for $sp^2$ domain (graphite) [73] . Among the tested samples, SLG exhibited an average value of 18.2 eV and a slight increase by approximately 1% after cleaning using acetone and isopropanol. Upon reduction via LightScribe method, rGO showed some variation across the defined pattern [373], with an average D-parameter of 20.9 eV, which is lower by 0.53 eV compared to its GO precursor material. The average value for LIG was 23 eV, while D-parameters for graphite have been reported as high as 22.6 eV [376].

### 3.2.2 *Raman spectroscopy analysis*

CVD-grown single-layer graphene (SLG) was used as reference due to its pristine nature and its Raman spectra was further compared with graphene oxide (GO), reduced graphene oxide (rGO) and laser induced graphene (LIG), being shown in Figure 3.10. All samples exhibited graphene-specific D and G bands, with their significations discussed in section 2.3.3.2.

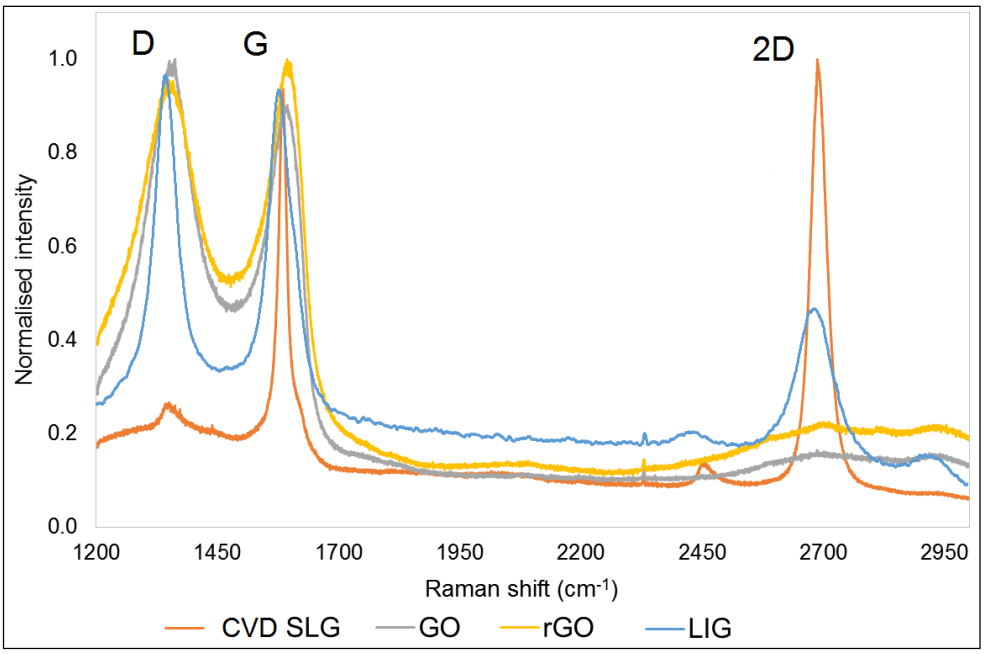


Figure 3.10. Normalised Raman spectra for: CVD single layer graphene (SLG), graphene oxide (GO), laser reduced graphene oxide (rGO) and laser-induced graphene from polyimide (LIG).

The 2D peak is well defined for SLG, while it has a bump-like aspect for LIG (30% laser power), suggesting the formation of $sp^3$ amorphous carbon [377]. The laser reduction of GO causes a decrease in peak intensity by 6 $cm^{-1}$ for the D (1346 $cm^{-1}$) band, with an $I_D/I_G$ decrease from 1.12 to 0.95. LIG's peaks of interests are 1341 $cm^{-1}$ for D band and 1574 $cm^{-1}$ for the G band. The G* peak at 2446 $cm^{-1}$ could be identified for the SLG sample and it represents an overtone of the G band [98], being associated with phonon modes in $sp^2$ carbon [374]. The Raman spectrum for the untreated PI film is not shown as the signal was abnormal due to its highly fluorescent background.

Based on the XPS results discussed in subsection 3.2.1, it was difficult to quantify the e-beam GO reduction due to the limited spatial resolution of the XPS probe, but its corresponding Raman spectrum in Figure 3.11 confirms the incomplete GO reduction. Interestingly, the $CO_2$ laser reduced nano-GO sample exhibits two well-defined bands with the 2D peak at 2689 $cm^{-1}$ and the D+G peak at 2940 $cm^{-1}$. The D+G band intensity can be correlated with the amount of disorder and it was previously reported for graphite [378] and graphene oxide [379]. It can be also recognised in the other rGO samples, but it is not evident as the 2D and D+G bands overlap in a wide 2600-3000 $cm^{-1}$ bump. Overall, the UV reduction of GO film as deposited on $SiO_2$ substrate is the most inefficient.

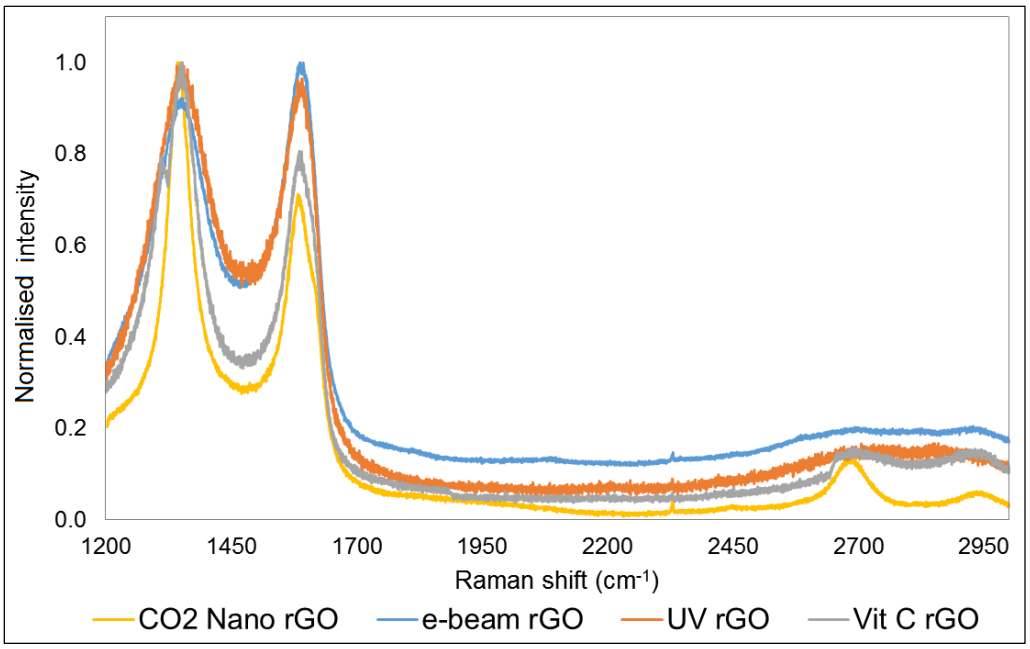


Figure 3.11. Normalised Raman spectra of various rGO materials: CO2 laser reduced Nano GO (nano rGO); e-beam reduced graphene oxide (e-beam rGO); UV reduced graphene oxide

The production of graphene based materials using the laser reduction method is of particular interest based on the ease of manufacture and patterning. Strong et al. [344] endorsed the controllability of the LightScribe process to produce few-layer stacked graphene. However, while the $CO_2$-laser patterns on rGO and LIG were uniform, a 4-5 µm gap in between tracks was observed for LightScribe rGO. The utilisation of graphene as sensing platform requires consistent material properties, so Raman spectroscopy was further employed to assess the graphene quality on the surface and at the edge of the laser tracks i.e. between tracks, with results presented in Figure 3.12.

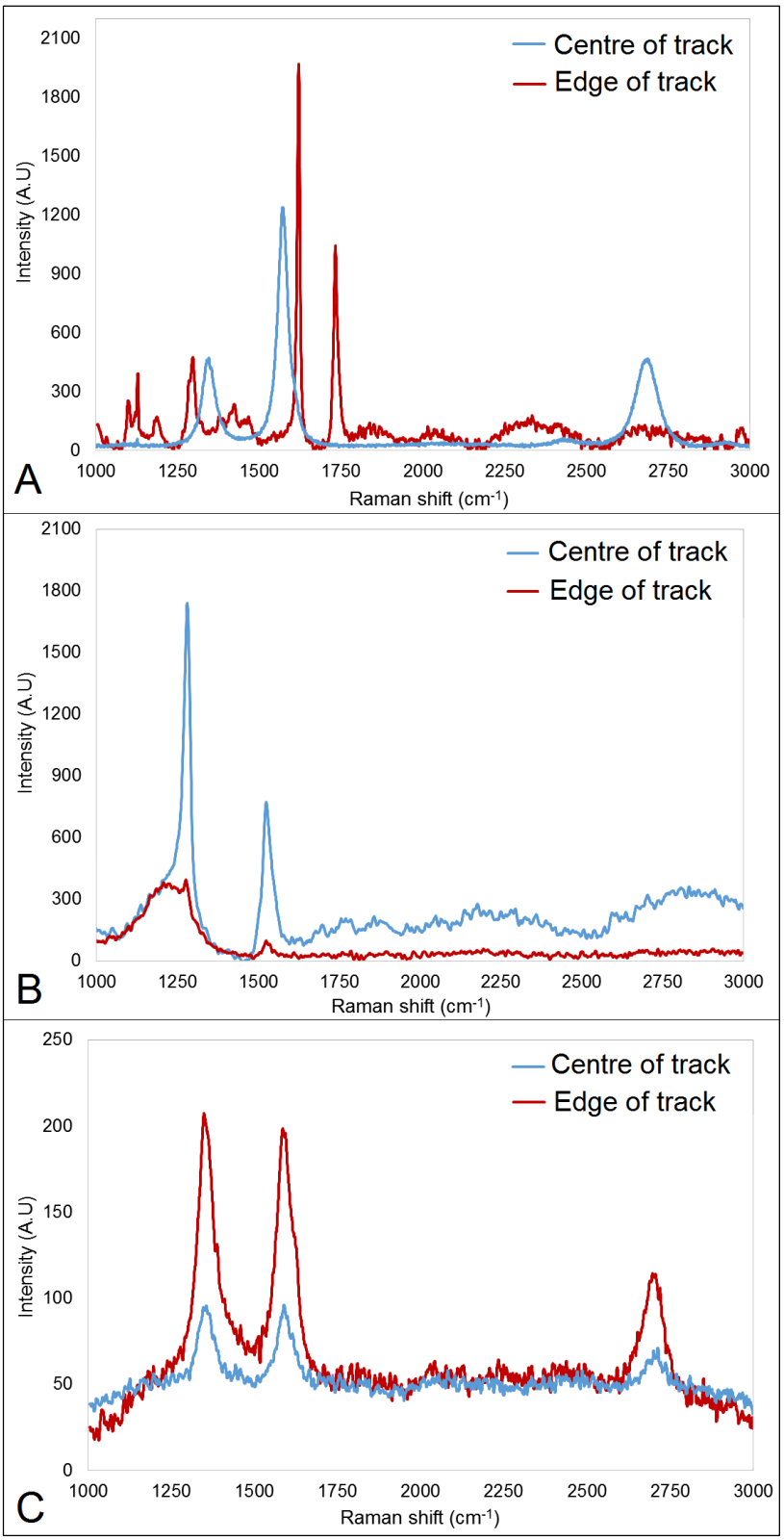


Figure 3.12. Comparative Raman spectra of the centre of the track (blue) and track edge (red) for graphene based materials formed by laser reduction: (A) $CO_2$ laser rGO; (B) LightScribe rGO; (C) $CO_2$ laser LIG.

While LIG (35% laser power) exhibits highly similar spectra at both locations of interest, the $CO_2$ laser reduction of GO (15% laser power) locally burns the material as there is a slight overlap (10 μm) between tracks during the engraving process.

The LightScribe rGO exhibits a high density of $sp^2$ disordered carbons [339] with $I_D/I_G$ = 2.2 and the local presence of incompletely reduced GO, as well as highly-defected rGO edges in between tracks indicated by the widening of the D band.

Overall, Raman spectroscopy is highly effective in distinguishing between different types of carbon allotropes and it has a high applicability in graphene identification and characterisation. The graphene based samples obtained via different reduction methods are composed of a multi-layer assembly of defective graphene sheets. Figure 3.13 summarises these findings, by quantifying $I_D/I_G$ and $I_{2D}/I_G$ ratio for the analysed samples. The experimental values are comparable to the literature reported results i.e. D-to-G Raman band peak ratio, captured in Table 2-4, with low values (up to 0.1) for pristine single and bi-layer graphene and up to 2 for multiple layer rGO materials. Moreover, the 2D peak (≈ 2670 $cm^{-1}$) is well defined for SLG and LIG samples, but LIG required careful surface focus due to its high porosity. On the other hand, the UV in-solution reduction of GO is more efficient compared to the reduction of the GO film as deposited on substrate or via l-ascorbic acid.

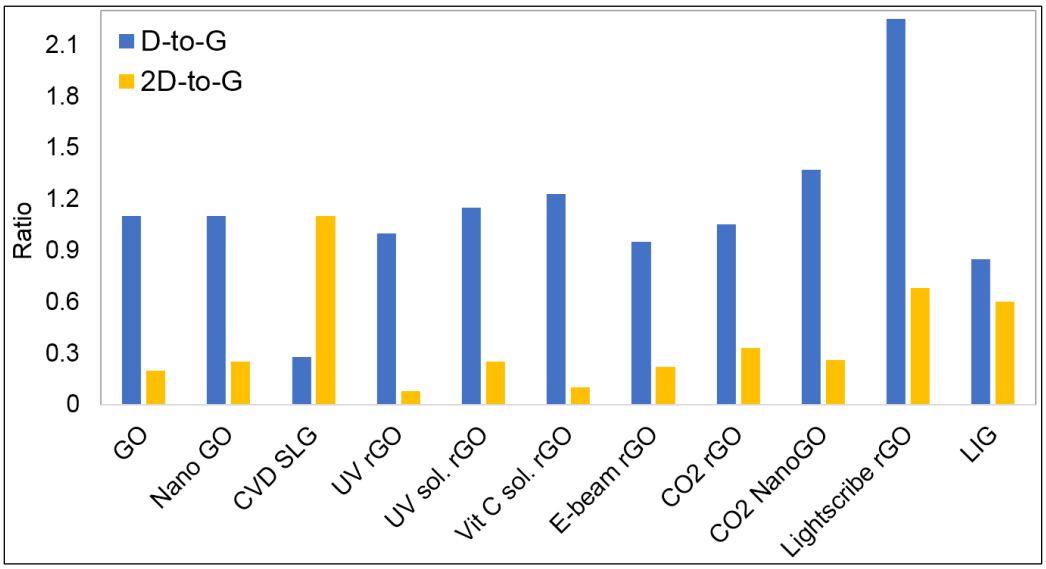


Figure 3.13. Raman D, G and 2D bands intensity ratio for analysed the graphene based samples.

### 3.2.3 *Microscope studies of the morphology of graphene based materials*

High-resolution microscopy i.e. HIM was further employed to visually compare various graphene based materials. In addition to its sub-nm capability, Iberi et al. [380] showed that the pattern contrast in graphene samples can be correlated to its electrical conductivity.

In the case of the CVD-grown SLG, creases are visible, expected to be caused by the transfer procedure from the catalytic substrate to $Si/SiO_2$ wafer. The inset image reveals a relatively poor adhesion of the graphene sheet on the substrate, also

confirmed upon mild chemical cleaning (acetone, isopropanol and $N_2$ blow dry), which led to some folds and local delamination of the graphene film (Figure 3.14B). Moreover, the surface changes for graphene oxide reduction via: UV (18 hours exposure), annealing in atmosphere (700 °C, 2 hours), vacuum (250 °C, 6 hours), and hydrazine (1 mL hydrazine, 74 °C on hot plate, vapour exposure for 6 hours) could be visualized. The rGO sheets look well aggregated, presenting folds, in agreement with Lilloja et al. [381] and a GO-like morphology.

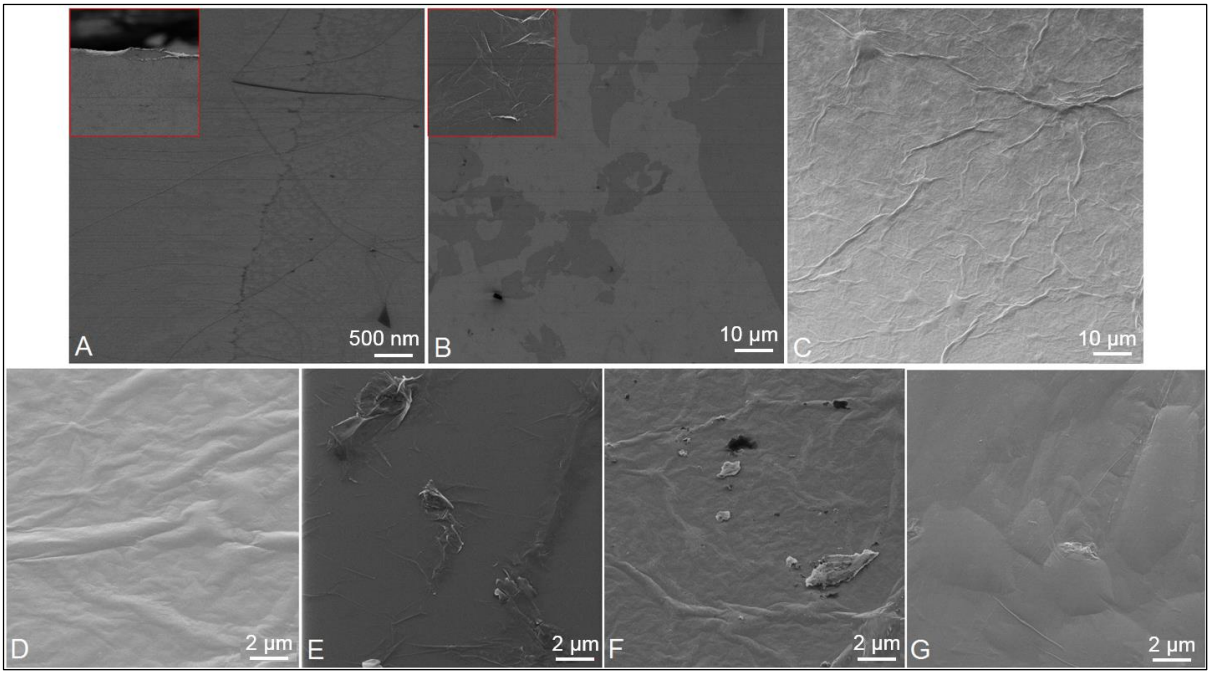


Figure 3.14. HIM images of different graphene based materials: (A) SLG with inset showing the edge of the graphene sheet; (B) SLG after chemical cleaning with inset showing graphene monolayer veils; (C) GO deposited on a $SiO_2$ substrate; (D) UV-rGO; (E) rGO obtained via thermal reduction of GO in atmosphere at 700°C for 2 hours; (F) rGO obtained via thermal reduction of GO in vacuum at 250°C for 6 hours; (G) hydrazine vapour rGO.

The photo-thermal reduction via laser irradiation (LightScribe, $CO_2$ laser) is faster and more aggressive compared do the above-discussed reduction methods. So far, taking into account the presence of the functional groups in the $sp^2$ backbone, rGO and LIG show a good potential for chemical and biological sensing applications.

Figure 3.15 presents the morphology of LightScribe rGO. The material is laterally expanded, with single and few-layers graphene sheets expanded like veils in a pocket-like arrangement, in a foam-like structure [382]. The number of rGO layers is dependent on the distribution of the GO flakes and possible variability in the GO layer thickness. The rGO layers are denser towards the edges and opened towards the centre of the track. The bright edges are indicative of high electrical conductivity.

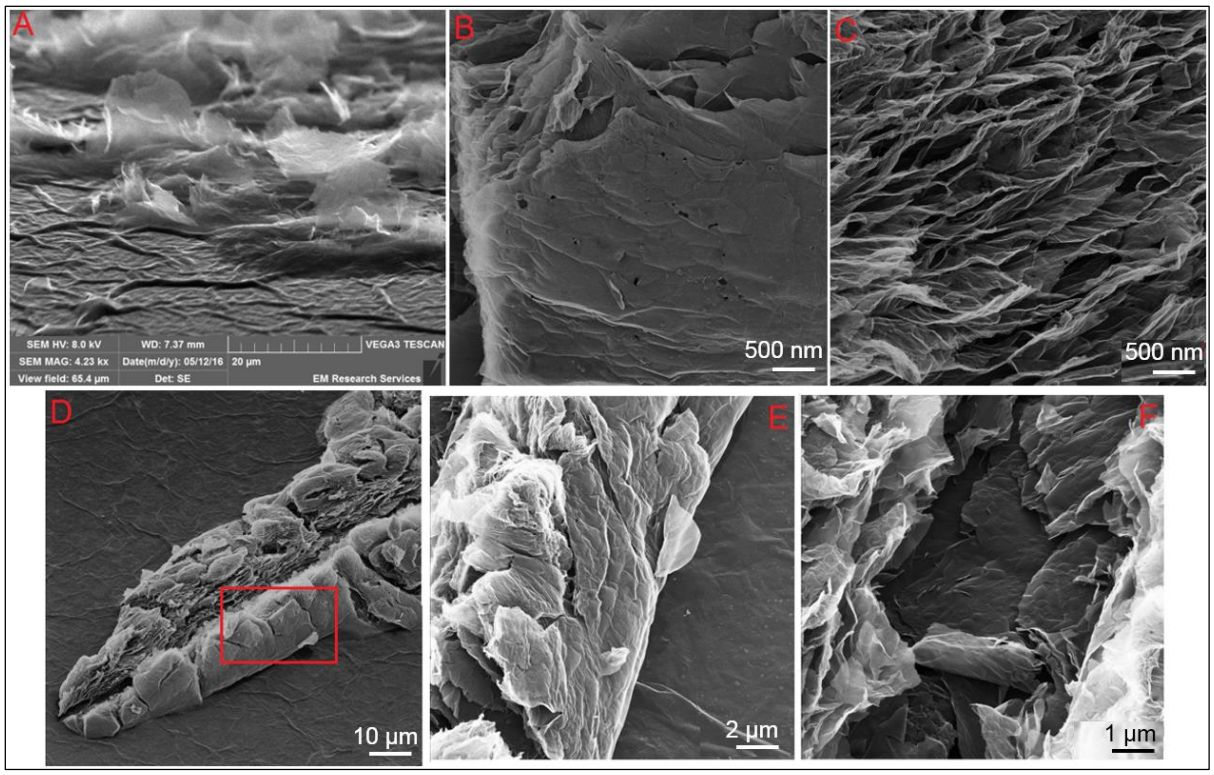


Figure 3.15. Electronic images of LightScribe rGO: (A) SEM, 20 µm scale bar; (B-F) HIM.

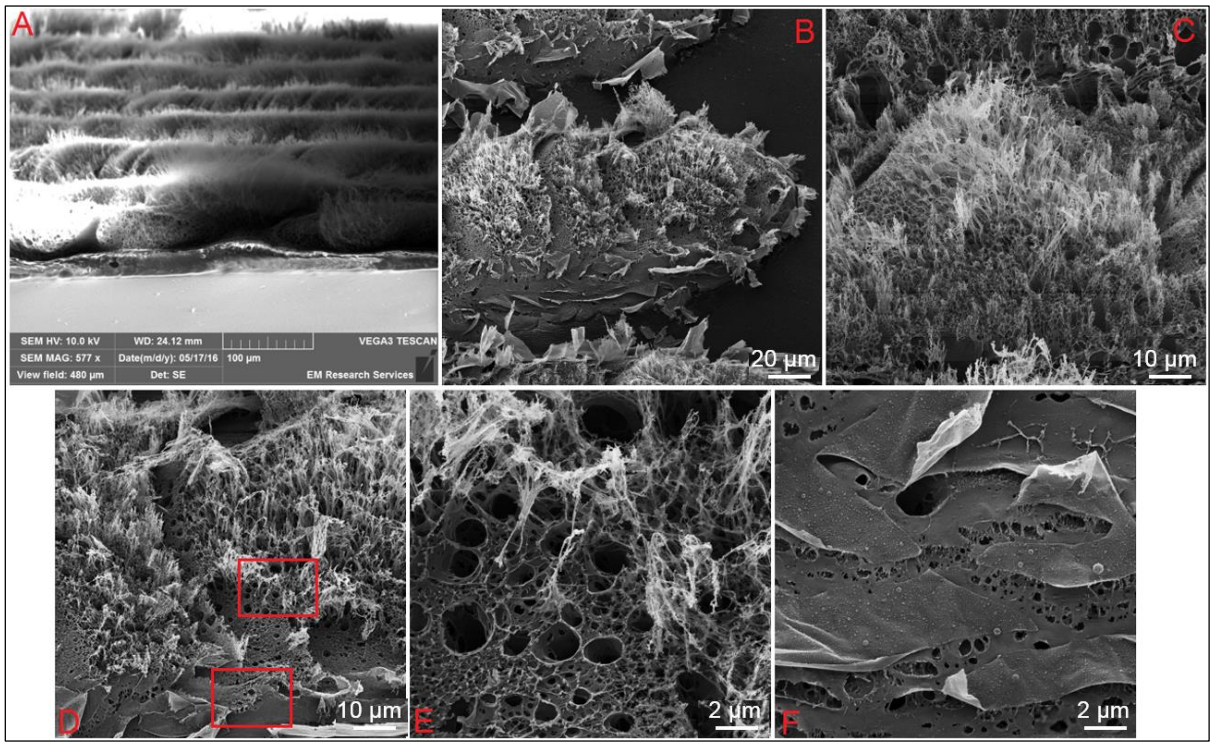


Figure 3.16. Electronic images of LIG: (A) SEM, 20 µm scale bar; (B-F) HIM.

Unlike rGO, LIG (see Figure 3.16) exhibits a vertical porosity, with the top layers presenting a grass like aspect and pores in the µm-range. This morphology is similar to the LIG obtained by Lin et al. [121], but significantly different than the hierarchical porous structure reported by Cai et al. [383]. One can distinguish between three types of porosities, indicated by the highlighted areas in Figure 3.16D: the top layer with a

"hairy", grass-like porosity; the intermediate layer with circular pores; and the underneath or bottom layer with trapped pores and flake layers. Similar to rGO, the brighter areas indicate improved conductivity, being evident for the top porous layers of LIG. The morphology differences between rGO and LIG are highly dependent on the precursor material via its chemical and mechanical structure, as well as the degree of energy localization (of the laser). The LightScribe DVD laser power is 35 mW, corresponding to a power density of 11.1 kW/cm$^2$ as $PD = \frac{P\ (W)}{\pi \cdot r^2}$, where *PD* is laser power density, *P* is the laser power and *r* is the radius of the laser diode. For LIG, the applied power density for 30% power setting, i.e. 18 W, is 102 kW/cm$^2$. For both materials, the formation of wrinkles and pores are attributed to thermal expansion as induced by laser radiation throughout the reduction process. The pore distribution and its morphology in these laser produced materials are dependent on the laser penetration depth. As the wavelength of the LightScribe laser diode is shorter compared to the $CO_2$ laser, (0.78 μm vs 10.6 μm) it also offers higher photon energy and penetration depth.

Moreover, the thickness of the rGO and LIG was measured using light interferometry on the graphene samples after they have been sputter coated (Polaron E5150 Sputter Coater, Electron Microscopy Research Services, Newcastle University) with 35 nm gold layer. The surfaces were still rough, especially in the case of LIG, posing focus problems during measurements (see Figure 3.17). The thickness of rGO is 5.76 ± 0.35 μm and 27.7 ± 8.6 μm for LIG (average based on 3 measurements).

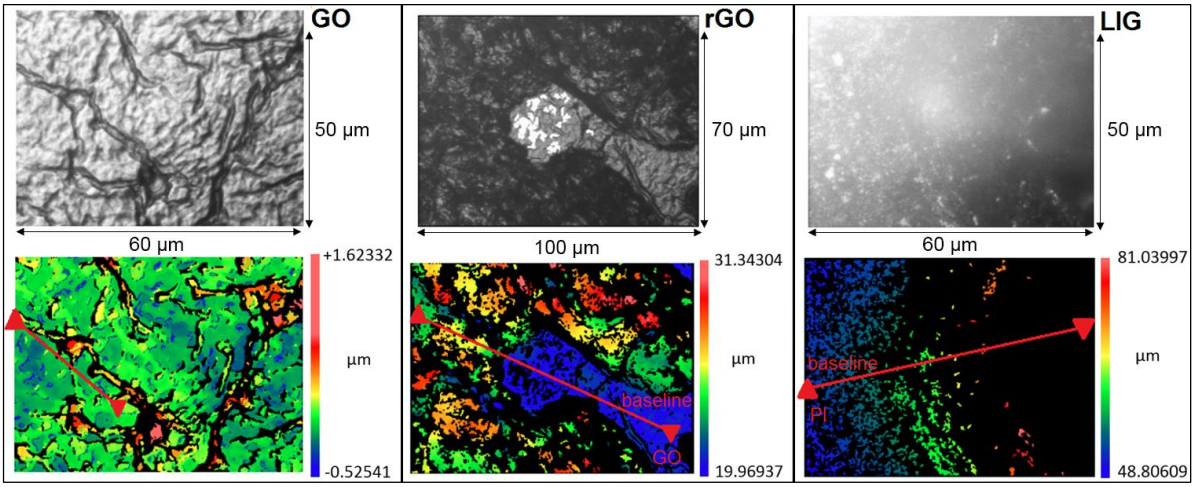


Figure 3.17. Representative Zygo profiler measurement screen capture of the microscope application for GO, rGO and LIG with 35 nm gold coating.

### 3.2.4 *Electrical properties of rGO and LIG*

The electrical properties of LightScribe rGO and LIG were further investigated. It is of interest to manufacture electrically conducting surfaces, where the presence of insulating biomolecular layers and /or chemical adsorption would trigger measurable changes in graphene electrical properties. 36 $mm^2$ rGO and LIG squares were patterned via LightScribe and on PI via $CO_2$ laser engraving, and silver conductive paint was placed on the corners of the samples for 4-point resistance measurements.

Firstly, the current-voltage characteristic of rGO and LIG was assessed, being presented in Figure 3.18. The I-V relationship is linear $R^2 = 1.000$ for both graphene based materials with $y = 1.516x + 9^{-6}$ for rGO and $y = 20.87x + 5^{-4}$ for LIG. Taking into account the slope of the two fitted trend lines, the resistance of the rGO is 14-fold higher than LIG's.

Moreover, the sheet resistance of the samples was measured and compared against CVD-grown single-layer graphene, which has an average $R_{sheet}$ of 350 Ω/sq. The starting materials GO and PI are electrically insulating with $R_{sheet}$ values in MΩ and GΩ-ranges prior to reduction. Interestingly, LIG was the most conductive with an average of 36.6 Ω/sq as produced using 35% $CO_2$ laser power (14 W) setting. The measurement range was between 33.4 and 43 Ω/sq ± 5.1 Ω/sq (standard deviation of 15%) across the three measured samples. Meanwhile, rGO obtained via LightScribe method showed significant sample-to-sample variability with an average $R_{sheet}$ of 521.7 Ω/sq ± 83.9 Ω/sq (standard deviation of 16%) for 2 g/L fixed GO concentration.

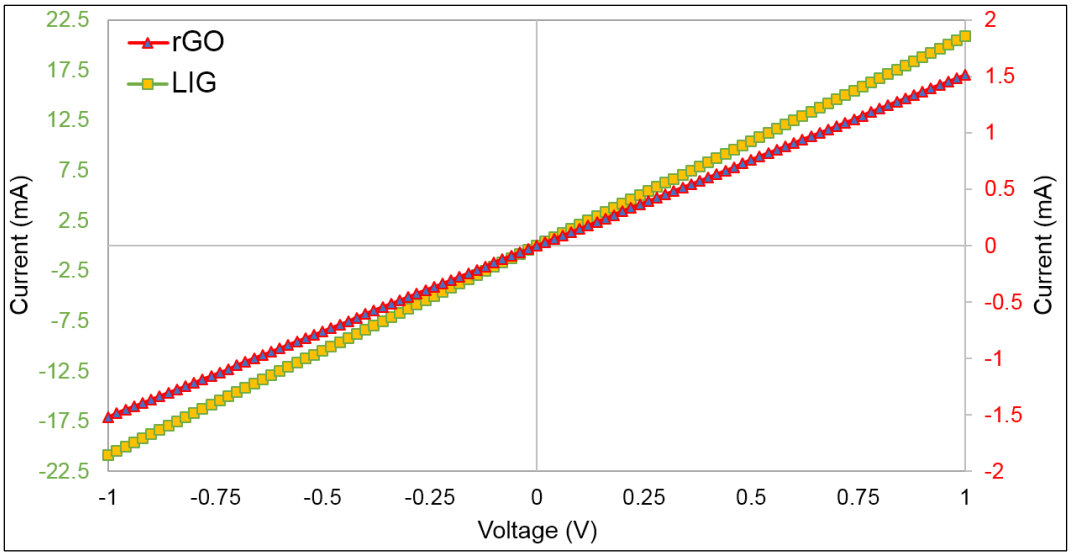


Figure 3.18. Representative I-V characteristic of rGO and LIG.

On the other hand, significant variability was found for LightScribe obtained rGO, mainly depending on the disc location. The $R_{sheet}$ was measured on multiple

samples from two discs with 2 g/L GO concentration, identical patterns and LightScribe cycle runs. The average sheet resistance was 787 ± 245.9 Ω/sq for disc no. 1 and 508.5 ± 72 Ω/sq for disc no. 2, with the results captured in Figure 3.19. Taking into account that the writing speed of the DVD drive is constant, the variation from exterior (position marked 1) towards the interior (labelled position 4) of the disc is rather intriguing. The variability is believed to be linked to track position / scribing direction on the patterns, but also to the laser exposure time, as longer towards the inner diameter (50 mm) compared to the external diameter (120 mm). Any discontinuities in material and patterns due to incomplete GO reduction or misalignment would locally cause higher material resistance. The measurement of 1223 Ω/sq on disc no. 1 at position 1 is believed to be an outlier, however, the sample-to-sample variation on disc no. 1 is significantly higher compared to disc no. 2.

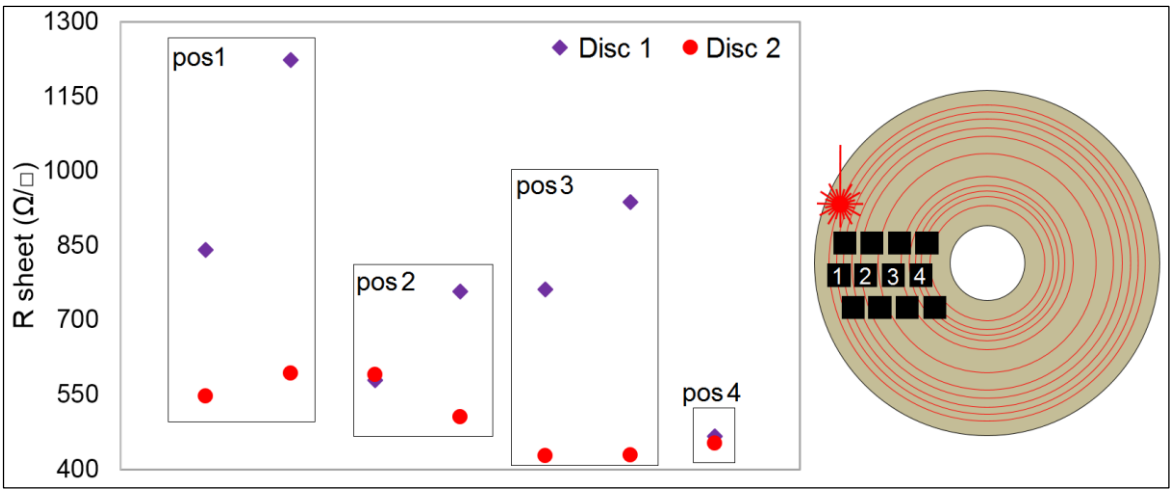


Figure 3.19. Sheet resistance measurements on rGO obtained via LightScribe method on two discs and various 36mm$^2$ samples selected from the same disc area, positions labelled 1-4.

Finally, the average LIG sheet resistance of 35 Ω/sq is highly comparable to the values reported by Lin et al. [121], the average $R_{sheet}$ for LightScribe rGO is significantly higher than the 80 Ω/sq reported by El-Kady et al. [57] or 165 Ω/sq reported by Tian et al. [384]. The differences can be explained by different quality levels of GO and slight variation in PI composition. It is well acknowledged that porous electrodes provide larger specific surface area, allowing for increased molecule loading and efficient electrochemical double-layer capacitors [385]. Ultimately, the different types of porosity in rGO and LIG are likely to account for differences in electrical properties [386].

### 3.2.5 *The selection of graphene-based materials*

The material selection process was driven by identifying graphene-based materials matching or close to some of the intriguing, but promising, graphene properties, cost of prototyping and large-scale production prospects. Their compositional characteristics are essential and, as discussed in 2.3, the ideal scenario for sensing applications would be 100% $sp^2$ carbon composition, in conditions of high electrical conductivity and ease of patterning.

Table 3-2 provides an overview of the advantages and disadvantages of the graphene materials discussed in this section. The laser synthesis method for rGO and LIG production offers a valuable an alternative to pristine, high cost, microfabrication based graphene. SLG is highly limited in terms of large-scale production, quality consistency and patterning. Moreover, via laser reduction, the obtained graphene materials present a clear increase in their surface area due to material expansion upon irradiation. As discussed in 3.2.2, $CO_2$ laser reduction is not suitable for GO. The minimum power setting of 11% (4.4 W) corresponds to a power density of 24.9 kW/cm$^2$, which is too high for the GO film reduction taking into account that the Lightscribe laser power density is 11.1 kW/cm$^2$. The available laser machine would require a very fine tuning in order to ensure material consistency, but at the cost of spatial resolution.

However, the $CO_2$ laser engraving method is compatible with PI film for the project purpose. Both Lightscribe and $CO_2$ laser engraving methods offer acceptable µm-range resolutions, and the presence of the functional groups in rGO and LIG allows for the immobilization a bioreceptor layer, suitable for biosensing applications.

Table 3-2. Summary of analysed graphene-based materials and their properties.

| Material | Pros (+) | Cons (-) |
|---|---|---|
| Graphene oxide (GO) | ▪ Commercially available<br>▪ Low cost | ▪ Quality variability depending on the production method, supplier, etc.<br>▪ Electrically insulating<br>▪ Solution-based, low viscosity<br>▪ Difficult to spin coat and to pattern using microfabrication techniques as GO film peels off |
| CVD grown single-layer graphene (SLG) | ▪ Pristine / pure graphene, it offers the discussed outstanding properties<br>▪ Electrically conductive | ▪ High cost of production / purchase<br>▪ Inconsistent quality depending on number of layers, transfer method, etc. |

| | | |
|---|---|---|
| | | ▪ No scale-up possibility ▪ High processing cost as based on microfabrication techniques<br>▪ Difficult to functionalize, it requires “defect” introduction atlering its initial properties |
| E-beam rGO | ▪ High spatial resolution (few nm-range) | ▪ High production and processing cost as fully microfabrication-based<br>▪ Reduction efficiency dependent on GO flake size and distribution (dispersion quality) |
| Lightscribe rGO | ▪ Low cost of production<br>▪ Accessible technology (DVD drive), scale-up opportunity<br>▪ Simultaneous reduction and patterning<br>▪ Electrically conductive<br>▪ Functionalization possible via oxygen surface groups | ▪ Significant sample-to-sample variability, depending on disc location and GO film thickness |
| UV rGO | ▪ In-solution reduction or via contact-mask (low-cost opportunity) | ▪ Incomplete reduction, chemical properties similar to GO<br>▪ Limited resolution |
| VitC rGO | ▪ Non-hazardous, in-solution reduction | ▪ Incomplete reduction, chemical properties similar to GO<br>▪ Difficult to pattern, eventually via microfabrication (high cost) |
| $CO_2$ rGO | ▪ Low-cost scale-up opportunity via engraving laser | ▪ Requires lower power laser (GO was entirely burned) |
| LIG ($CO_2$ if PI film) | ▪ Low-cost source material (PI tape)<br>▪ Low-cost scale-up opportunity via engraving laser<br>▪ Simultaneous material synthesis and patterning<br>▪ Electrically conductive<br>▪ Good sample reproducibility, especially in terms of electrical properties | ▪ Laser tuning required as variability is expected for different laser machines<br>▪ Limited amount of oxygen functional groups (1-3%) |

### 3.3. Conclusions

The understanding of graphene “quality” is essential in order to employ the material in suitable applications. XPS and Raman spectroscopy characterisation techniques are compulsory and complementary in this respect, with a growing body of literature available for comparison. Depending on the reduction method, as well as

graphene oxide source and quality, the reduction process can be incomplete, like in the case of e-beam rGO or UV rGO.

rGO produced via the LightScribe method is preferred over $CO_2$ laser reduction method due to its original design intent (engraving, fixed parameters) and its demonstrated fluence / energy consistency. It was observed that for larger patterns (> 100 $mm^2$), the $CO_2$ laser would completely burn the GO in spite of using minimum power settings.

LIG presented smooth and more uniform track patterns compared to rGO, but its surface was significantly rougher. Suitable laser power varies between 12 W and 16 W at maximum speed, but this depends on machine's continuous utilisation e.g. the power had to be reduced if the $CO_2$ laser was previously used in cutting mode. Also, the spatial resolution of the $CO_2$ laser is 150 µm compared to 20 µm for LightScribe.

It was also attempted to carefully remove the top layers by sticky tape and it was found that the material underneath had insulating properties in spite of presenting the same "reduced" black colour. An early indication from this study is that LIG is a better electrical conductor than rGO, but the conductivity of both materials seems to rely on their top and edge exfoliated graphitic layers.

The measurements performed on different graphene samples highlight their complexity and variety. Targeting biosensing applications, the material selection constitutes an engineering compromise between graphene purity, presence of functional groups, the possibility of patterning without impacting initial material properties and upscale production potential. Using laser engraving methods, patterned graphene based materials with rich morphological features were easily obtained and at a low cost, reason for which LIG and LightScribe rGO were further employed as biosensing platforms.

# Chapter 4. A novel approach on electrical biosensors

This chapter provides a preliminary study of high-frequency, RF-based detection method as an alternative to current electrochemical impedance (EIS) techniques, of interest for prostate specific antigen (PSA) diagnosis. Conventional capacitive biosensors such as interdigitated electrode arrays (IDE) can be converted into electrical resonators with the addition of external circuit components or in-place design modifications. The first part of this study focused on computational models based on capacitive circuits and prediction of the interfacial or double-layer induced impedance variation upon biomolecules addition. The results justified the potential of using the RF-based electrical detection approach via impedance matching. The hypothesis was further verified in practice by employing commercially available gold IDE devices and comparing the obtained results against the conventional EIS method.

## 4.1. Methodology

### 4.1.1 *Materials*

The chemicals (>99% purity) were purchased from Sigma Aldrich, UK, unless otherwise stated: acetone ($CH_3COCH_3$), ethanol ($CH_3CH_2OH$), phosphate buffer saline (10 mM, PBS, pH 7.4), potassium ferricyanide ($K_3Fe(CN)_6$Tween 20, DTSP (3,3′-Dithiodipropionic acid di(N-hydroxysuccinimide ester, $C_{14}H_{16}N_2O_8S_2$), DMSO (methyl sulfoxide, $(CH_3)_2SO$), BSA (bovine serum albumin), glycine ($NH_2CH_2COOH$), hydrochloric acid (HCl). Natural human prostate specific antigen antibody (PSA-10) was purchased from Fujirebio, US and the coupling protein (PSA, PN: ab78528) was procured from from abcam, UK. 1 M ethanolamine ($NH_2CH_2CH_2OH$) was supplied by Biacore, Sweden. Potasisum ferrocyanide trihydrate ($K_4Fe(CN)_6 \cdot 3H_2O$) was procured from BDH.

DropSens gold IDE devices on a glass substrate were purchased from Metrohm (UK), with the geometry: 5 µm width and gap, 6.76 mm length and a total of 500 electrodes. A customized generic PCB which allows for series and shunt component addition, as well as edge mount of IDE was designed in Eagle, Cadsoft (see Figure 4.1) with the help of Mr. Richard Burnett (Newcastle University) and produced by Newbury Electronics Ltd (UK). Standard surface mount resistors, inductors and capacitors were purchased from Farnell, UK.

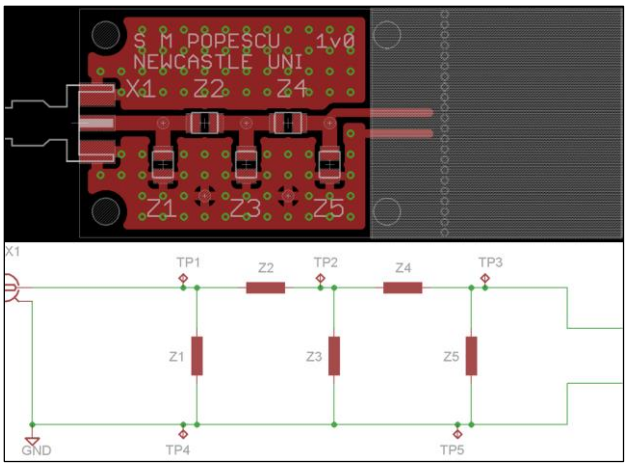


Figure 4.1. PCB design and circuit schematics (Eagle, Cadsoft).

### 4.1.2 *Software*

The impedance and RF responses were simulated using NI Multisim 13.0 and AWR Design Environment 12, using a logarithmic sweep with 1000 points per decade. The experimental data was statistically analysed using SigmaPlot software.

### 4.1.3 *Experimental*

Figure 4.2 presents the gold IDE device as soldered on the custom PCB and used throughout the experimental work. The functionalization protocol for PSA antibody-antigen capture on the gold IDE surface is detailed below.

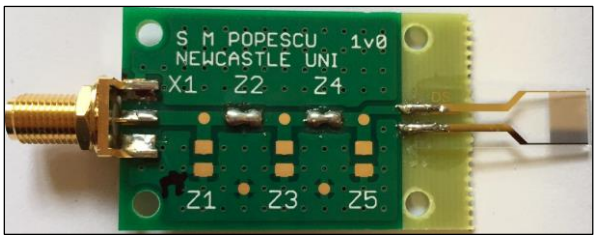


Figure 4.2. Experimental arrangement and attachment of the IDE on the custom PCB.

1. The IDE was cleaned in 3-minute cycles by mild sonication in acetone and ethanol and dried under nitrogen flow prior to being cleaned in oxygen plasma (30 seconds).

2. The IDE sensing area was incubated in 4 mg/mL DTSP in DMSO for 15 minutes. The devices were then rinsed in DMSO, PBS-Tween 0.005% and PBS.

3. The 20 µg/mL PSA-10 antibody solution in PBS was pipetted on the IDE surface and allowed to react for 30 minutes, after which it was washed in PBS.

4. The IDE was incubated in ethanolamine for 10 minutes in order to quench unreacted DTSP. The IDE was then washed in PBS-Tween 0.005% and PBS.

5. 2% BSA in PBS was applied on the electrode surface to prevent any non-specific adsorption, followed by a PBS washing step.

6. PSA solution in PBS was prepared at various concentrations (1-1000 ng/mL). The IDE was incubated in PSA solution for 20 minutes, after which it was thoroughly washed in PBS-Tween 0.005% and PBS.

7. The gold layer was regenerated by washing the sensor surface in 0.1 M glycine of pH 2.2-2.3 for approximately 20 seconds. The pH of the glycine was adjusted using concentrated HCl (1 M). The IDE was then washed in PBS buffer.

8. Steps 5 and 6 were repeated to test different PSA concentrations.

#### 4.1.4 *Measurements*

The devices were soldered on the PCB to allow for same device utilisation on both machines, as well as a back-to-back comparison of the results. In order to test the PCB on EIS, an adaptor was used i.e. PCB SMA female-to-banana female plug. As good practice, the wires and device were fixed in place during measurements. Also, control measures have been implemented in order to reduce measurement and operator variability: controlled volume of solution i.e. 80 µL, sufficient to cover the IDE sensing area and controlled level of immersion in electrolyte.

EIS measurements were acquired using a Solartron Modulab XM ECS system (Ametek) system with the settings: 10 mV AC (0 DC) input signal, 1 Hz-100 kHz frequency range, logarithmic sweep with 1000 points / decade.

A Rohde & Schwarz ZVL VNA system was used for one-port RF measurements, using: 0 dBm input signal in the frequency range 100 kHz-1 GHz, a linear sweep with a maximum number of 4001 points, data acquired at 1 kHz bandwidth. The system was fully calibrated (Short-Open-Match) using the corresponding calibration kit (R&S ZV-Z121) prior to measurements.

### 4.2. Results and discussion

#### 4.2.1 *Computational modelling: electrical impedance (EIS) vs. power (RF) for biomolecules detection*

The aim of this study was to improve the biosensor performance via $C_{dl}$ signal amplification, as addressed in subsection 2.5.3, while minimizing the solution resistance effect. The impedance response of capacitive biosensors exhibits three frequency regions: low frequency - where the capacitance (geometrical and interfacial) of the IDE is dominant; intermediate frequencies - reflecting the effect of resistive

components, such as contact resistance and solution resistance; high frequency - inductive response originating from the electrochemical cell and connection wires, but this is usually negligible in the EIS measurement range (up to 100 kHz). However, electrical measurements using RF machines should allow for monitoring of the power fluctuation during immobilization and detection stages. Enhanced sensitivity is expected at 50 Ω-input port matched impedance as ensuring maximum power transfer between source and load (see 2.6.2). Changes in IDE conductance or dielectric constant are most applicable at high frequencies due to restrictions on component values.

### 4.2.2 *Electrical impedance-based detection*

In order to identify the optimum detection solution, electrical impedance simulations were performed in order to compare several circuits: capacitive (IDE-like), series resonant and impedance-matched at 1 MHz. A basic equivalent circuit of the IDE [312] consisting of the geometrical capacitance and solution resistance was used. Initial EIS measurements of the gold IDE in PBS buffer indicated an average capacitance of 300 nF. The inductor value for the series resonant circuit i.e. 1 μH, was selected based on the frequency range conditions for the EIS measurements (< 1 MHz). The impedance matching was obtained at 1 MHz, by adding a corresponding LC network. For the capacitive layout, the impedance spectrum was recorded at in the range 0.1 Hz-100 kHz, so that the interfacial properties of the electrode are detectable. It is well acknowledged that resonant biosensors function on the principle of frequency shift and / or damping as an effect of biomolecules loading [387]. For the source (50 Ω) impedance matched circuit, changes in the electrical properties are expected at the targeted frequency, with the addition of a resonant peak.

Moreover, Rana et al. [388] showed that the immobilization of a molecular layer to the IDE sensing area triggers a maximum impedance change of just over 7%. Therefore, the variation in electrical impedance of the three circuits was assessed for changes in the $C_{biosensor}$ by 1%, 5% and 10% due to double-layer formation. The study focused on identifying the most sensitive impedance-related parameter among: Re(Z), Im(Z), $Z_{mag}$, θ. Figure 4.3 presents the obtained calibration curves obtained based on the performed simulations.

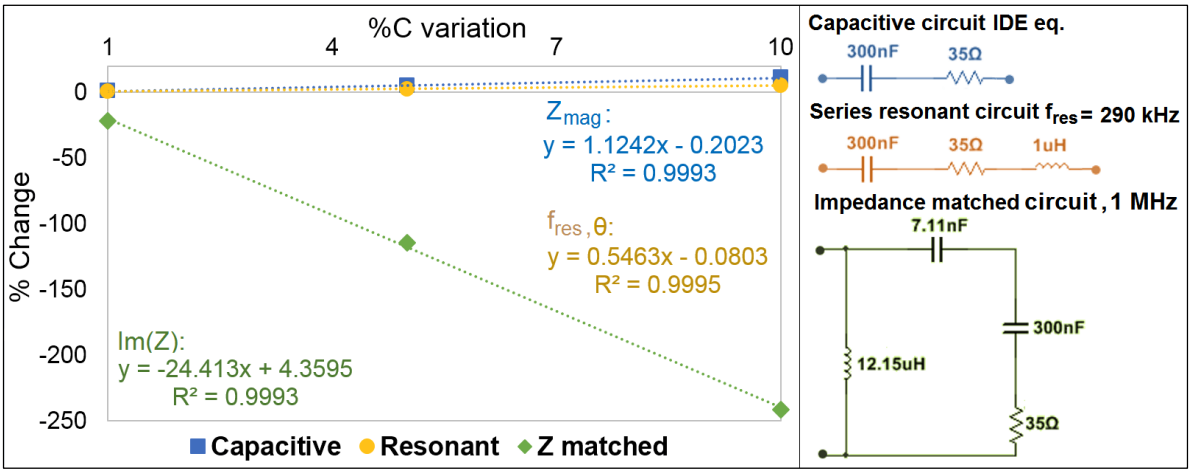


Figure 4.3. Simulation-based impedance calibration plot for capacitive, resonant and impedance matched circuits (right) as induced by capacitance changes of 1, 5 and 10%.

The electrical circuit simulations showed that the double-layer induced changes for the simple RC circuit are reflected by the magnitude of impedance at lower frequencies (1 Hz-5 kHz). Some changes can also be quantified by using the phase of impedance at higher frequencies (>10 kHz) in the transitional region between capacitive and solution resistance dominance. For the electrical resonant circuit, the impedance changes are highly detectable at resonant frequency of 290 kHz, while the inductor effect is visible at frequencies above 400 kHz. However, the performance of a resonant circuit is highly dependent on its Q-factor. By matching the source impedance at 1 MHz, Im(Z) and θ exhibit significant changes. The slope of the linearly fitted trendline gives an indication of sensor's sensitivity, with a maximum change of 24.413 Ω per C unit (nF) obtained by using the Im(Z) for the source impedance matched circuit, and superior to the other types of circuits.

Other aspects regarding the electrical impedance of the matched circuit were further investigated. A linear trend was obtained at lower matching frequencies of up to 1 kHz, where the signal is further amplified by the geometrical and substrate capacitance. However, the inductor and capacitor values required to achieve this are very high i.e. mH, μF ranges, not off the shelf components. By increasing the matching frequency to 10 MHz, $R^2$ can be slightly improved by 0.2% to 0.9967, but the 1% capacitance decrease triggers only 1.32% change in the phase compared to 21.94% for the matched circuit at 1 MHz. The inductor self-resonant frequency should be at least one octave higher than the matching circuit resonance. This condition is further restricted when targeting high Q-factors, as more complex arrangements are needed (for example, T or π networks), which require a higher number of components.

### 4.2.3 *RF impedance matching-based detection*

The concept of the impedance matching was further explored by simulating the reflection coefficient $S_{11}$, shown in Figure 4.4. The coefficient decreases steadily up to 250 kHz, but at higher frequencies above 100 kHz it remains constant at -15.07 dB. On the other hand, the impedance matched circuit presents a minimum point of -76.92 dB.

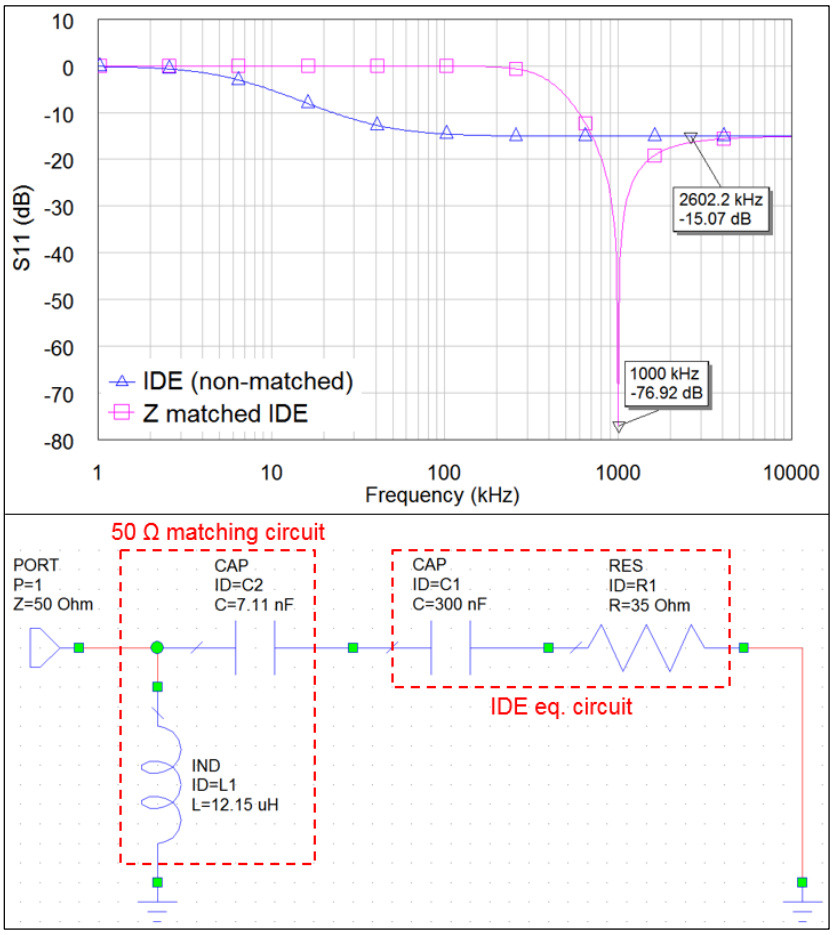


Figure 4.4. Simulated reflection parameter ($S_{11}$) variation for the initial capacitive circuit and upon source impedance matching at 1 MHz.

Also, in RF applications, a high Q-factor is highly desirable for lower energy loss rate [232]. Therefore, the effect of the Q-factor of the matching circuit was further investigated in this particular scenario to assess its importance for $S_{11}$ detection. The simulation results for the impedance matched IDE circuits with low and high Q-factors are shown in Figure 4.5

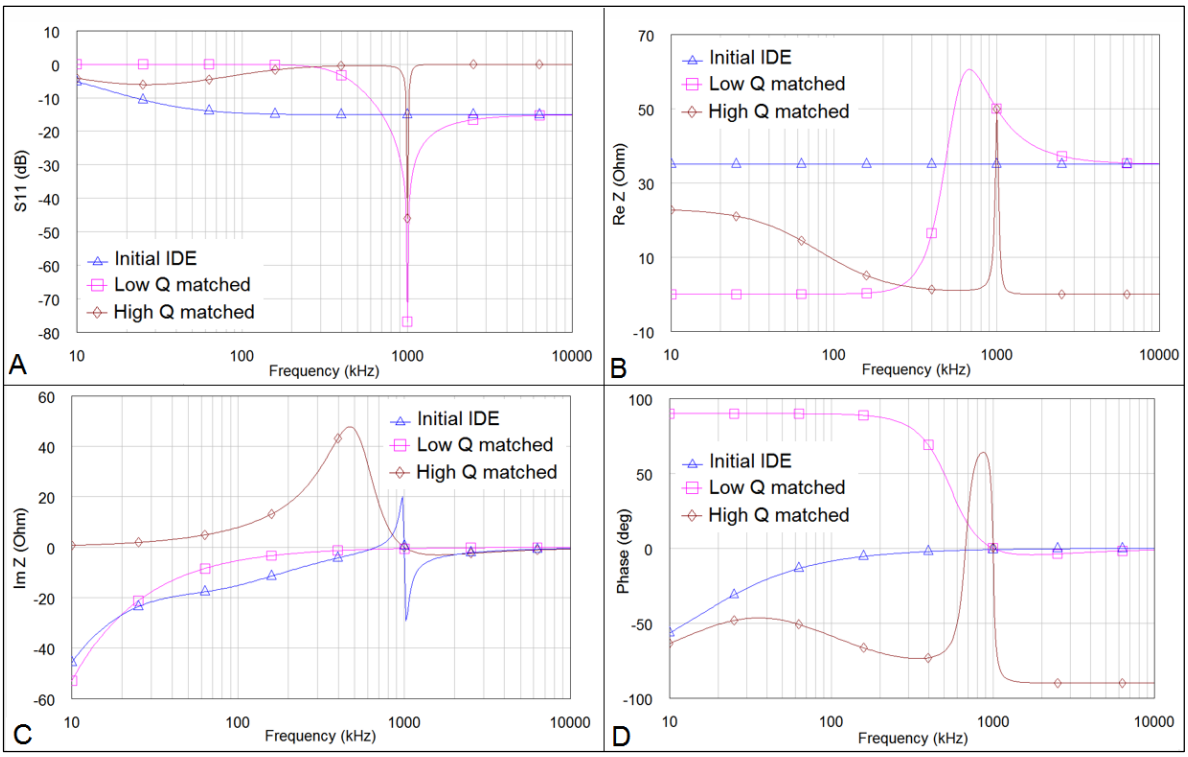


Figure 4.5. Comparative reflection parameter ($S_{11}$) and impedance related simulation plots for the initial (capacitive), non-matched circuit and 50 Ω impedance matched circuits with low (0.65) and high Q-factor (10).

The reflection parameter $S_{11}$ has a minimum value of -76.9 dB at matching frequency for a low-Q matching circuit (Q=0.65), compared to the high-Q factor circuit (Q=10) with a minimum of -46 dB. While the Re(Z) peak profile is distributed around its maximum value of 60.58 Ω, crossing 50 Ω in two points at 548 kHz and 1.1 MHz, the high-Q matching circuit exhibits a sharp unique peak at a maximum of 50 Ω. As the S11 (dB) value is a reflection of the 50 Ω impedance matching quality of the circuit, the low-Q matching circuit is in vicinity of the value for a larger part of the response. Hence, the Q-factor involves a compromise between its bandwidth and sensitivity, and in this case, one can target the alteration of the reflection parameter rather than a frequency shift.

As per impedance simulations, the variation of $S_{11}$ for IDE capacitance changes was also investigated (see Figure 4.6). $S_{11}$ increases for lower $C_{sensor}$ values due to the increase in Im(Z). A slight frequency upshift by 2.3. kHz for the reflection parameter can be observed for 10% capacitance change. Hence, a combined effect of the reflection parameter and frequency shift can be eventually employed to improve the detectability of the capacitive surface changes.

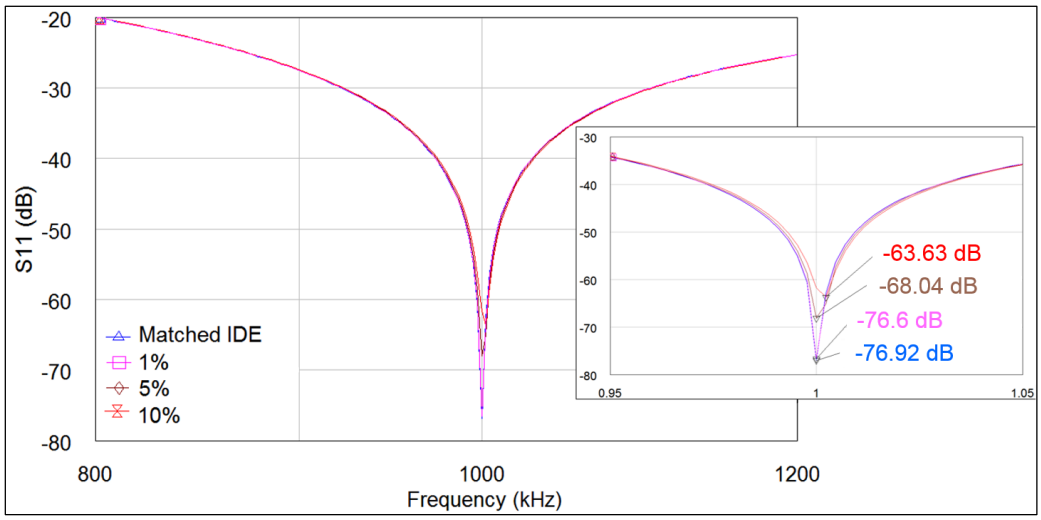


Figure 4.6. Simulated reflection parameter ($S_{11}$) for the impedance matched circuit for capacitive changes of 1, 5 and 10%.

Furthermore, depending on the effects triggered by the biomolecules attachment to the electrode surface, one can expect an increase ($C_{biomolecules}$ in parallel) or decrease ($C_{biomolecules}$ in series). Figure 4.7 illustrates the predicted biosensor calibration curve for the two scenarios, with the simulated values fitted by a second order polynomial. If deviating from the matched impedance point, either of the cases would lead to an increase in the reflection parameter, however, the increasing $C_{dl}$ case (biomolecular layer with an equivalent parallel capacitive element) shows a good potential for $S_{11}$-based detection mode, with $R^2 = 0.9994$.

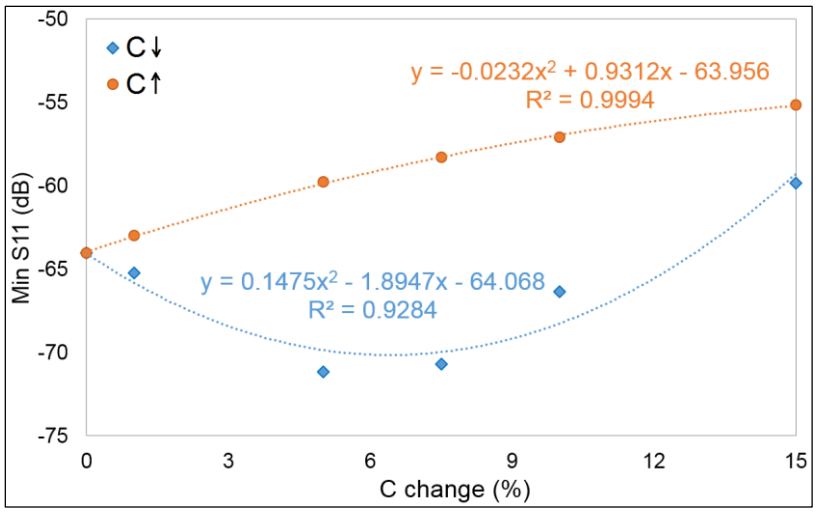


Figure 4.7. Simulation-based calibration curve showing the relationship between the reflection parameter ($S_{11}$) and capacitance changes for the impedance matched circuit (Q=0.65).

These findings, suggest that through a backwards approach, using the RF characteristic of the SUT, one can match its equivalent circuit to the 50 Ω source port impedance in order to maximise the signal. While the impedance measurements look

more promising in terms of linearity, this power ratio approach is novel and can be eventually applied to a variety of circuits.

## 4.3. Case study: gold IDE immunosensor for prostate specific antigen (PSA) detection

This section presents practical results using commercially available gold IDE, allowing to assess the proposed RF-based detection principle as compared against conventional EIS. The outcome of this work is essential to assess the potential of this novel detection approach on graphene based IDE biosensors.

### 4.3.1 *Electrical response of the gold IDE devices*

In order to gain an understanding of the behaviour of the gold IDE sensors at low and high frequencies, the devices were electrically tested at low and high frequencies, using EIS and VNA measurements respectively. Figure 4.8 presents the Bode impedance response of several IDE devices, freshly cleaned and measured in PBS electrolyte.

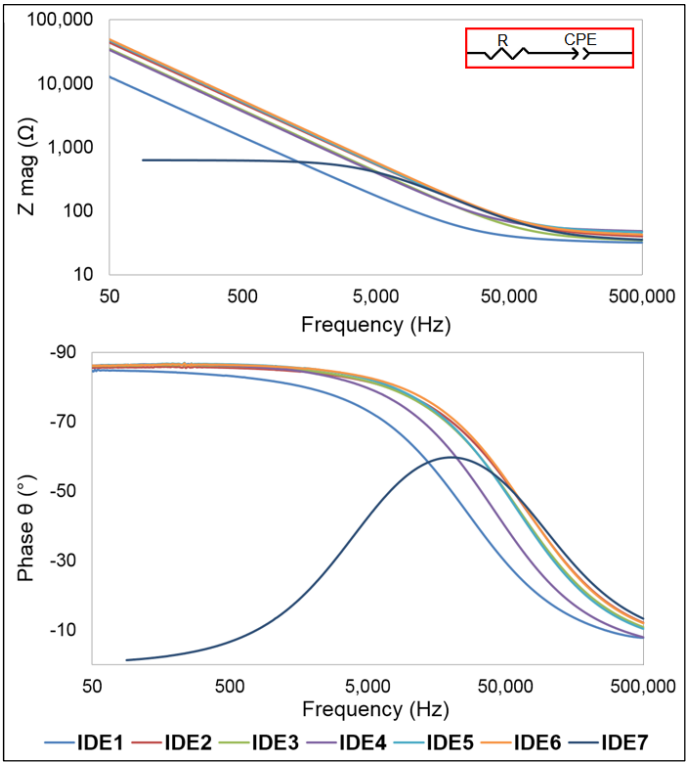


Figure 4.8. Bode plots (magnitude and phase of impedance) for different gold IDE devices at low frequencies; EIS measurements taken in 10 mM PBS, pH 7.4, RT; inset: equivalent circuit.

The repeatability of the IDE properties is acceptable, however IDE 7 had some electrodes shorted due to manufacturing defects. The identified equivalent circuit is comprised of series solution resistance (≈ 40 Ω) with constant phase element (CPE),

introduced in Table 2-5. The CPE accounts for non-ideal capacitive behaviour; the average phase angle across the six repeatable devices is 86.35° compared to 90° for an ideal capacitor. The average CPE-T fitted value is $44.2 \cdot 10^{-6} \pm 8.56 \cdot 10^{-8}$ F (std. dev) with average CPE-α of 0.957 ± 0.0096 (std. dev). This can be explained by some level of surface roughness and impurities on the gold layer.

Moreover, Figure 4.9 shows the $Z_{mag}$ and $S_{11}$ responses of the gold IDE devices as recorded on the VNA in the frequency interval 100 kHz-1 GHz. The steady impedance response is due to the resistive effect of the electrolyte i.e. PBS buffer and contact resistance; its limited repeatability can be explained by a slight variation in the contact resistance due to operator and soldering conditions. The resonant peak at 300 MHz is common for all samples and it was introduced by the PCB-VNA connection. The average minimum reflection parameter was -17.33 ± 5.45 dB, corresponding to an electrical impedance of 36.2 ± 5.9 Ω. The $S_{11}$ measurements demonstrate the high sensitivity of the VNA equipment, but also substantial device variability. For this reason, the impedance matching process was individually and separately applied to each IDE.

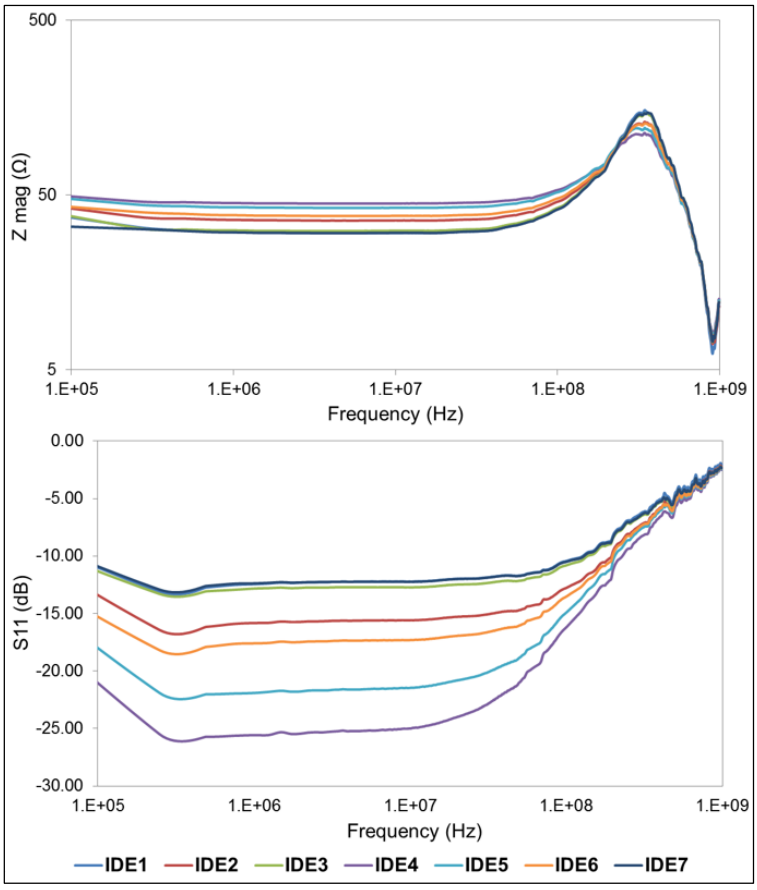


Figure 4.9. Impedance and reflection parameter ($S_{11}$) of different basic gold IDE devices at high frequencies (no impedance matching); VNA measurements taken in 10 mM PBS, pH 7.4, RT.

### 4.3.2 *Impedance matching process*

In practice, the impedance matching process was firstly verified using a known load i.e. a 330 Ω resistor, soldered on the PCB similarly to the IDE (see Figure 4.2). An LC network with a series inductor of 1.8 μH and a parallel capacitor of 114 pF should match the impedance to 50 Ω at 10 MHz. The high frequency measurements were acquired using the VNA for different circuit arrangements and NI Multisim was used to determine the equivalent circuit of the experimental data:

- Ideal case: load and impedance matching network components, simulation based
- Expected case: as ideal, but including manufacturer specifications i.e. self-resonant frequency due to $C_{stray}$ and $R_{DC}$ for inductor, variability in component's actual performance; simulation based
- Actual case: as expected, but including tracks and soldering effects; experimental (measured)
- Adjusted case: as actual but representing the best match of the experimental data and compensating for unwanted variability, PCB, tracks length and cabling effects; experimental (measured).

The impedance matching was performed at 11 MHz as using standard off-the-shelf components. The impedance response for each of the four cases is presented in Figure 4.10, with the corresponding circuits shown in Figure 4.11. It is expected and realistic that in practice, the electrical components do not behave as in the Ideal or Expected scenarios. Hence, by determining the corresponding circuit i.e. Adjusted, one can understand the parasitic effects.

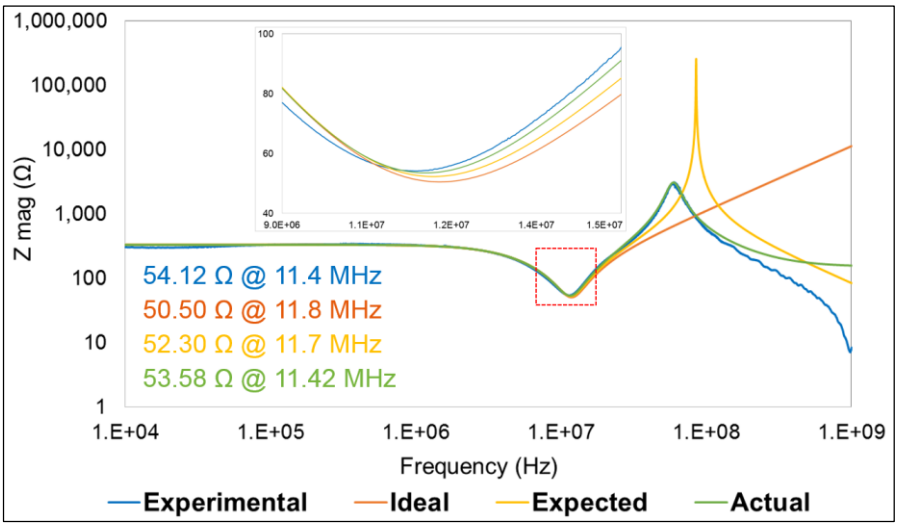


Figure 4.10. Magnitude of impedance response of the 330 Ω resistive load matched to 50 Ω in practice (Experimental) and simulated responses (Ideal, Expected and Actual circuit models).

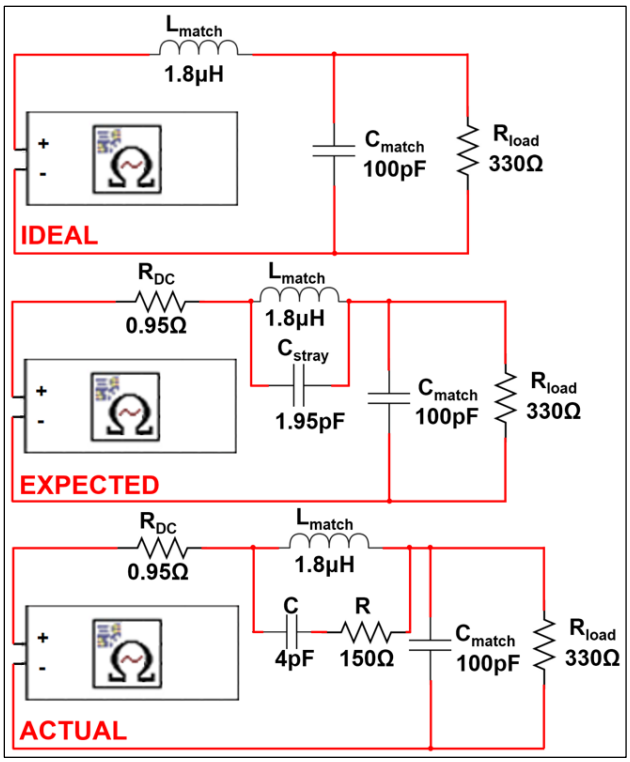


Figure 4.11. Circuits corresponding to 330 Ω impedance matched to 50 Ω as per Figure 4.10 .

One can notice that the Actual circuit arrangement shows an increase in stray capacitance ($C_{stray}$) by just over 100% due to the shorted track, with a parallel capacitive effect. The resistive component in series with $C_{stray}$ can be explained by the poor capacitor quality (dielectric). The stray inductance is not represented here as negligible compared to the high value of the $L_{match}$ (µH-range). These results were confirmed by conducting additional tests of the shorted PCB. Knowing the real/practical impedance characteristics of the circuit, further simulations were performed to further improve the 50 Ω matching. In terms of the reflection parameter, there is an improvement by -20.87 dB if using the theoretical matching circuit (Expected) and by -29.94 dB for the Adjusted matching circuit - see Figure 4.12. By increasing the $C_{match}$ by 10%, the obtained magnitude of impedance was 50.04 Ω at 10.62 MHz.

Moreover, Figure 4.13 presents the $S_{11}$ values for the Adjusted impedance matched circuit, with a minima of -33.79 dB at 10.28 MHz, which is remarkably close to the practical result of -33.05 (2.19% higher) at 10.18 MHz (upshifted by 1%).

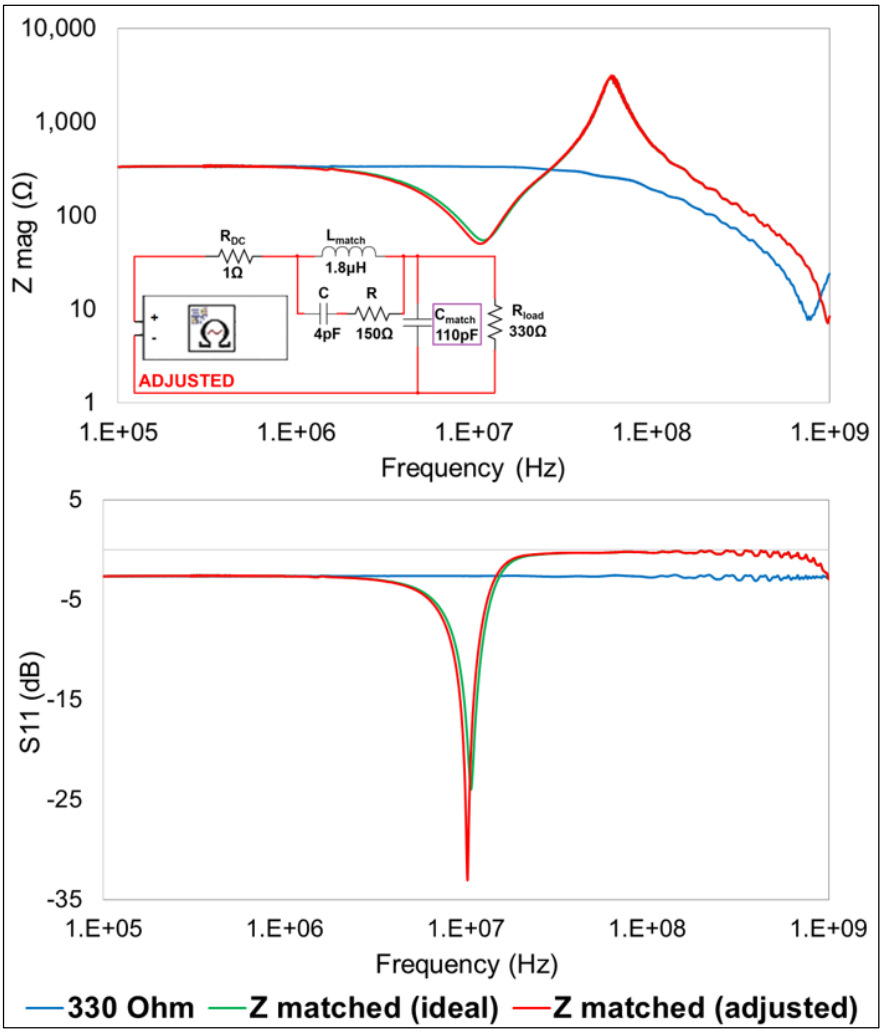


Figure 4.12. Magnitude and reflection parameter ($S_{11}$) measurements for the 330 Ω resistive load and the corresponding simulation-determined circuit.

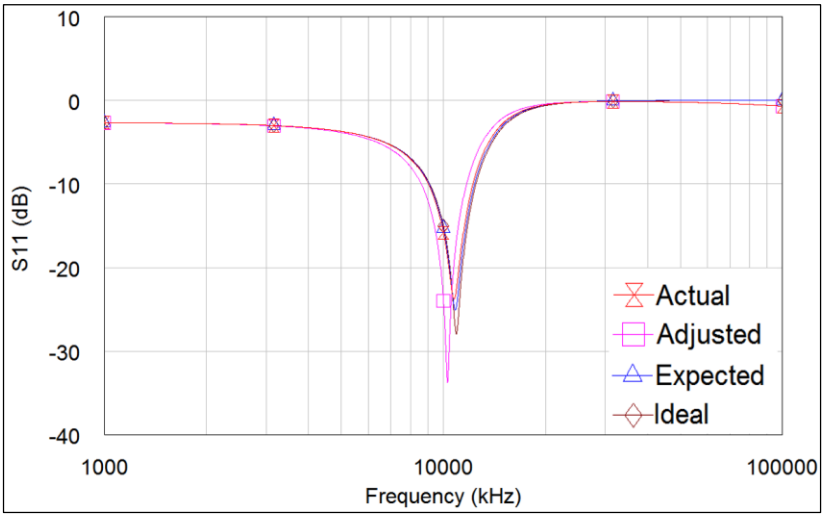


Figure 4.13. Simulated reflection parameter ($S_{11}$) for the ideal, expected, actual and adjusted matching circuits for a 330 Ω resistive load.

### 4.3.3 *Impedance matching of the gold IDE devices*

The impedance matching exercise of a simple, resistive load in section 4.3.2, allowed for an understanding of stray and parasitic effects introduced by the PCB and circuit arrangement. Moving onto more complex loads, such as IDE, the experimental response upon impedance matching attempts can be predicted.

The gold IDE devices were tested at low and high frequencies, with results presented in section 4.3.1. The average impedance of the IDE in PBS buffer at 1 MHz is *36-0.43 j*. The selected LC arrangement is a high-pass matching network with a 12.8 µH shunt inductor and 7.2 nF series capacitor. Considering the availability of standard components and the above-discussed parasitic effects, NI Multisim simulations were further performed in order to predict and adjust the matching circuit prior to soldering the components. In practice, a 13.1 µH inductor was obtained by an inductive series arrangement (4.9 µH, 8.2 µH) and 7.08 nF obtained by a capacitive parallel arrangement (6.8 nF, 280 pF). Figure 4.14 shows the response of the gold IDE as initially tested and after the addition of components as impedance matched at 1 MHz.

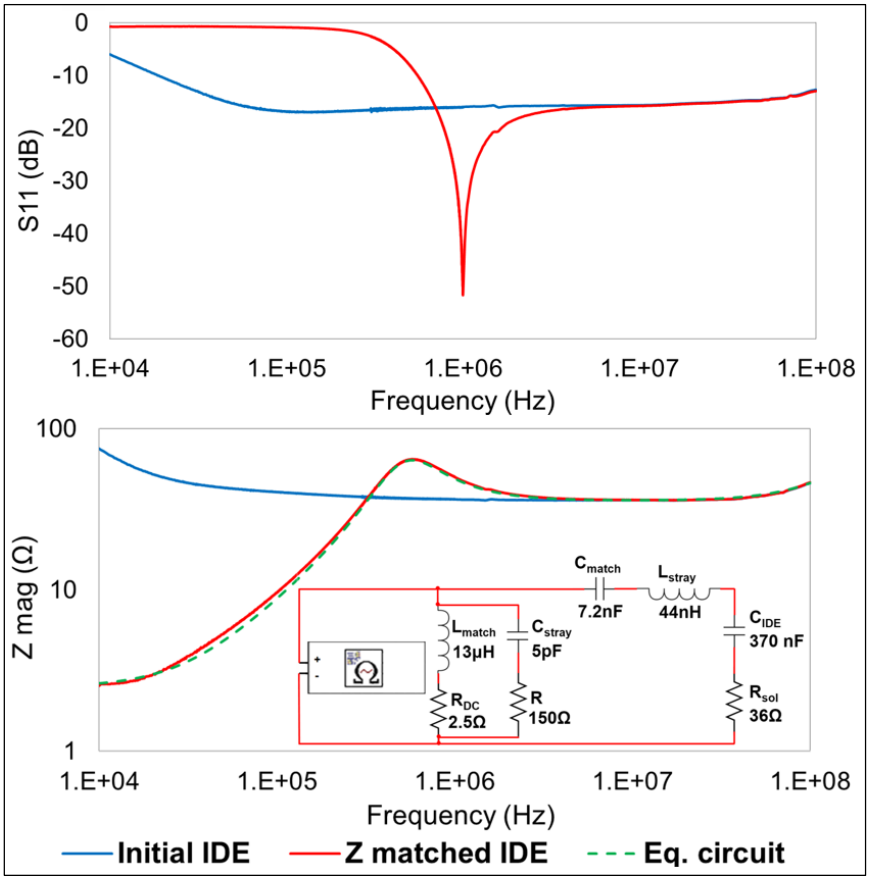


Figure 4.14. Measurements (experimental) of the impedance matched gold IDE reflection parameter ($S_{11}$) and its impedance response, PBS buffer; inset: equivalent circuit of the impedance matched IDE.

The obtained circuit performance for the matched IDE was highly satisfactory in this case. Subsequent fine tuning was avoided in order to not damage the PCB and/or further alter its response by replacing, adding or re-soldering other components.

### 4.3.4 *Surface sensitivity and PSA detection on 50 Ω impedance matched gold IDE devices*

Some brief initial experiments were performed in order to assess the sensitivity of the VNA to the testing medium and interface changes. After gold surface activation with thiols (PEG-OH:PEG-COOH), the non-specific adsorption was assessed by using BSA in the testing electrolyte. The VNA full frequency range measurements are presented in Figure 4.15.

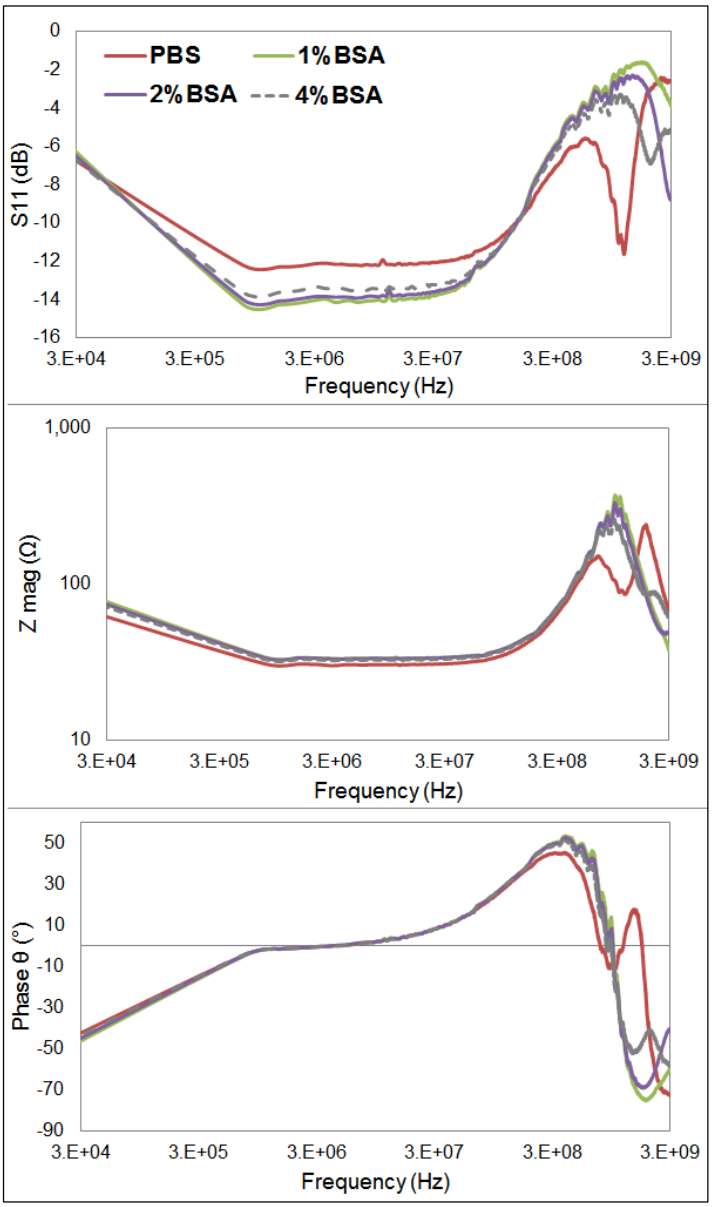


Figure 4.15. VNA recorded reflection parameter ($S_{11}$) and impedance measurement of the gold IDE in PBS buffer and in PBS+BSA solution of 1-4% concentration.

It can be observed that the $S_{11}$ peak at 1.5 GHz is upshifted with attenuated intensity for higher BSA concentrations, and a corresponding increase in the magnitude of impedance. The phase at 2.8 GHz slightly moves away from -90° as an effect of the sparse attachment of the BSA molecules to the gold surface. This level of variation, identified for all measured parameters, confirms the sensitivity of the VNA and its promising potential for the measurement of surface and interface interactions.

Moreover, conventional, non-faradaic EIS measurements of the gold IDE (non-matched) were compared against its reflection parameter $S_{11}$ (as impedance matched) during functionalization and upon PSA capture in order to test the feasibility of the proposed electrical detection principle. The functionalization of the gold surface for PSA capture is schematically shown in Figure 4.15.

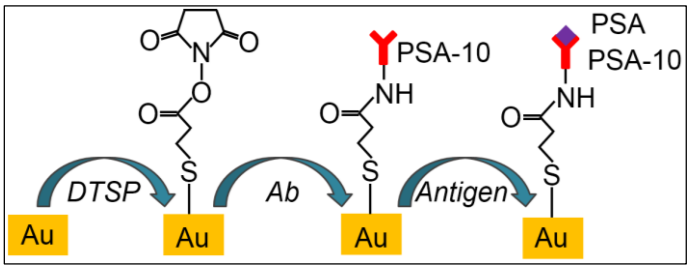


Figure 4.16. Schematic diagram of functionalization method of the gold IDE for prostate specific antibody-antigen (PSA) interaction.

Figure 4.17 presents the interface changes detected during functionalization and PSA detection for various protein concentrations using impedance spectroscopy. The prostate-specific antigen immobilization on the gold electrodes via DTSP triggers an increase in the magnitude of impedance by 42% (at 1 Hz) due to its insulating properties. The presence of the biomolecules is detectable as a double-layer is formed and its thickness varies for increasing PSA concentrations.

A calibration plot was built and fitted by a one-side binding curve. The identified $C_{dl}$ variation confirmed that the IDE functionalization was successful, but the measurement repeatability was quite limited. The working range is 1-100 ng/mL, with a predicted lowest limit of detection (LOD) of ≈ 900 pg/mL (calculated from blank response and 3 x std. dev). Remarkable literature results for PSA detection reported LOD easily within 1-10 pg/mL [349], but these were reported in conditions of redox probes i.e. faradaic EIS and optimised surface chemistry.

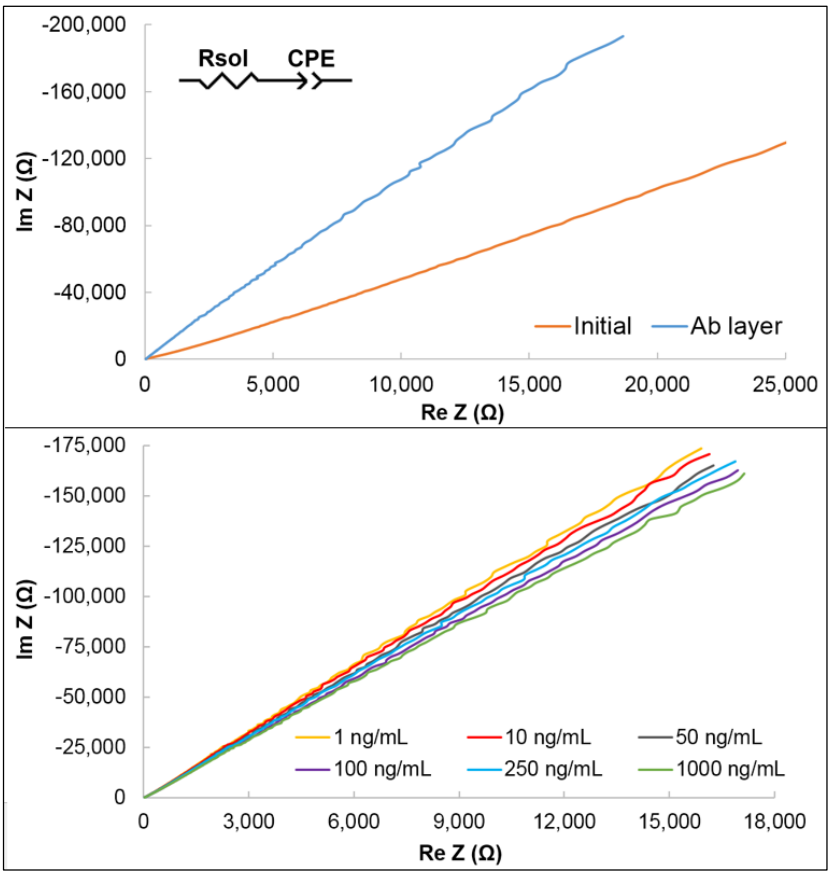


Figure 4.17. Nyquist plots of the non-faradaic EIS of the gold IDE upon antibody layer immobilization and antigen capture, 10 mM PBS, pH 7.4; inset: equivalent circuit.

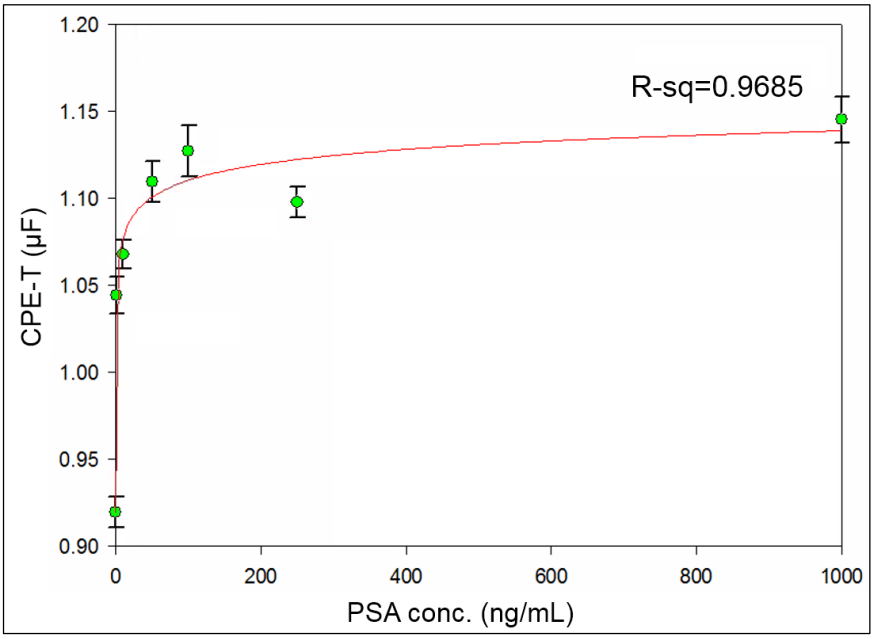


Figure 4.18. Calibration curve showing CPE-T at 1 Hz as function of PSA concentration as detected on the gold IDE, fitted by one-side binding curve. The plotted points represent the average between two consecutive measurements (error bars).

Furthermore, the measurement range on the VNA was reduced around the matching frequency (1 MHz) to 0.5-5 MHz with maximum number of points to improve

data resolution. Figure 4.19 shows the $S_{11}$ response recorded during surface functionalization and prostate specific protein capture. The double layer formation had a clear impact on the IDE impedance, with increasing reflection parameter, but there was no clear correlation between the minimum $S_{11}$ value and PSA concentration.

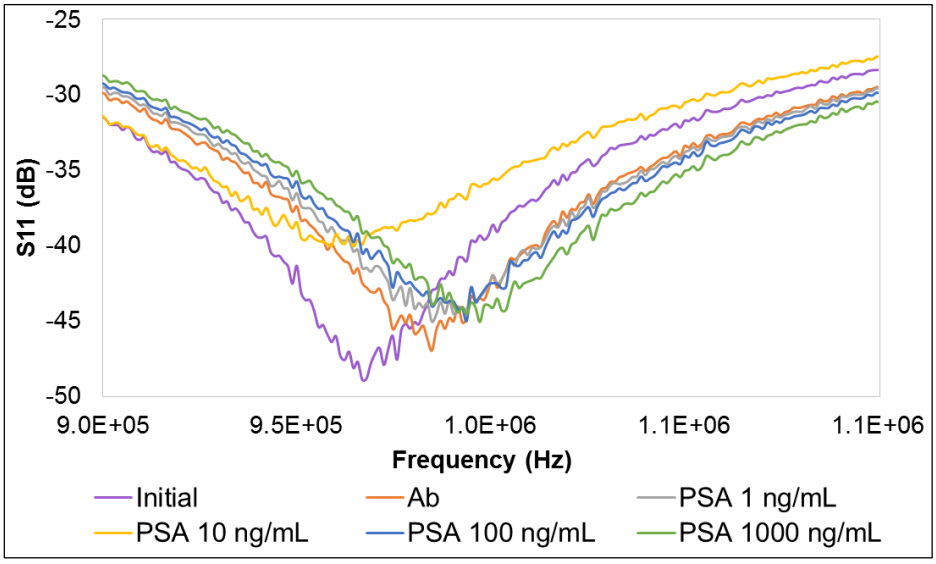


Figure 4.19. Measured $S_{11}$ for impedance matched gold IDE for PSA detection; each data point is the average across 10 measurements.

The measurements performed on the VNA were significantly noisy. The minimum $S_{11}$ points were extracted as the minimum average value at the peak frequency using a polynomial fit function (Matlab). The noise source is nearly impossible to be identified as the VNA is highly sensitive to the surrounding equipment and faults in materials, and the setup for these experiments were standard and similar to low frequency measurements on the potentiostat. The extracted data is shown in Figure 4.20. While a satisfactory calibration curve could not be obtained, the minimum $S_{11}$ and its corresponding frequency showed a linear trend in the range 0-10 ng/mL.

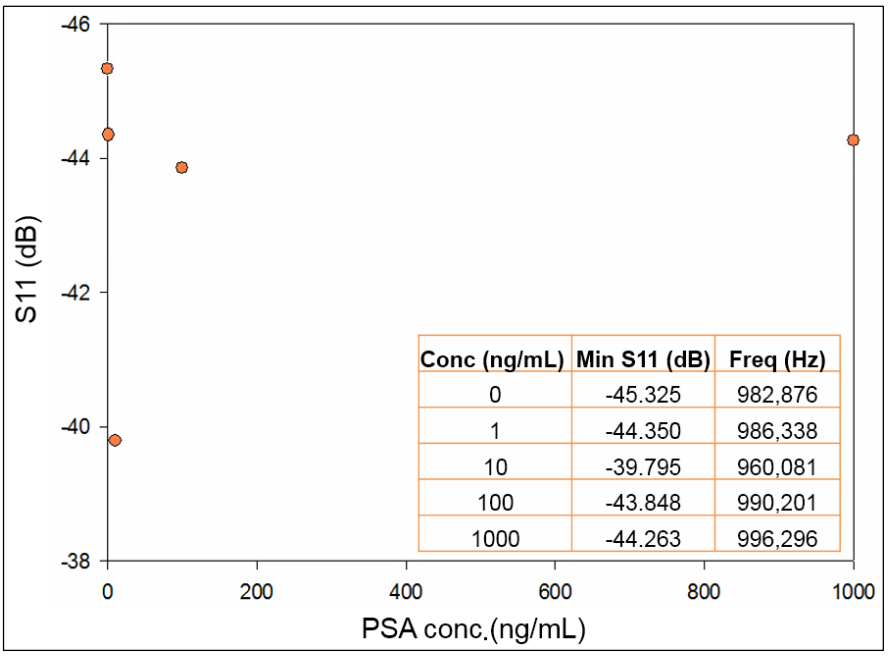


Figure 4.20. Relationship between $S_{11}$ and PSA concentration for the impedance matched gold IDE sensor upon functionalization and PSA detection; inset: data table.

More experimental work was attempted on other IDE devices for impedance matched-based detection. However, the above presented results were the best obtained in terms of impedance matching and high-frequency detection. The same calibration parameters were recalled for different measurements on the VNA to compensate for operator, environment and manufacturing errors. Also, a 50 Ω load was tested to verify the VNA response prior to testing the IDE devices. Overall, the impedance matching was a time consuming process as it required very fine adjustment. Lumped circuit elements, such as the surface mount inductors and capacitors soldered on the PCB for impedance matching in these experiments, are limited by parasitics at high frequencies [230], where distributed elements are preferable.

In order to confirm the efficiency of the gold IDE functionalization for PSA detection, faradaic EIS was also performed on the gold IDE. As discussed in section 2.5.3, the faradaic detection mode is preferred to the non-faradaic one due to its simplified interpretation, as quantifying the charge transfer mechanism via $R_{ct}$. The measurement range is slightly limited, but the identified variability trend is consistent with the one reported by Arya et al. [315].

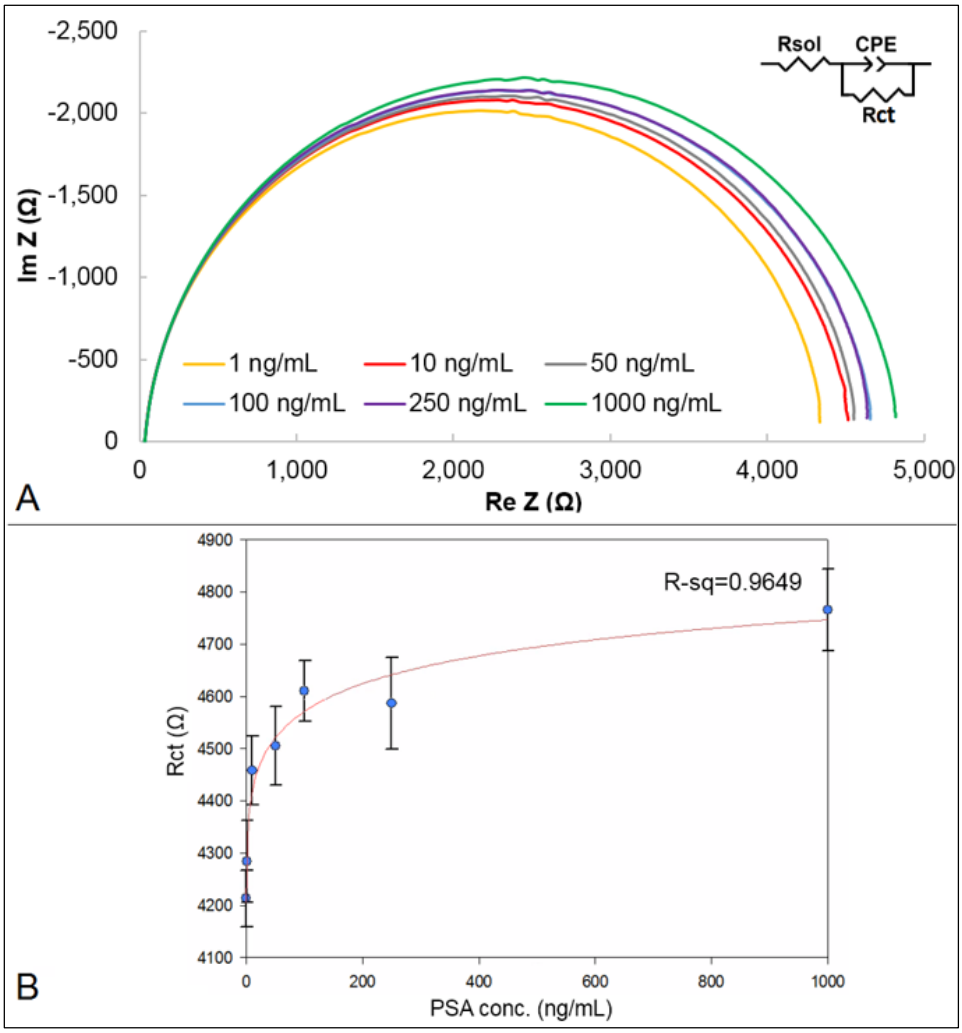


Figure 4.21. (A) Nyquist plots showing the faradaic EIS of the gold IDE for different PSA concentrations; (B) one-side binding curve fit showing the relationship between $R_{ct}$ and PSA concentration, 5 mM $Fe(CN_6)^{3-/4-}$ in 10 mM PBS, pH 7.4; inset: equivalent circuit.

## 4.4. Conclusions

The investigations conducted in this chapter targeted a novel, generalised approach for biomolecules detection with improved sensitivity. Using RF signal power measurements, the impedance-matching approach presents two main advantages:

1) Impedance matching can be achieved on any device, without the need of specific RF design

2) It enables the development and testing of more recent biosensor designs, such as looped IDE structures (LC-equivalent).

The scattering parameters can be measured throughout sensor functionalization and detection stages similarly to EIS. The electrical simulations presented in section 4.2 provided strong evidence in this sense, using an RC circuit as usually found in IDE-based (bio)sensors. While the impedance changes were almost negligible in this capacitive circuit arrangement, the reflection parameter $S_{11}$ for the

50 Ω source impedance matched circuit showed a five-fold decrease, with a sharp, well-defined peak. Variations in the capacitive element as triggered by the molecular double layer formation at the electrode surface, confirmed a linear and significant increase in $S_{11}$.

However, when tested in practice (section 4.3), this hypothesis was limited by several factors, such as parasitic effects and a drawback in VNA sensitivity. The gold functionalization was successful for PSA detection, confirmed by conventional EIS measurements. At higher frequencies, the results showed some level of variation in the $S_{11}$ intensity and corresponding frequency shift, but further work is required to perfect the RF based detection method. The impedance matching process was successful on the IDE devices, but it required several practical attempts and it was time consuming and delicate. In order to improve the sensitivity, if using off-the-shelf sensors, one should consider to use adjustable components where possible e.g. trimmer capacitor. Ultimately, by altering the IDE geometry, length and shape of tracks, one can target the resonant behaviour of an IDE as an LC equivalent circuit, eliminating the need of the external components. Also, further studies are recommended to improve the biosensor performance by the using self-assembled monolayers (SAM), for example.

The work presented in this chapter identified practical limitations of the RF impedance matching concept on standard electrochemical IDE sensors. While representing an interesting option, further work is required to validate the promising theoretical results. Working with novel materials, the conventional EIS represents a safer option while allowing for a better understanding of graphene based materials properties and behaviour.

# Chapter 5. Graphene based IDE biosensors for PSA detection

Graphene based IDE devices (rGO, LIG) were functionalized for prostate specific antibody-antigen interaction, with a direct application for prostate cancer detection. The geometry was chosen to be compatible with both graphene production methods to enable feasibility of rGO and LIG as a generic biosensing platforms. Quantum dot labelling and XPS analysis were used to evaluate the EDC-NHS chemical modification of graphene based surfaces and to confirm its successful functionalization. Based on the detection study presented in Chapter 4, electrochemical impedance spectroscopy (EIS) was applied to identify graphene surface changes upon functionalization, antibody immobilization and protein capture. Calibration curves were investigated for both rGO and LIG IDE structures in non-faradaic and faradaic conditions. Finally, systematic EIS studies were performed to understand the feasibility of these graphene based materials for impedance biosensor development.

## 5.1. Methodology

### 5.1.1 *Materials*

The chemicals (> 99% purity) were purchased from Sigma Aldrich, UK, unless otherwise stated: phosphate buffer saline, MES (2-(N-morpholino)ethanesulfonic acid hydrate), potassium ferricyanide ($K_3Fe(CN)_6$, EDC (N-(3-Dimethylaminopropyl)-N′-ethylcarbodiimide, $C_8H_{17}N_3$, >97%), BSA (bovine serum albumin), glycine ($NH_2CH_2COOH$), sodium hydroxide (NaOH), hydrochloric acid (HCl). Potasisum ferrocyanide trihydrate ($K_4Fe(CN)_6 \cdot 3H_2O$) was procured from BDH. Sulfo-NHS (N-hydroxysulfosuccinimide, $C_4H_4NNaO_6S$) and amino (PEG)-coated quantum dots (CdSe, 8 µM, Life Technologies) were sourced from ThermoFisher Scientific, UK. 1 M ethanolamine ($NH_2CH_2CH_2OH$) was obtained from Biacore, Sweden. Natural human prostate specific antigen antibody (PSA-10) and protein (PSA, PN: ab78528) were purchased from Fujirebio, US and abcam, UK.

Ultra-highly concentrated single layer graphene oxide (6.2 g/L) was purchased from Graphene Supermarket, US. Polyimide (Kapton) adhesive film was purchased from Farnell, UK. PET foil (transparent, 100 µm thick, Office Depot brand) was purchased from Viking, UK. Conductive silver paint and conductive copper tape were purchased from RS Components, UK.

### 5.1.2 *Fabrication of the graphene IDE devices*

The IDE sensing platforms were designed considering the resolution of the manufacturing equipment (discussed in section 3.2.3): 10 electrodes, 0.5 mm width and 6 mm length. More details on the equipment and synthesis method were provided in section 3.1.2.

Based on the lessons learnt from previous experiments, the acetate film underwent an oxygen plasma treatment (PE-50 XL Benchtop Low Pressure Plasma System) for 1 minute at 50% power (200 W) in order to improve its hydrophilicity prior to GO dropcasting. The LIG IDE patterns were defined using 35% laser power and in engraving operation mode. The IDE patterns were cut and attached to a flexible PET substrate for improved support. Conductive silver paint was used to secure the adhesive conductive copper tape to the IDE pad areas for enhanced contact and robustness. PI tape was used on both rGO and LIG IDE devices to insulate the contact area and to protect it from contact with solutions during testing, incubation and rinsing steps. Figure 5.1 shows the devices as ready to be tested.

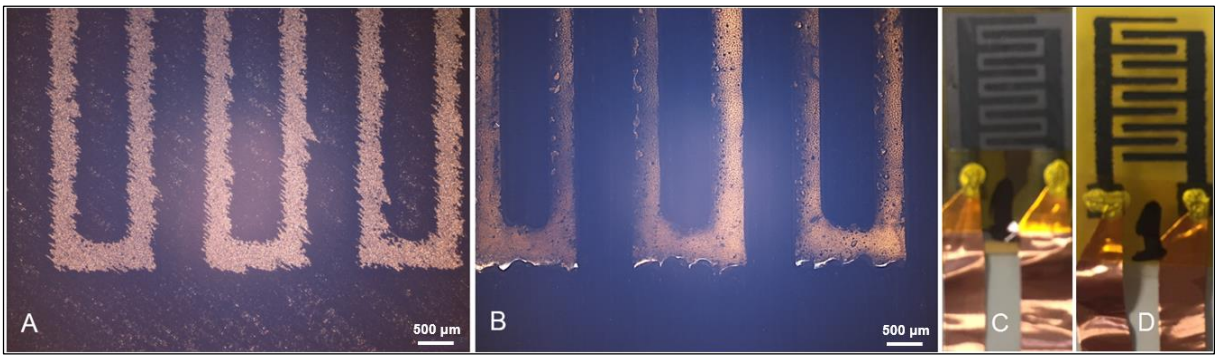


Figure 5.1. Microscopy and optical images (inset) of the IDE-patterned (A) rGO and (B) LIG, 20x magnification, 500 µm bar scale.

### 5.1.3 *Graphene functionalization for PSA detection*

The functionalization protocol for the PSA antibody-antigen capture on the graphene IDE devices is detailed below. During the incubation steps, the devices were enclosed in a humid environment (closed, wet container) to avoid surface drying. The general protocol consists of steps 1-5, while step 6 was applied to regenerated samples only and it is accordingly mentioned in the text.

1. The IDE sensing area was incubated in freshly prepared 5 mM EDC/ 5mM sulfo-NHS in MES buffer (pH 5, ultrapure water) for 15 minutes, followed by a brief rinse step in MES buffer.

2. The 20 µg/mL PSA-10 antibody solution in PBS was pipetted on the IDE surface and allowed to react for 20-25 minutes. After incubation, the sensing area was washed in PBS buffer.

3. The IDE was incubated in ethanolamine (0.1 M) for 5 minutes to quench unreacted sulfo-NHS esters, followed by a brief rinse step in PBS buffer.

4. A solution of 0.2% BSA in PBS was applied on the electrodes surface for 10 minutes to control non-specific adsorption. The IDE was then washed in PBS buffer.

5. PSA solutions in PBS were prepared at various concentrations (1-1000 ng/mL). The IDE sensing area was incubated in PSA for 30 minutes and then thoroughly washed in PBS buffer.

6. The regeneration step implied 10-second surface wash in 0.1 M glycine of pH 3.1, after which the electrodes were thoroughly washed and briefly incubated (10 s) in PBS buffer.

Step 5 and 6* were repeated for different PSA concentrations.

### 5.1.4 *Measurements and software for statistical data analysis*

Impedance measurements were taken in duplicates using a Solartron Modulab XM ECS system (Ametek) sourcing a 10 mV AC input signal (0 DC) across 0.5 Hz-100 kHz frequency range, in a logarithmic sweep, with 1000 points per decade and an integration period of 0.1 s. The tests were performed in 10 mM, pH 7.4 PBS for non-faradaic EIS and in 5 mM potassium ferricyanide/ferrocyanide $Fe(CN)_6^{3-/4-}$ in PBS (10 mM, pH 7.4) for faradaic EIS measurements. It was essential to control the depth of immersion in testing solution for reproducibility and avoid damage of contact area, reason for which the volume of incubation was fixed at 100 µL.

The XPS spectra (K-Alpha XPS, Thermo Scientific, East Grinstead) were processed in CasaXPS. Identical samples were used corresponding to each functionalization step: after EDC-NHS chemical modification (step 1, protocol 5.1.3), PSA-10 antibody immobilization (step 2, protocol 5.1.3) and PSA capture (step 5, protocol 5.1.3). Available graphene literature and XPS databases [69][70] were used for peak identification.

EIS data analysis was performed using Z-View software (Scribner Associates Inc.) which was available on the Solartron system. Two consecutive measurements were averaged in order to build the relationship (calibration) curves. The data was extracted in the frequency range corresponding to maximum sensitivity. The one-side binding calibration curve (Sigmoidal Logistic 4-Parameter) was fitted in SigmaPlot.

## 5.2. Results and discussion

### 5.2.1 *Assessment of the functionalization of graphene based materials*

#### *5.2.1.1 Quantum dots (QD) labelling of rGO*

In an initial study, CdSe quantum dots (QD) were covalently deposited on the rGO surface to test the efficiency of the EDC-NHS functionalization. The available carboxyl groups were activated via carbodiimide and the amino-coated CdSe quantum dots were bound to edges and defective sites on rGO. The results of the test, control and background samples are shown in Figure 5.2.

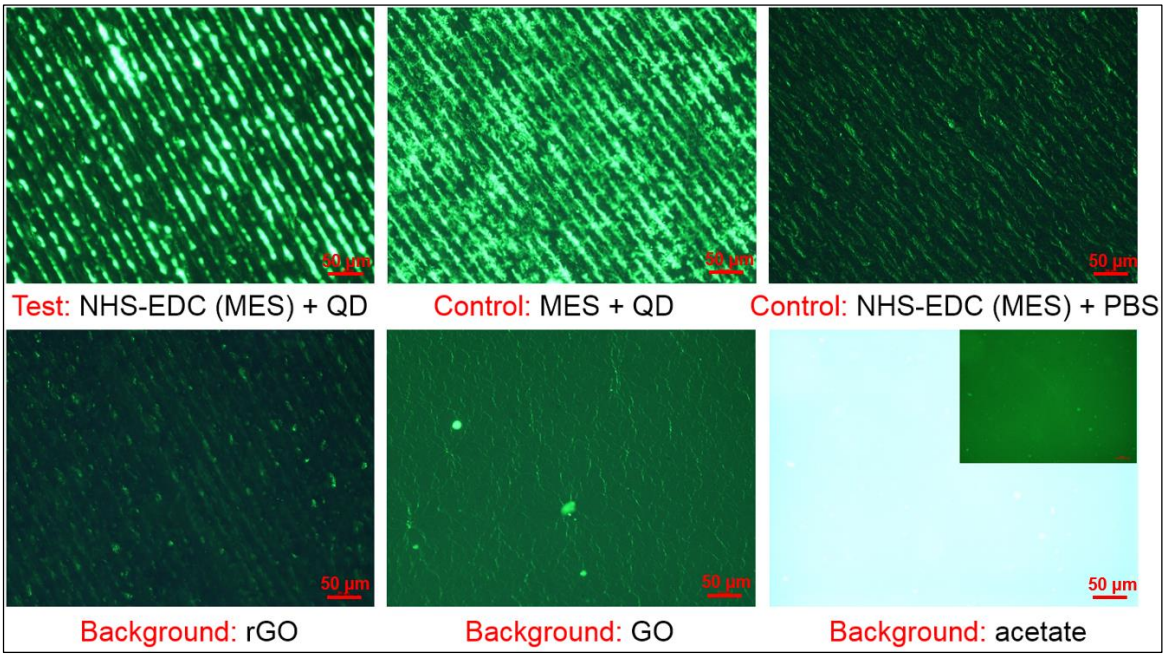


Figure 5.2. Fluorescence microscopy images of test sample (EDC-NHS, then QD), control 1 (MES buffer, then QD), control 2 (EDC-NHS, then PBS) and substrates background (no chemical treatment); 525 nm band pass filter, manual, 60 s exposure, 1.7 gain, 200x magnification, 50 µm scale bar; inset: 10 s exposure.

Lightscribe rGO samples' laser tracks are visible in Figure 5.2 and present different fluorescence levels based on the chemical treatment applied, background fluorescence and QD density. The background fluorescence was verified using the substrate materials only, with no chemical treatment: rGO, GO and acetate foil respectively. The first control sample (MES buffer + QD incubation, in the absence of EDC-NHS) revealed some non-specific adsorption, with the quantum dots agglomerating over the rGO surface, but its fluorescence intensity was reduced compared to the test sample (EDC-NHS activation + QD). The presence of the quantum dots was apparent, with a diminished quenching effect due to the rGO substrate, which is in agreement with the literature [389], while GO is well known as a

suitable platform for fluorescent biosensors [133][390]. It is worth noting that the rinsing step in PBS buffer was brief, as trying to protect the expanded rGO layers from delamination. The second control sample (EDC-NHS in MES + PBS, with no QD) exhibited similarities with the fluorescent background of the rGO. This experimental work (visually) demonstrates the successful functionalization of rGO, with a higher density of quantum dots present at the edges of the laser tracks within produced Lightscribe rGO.

Moreover, XPS analysis was performed in order to compare the control and test samples (see Figure 5.3) and to confirm the fluorescence microscopy findings. Three main peaks corresponding to C 1s (≈ 285 eV), O 1s (≈ 532 eV) and N 1s (≈ 400 eV) were identified for the test sample, in agreement with Permatasari et al. [391].

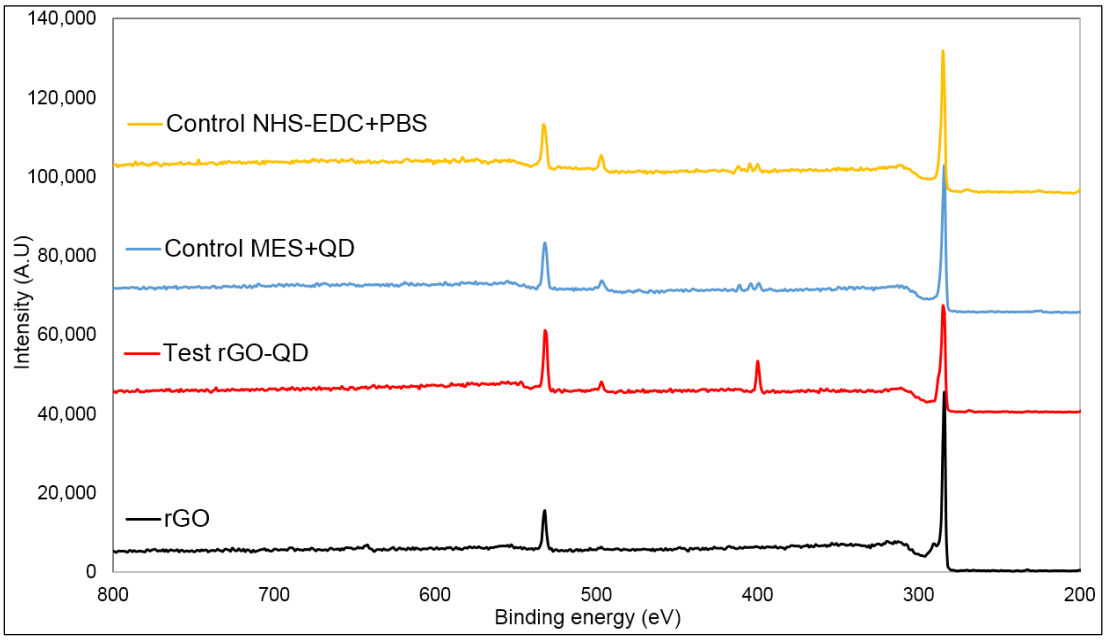


Figure 5.3. XPS survey for initial rGO, test and control samples.

#### *5.2.1.2 Graphene surface changes induced by antibody-antigen interaction*

Aiming for PSA detection, further XPS studies were performed on the functionalized graphene samples at subsequent chemical modification stages, schematically presented in Figure 5.4:

- COOH activation via EDC-NHS
- Covalent binding of PSA-10 antibody
- Interaction between prostate specific antibody (PSA-10) and antigen (PSA).

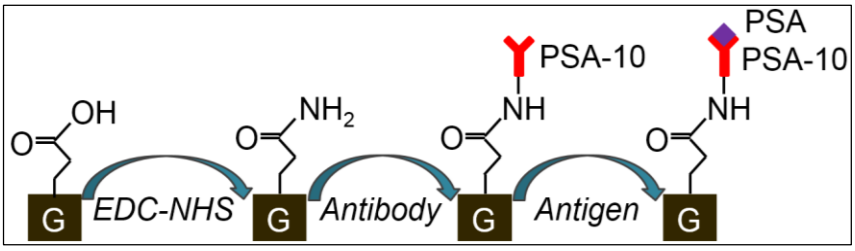


Figure 5.4. PSA antibody-antigen interaction on graphene based IDE.

The representative XPS surveys for the two materials is presented in Figure 5.5. In the case of rGO, the nitrogen peak was visible upon functionalization, with a simultaneous reduction in the carbon signal due to surface activation. Interestingly, LIG showed no major changes in the oxygen peak, but exhibited an increase in the carbon content upon protein binding. Table 5-1 captures the elemental analysis results for both materials.

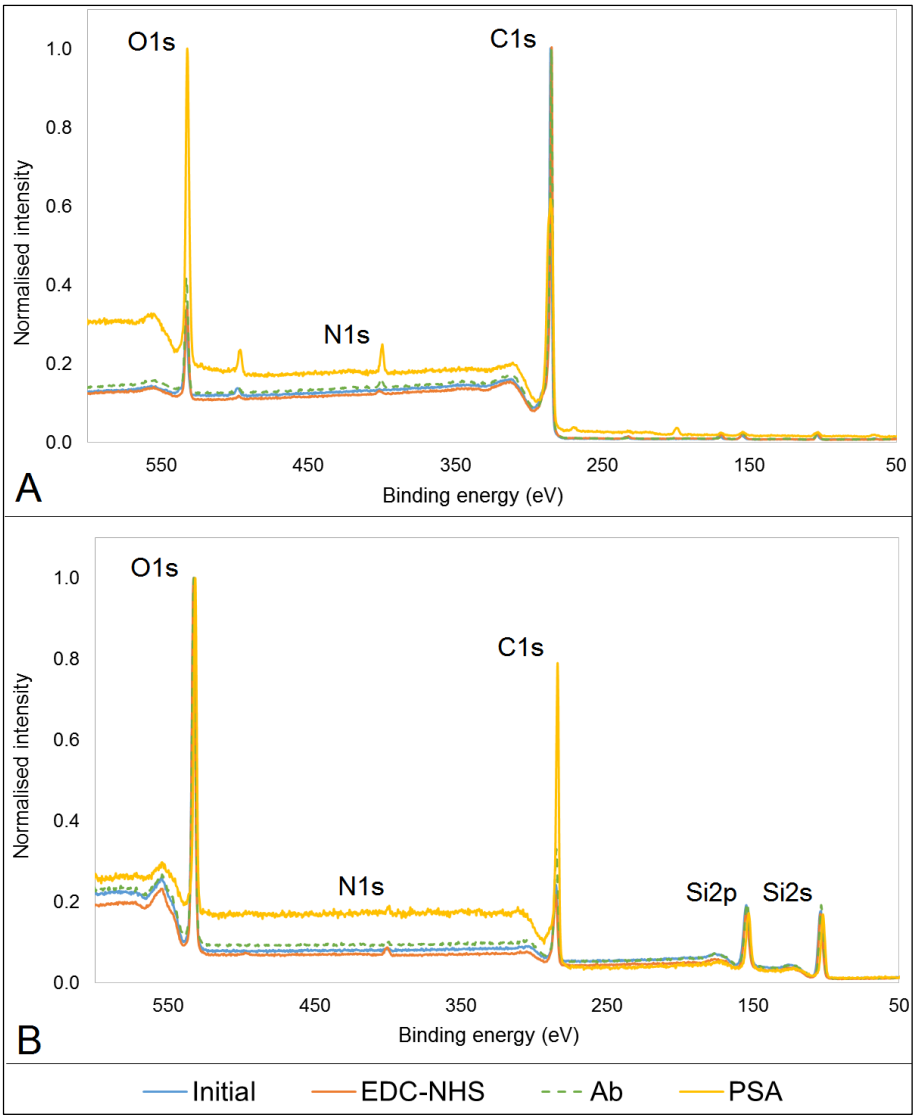


Figure 5.5. Normalised XPS survey of (A) rGO and (B) LIG electrodes for subsequent functionalization stages.

The functionalization of LIG was also successful, however, the surface changes were probably driven by a strong adsorption mechanism as the nitrogen peak diminished for antibody and antigen immobilization steps. The high initial nitrogen content is explained by the chemical structure of the polyimide tape, with an amino nitrogen atom of the diamine [392]. Moreover, possible nitrogen doping is possible during the reduction mechanism, being reported Lamberti et al. [393]. Traces of sodium (0.5 at%) were present in the composition of the chemically treated LIG, due to the sulfo-NHS activation Step 1 as presented in section 5.1.3, decreasing to 0 at% upon antibody immobilization. Some level of variability is expected due to the complex porosity and reduced smoothness of the LIG. The identified silicon peak originates from the polyimide tape adhesive and silicon atoms diffusion during the reduction process.

Table 5-1. Carbon, oxygen and nitrogen composition of rGO and LIG samples for subsequent functionalization steps, based on XPS elemental analysis.

| **rGO** | **Initial** | **EDC-NHS** | **Ab** | **PSA** |
|---|---|---|---|---|
| C 1s (at %) | 91.3 | 86.7 | 84.5 | 71.1 |
| O 1s (at %) | 8.2 | 9.9 | 11.7 | 23.8 |
| N 1s (at %) | 0 | 0.6 | 1.1 | 2.5 |
| **LIG** | **Initial** | **EDC-NHS** | **Ab** | **PSA** |
| C 1s (at %) | 25.3 | 42.4 | 35.2 | 57.4 |
| O 1s (at %) | 44.5 | 33.9 | 37.6 | 25.9 |
| N 1s (at %) | 0.2 | 3.6 | 0.4 | 0.5 |

While the carboxylic groups of rGO represent ≈ 10% of its chemical groups, the fitted spectrum for LIG did not show a clear –COOH equivalent peak, as presented in section 3.2.1 and it is estimated to be 1-2% based on previous measurements. The XPS vertical depth is limited (5-10 nm) and considering LIG's surface roughness and silicon contamination, it was challenging to identify marginal surface chemical bonds.

Furthermore, Figure 5.6 illustrates the corresponding high resolution C 1s spectrum for the rGO electrodes. rGO surface modification by EDC-NHS and the presence of the biomolecular layer caused a downshift by approximately 0.5 eV as a result of the covalent bonding with PSA-10 antibody.

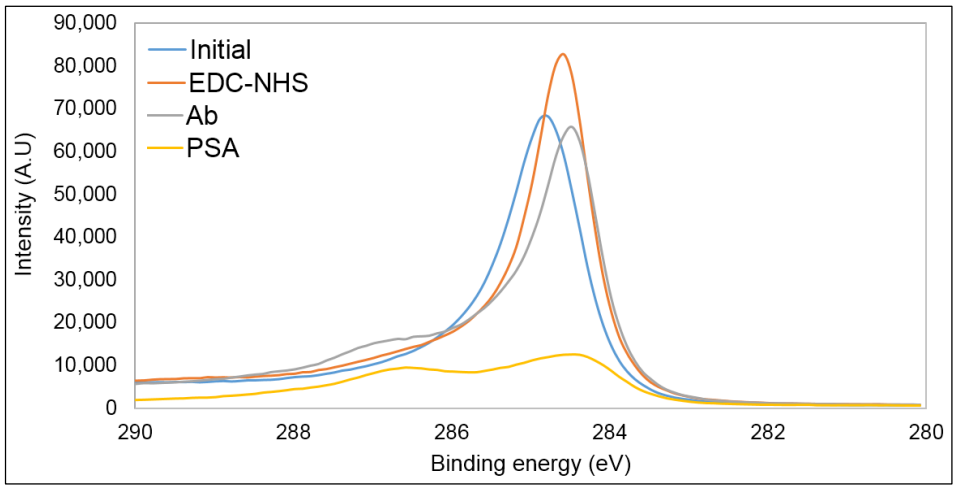


Figure 5.6. XPS C 1s spectrum of rGO upon functionalization and protein capture.

In the presence of the protein (PSA), the profile of the C 1s spectra (see Figure 5.7) shows some resemblances with its source material i.e. GO [42]. The chemical treatments induced some damaged the graphitic $sp^2$ network, result comparable with GO-$NH_2$ in the work of Ederer et al. [394].

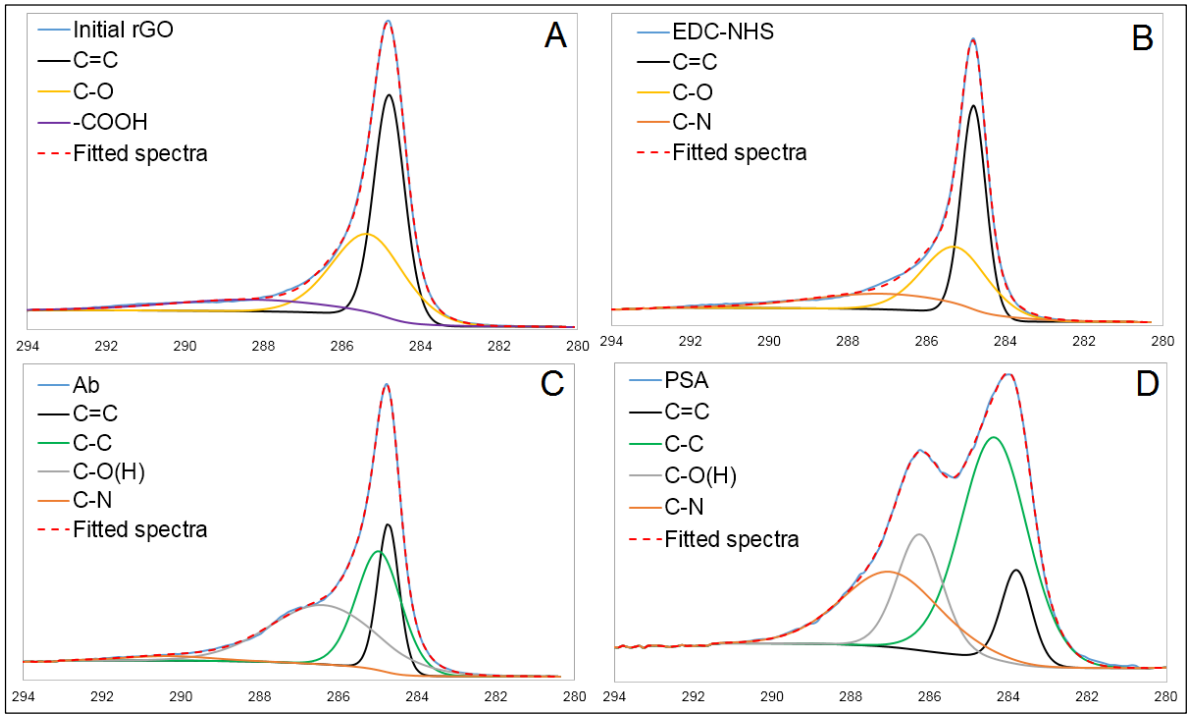


Figure 5.7. C 1s fitted spectra with corresponding functional groups for rGO: (A) initial; (B) after EDC-NHS; (C) upon PSA-10 antibody attachment; (D) with prostate specific antibody-antigen couple.

Moreover, Figure 5.8 illustrates the C 1s spectrum for LIG, which showed a peak downshift similarly to rGO upon functionalization. Significant variation in the functional groups could be identified for subsequent chemical treatments (see Figure 5.9). These are believed to be caused by sample variation and local variability in LIG's expanded

layers, and possibly due to a desorption mechanism. Also, the peak at 288 eV is indicative of O=C-N bonds [395], being visible after the EDC-NHS chemical modification. The peak at 285.5 eV corresponds to Si-O-C bonds, in agreement with Cao et al. [121].

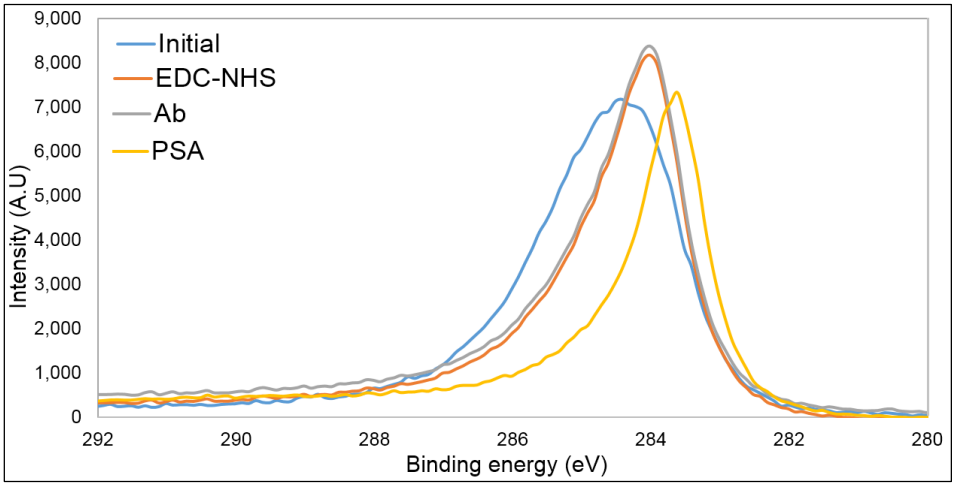


Figure 5.8. XPS C 1s spectra of LIG upon functionalization and protein capture.

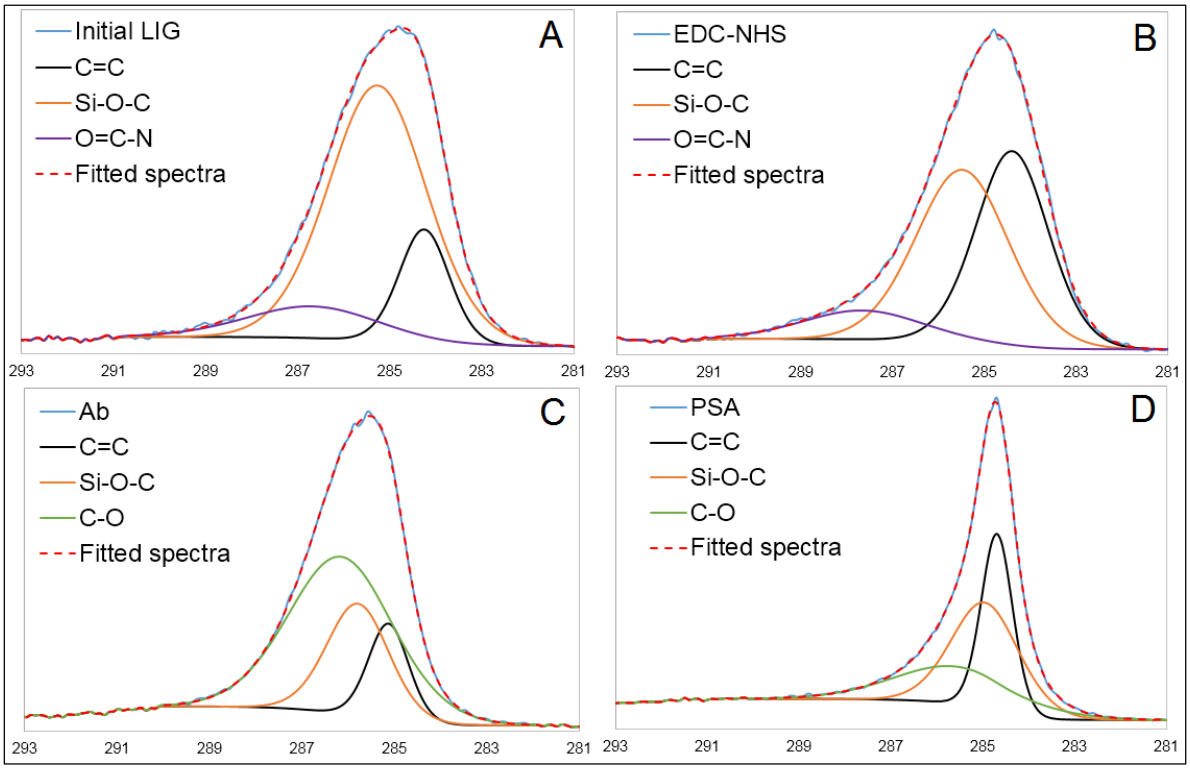


Figure 5.9. C 1s fitted spectra with corresponding functional groups for LIG: (A) initial; (B) after EDC-NHS; (C) upon PSA-10 antibody attachment; (D) with prostate specific antibody-antigen couple.

Furthermore, Raman spectroscopy measurements were acquired on the graphene based materials before functionalization and after PSA capture, shown in Figure 5.10. There was an increase in the defective D peak at 1355.4 $cm^{-1}$ for rGO and

1344.6 $cm^{-1}$ for LIG. Due to its high surface roughness, LIG posed some challenges during measurements, with significant noise levels. Upon PSA capture on the functionalized graphene surface, the $I_D/I_G$ ratio increased by just over 38% for rGO, and 36% for LIG. Also, structural changes in rGO were confirmed by its 2D peak intensity reduction by approximately 50%.

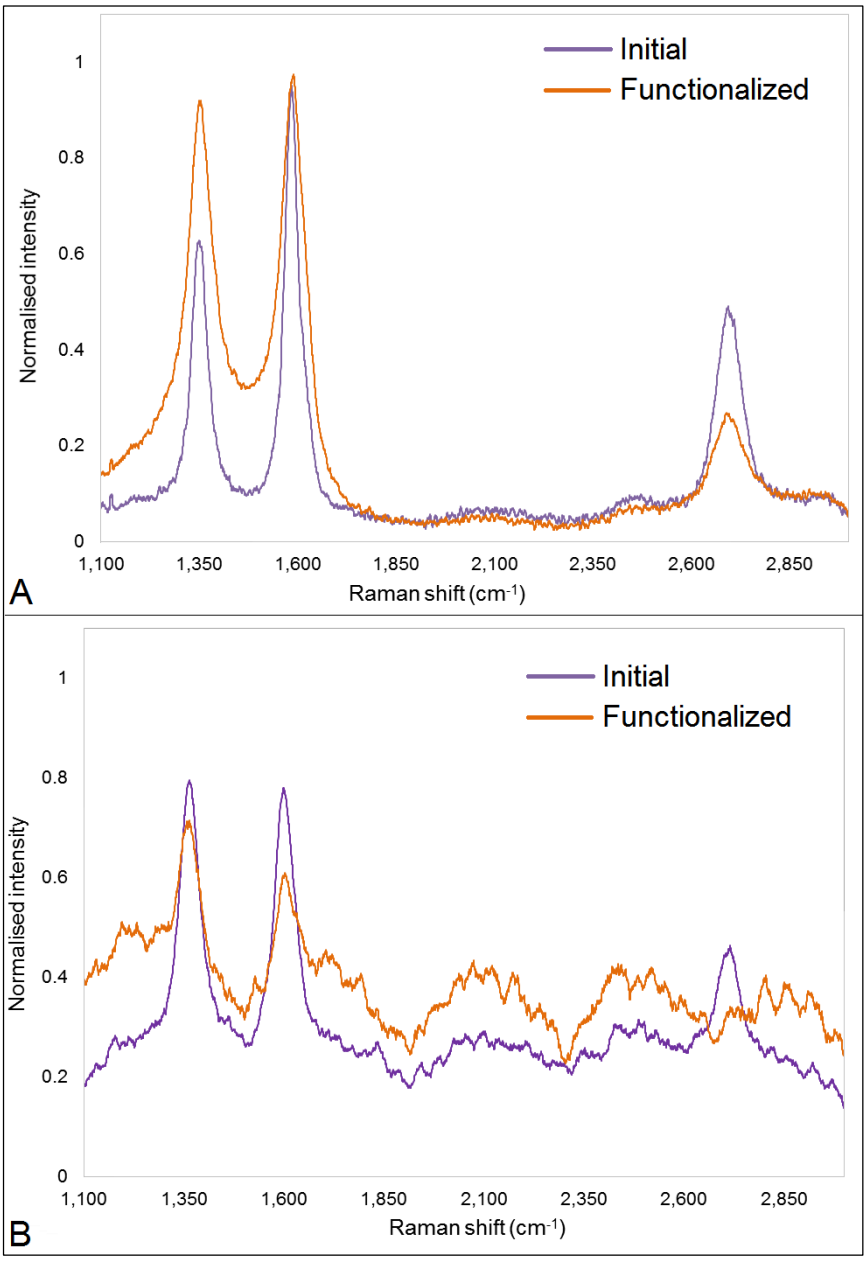


Figure 5.10. Normalised Raman spectra before and after PSA capture on (A) rGO, (B) LIG.

Furthermore, the EDC-NHS chemistry is known to be efficient on materials where carboxylic groups are available and can even facilitate the protein adsorption [396]. This aspect was investigated via XPS measurements on the dielectric area (see Figure 5.11), on the GO and PI precursor materials. The protein capture at the inter-electrode area was considered highly unlikely taking into account the limited

amount of –COOH groups, in addition to the hydrophobic nature of the PI tape. A double nitrogen peak at 399.3 eV (pyrrolic N) and 401.5 eV (graphitic N species) was identified for the LIG sample upon protein capture, confirming structural changes in the $sp^2$ network [397]. Significant changes in the C 1s spectrum for rGO are also indicative of some level of adsorption of the biochemical species on the dielectric area.

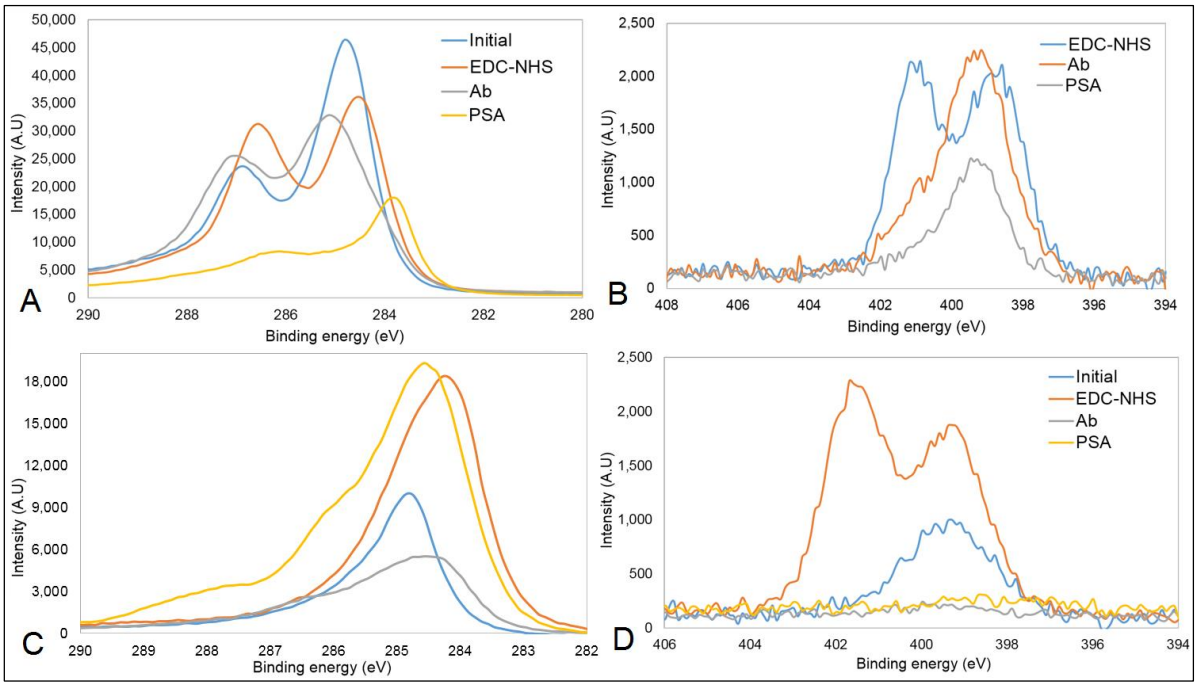


Figure 5.11. XPS C 1s (left) and N 1s (right) spectra of the dielectric (inter-electrode) area: (A,B) graphene oxide and (C,D) polyimide.

### 5.2.2 *EIS behaviour of the graphene based IDE sensors*

Firstly, it was essential to understand the electrochemical impedance behaviour and repeatability of rGO and LIG IDE sensors in both non-faradaic and faradaic conditions. It is known that the electrochemical response of imperfect, rough or porous electrode materials cannot be represented by simple RC models [398] and some relevant examples were presented in section 2.5.5.

#### *5.2.2.1 Non-faradaic EIS response of rGO IDE*

Figure 5.12 presents the non-faradaic impedance response of the rGO IDE and its corresponding equivalent circuit. Being laterally exfoliated, rGO behaves like a porous coating (see Figure 2.33a) as its pockets retain the electrolyte solution. Considering the electrical resistance measurements presented in section 3.2.4, significant variability was expected due to some level of inconsistency in material properties as depending on the pattern location on the disc. Regarding the EIS results, this variability was also reflected in the resistive element $R_{sol}$. This element usually

accounts for fixed resistance components, such as: solution, contact and material. The parallel R-CPE arrangement is justified by material's morphology, where $CPE_{IDE}$ represents the geometrical capacitance of the IDE, in conditions of surface imperfections and according to Helmholtz theory [399] it is expected to be sensitive to double layer formation.

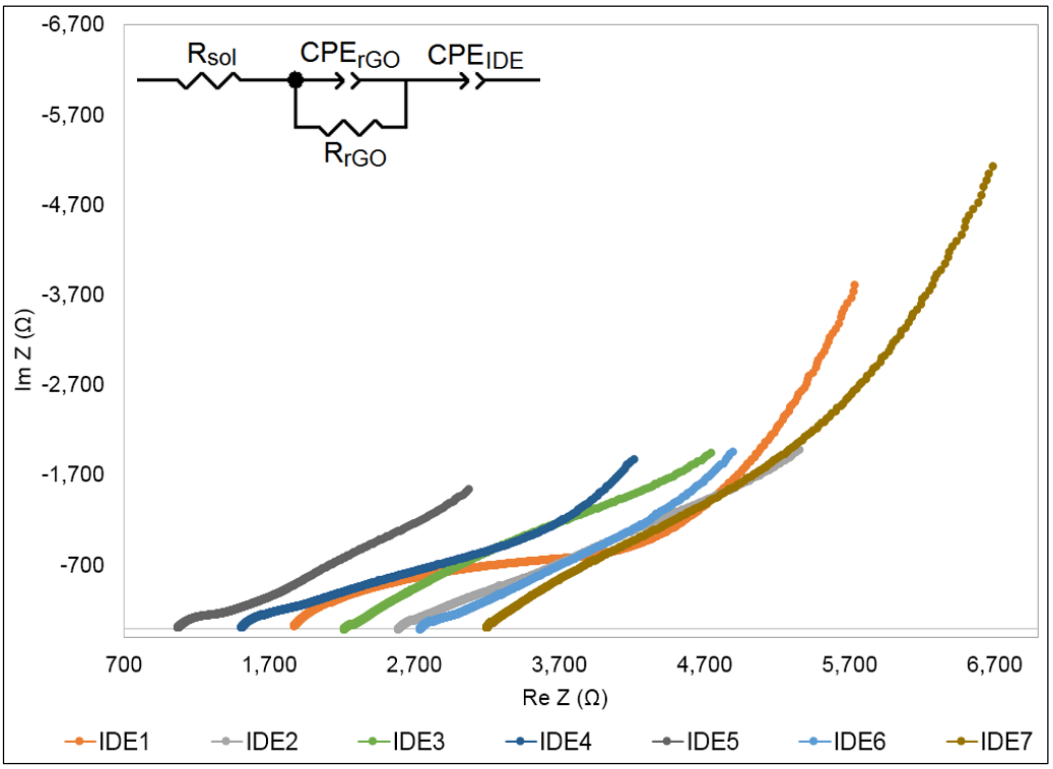


Figure 5.12. Nyquist plot of the non-faradaic EIS response of the rGO IDE devices; inset: equivalent circuit.

The magnitude of impedance for the tested rGO IDE devices (see Figure 5.12) is in the range 3400 Ω - 8300 Ω, which is relatively high and can be associated with a lower degree of reduction of the initial GO and discontinuities in the electrode patterns. The rGO IDE is a non-ideal capacitor, with the phase of impedance varying between -20° and -38. The corresponding Bode plots are presented in Figure 5.13.

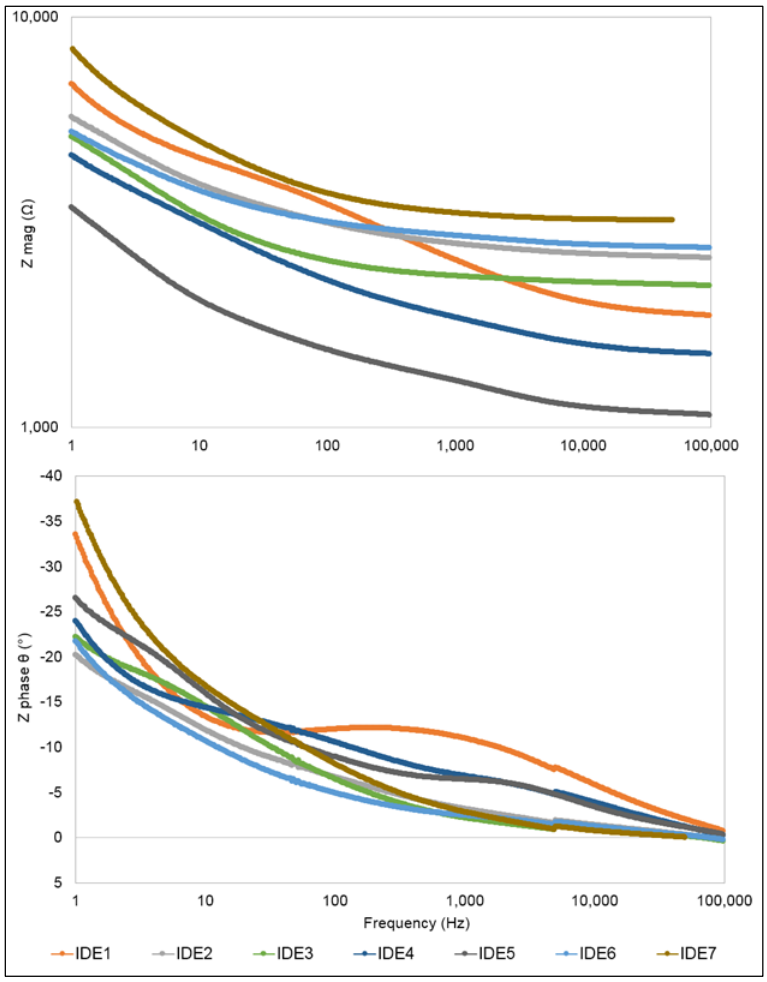


Figure 5.13. Bode plots of the non-faradaic EIS response of the rGO IDE devices.

#### *5.2.2.2 Faradaic EIS response of rGO IDE*

The faradaic EIS response of the rGO IDE devices is shown in Figure 5.14, being fitted by a modified Randles circuit, in agreement with previously reports on laser-induced graphene [122] and graphene composites [400][401]. A CPE replaces the standard capacitive element, as it accounts for the surface roughness of the rGO. Also, Figure 5.15 illustrates the corresponding Bode plots, with variation levels similar to the non-faradaic case.

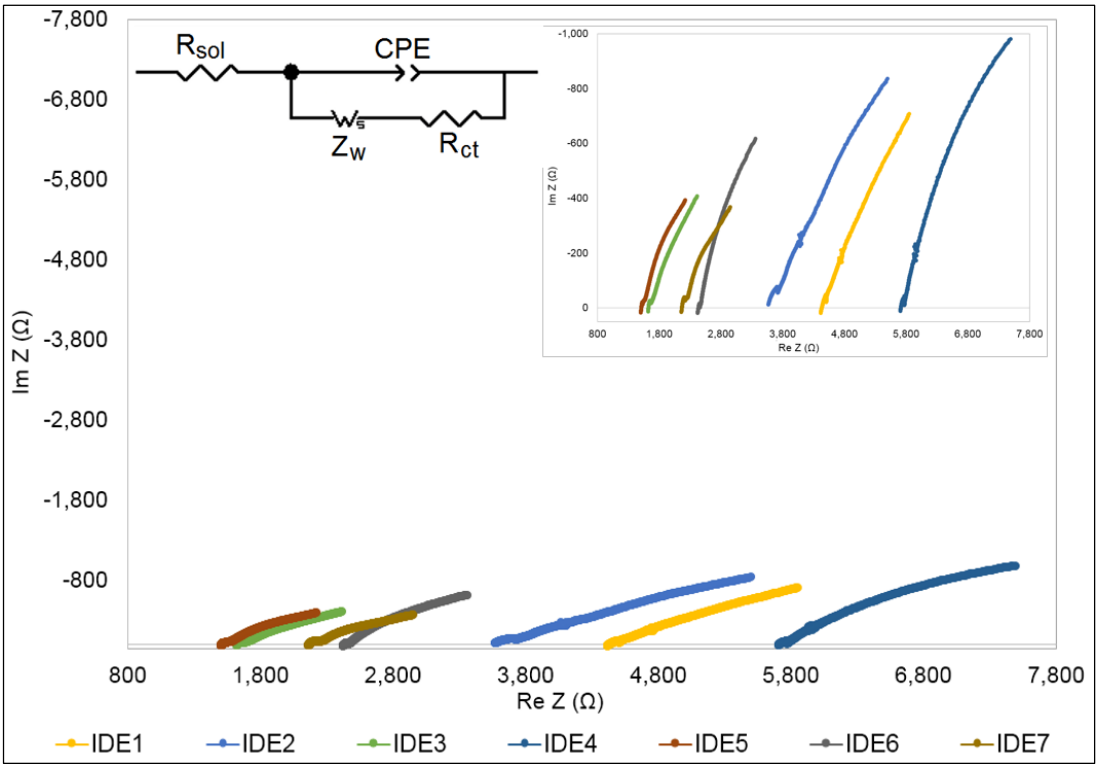


Figure 5.14. Nyquist plot of the faradaic EIS response of the rGO IDE devices; inset: equivalent circuit.

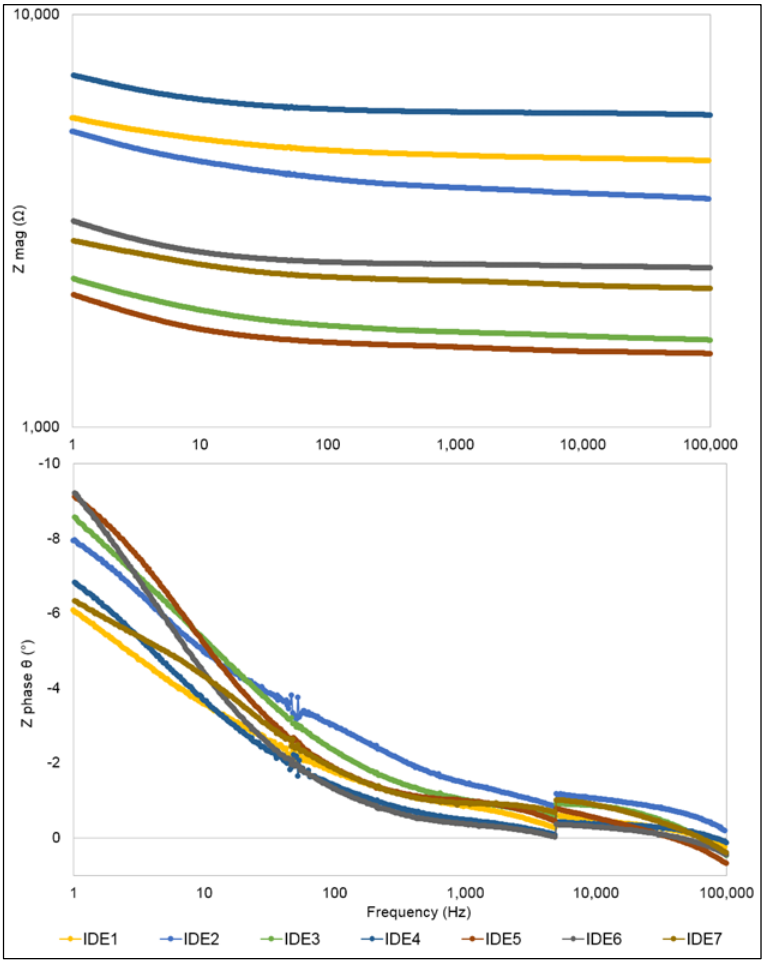


Figure 5.15. Bode plots of the faradaic EIS response of the rGO IDE devices.

### *5.2.2.3 Non-faradaic EIS response of LIG IDE*

Moreover, the non-faradaic impedance response across several LIG IDE devices is presented in Figure 5.16. Employed for engraving a soft material film, the industrial $CO_2$ laser equipment is not fit for purpose, with limited pattern/properties reproducibility. $C_{IDE}$ represents the geometrical capacitance of the IDE, while the CPE reflects LIG's porosity in addition to its representative resistance $R_{LIG}$.

Compared to rGO, CPE-P is nearly double with a value of approximately 0.9, but the complex morphology, which was shown in Figure 3.16, leads to a distinctive Nyquist profile compared to standard porosities (per Figure 2.34). Figure 5.17 shows the corresponding Bode plots of the LIG IDE samples, with the magnitude of impedance varying between 12 kΩ and 77 kΩ, while the minimum phase ranges between -77° and -85° at 1 Hz. One can notice that there is significantly less variability in terms of $R_{sol}$ for LIG compared to rGO.

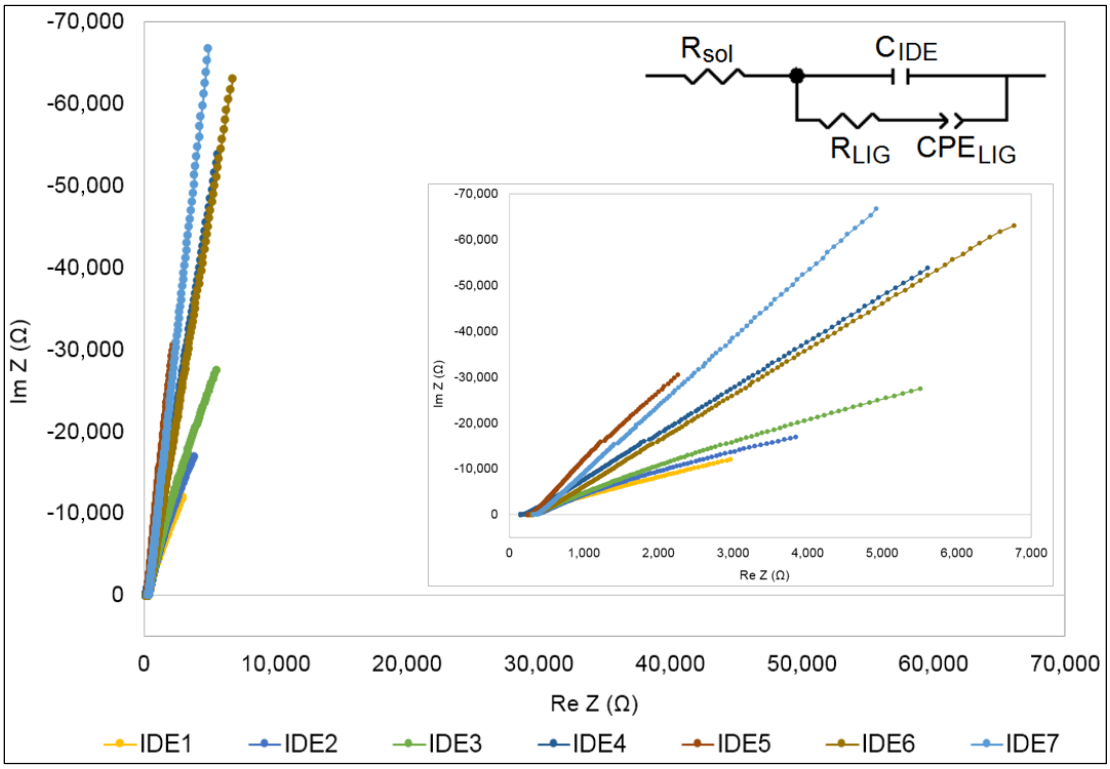


Figure 5.16. Nyquist plot of the non-faradaic EIS response of the LIG IDE devices; inset: equivalent circuit.

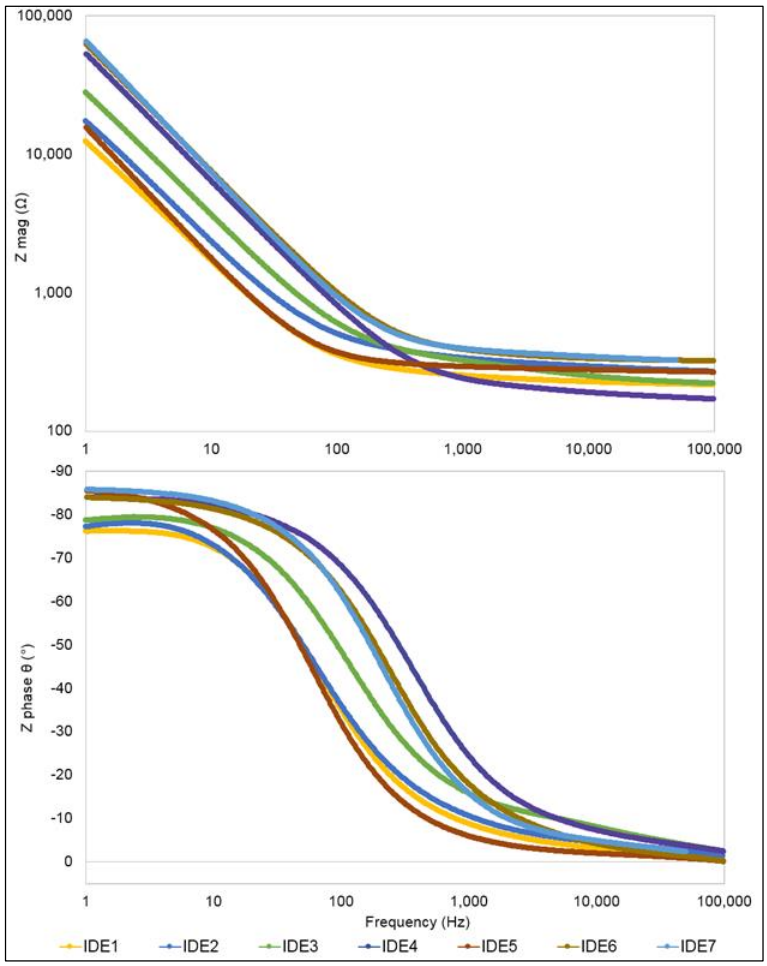


Figure 5.17. Bode plots of the non-faradaic EIS response of the LIG IDE devices.

#### *5.2.2.4 Faradaic EIS response of LIG IDE*

The faradaic impedance response of the LIG IDE sensors is presented in Figure 5.18. The equivalent circuit was built starting with a Randles circuit, with the consideration of LIG's porosity i.e. $CPE_{LIG}$. Two time constants were needed to fit the Nyquist profile. The $CPE_{IDE}$ accounts for IDE's geometrical capacitance.

Figure 5.19 shows the corresponding Bode plots of the LIG devices in faradaic conditions. The phase of impedance at low frequencies ranges between -14° and -38°, while $Z_{mag}$ varies by up to one order of magnitude across different LIG IDE devices.

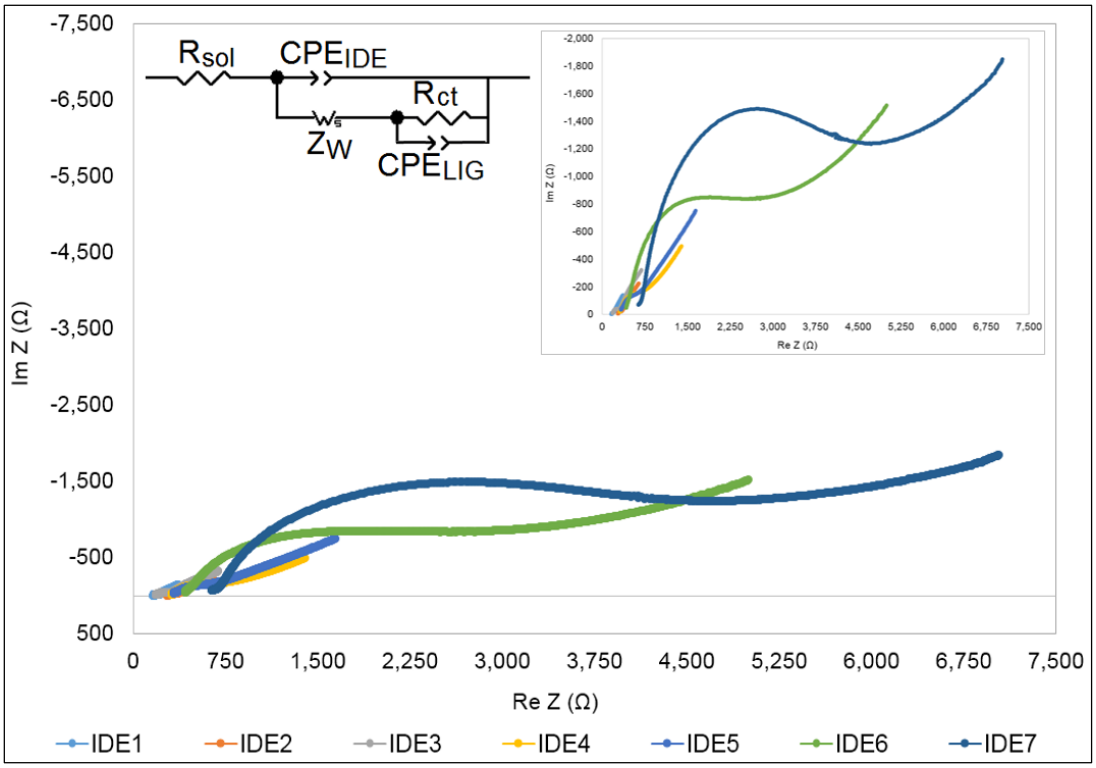


Figure 5.18. Nyquist plot of the faradaic EIS response of the LIG IDE devices; inset: equivalent circuit.

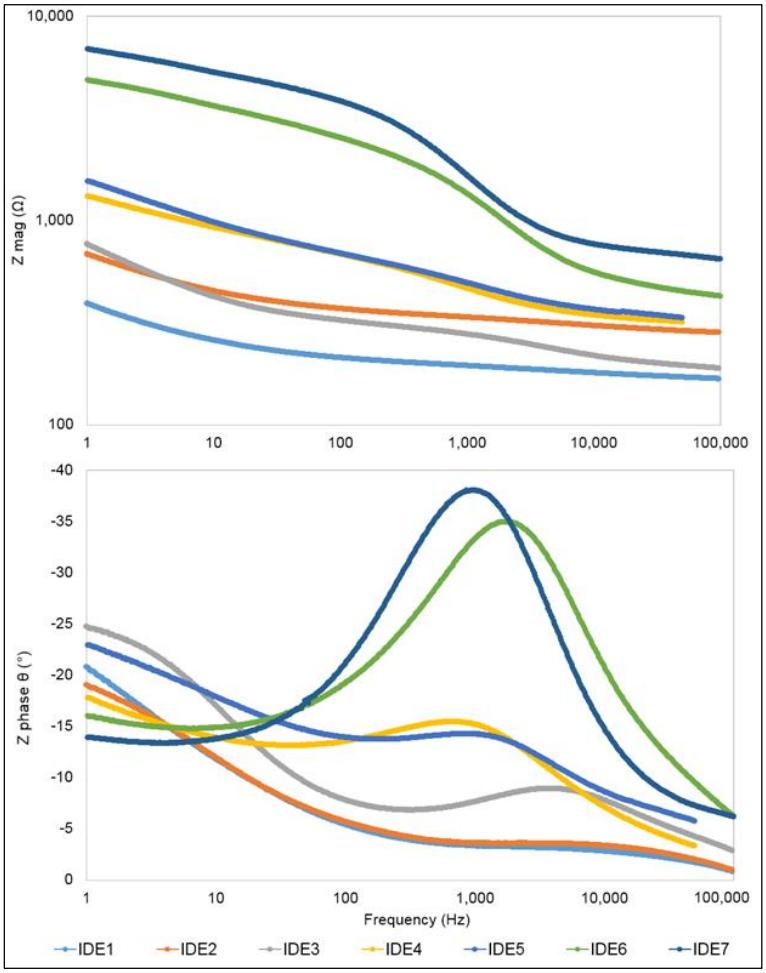


Figure 5.19. Bode plots of the faradaic electrical impedance response of the LIG IDE devices.

### *5.2.2.5 An overview of the electrochemical impedance (EIS) response of the graphene-based (rGO, LIG) IDE sensors*

The selected graphene materials, i.e. Lightscribe rGO and LIG, exhibit significantly different impedimetric behaviours. This is influenced by their morphology and electrical conductivity properties, already discussed in 3.1.3. This section provides an overview of the non-faradaic and faradaic EIS results as presented in sections 5.2.2.1-5.2.2.4.

The non-uniformity and roughness of rGO, induced by the Lightscribe laser pulse patterning and circular track formation leads to an geometrical capacitance expressed by a constant phase element ($CPE_{IDE}$) and placed in series with a RC-based circuit ($CPE_{rGO}$, $R_{rGO}$) – see Figure 5.12. On the other hand, the non-faradaic impedance equivalent circuit of the LIG IDE devices was fitted by a parallel arrangement of the capacitive effect of IDE geometry ($C_{IDE}$) and material's porosity - Figure 5.16.

The lateral exfoliation of rGO during Lightscribe leads to the formation of electrochemical dominant top layers. The redox label i.e. ferri-/ferro-cyanide couple successfully reach and react at the electrode surface, with rGO IDE electrochemical behaviour fitted by a Randles-based circuit (presented in 2.5.3) – see Figure 5.14. A constant phase element (CPE) replaced the standard double-layer capacitance due to rGO's morphology, justified by the same rationale discussed above for its non-faradaic EIS. However, the geometrical capacitance of LIG sensor ($CPE_{IDE}$) appears to play an important role in its faradaic impedance response, being placed in parallel with the charge-transfer resistance ($R_{ct}$) in the equivalent circuit – see Figure 5.18.

Finally, Figure 5.20 exemplifies the quality of the equivalent circuits discussed above as fitting the experimental data. The average standard deviation across the measured IDE devices is high, with an average of 58.9% for rGO and 77.2% for LIG across all circuit components. The identification and quality of the equivalent circuit for the rGO IDE was more straightforward compared to LIG, which has a sandwiched morphology.

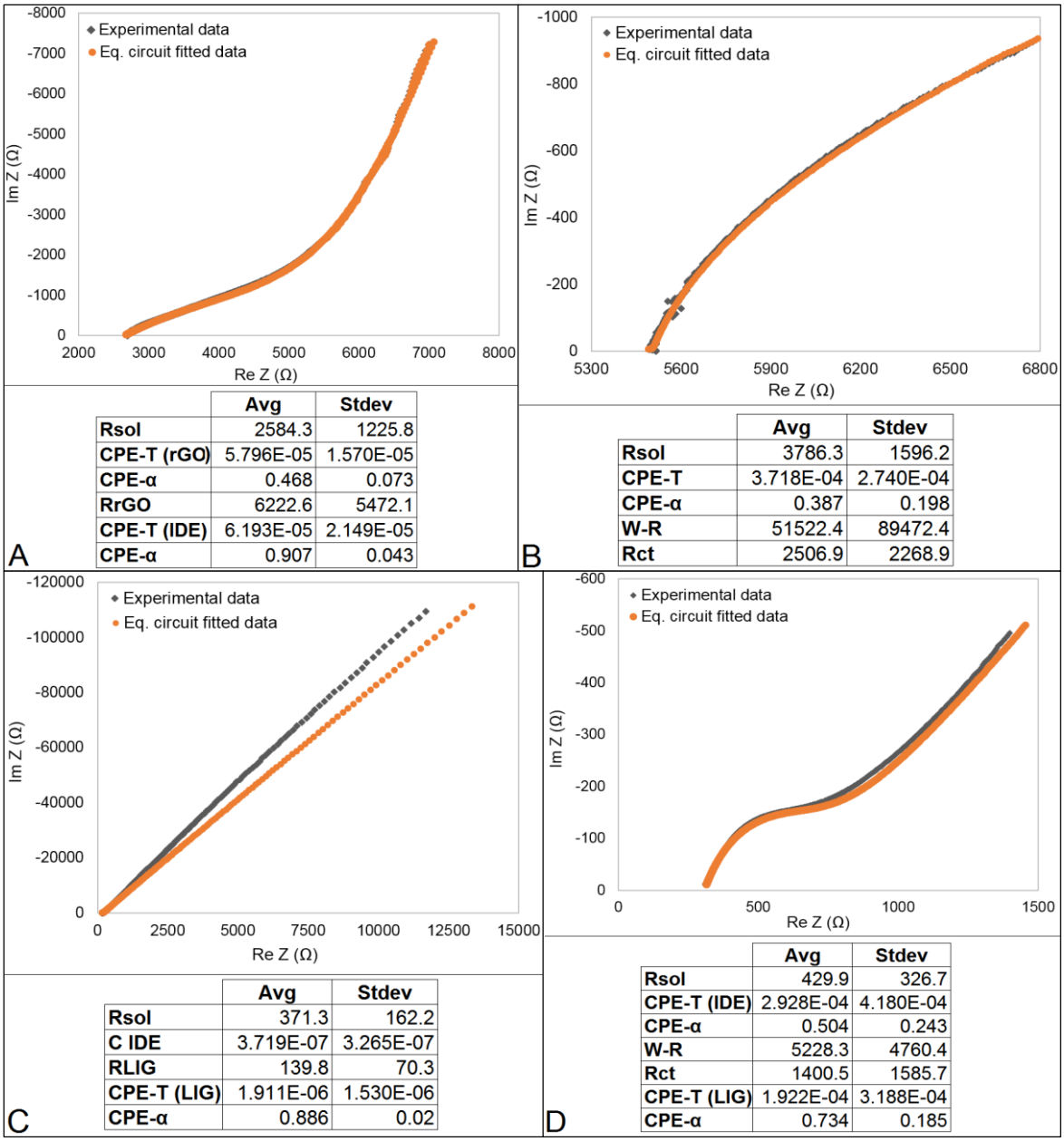


| | Avg | Stdev |
|---|---|---|
| Rsol | 2584.3 | 1225.8 |
| CPE-T (rGO) | 5.796E-05 | 1.570E-05 |
| CPE-α | 0.468 | 0.073 |
| RrGO | 6222.6 | 5472.1 |
| CPE-T (IDE) | 6.193E-05 | 2.149E-05 |
| CPE-α | 0.907 | 0.043 |

| | Avg | Stdev |
|---|---|---|
| Rsol | 3786.3 | 1596.2 |
| CPE-T | 3.718E-04 | 2.740E-04 |
| CPE-α | 0.387 | 0.198 |
| W-R | 51522.4 | 89472.4 |
| Rct | 2506.9 | 2268.9 |

| | Avg | Stdev |
|---|---|---|
| Rsol | 371.3 | 162.2 |
| C IDE | 3.719E-07 | 3.265E-07 |
| RLIG | 139.8 | 70.3 |
| CPE-T (LIG) | 1.911E-06 | 1.530E-06 |
| CPE-α | 0.886 | 0.02 |

| | Avg | Stdev |
|---|---|---|
| Rsol | 429.9 | 326.7 |
| CPE-T (IDE) | 2.928E-04 | 4.180E-04 |
| CPE-α | 0.504 | 0.243 |
| W-R | 5228.3 | 4760.4 |
| Rct | 1400.5 | 1585.7 |
| CPE-T (LIG) | 1.922E-04 | 3.188E-04 |
| CPE-α | 0.734 | 0.185 |

Figure 5.20. Representative experimental and fitted equivalent circuits with average and standard deviation values across seven IDE devices: (A) non-faradaic rGO; (B) faradaic rGO; (C) non-faradaic LIG; (D) faradaic LIG.

### 5.2.3 *rGO IDE immunosensor for PSA detection*

#### *5.2.3.1 Non-faradaic impedance detection of PSA on rGO IDE*

Targeting protein biosensing applications, EIS measurements were performed to quantify changes in the rGO IDE properties during functionalization, PSA-10 antibody immobilization and prostate specific protein binding. Batch testing using several IDE samples was initially attempted, but the results were inconsistent and showed no correlation with the analyte concentration, with the obtained results presented in Figure 5.21.

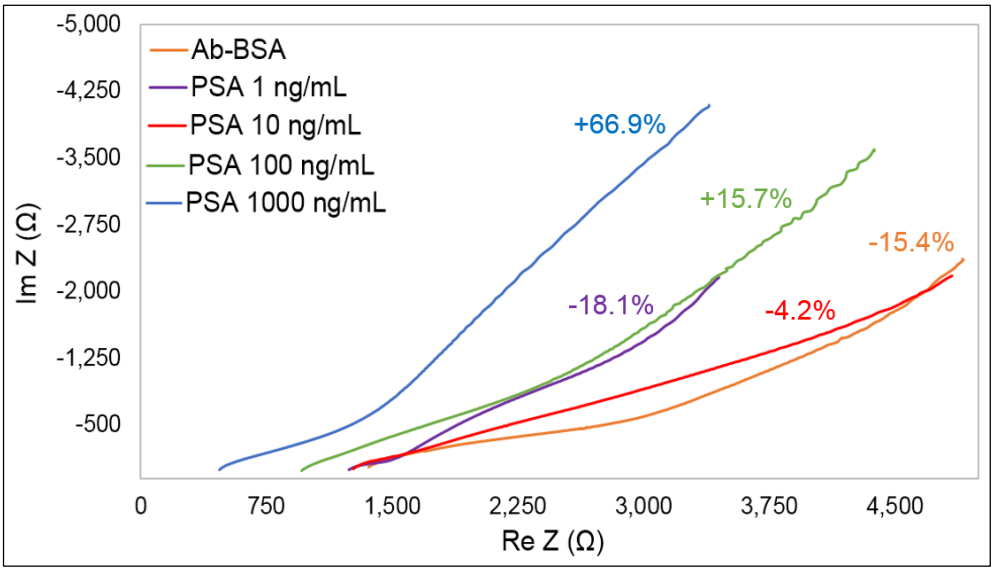


Figure 5.21. Nyquist plot (0.5 Hz-100 kHz) of the non-faradaic EIS for rGO IDE batch testing and quantified Δ Im(Z) related to the initial values extracted at 1 Hz.

The rGO IDE was further investigated using sequential PSA addition, with representative non-faradaic impedance results shown in Figure 5.22. The double layer formation lead to an increase in Im(Z) within 7.6% and 33% for maximum PSA concentration. The variation in Re(Z) can be attributed to changes in the rGO resistance in the presence of the biomolecular layer.

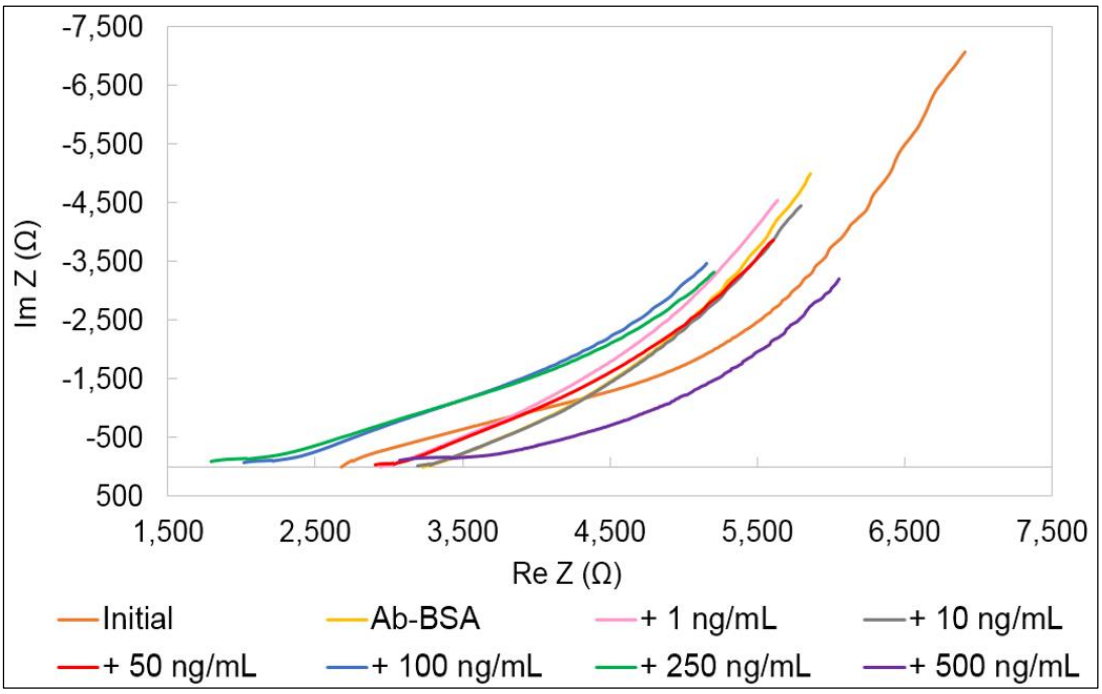


Figure 5.22. Nyquist plot (0.5 Hz-100 kHz) of the non-faradaic EIS for rGO IDE as functionalized and with successive analyte addition.

The electrochemical impedance was further analysed at low frequencies i.e. 0.5 Hz-5 Hz, where it was mostly sensitive due to its capacitive component. The

relationship between analyte concentration and $C_{dl}$ on the rGO surface is presented in Figure 5.23. Im(Z) was used to calculated the corresponding capacitive component according to eq. 2-2. The 0 ng/mL point represents the “blank” and it corresponds to the rGO surface after PSA-10 antibody layer deposition and subsequent blocking step via BSA (step 4 of the protocol, see section 5.1.3). The tested samples exhibited $R^2 > 0.94$, saturating above 411 ng/mL; the measurement repeatability variation is below 8% for the first sample and significantly lower (<5%) for the second sample. The noise and fluctuations in the measurements were observed to increase with the frequency to maximum 15% above 5 kHz and this is believed to be an effect of the surrounding electrolyte media and its adsorption-related processes in the rGO pores.

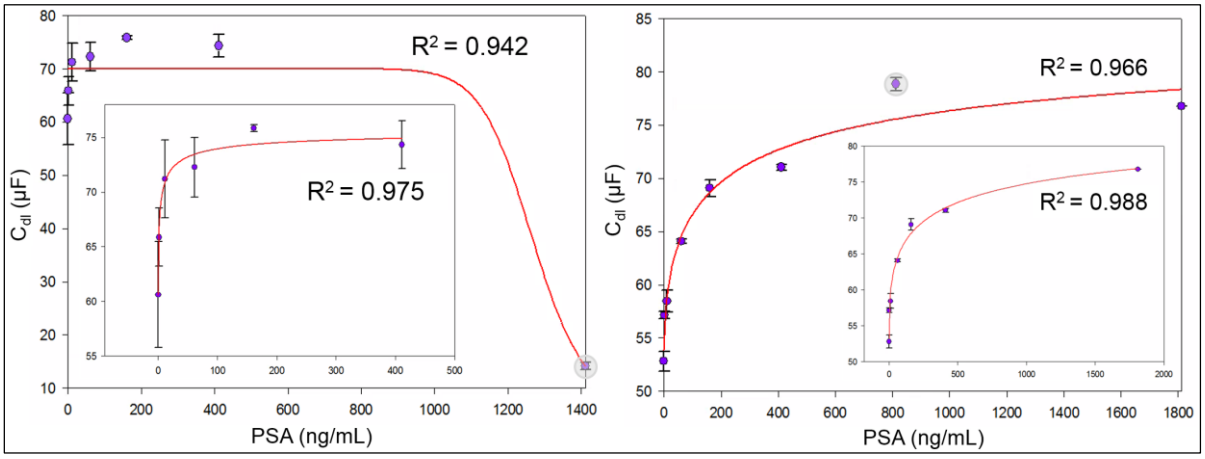


Figure 5.23. One-side binding curve showing the relationship between PSA concentration and $C_{dl}$ at 1 Hz for two rGO IDE samples. The plotted points correspond to the average between two consecutive measurements (error bars); inset: adjusted calibration curve without outliers (marked in grey).

### *5.2.3.2 Faradaic impedance detection of PSA on rGO IDE*

Figure 5.24 shows the faradaic impedance response of the rGO IDE for successive PSA addition. The magnitude of impedance was found to slightly decrease with antigen concentration by 3.5% on average, with a steady decrease in $C_{dl}$ for both tested samples. This indicates the non-uniform PSA binding to the functionalized rGO and a possible charging effect. Also, an interfacial diffusion-based mobile layer is possible to be displaced away from the expanded electrode surface of the rGO as a result of the increase in thickness when capturing the probe layer [402].

As exemplified in section 2.5.3, $R_{ct}$ is usually solely employed to build calibration curves for faradaic measurements. The binding curve based on the magnitude of impedance is shown in Figure 5.25, and one can notice a significant difference between the two rGO samples, with the best $R^2 > 0.99$. The complex morphology of

rGO triggers surface changes based on a combined effect of the charge transfer and electrical double layer. Hence, the capacitive reactance was further correlated with analyte concentration (see Figure 5.26). The measurement variation is lower than 5% on average.

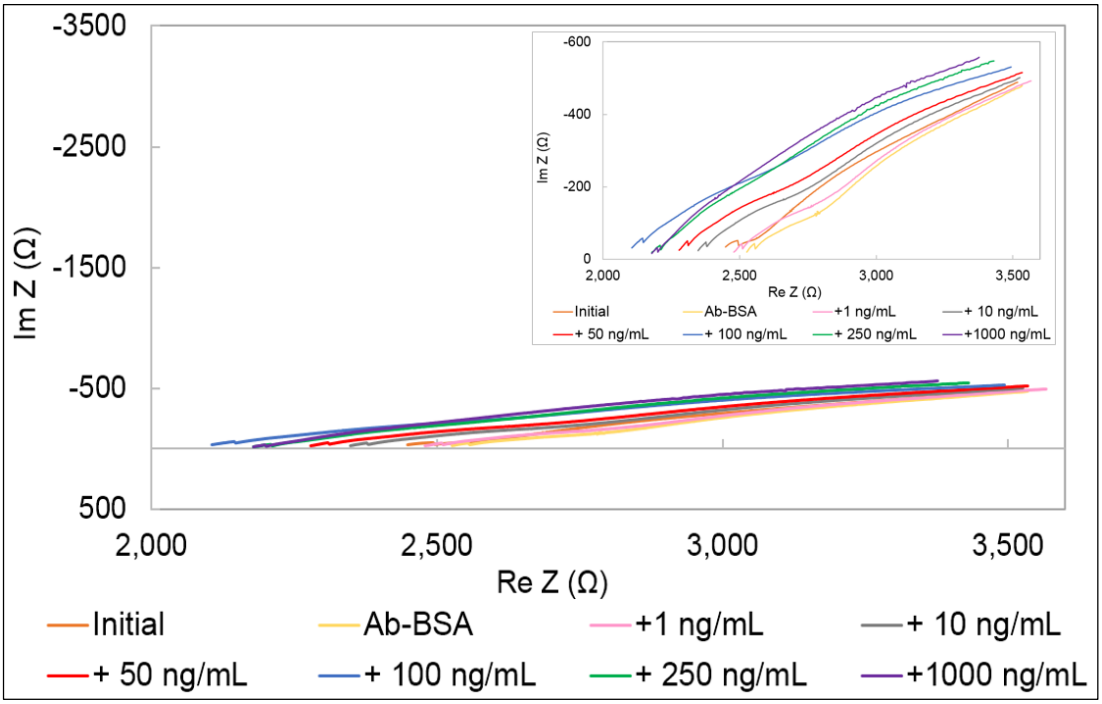


Figure 5.24. Nyquist plot (0.5 Hz – 100 kHz) of the faradaic EIS for rGO IDE surface as functionalized and with successive analyte addition.

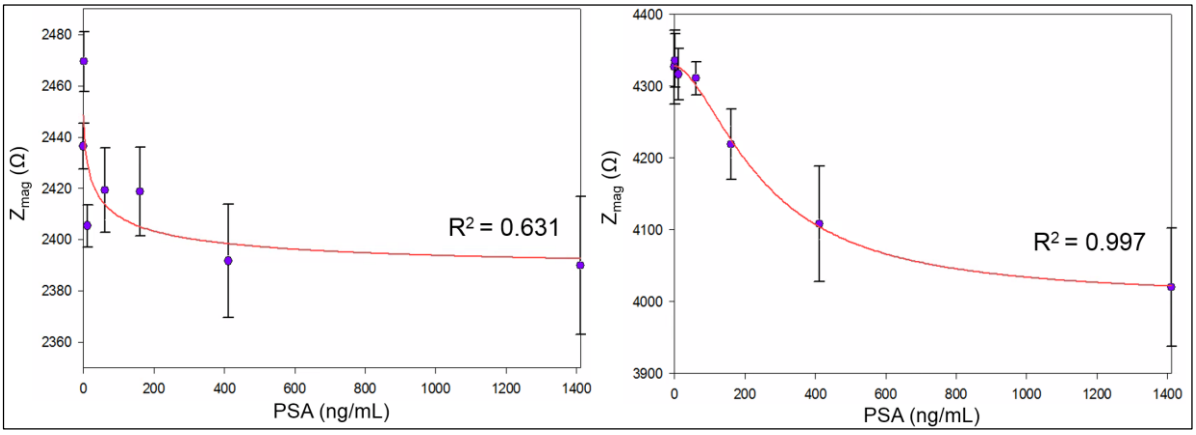


Figure 5.25. One-side binding curve showing the faradaic relationship between PSA concentration and $Z_{mag}$ at 1 Hz for two rGO IDE samples. The plotted points correspond to the average between two consecutive measurements (error bars).

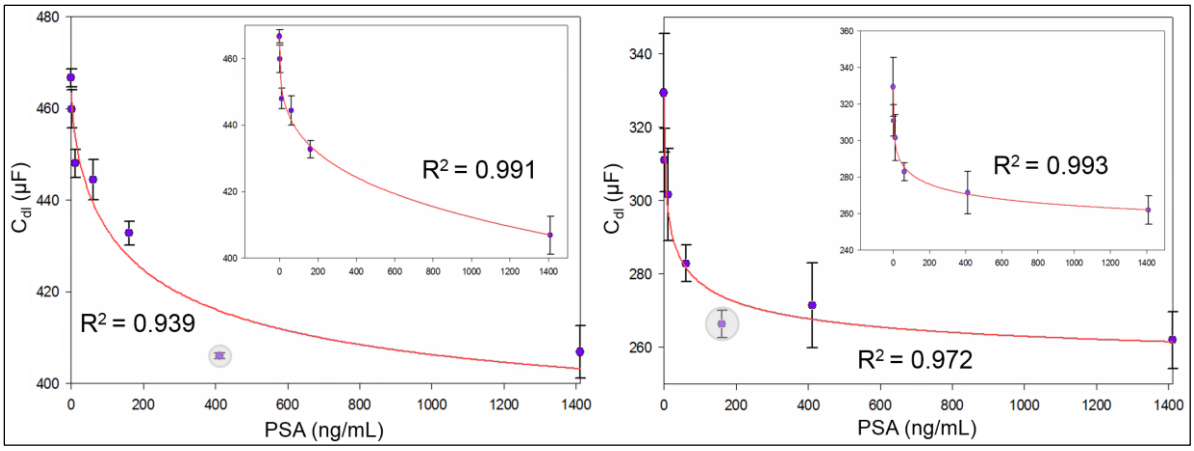


Figure 5.26. One-side binding curve showing the faradaic relationship between PSA concentration and $C_{dl}$ at 1 Hz for two rGO IDE samples. The plotted points correspond to the average between two consecutive measurements (error bars); inset: adjusted calibration curve without outliers (marked in grey).

The Lightscribe sample repeatability was limited, due to variability in material properties, which was earlier addressed in section 3.2. The maximum impedance change was 25.2% in non-faradaic detection mode and respectively 24.2% for faradaic measurements for sequential PSA addition to a total of 1411 ng/mL.

### 5.2.4 *LIG IDE immunosensor for PSA detection*

#### *5.2.4.1 Non-faradaic impedance detection of PSA on LIG IDE*

Firstly, LIG IDE devices were batch tested using non-faradaic EIS, with the measurements presented in Figure 5.27. In spite of LIG's more reproducible manufacturing method compared to rGO, no evident data trend could be identified for increasing analyte concentrations.

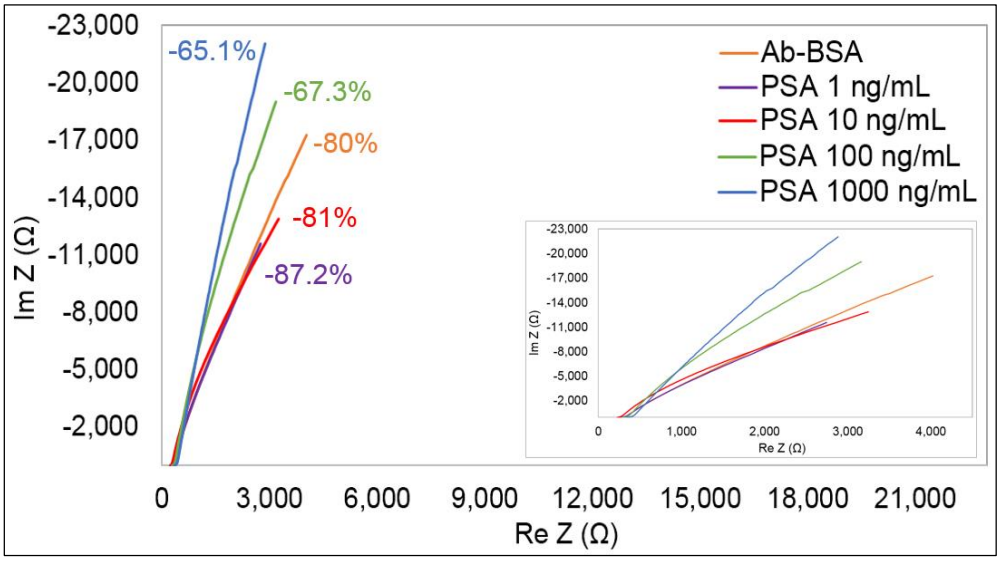


Figure 5.27. Nyquist (0.5 Hz-100 kHz) plot of the non-faradaic EIS for LIG IDE batch testing and quantified Δ Im(Z) related to the corresponding initial values extracted at 0.5 Hz.

Following the same approach as for rGO, the LIG IDE performance was further assessed using sequential protein addition on the same surface. A representative Nyquist plot for one of the tested LIG IDE sample is shown in Figure 5.28. The LIG surface was observed to be highly hydrophobic compared to rGO and it also presented some local variability. Im(Z), representative of capacitive effects, accounted for 92.7% of magnitude of impedance changes at 0.5 Hz, varying between 10.7% and 69.6% across the two samples.

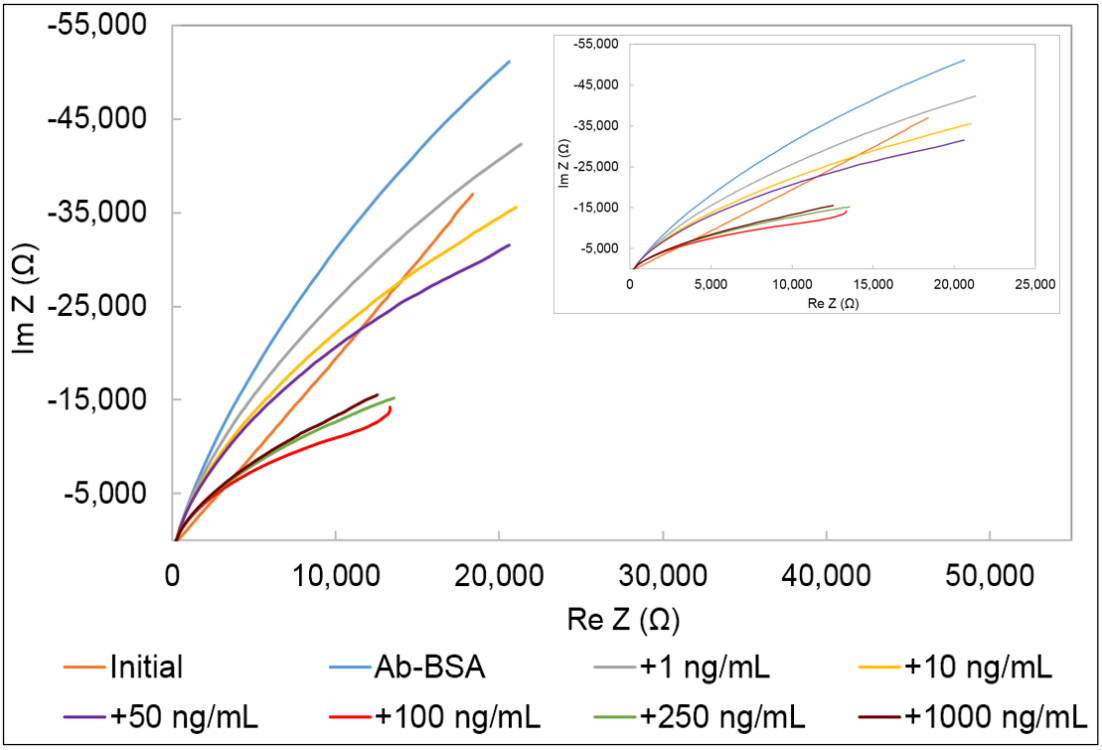


Figure 5.28. Nyquist plot (0.5 Hz-100 kHz) of the non-faradaic EIS for LIG IDE as functionalized and with successive PSA addition.

Both samples exhibited a steady decrease in the magnitude of impedance and an increase in the phase upon functionalization and antigen-antibody binding. The interfacial layer led to an increase in $C_{dl}$, which was quantified at low frequencies to construct the binding curve shown in Figure 5.29. Similar data trends have been reported in the literature for highly porous polymer-based structures [403]. The first sample showed enhanced sensitivity, with $R^2$ goodness of fit of 0.994.

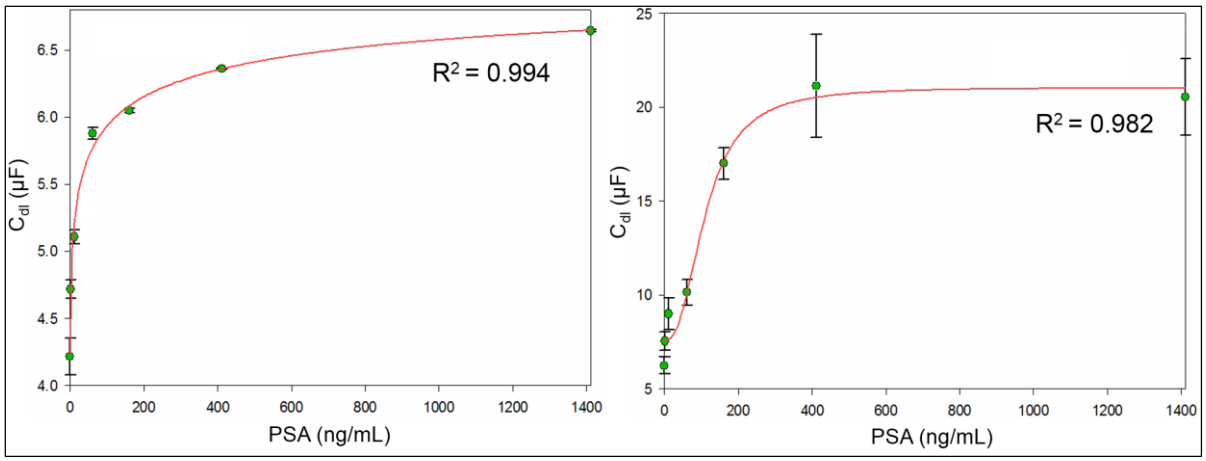


Figure 5.29. One-side binding curve showing the relationship between PSA concentration and $C_{dl}$ at 0.5 Hz for two LIG IDE samples. The plotted points correspond to the average between two consecutive measurements (error bars).

### *5.2.4.2 Faradaic impedance detection of PSA on LIG IDE*

The faradaic impedance of LIG IDE devices showed a decrease in the magnitude of impedance at low frequencies, up to 1 kHz. A representative Nyquist plot for successive PSA addition on the LIG surface is shown below in Figure 5.30.

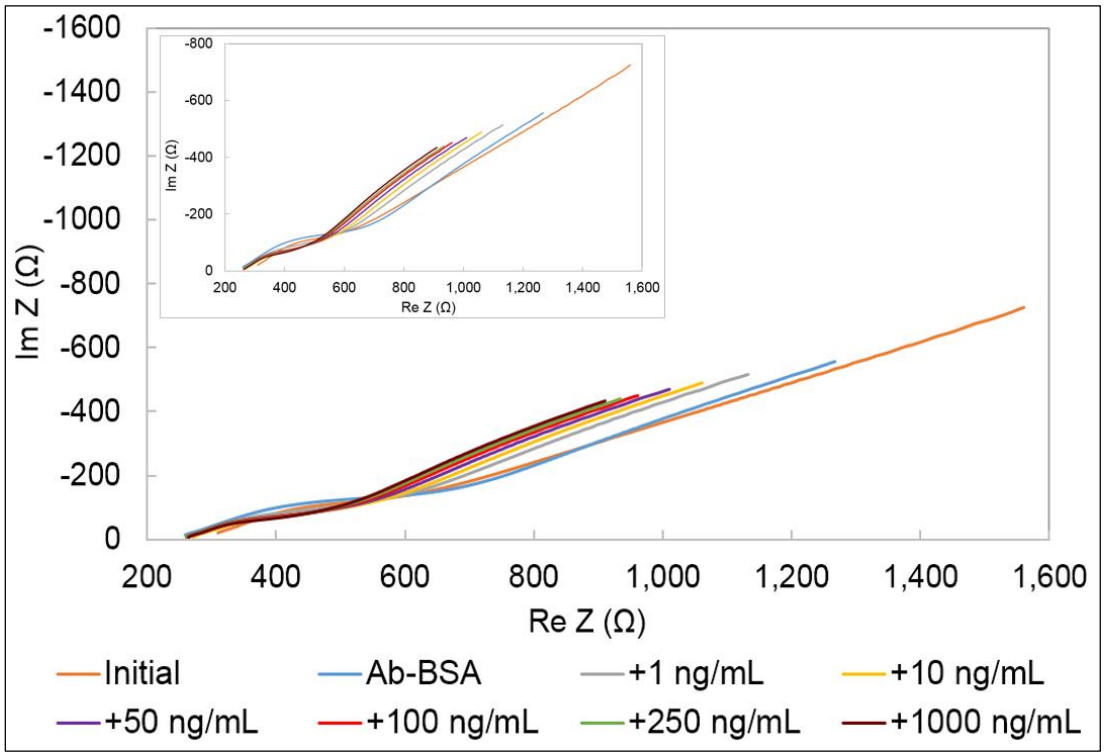


Figure 5.30. Nyquist plot (0.5 Hz-100 kHz) of the faradaic EIS for LIG IDE as functionalized and with successive PSA addition.

The impedance surface changes were further quantified using the charge transfer and double layer formation phenomena, and corresponding binding curves

were built using the magnitude of impedance $Z_{mag}$ (see Figure 5.31) and $C_{dl}$, calculated based on Im(Z) (see Figure 5.32).

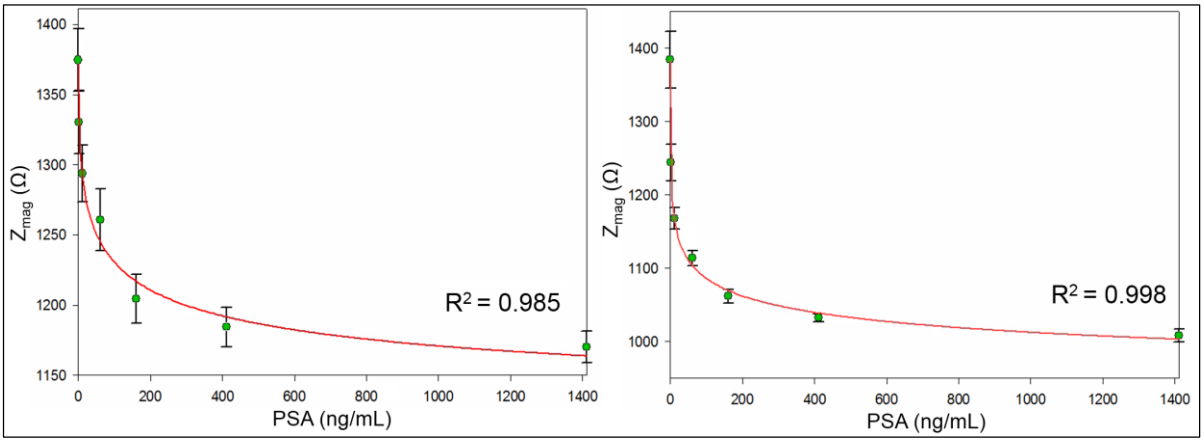


Figure 5.31. One-side binding curve showing the faradaic relationship between PSA concentration and $Z_{mag}$ at 0.5 Hz for two LIG IDE samples. The plotted points correspond to the average between two consecutive measurements (error bars).

Both parameters showed a good level of correlation with PSA concentration, but the measurement repeatability was highly limited for the first sample. While the repeatability error across the two samples is lower and more consistent compared to the non-faradaic measurements i.e. 2%, there is notable difference between the two LIG IDE samples in terms of their sensitivity and detection capability. The fabrication method might be simpler, but there is local variation in material properties.

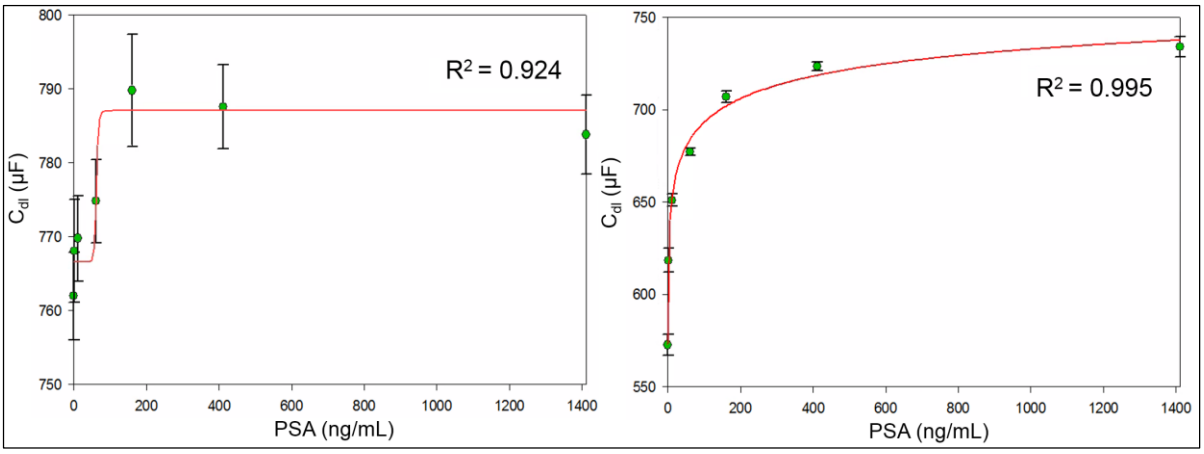


Figure 5.32. One-side binding curve showing the faradaic relationship between PSA concentration and $C_{dl}$ Ia at 0.5 Hz for two LIG IDE samples. The plotted points correspond to the average between two consecutive measurements (error bars).

For LIG, the reproducibility is slightly improved compared to rGO, but the measurement repeatability is limited. The maximum non-faradaic impedance change was 58.9% and 27% in the faradaic detection mode for sequential PSA addition up to a maximum concentration of 1411 ng/mL.

### 5.2.5 *Performance and limitations of graphene based IDE biosensors*

#### *5.2.5.1 A brief specificity study of graphene based IDE biosensor*

The specificity of the graphene electrodes was assessed by introducing a control sample consisting of PSA 0% + BSA 0.5%. Faradaic impedance measurements were performed on both rGO and LIG IDE, as presented below in Figure 5.33. To simplify the comparison of the impedance plots, the X-axis was normalized to compensate for any variation in electrodes' and contact resistance.

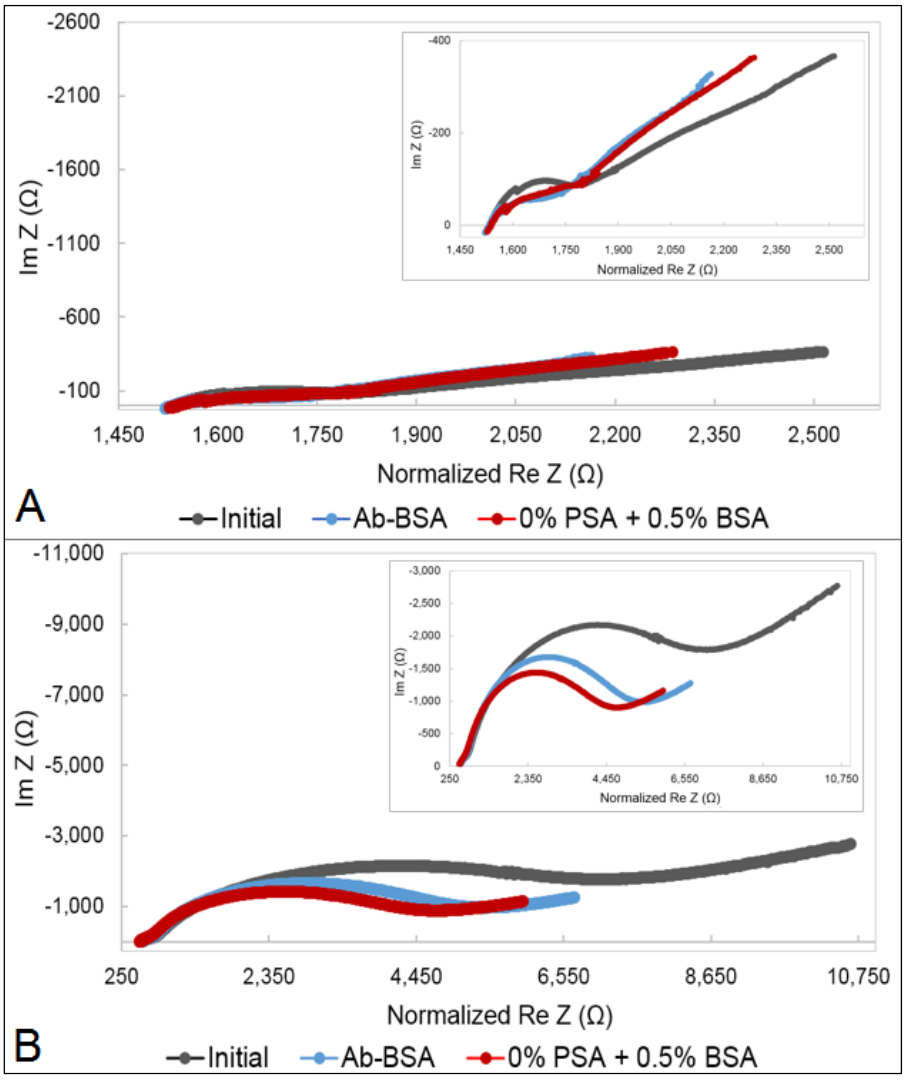


Figure 5.33. Nyquist plots (0.5 Hz-100 kHz) of the faradaic EIS showing the effect of non-specific adsorption onto functionalized and blocked surface of (A) rGO and (B) LIG.

The rGO IDE samples showed a distinctive behaviour, but the average ΔC across the two samples was -5.3%, which corresponds to the impedimetric surface variation (series $C_{dl}$) in the presence of 1-10 ng/mL PSA. Δ Zmag increased by 4.8% due to non-specific adsorption, showing an opposite trend compared to previous tests, where it was found to decrease upon antibody-antigen interaction. Re(Z) dominated the magnitude of impedance response by 90% and hence, this result confirms the

surface passivation by BSA molecules adsorption. However, in the case of LIG IDE sensors, $Z_{mag}$ decreased by 12% for the test sample, which is within the determined PSA detection range at a concentration of up to 10 ng/mL. The corresponding $C_{dl}$ at 0.5 Hz showed an increase of just over 20%, which was previously identified for maximum PSA concentrations in faradaic EIS measurements with sequential PSA addition.

Overall, the changes in capacitive reactance as induced by the non-specific adsorption of BSA corresponds within PSA detected changes in the range of 1-10 ng/mL for both rGO and LIG.

#### *5.2.5.2 Biosensor calibration curves using surface regeneration*

The graphene based substrates were attempted to be regenerated using glycine (step 6 in the protocol, see 5.1.3) in order to circumvent the issue of limited repeatability and lack of reproducibility of their fabrication method. The presented data was acquired for increasing protein concentrations (low → high) with glycine washing steps in between concentrations and compared with the reverse calibration curve, obtained by decreasing the protein concentration (high → low).

When the measurements were taken for increasing PSA concentrations (low → high concentration), the data showed some consistency with the case of sequential PSA addition on the same IDE surface. However, when inversely applied (high → low concentration), significant differences were identified for both rGO and LIG. The reverse regeneration curves exhibited opposite trends, with a clear trend for the LIG electrodes. Figure 5.34 and Figure 5.36 present the magnitude of impedance and corresponding double layer measurements for rGO and LIG, with representative Bode plots shown in Figure 5.35 and Figure 5.37.

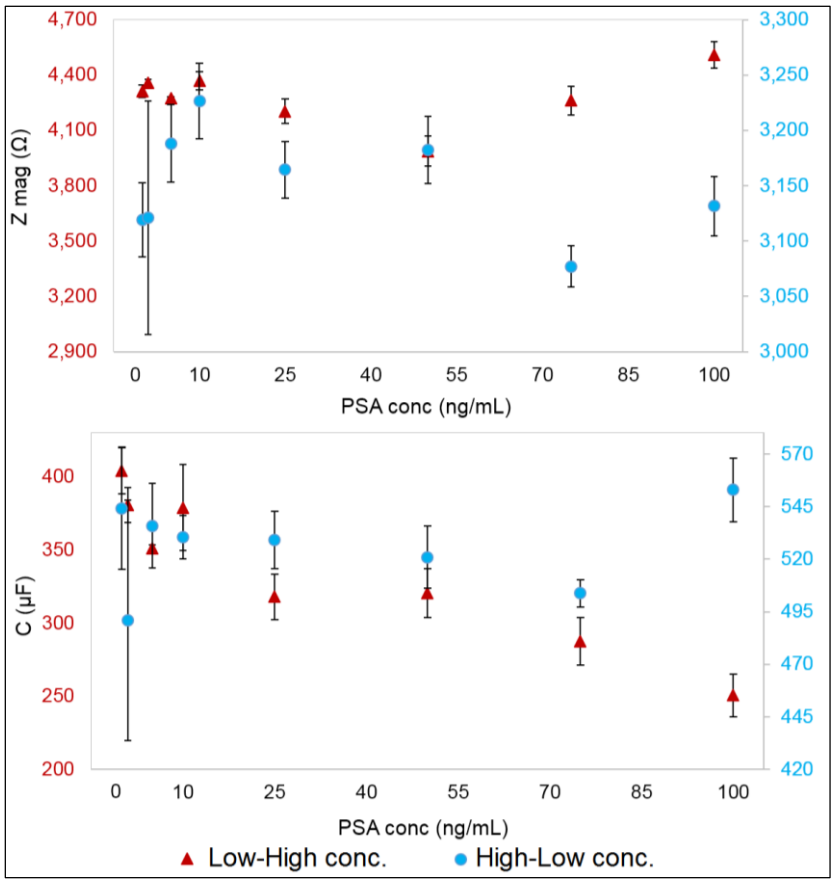


Figure 5.34. Plots showing the relationship between PSA concentration and $Z_{mag}$ (A) and $C_{dl}$ (B) using faradaic impedance detection on rGO IDE with surface regeneration.

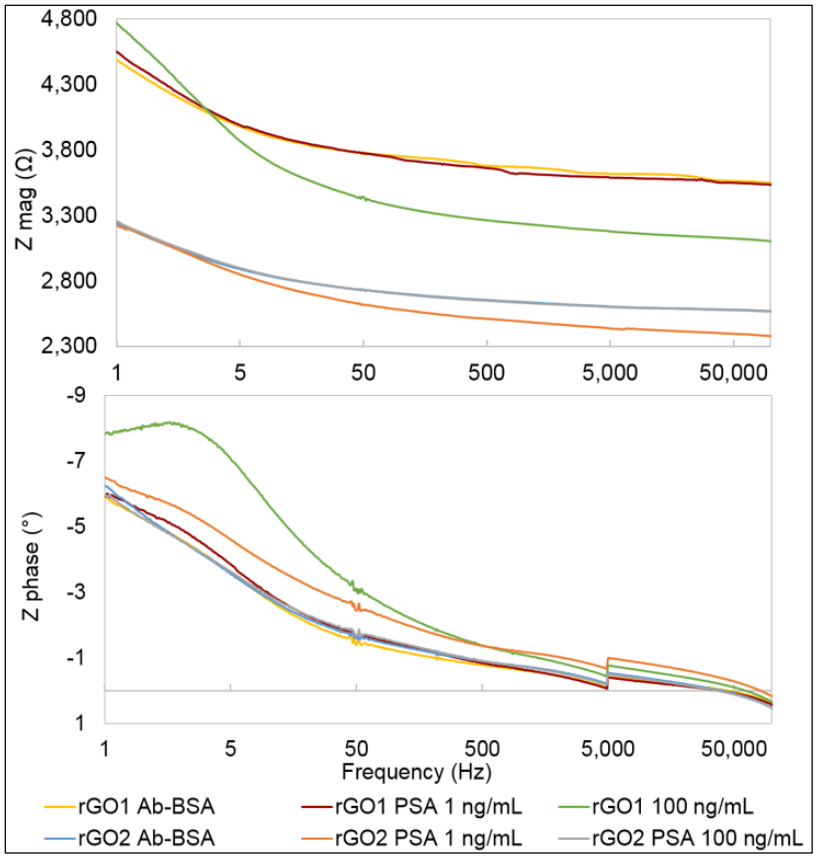


Figure 5.35. Representative Bode plot for the regenerated rGO IDE using faradaic EIS.

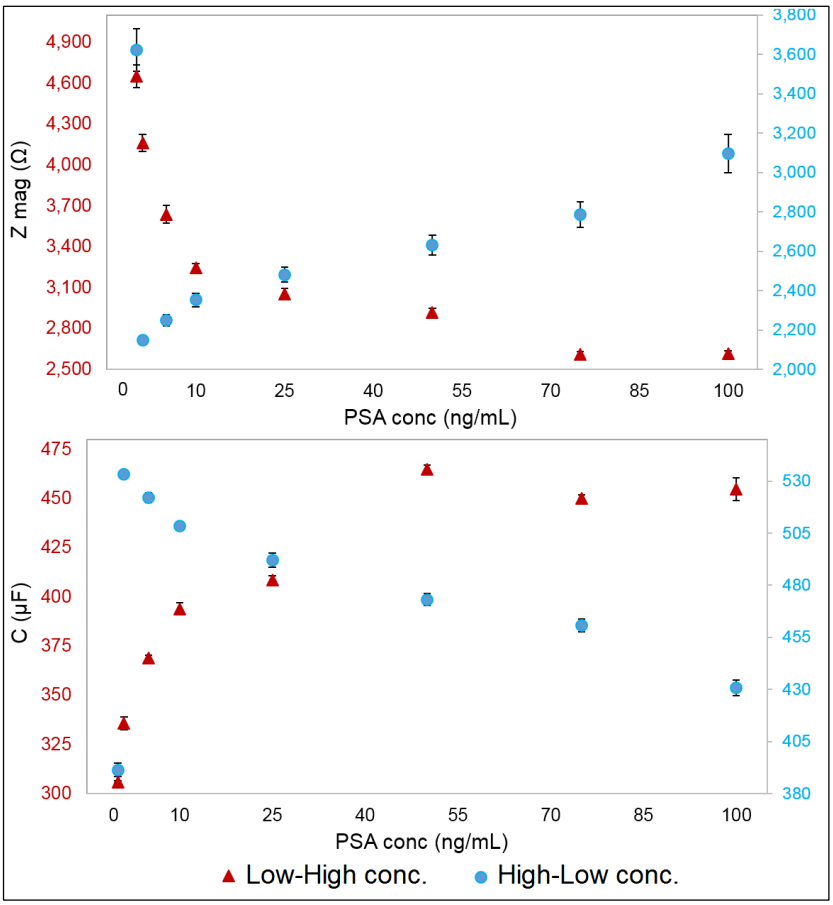


Figure 5.36. Plots showing the relationship between PSA concentration $Z_{mag}$ (A) and $C_{dl}$ (B) using faradaic impedance detection on LIG IDE with surface regeneration.

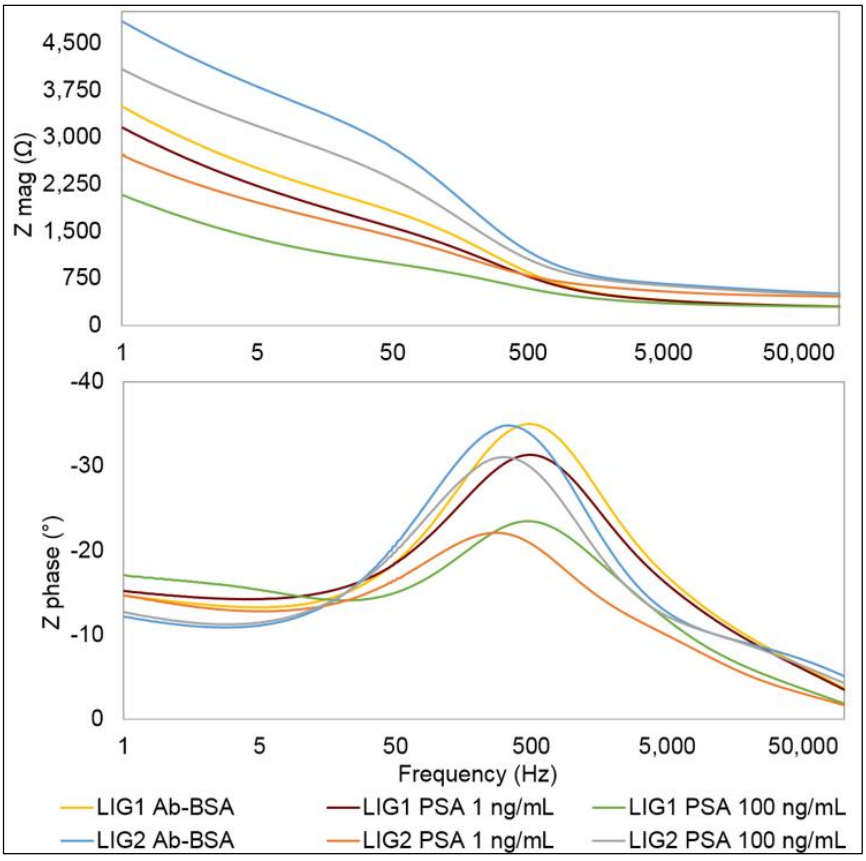


Figure 5.37. Representative Bode plot for the regenerated LIG IDE using faradaic EIS.

Overall, these results indicate that a strong adsorption-based mechanism dominates the graphene based IDE impedance response for the antibody and antigen molecular layers.

### 5.2.6 *Performance studies of the graphene based IDE biosensor*

Further studies were conducted in order to understand the response stability of the graphene based electrodes: time dependent impedance measurements for blank and prostate specific antibody-antigen immobilized on graphene surface, as well as protein desorption / dissociation. The non-faradaic tests were undertaken using rGO and LIG IDE devices from the same batch as $C_{dl}$ was earlier identified as a valid parameter for both materials, but also to avoid redox probe adsorption in the graphene layers. The capacitive changes were quantified using eq. 2-1.

#### *5.2.6.1 Blank measurements on graphene based IDE*

Firstly, repeated measurements of the blank (PSA-10 antibody with BSA blocking layer) were taken by varying the immersion time in the PBS buffer. In the ideal scenario, a constant and steady response would imply that any impedance deviation is exclusively triggered eby the presence of the biomolecular layer. The obtained results are shown in Figure 5.38, with two out of the three tested rGO IDE devices exhibiting a linear decreasing in Im(Z) as function of buffer immersion time. The dramatically different behaviour of rGO2 is believed to be due to poor manufacturing repeatability. The maximum measurement repeatability error was 0.96%.

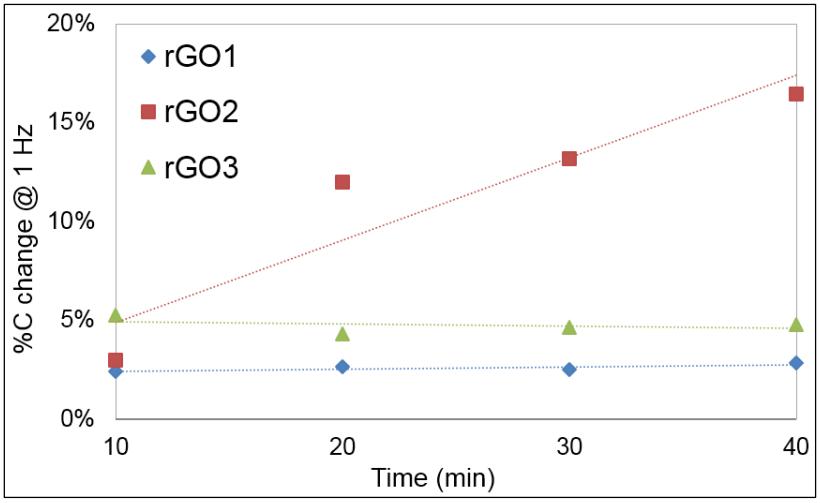


Figure 5.38. Repeated blank measurement at 0.5 Hz on rGO IDE after 10, 20, 30 and 40 minutes immersion in PBS. The plotted points are the average across two consecutive measurements (error bars). The % change was quantified relative to the initial measurement (t=0).

The LIG IDE sensors showed even a poorer stability. The large pores (µm-range), part of a complex morphology (see Figure 3.16), are easily filled with the electrolyte. The samples showed a linear decrease in Im(Z) with sensitivities (slope of fitted linear curve) varying between of 0.006-0.03 µF/min. Figure 5.39 presents the capacitive changes upon PBS immersion. The maximum measurement repeatability error was 5.3%, which is 5-fold higher compared to rGO.

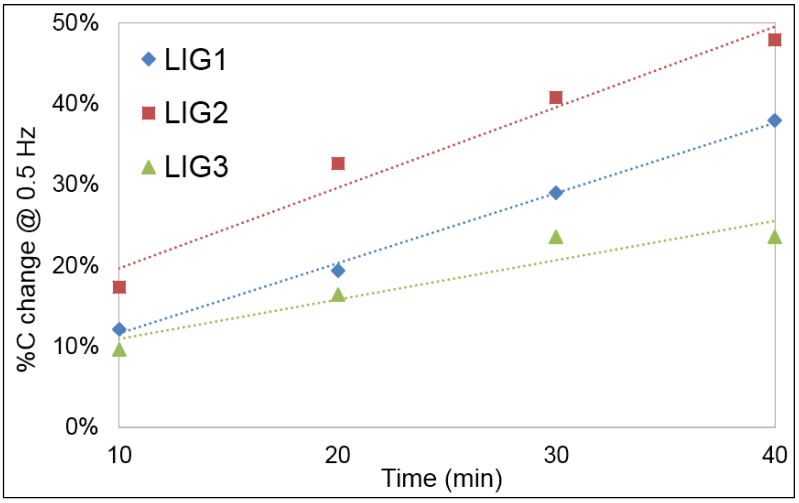


Figure 5.39. Repeated blank measurement at 0.5 Hz on LIG IDE after 10, 20, 30 and 40 minutes immersion in PBS. The plotted points are the average across two consecutive measurements (error bars). The % change was quantified relative to the initial measurement (t=0).

### *5.2.6.2 Sequential protein addition on graphene based IDE*

It was essential to understand the interaction between the functionalized graphene and the target prostate specific protein. In this respect, a fixed PSA concentration was sequentially added within the determined working range of the graphene based electrodes. The IDE substrates were incubated with 25 ng/mL PSA for 10 minutes, followed by a washing step, measurement and protein re-incubation. In these conditions, concentration-proportional impedance changes were expected, with an ideal linearly increasing trend.

Figure 5.40 shows similarities with the results discussed in section 5.2.6.1 as the three rGO IDE samples exhibit different behaviours. Two out of three samples exhibited a linear increase in $C_{dl}$ with $R^2 = 0.96 - 0.976$. The maximum measurement error was 1.8%.

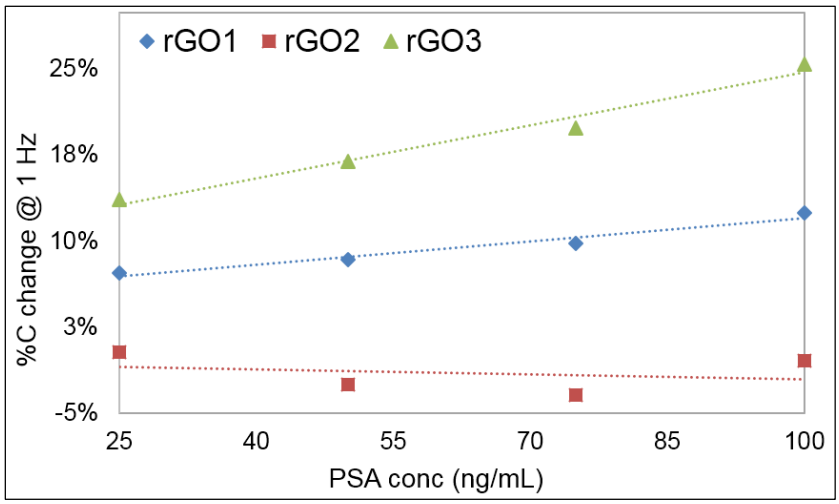


Figure 5.40. Protein test of rGO IDE performed by repeating fixed PSA concentration addition (25 ng/mL) with 10 minute incubation time at 0.5 Hz.

Moreover, the LIG samples showed a higher sensitivity compared to rGO, with approximately 0.35% increase per 1 ng/mL PSA (Figure 5.41) and average $R^2 > 0.99$. These results suggest that the impedance response changes are driven by both protein desorption (and possible diassociation) and buffer adsorption. The maximum measurement repeatability error for LIG was 2.6%.

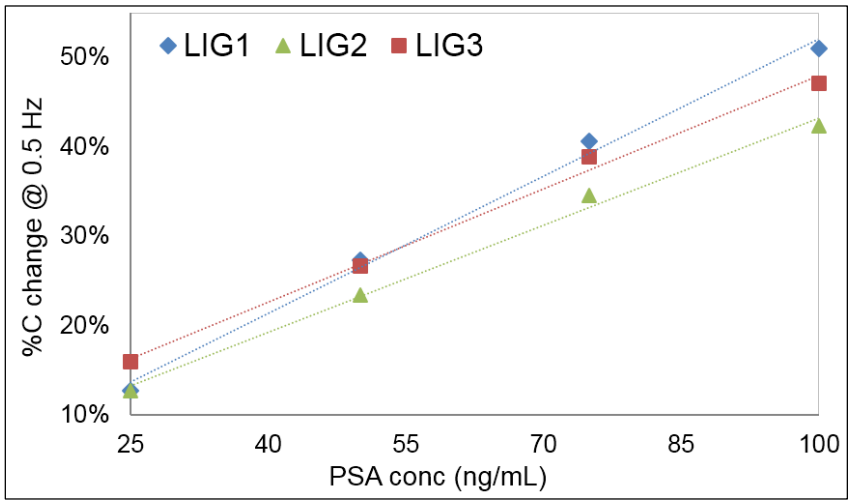


Figure 5.41. Protein test of LIG IDE performed by repeating fixed PSA concentration addition (25 ng/mL) with 10 minute incubation time at 0.5 Hz.

### *5.2.6.3 Protein measurements on graphene based IDE*

The drifting aspect was thus investigated as it was identified to be a major concern especially for the LIG structures (see 5.2.5.2). After the PSA (25 ng/mL) attachment on the immobilized PSA-10 antibody layer, the electrodes were immersed in the PBS electrolyte and measurements were taken at different time intervals, between 10 and 90 minutes. These measurements provide further information

concerning protein desorption. Ideally, no variation should occur, or at least within short incubation times.

Figure 5.42 presents the non-faradaic response of the rGO IDE sensors, found to be quite inconsistent, likely to be caused by some level of variability in its structure and functionalities. Unlike rGO, the LIG samples (see Figure 5.43) showed a better response repeatability, but there was a linearly increasing trend in $C_{dl}$ with PBS incubation times. Thus, the pores' filling with the buffer dominated the impedance response of the electrodes.

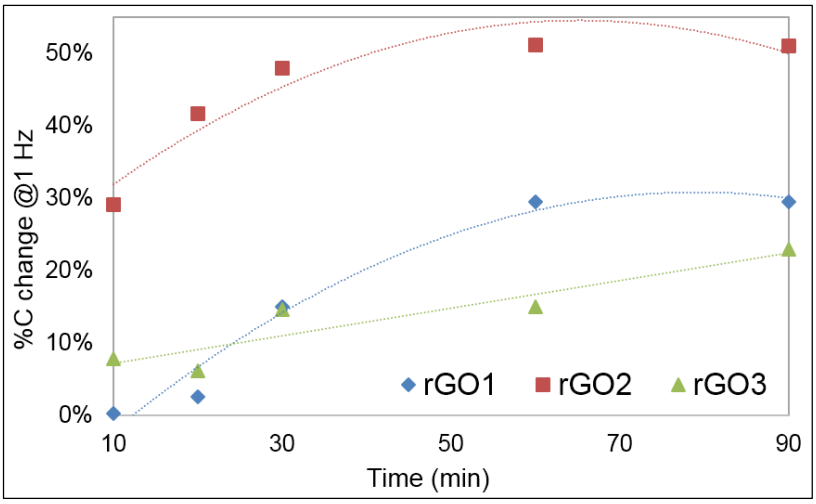


Figure 5.42. Repeated measurement of 25 ng/mL PSA on rGO IDE at 0.5 Hz after various PBS incubation times.

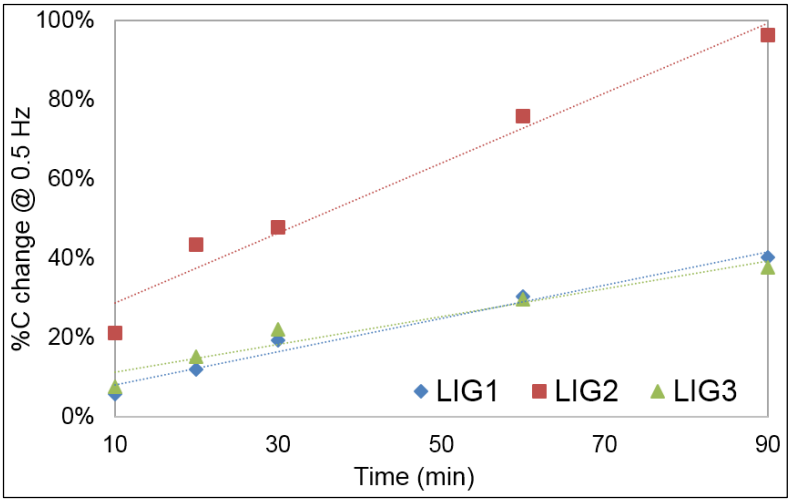


Figure 5.43. Repeated measurement of 25 ng/mL PSA on LIG IDE at 0.5 Hz after various PBS incubation times.

#### *5.2.6.4 Baseline drifting on graphene based IDE*

Finally, baseline drift measurements of the non-functionalized graphene surfaces were conducted in order to assess the electrochemical stability of the graphene based materials. The non-faradaic impedance measurements are presented

below in Figure 5.44 and Figure 5.45. Interestingly, the relationship between the incubation time and $C_{dl}$ change (%) can be statistically described by a power function in the case of rGO and an inverse exponential for LIG. While the rGO capacitance doubled for maximum incubation time, LIG's dramatically increased by approximately 20-fold.

A significant variation was identified for duplicate measurements of LIG IDE samples, with a standard deviation above 100%. The adsorption of the PBS in the micro-size pores of the LIG had a dramatic effect on its impedance response, with an increase of up to 310% within 1 hour of immersion; the impedance response was dominated by its high porosity, as "pockets" filled with electrolyte solution were formed.

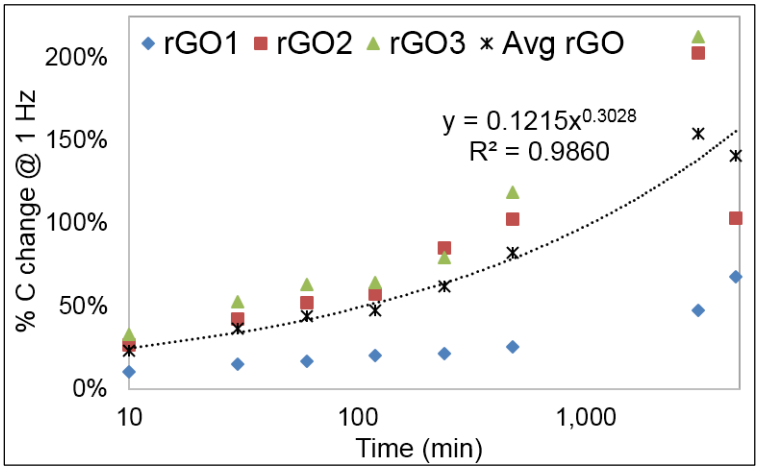


Figure 5.44. Impedance response drifting of rGO IDE in PBS as function of incubation times.

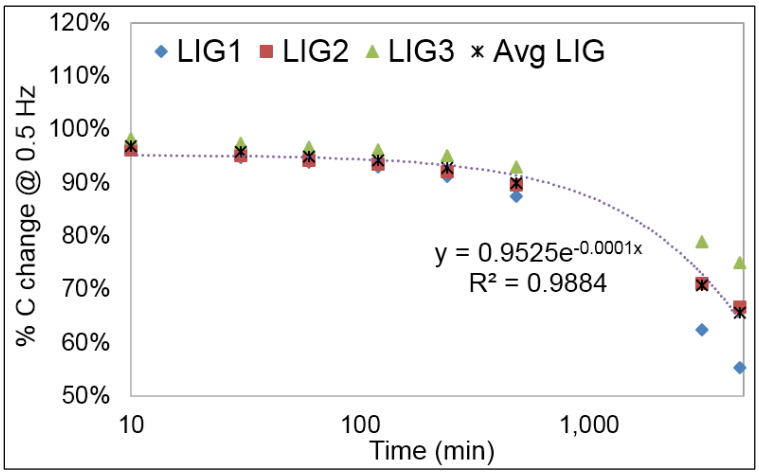


Figure 5.45. Impedance response drifting of LIG IDE in PBS as function of incubation times.

#### *5.2.6.5 Results overview*

Figure 5.46 and Figure 5.47 provide an overview of the conducted graphene based material performance studies for rGO and LIG, with a focus on non-faradaic double layer induced changes at low frequencies ($C_{dl}$). If the baseline drifting effect is

subtracted from the obtained calibration curves, the direct and reverse calibration curves are comparable. The PBS adsorption in the graphene pores and layers dominate the impedance response, evident from the repeated measurements of fixed PSA concentration of 25 ng/mL and dramatically affecting the LIG IDE performance.

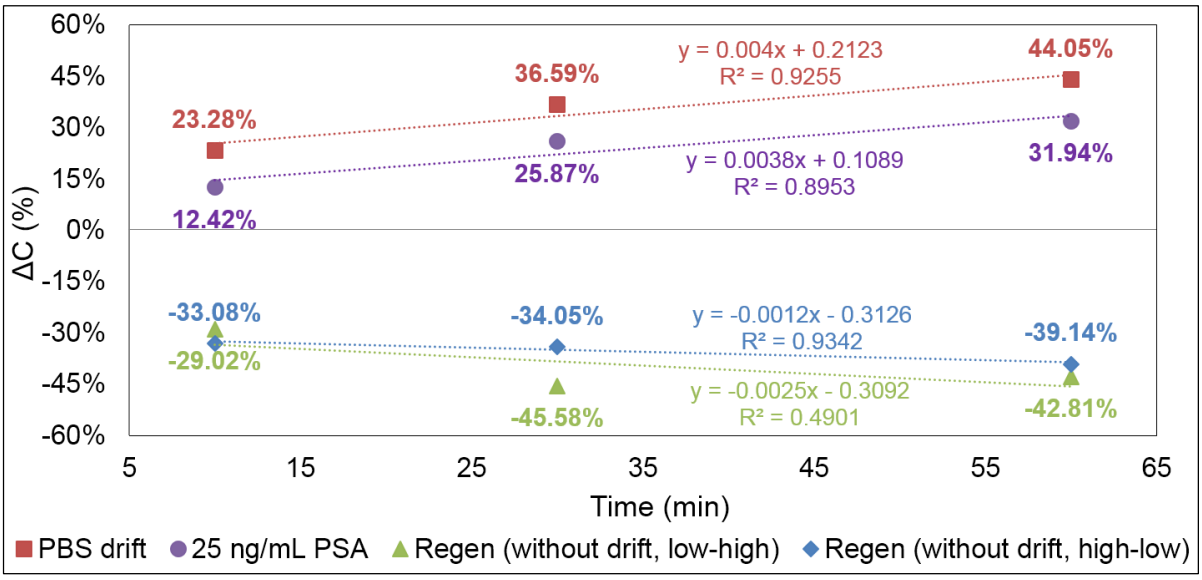


Figure 5.46. Cdl variation for rGO IDE biosensors: drift due to baseline (PBS, repeated measurements of PSA 25 ng/mL) and calibration curves as function of immersion time.

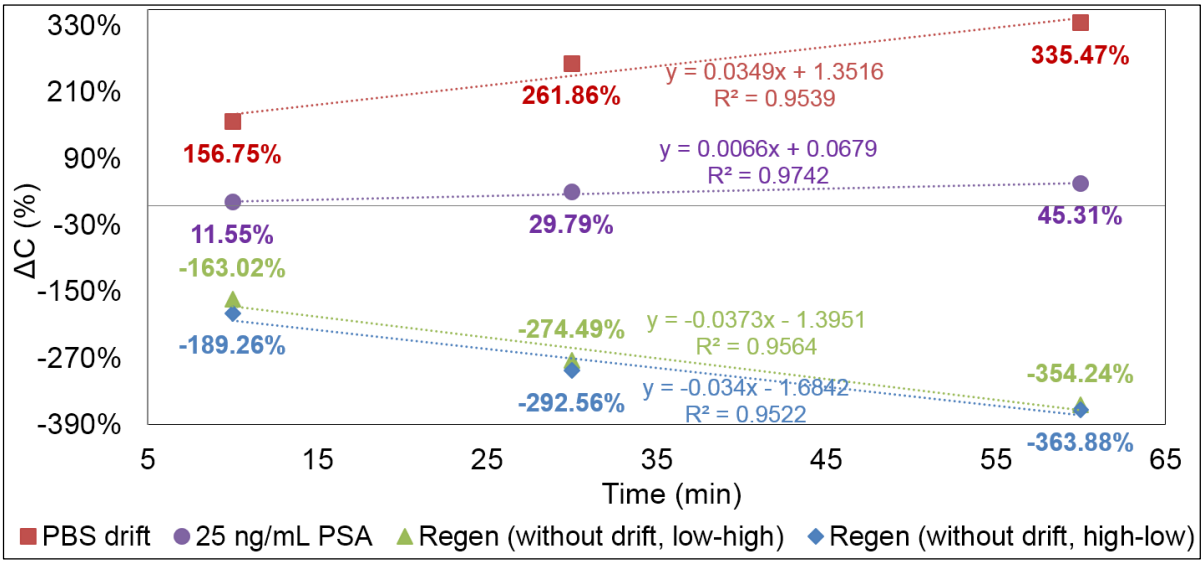


Figure 5.47. Cdl variation for LIG IDE biosensors: drift due to baseline (PBS, repeated measurements of PSA 25 ng/mL) and calibration curves as function of immersion time.

Furthermore, upon prolonged immersion times, the graphene electrodes showed signs of degradation due to swelling of the exfoliated layers. Local delamination of the GO dielectric film from the acetate substrate and porous layers collapse were observed for the rGO electrodes, which can lead to electrode failure, shown in Figure 5.48. As LIG is highly and vertically porous, it was challenging to visualise it with an optical microscope, but the material preserved a rich porosity after

testing. Some displaced flakes were visible towards the edges and some broken pores exposed the beneath thin LIG layer, as presented in Figure 5.49.

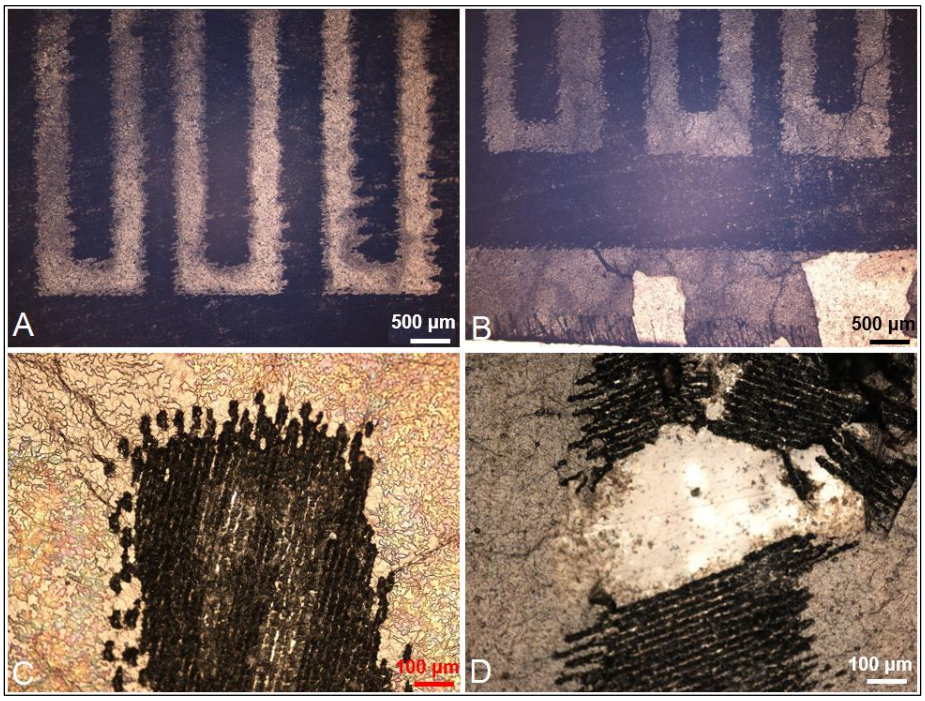


Figure 5.48. Optical images showing defects on rGO IDE structures after impedimetric testing (exposure in testing electrolyte > 3 hr): (A) electrodes edge defects and local delamination, 20x; (B) GO film delaminated from the acetate substrate, 20x; (C) discoloration of rGO tracks due to layers swelling and peeling, 100x; (D) broken electrode, 100x magnification.

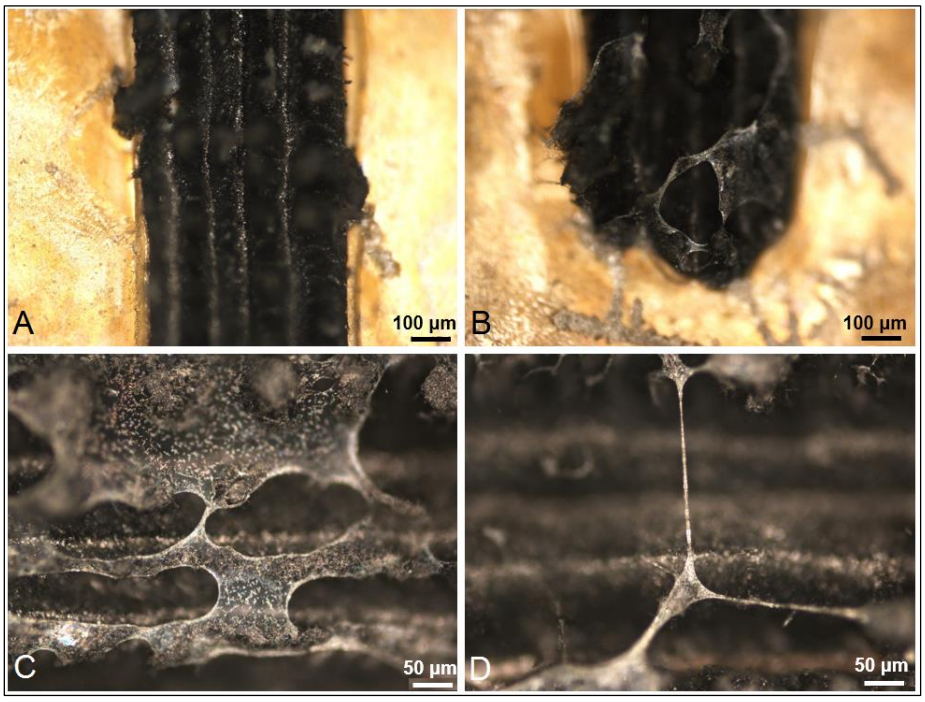


Figure 5.49. Optical images showing defects for LIG IDE after impedimetric testing (exposure in testing electrolyte > 3 hr): (A,B) edge flakes delamination 10x; (C) thin LIG layer with µm-range pores, 200x; (D) collapsed pores revealing the underneath LIG layer, 200x magnification.

## 5.3. Conclusions

The systematic impedance studies of the rGO and LIG-based IDE structures provide a valuable insight in their feasibility as disposable biosensing platforms. While the preliminary calibration curves look promising, the graphene based materials pose two major challenges: limited reproducibility and response instability due to baseline drifting. The results show that the antibody-antigen interaction occurs simultaneously with electrolyte adsorption. This can be ultimately solved by subtracting the baseline drift response. Data processing within PoC testing systems can compensate for these variations. In order to improve the response stability, the rGO and LIG sensors should be immersed in the testing buffer for 30 minutes, respectively 60 minutes prior to any measurements. However, further work is required to investigate the immersion effect on the antibody layer and protein diassociation, as this might not be suitable for PoC applications.

The identification of a suitable equivalent circuit was rather challenging for the two graphene based materials and it was developed from a basic R-CPE circuit, similarly to the gold IDE sensor assessed in section 4.3.1, but additional circuit elements were needed to account for the complex porosity of the low-cost, defective graphene. The LightScribe reduction method introduces device variability during engraving / patterning based on disc location. Also, the power setting for the carbonization of the PI tape varies depending on the laser warming cycle and therefore, its power stabilization time. Therefore, the laser-based reduction methods for large-scale graphene synthesis must be optimally tuned and should be independent of the electrode design. LIG's vertical and asymmetric porosity led to local variability in terms of its physical properties. During experiments, LIG was observed to be highly hydrophobic. Long-time immersion in aqueous solutions (> 2 h) can improve its wettability, which was noticed during baseline drifting test, with the disadvantage of delamination of the top porous layers.

rGO exhibited improved response stability compared to LIG, but due to its poor manufacturing repeatability, the impedance response required careful analysis as data trends were not evident for all samples. The IDE structures were selected from the same disc area and pattern continuity was confirmed prior to testing. Batch testing involves parallel measurements and longer electrodes storage in PBS, which is undesirable for these graphene based materials due to their morphology.

Finally, the findings of this study are rather intriguing as the successful functionalization and PSA capture on rGO and LIG substrates was confirmed by XPS

and Raman spectroscopy. The presented preliminary calibration curves justify further experimental work; by optimising the blocking layer, one can improve the goodness of fit ($R^2$) and minimise the non-specific response. However, the uncontrolled morphology of these laser engraved graphene materials represents a limiting factor in terms of their applicability.

# Chapter 6. Electroless nickel deposition for graphene contacting

Electroless deposition represents an accessible and scalable method for nickel deposition on a variety of substrates. This technology is well established for printed circuit boards (PCB) surface plating due to its repeatability, strong and uniform coating. In this chapter, the electroless nickel deposition was assessed as a low-cost and low temperature (< 100 °C) alternative for metal contacting on graphene materials. Using selective surface treatment, it was aimed to be implemented in the rapid and inexpensive manufacturing process to deliver functional graphene-based sensing structures. Due to the chemical complexity of the electroless deposition method, a basic statistical model was used to tune the pH and the temperature of the nickel bath for CVD transferred single-layer graphene (SLG). Raman spectroscopy, XPS and EDX measurements were performed to investigate the nickel-graphene interface. The study was further extended to demonstrate technique's compatibility with other graphene based materials, such as rGO.

## 6.1. Introduction: electroless nickel deposition

Discovered as early as 1845 by Wurtz, the electroless nickel plating did not represent a valuable research topic until a century later, when it was officially reported by Brenner and Riddell [404]. As its name suggests, the electroless plating is an autonomous, self-catalytic process [405]. The first deposited metal layer(s) perpetuates the catalytic action, allowing for thicker and more coherent coatings [406] compared to its electrochemical counterpart i.e. electroplating. The electroless nickel deposition reaction is based on the reduction of metallic ions from an aqueous metal salt-based solution [404], for example a hypophosphite:

$$\mathrm{Ni}^{2+} + (\mathrm{H_2PO_2})^- + \mathrm{H_2O} \rightarrow \mathrm{Ni} + 2\mathrm{H}^+ + \mathrm{H(HPO_3)}^- \qquad (6\text{-}1)$$

As with any chemical process, the method is sensitive to experimental conditions. The plating rate and metal coating purity have been shown to be highly dependent on the nickel bath's pH and temperature [407], but also on the concentration ratio between the reducing agent (e.g. phosphorous, boron or hydrazine-based [408]) and the metal salt (e.g. nickel sulphate, nickel chloride [404]). Achieving the right balance between pH and temperature for the substrate to-be-coated is essential to control the nickel coating properties. While a too high temperature of the nickel based plating bath can lead to decomposition, the temperature has to be high enough to ensure a good deposition rate, as summarised in Table 6-1. The pH controls the

reducing agent solubility into the nickel bath, such as phosphorous or boron, but also the deposition rate and the roughness of the nickel coating.

Table 6-1. Summary of the consulted electroless nickel literature, where pH: low < 5, high > 9; temperature: low < 40°C, high > 85°C [409][410][411][412][413][414].

| **pH** | | **Temperature** | |
|---|---|---|---|
| ***High*** | ***Low*** | ***High*** | ***Low*** |
| Less P, decrease in Ni conc. | Increased P content as more soluble | Unstable bath, decomposition | Possibly no plating |
| Rougher surface | Matte finish, smooth | High deposition rate | Increased P content |
| High deposition rate | Low deposition rate | Thicker coatings | Thin films |
| Decreased bath stability | Dark deposits | - | Dark deposits |

The main advantages of the electroless nickel plating are its low-cost and accessibility, requiring basic laboratory equipment presented in Figure 6.1. Electroless nickel plating can be achieved in single or multi-steps, usually involving [415][416]:

- Surface cleaning
- One or two-step surface activation using tin and palladium-based solutions
- Electroless nickel growth.

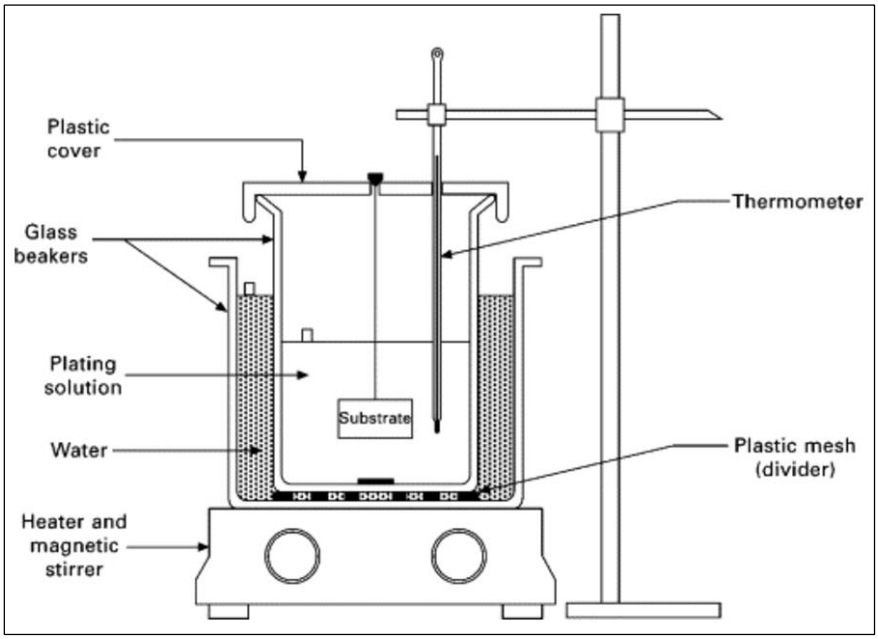


Figure 6.1. Laboratory equipment required for electroless nickel deposition [31].

The process is compatible with a variety of substrates, with some exemplified in Table 6-2. However, a search of the literature revealed limited studies on electroless nickel film deposition and a main focus on (nano)composites and coatings [417]. In

industrial applications, the control of the electroless nickel bath parameters is statistically approached. Muraliraja and Elansezhian [418] investigated the electroless nickel parameters' in order to allow for the reusability of the nickel bath for mild steel coating. Using the Taguchi statistic method for robust design and optimization, the authors identified a required optimum pH of 9 and a 50% increase in the reducing agent.

Table 6-2. Various substrates and deposition conditions for electroless nickel method.

| Substrate | pH | Temp [°C] | Metal source | Metal [g/L] | R.A [g/L] |
|---|---|---|---|---|---|
| carbon nanotubes (CNT) [409] | - | 80 | $NiCl_2$ | 21 | 24 |
| plastic [404] | 8-9 | 30-40 | $NiCl_2$ | 21 | 24 |
| glass [419] | 9.8 | 85 | $NiSO_4$ | 40 | 20 |
| carbon nanofibers [412] | 10 | 90 | $NiSO_4$ | 40 | 20 |
| oxidised CNT [413] | 8.25 | 25 | $NiSO_4$, $NiCl_2$ | 30, 10 | 100 |

With a direct application in IC/MEMS industry, electroless nickel deposition provides opportunities for lower temperature (below 100°C) metallization compared to other conventional techniques, such as thermal evaporation [420]. Aiming for low contact resistance on graphene, it is ideal to match the work function of the metal and the substrate. Nickel is a suitable candidate for contacting graphene, with a work function of 5.15 eV [407], closest to graphene's i.e. 4.89-5.16 eV [421], and followed by gold (Au, 5.1 eV) and cobalt (Co, 5.0 eV).

A brief, preliminary study in our research group showed the possibility of applying the electroless coating technique onto CVD multi-layer graphene [422]. It is believed that by tuning the electroless nickel bath parameters based on substrate properties, the properties of the nickel film can be optimized as per targeted application.

## 6.2. Methodology

### 6.2.1 *Materials*

Chemicals (>99% purity) were purchased from Sigma Aldrich, UK unless otherwise stated. Based on preliminary trials, the concentrations for the electroless nickel process were: 80 g/L tin chloride ($SnCl_2$) in 50ml/L hydrochloric acid (HCl, 37%) in deionised water; 0.15 g/L palladium chloride ($PdCl_2$) in 2 ml/L hydrochloric acid (HCl, 37%) in deionised water; 35g/L nickel sulfate ($NiSO_4$); 50g/L ammonium chloride ($NH_4Cl$); 15g/L sodium hypophosphite ($NaPO_2H_2$); 50g/L sodium citrate ($Na_3C_6H_5O_7$).

Single-layer CVD grown graphene transferred on $SiO_2$ was purchased from Graphenea, Spain. Graphene oxide was purchased from Graphene Supermarket (6.2 g/L) and reduced using the LightScribe method to obtain rGO (see section 3.1.2.1). The micro-fabrication procedures for patterning the CVD graphene and nickel etching were carried out using the clean room facilities in the School of Electrical and Electronics Engineering at Newcastle University. The negative photoresist AZ 5214E and developer AZ 326MIF were supplied by AZ Electronic Materials, Germany.

### 6.2.2 *Characterisation*

The electrical measurements on CVD graphene were performed using a four-probe Agilent B1500 system in the Characterisation Lab, School of Electrical and Electronics Engineering, Newcastle University. A Fluke digital multimeter was used for two-point resistance measurements on rGO.

The deposited nickel layer and graphene surface were imaged using scanning electron/energy dispersive microscopy (SEM-EDX, Hitachi TM3030). High-resolution images were acquired using a XL30 ESEM (Environmental Scanning Electron Microscopy) system at the Electron Microscopy Unit, respectively Zeiss Orion NanoFab HIM (Hellium Ion Microscope) at NEXUS (National EPSRC XPS User's Service), Newcastle University. The surface roughness of the deposited nickel film was measured using a XE-150 AFM (Atomic Force Miscroscopy, Park Systems) in non-contact mode.

Qualitative nickel coating and graphene measurements were completed using various techniques. X-ray photoelectron spectroscopy (XPS) analysis was performed with a K-Alpha XPS, Thermo Scientific, East Grinstead at NEXUS. The Raman spectra was acquired using a Horiba Jobin Yvon HR800 Raman spectrometer with a 514 nm excitation laser at 10% power. The Raman system was calibrated prior to measurements using Silicon peak position definition (521 nm). XRD (X-ray powder diffraction) measurements were performed using a Bruker D8 ADVANCE instrument with a Cu source ($\lambda$= 0.154 nm).

### 6.2.3 *Experimental*

Figure 6.2 is a schematic representation of the experimental steps for conventional electroless nickel deposition method described in section 6.1 involving: sensitization, activation and nickel deposition. The sequence, immersion times and nickel bath conditions (pH, temperature) have been tuned for the CVD single-layer

graphene on $SiO_2$ substrate and rGO on acetate substrate (Lightscribe), as explained in sections 6.2.3.1 and 6.2.3.2.

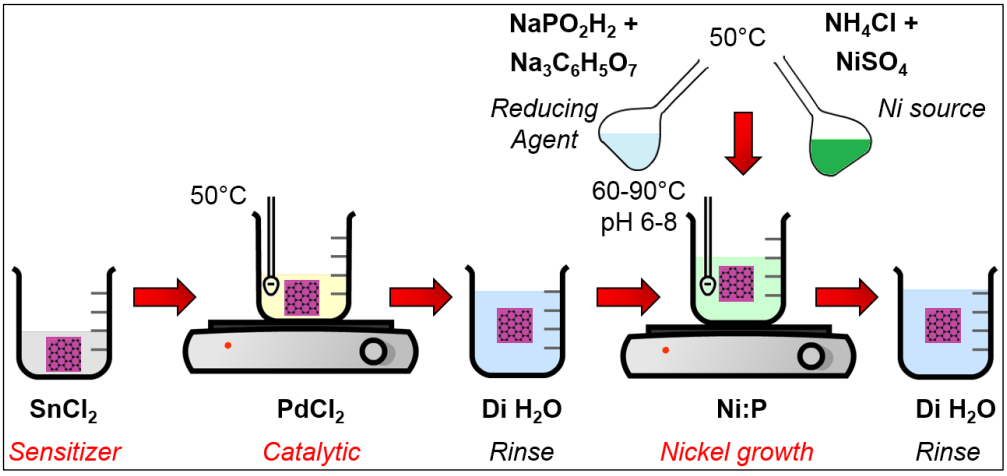


Figure 6.2. The experimental setup for the electroless nickel deposition on graphene substrates.

### *6.2.3.1 Electroless nickel deposition on CVD single-layer graphene*

The experimental steps undertaken for electroless nickel deposition on CVD graphene are detailed below. The employed activation and nickel bath concentrations were as specified in section 6.2.3.

1. The CVD graphene samples were briefly cleaned by dipping in acetone, followed by isopropanol and then blow dried with nitrogen. Prior to nickel deposition, the samples were dehydrated in the oven at 100°C for 10 minutes and then allowed to cool down at room temperature.

2. The graphene substrates were patterned using a photolithographic technique (reverse patterning). The photoresist was spun coated for 45 seconds at 3,000 rpm. The samples were then soft baked at 90°C for 10 minutes to dry the photoresist film, then allowed to cool down while protected from light.

3. The mask presented in Figure 6.3 was loaded on the mask aligner and the samples were exposed to UV (Karl Suss MJB-3, proximity mode) for 12 seconds. Post exposure, the samples were baked at 100°C for 10 minutes.

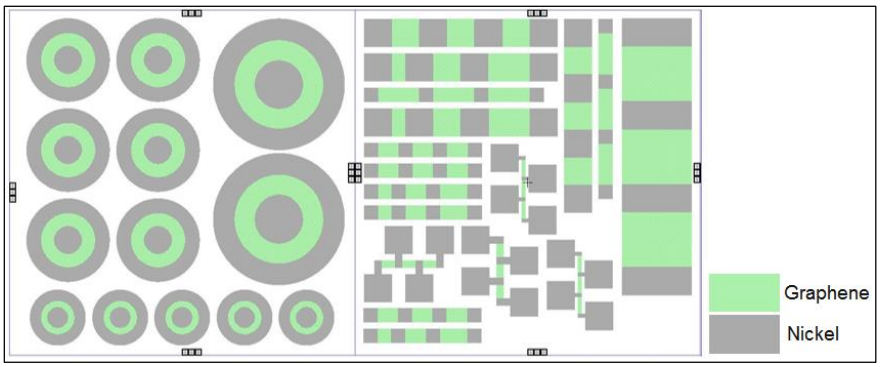


Figure 6.3. Mask design (L-Edit) used for graphene photolithography pattern definition on CVD SLG.

4. A second (blank) UV exposure was performed for 45 seconds, followed by selective photoresist etching by immersion in photoresist developer for 18 seconds. Finally, the samples were washed in deionised water and blow dried with nitrogen.
Upon the completion of step 4, the CVD graphene was ready for selective nickel deposition. The employed activation and nickel bath concentrations were as specified in Experimental.

5. The patterned graphene samples were immersed in the sensitizer solution ($SnCl_2$) at room temperature for 3 minutes, followed by a brief rinsing step in deionised water.

6. The samples were immersed in the activating solution ($PdCl_2$) at 50°C for 5 minutes under stirring, then rinsed twice in deionised water.

7. The freshly prepared nickel based bath was obtained by mixing the previously prepared reducing agent (hypophosphite) and metal (nickel sulphate) solutions in 1:1 ratio. The pH was adjusted using ammonium hydroxide and the bath was slowly heated using a hot plate. Depending on the deposition rate, the sample was left in the nickel bath for sufficient time to acquire a nickel coating on the surface. Then the samples were removed, carefully rinsed in warm deionised water (35°C) and slowly dried in the oven at 50°C for 15 minutes.

8. A final lift-off step in acetone was undertaken to release the selectively deposited nickel contacts on the graphene substrates.

#### *6.2.3.2 Electroless nickel deposition on rGO*

The experimental steps undertaken for electroless nickel deposition on rGO are sequentially described below. The employed activation and nickel bath concentrations were as specified in section 6.2.3.

1. The rGO samples were immersed in the activating solution ($PdCl_2$) at 50°C for at least 30 seconds, then they were rinsed in deionised water.

2. The samples were quickly immersed in the nickel-based bath (pH 7.4 ± 0.1, 68 ± 2°C) for maximum 1 minute, followed by a rinsing step in deionised water.

3. A brief second activation step was undertaken by immersing the samples in the $PdCl_2$ solution for 10 seconds, followed by a rinsing step.

4. Nickel was allowed to deposit on the rGO surface by immersion in the nickel bath for 1-3 minutes.

5. The samples were finally dried the oven at 55°C for 10 minutes.

Figure 6.4 shows the arrangement used to control the length of the features and extract the electroless nickel contact resistance on rGO. Rectangular patterns of varying track lengths were attached to an acetate substrate and simultaneously immersed for electroless nickel deposition.

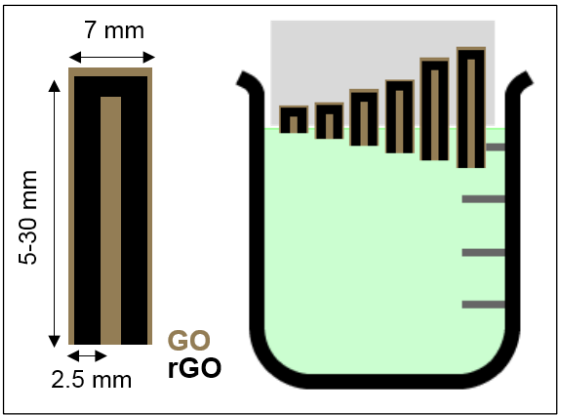


Figure 6.4. The arrangement of rGO samples for electroless nickel deposition.

## 6.3. Results and discussion

### 6.3.1 *Electroless nickel deposition on CVD single-layer graphene*

#### *6.3.1.1 The assessment of the compatibility of the electroless nickel process with CVD graphene*

Firstly, the electroless nickel deposition was assessed on non-patterned, transferred CVD graphene surfaces and tuned to ensure the method's compatibility with the substrate. The tin-senzitisation step ($SnCl_2$) was necessary due to the observed poor nickel layer coverage for one-step i.e. Pd activation-only process. For this assessment, adhesive tape was used to define and expose a "window" in the graphene surface. Figure 6.5 shows increased nickel coverage and uniformity for the sensitized sample.

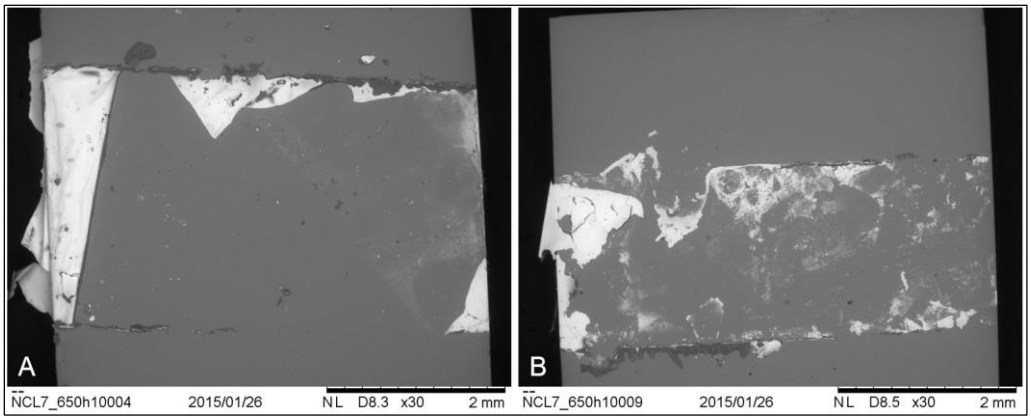


Figure 6.5. SEM images of the electroless nickel deposited on CVD graphene, after: (A) activation step only; (B) sensitization and activation step, x300 magnification, 2 mm scale bar.

The nickel film present on the edges of defined area for the non-sensitised sample (A) remained from the tape and silicon face, while upon sensitization, nickel deposited directly on the graphene surface. It was observed that the electroless nickel easily deposits on the tape due to its smooth surface and high hydrophilicity. A 3-minute sensitizer immersion time was adopted taking into account the minimum contact angle reported by Wei and Roper [419].

Subsequently, the activation time was varied between 1, 5 and 10 minutes, with the outcome presented in Figure 6.6. While 1 minute was insufficient for a uniform coating, 10-minute activation led to a fast deposition resulting in a thick coating which delaminated from the surface due to surface stresses. Hence, it was opted for 5-minute activation time.

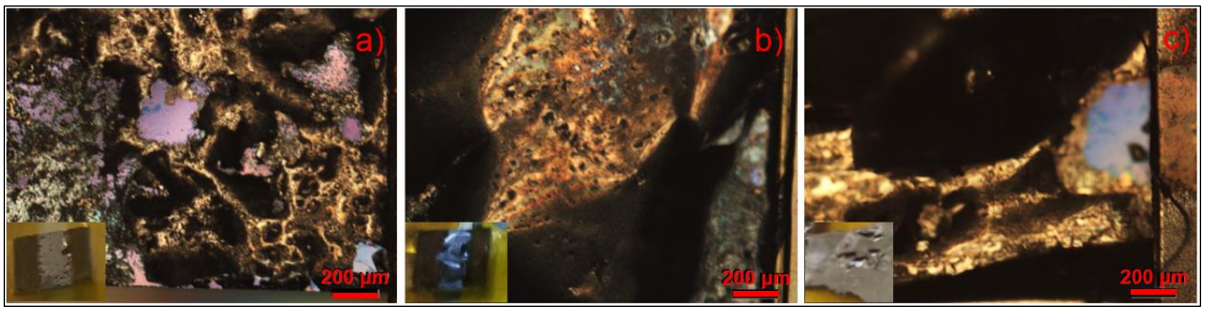


Figure 6.6. Optical images (50x magnification, 200 µm scale bar) of the electroless nickel film deposited on CVD graphene after activation step of: (a) 1 minute; (b) 5 minute; (c) 10 minute; inset: samples image.

In these conditions, i.e. 3-minute sensitization and 5-minute activation steps, the graphene surface preparation was successful at facilitating the electroless nickel deposition in just over 3 minutes. In order to exemplify the complexity of the electroless chemistry, Figure 6.7 presents the aspect of the coated graphene from one of the early experiments, with no adaptation of the chemical bath parameters.

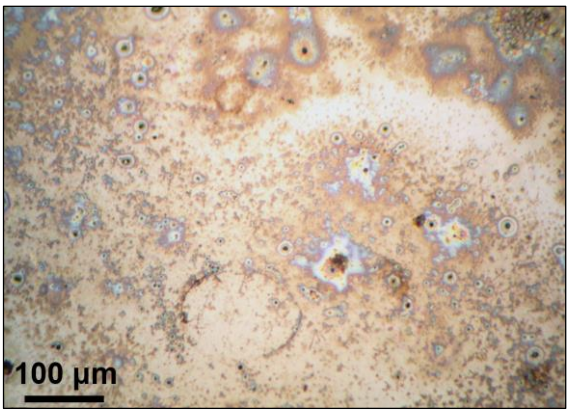


Figure 6.7. Optical image (10x magnification, 100 µm scale bar) of electroless deposited nickel on CVD SLG at 80°C, pH 5.

The experiment was performed in standard literature reported conditions with an acidic nickel bath (pH ≈ 5) and a metal-reducing agent ratio of 1:1. One can notice surface aspect variability and reduced smoothness, as well as the presence of some dark islands and dullness. According to Aleksinas [423], this can be caused by low pH and / or temperature, some level of organic contamination and low nickel or reducing agent concentration. This result clearly indicated the need for parameter optimisation, particularly for novel surfaces such as graphene.

#### *6.3.1.2 Integration of the electroless nickel process with microfabrication for contact deposition on CVD graphene*

In order to define the electrodes, a lift-off procedure was adopted using photolithography. The mask was defined on SLG prior to sensitization, after a mild chemical cleaning step. Lift-off was attempted either for both after activation or deposition as it was essential to understand its impact on the nickel growth. When performed after activation, the electroless deposition process was interrupted. The acetone lift-off step removed the Sn / Pd molecular layer, hence inhibiting the nickel growth. Few traces of nickel remained on the surface, as shown in Figure 6.8A. However, when performed after metallization, the lift-off revealed clear nickel patterns (Figure 6.8B), but issues of adhesion and consistency were further acknowledged.

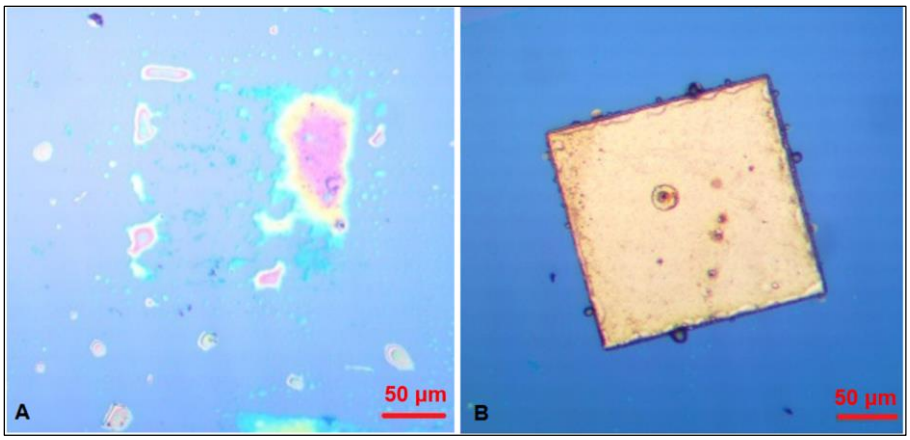


Figure 6.8. Lift-off step effect on electroless nickel deposition on SLG surface: (A) after sensitization; (B) after nickel deposition, x200 magnification, 50 µm scale bar.

The electroless nickel plating process was finally integrated with mask definition, presented in Figure 6.9 [424].

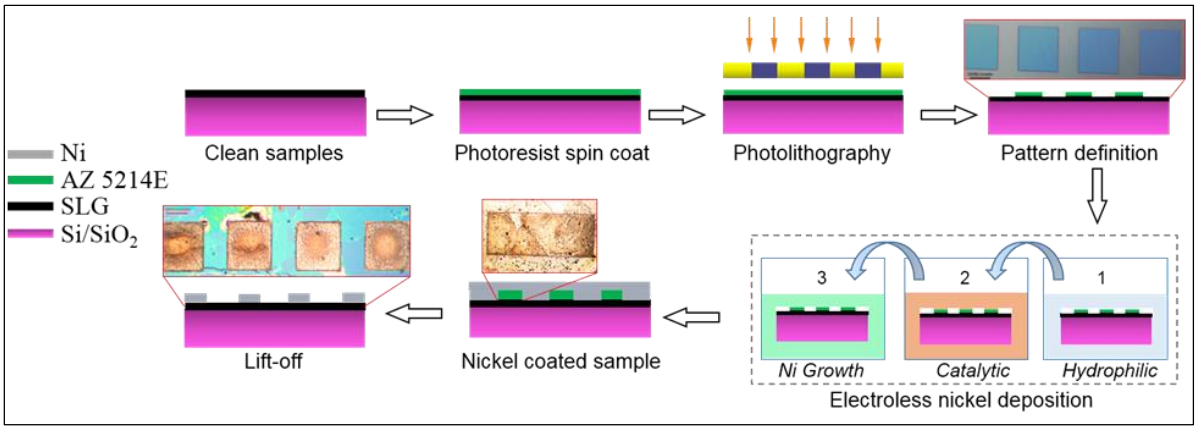


Figure 6.9. Electroless nickel deposition method on patterned CVD SLG substrates; inset: microscope images, x100 magnification, 100 µm scale bar [424].

As the thickness of the nickel film is time dependent, it was essential to ensure a thick photoresist coating to facilitate the lift-off step. Following the protocol presented in 6.2.3.1, the photoresist thickness was 1.5 ± 0.2 µm. Moreover, the graphene surface was inspected at different stages of the electroless nickel deposition. Colloidal particles were visible under the optical microscope after the sensitization step, while a smoother aspect could be noticed for the catalysed surface after the activation step. XPS analysis confirmed the presence of Sn and Pd species on the two samples (see Figure 6.10). The overall XPS survey showed an increase in the oxygen species upon sensitization and activation, indicative of its improved surface hydrophilicity. This is expected to enhance the nickel deposition rate and the surface coverage.

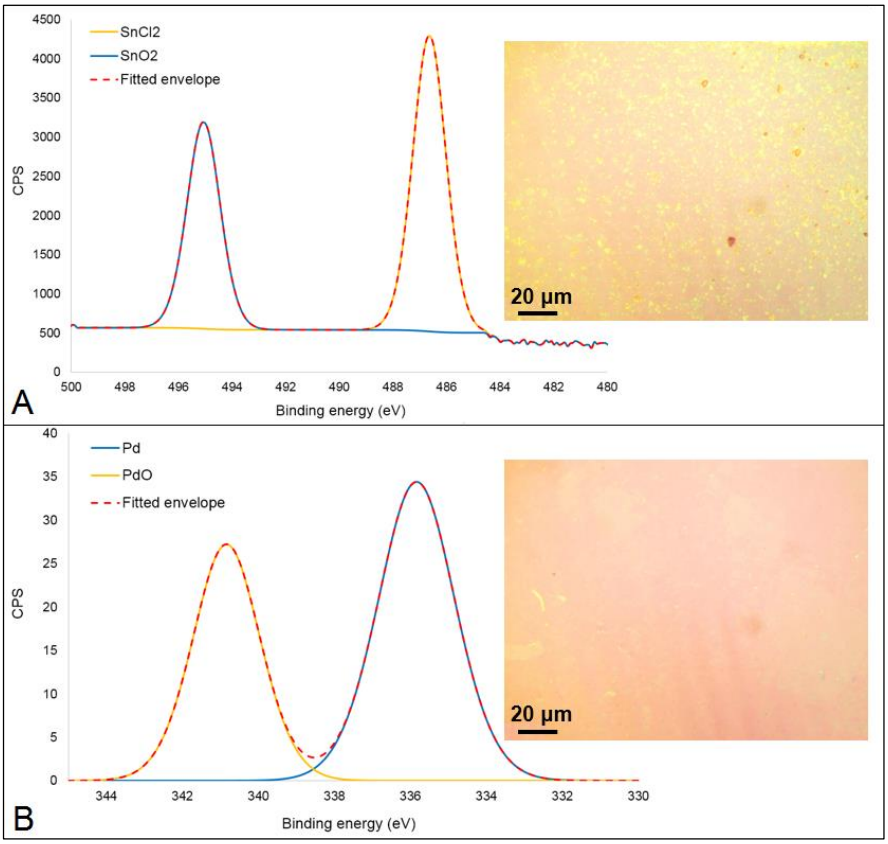


Figure 6.10. XPS spectrum for CVD SLG after: (A) sensitization step, Sn 3d; (B) subsequent activation step, Pd 3d. Inset: optical image of the CVD graphene samples, 200x magnification, 20µm scale bar, image adapted from [424].

#### *6.3.1.3 Statistical modelling and prediction of suitable electroless nickel bath parameters for low contact resistance on CVD graphene*

A basic statistical model was adopted in order to determine the suitable metallization conditions for the CVD single-layer graphene surface. The most and least extreme pH and temperature conditions (*i.e.* 60-90°C, pH 6-8) were chosen based on previous experimental observations and literature reported studies summarised in Table 6-1 and Table 6-2. The main parameters of interest are the pH and temperature, hence a two-factor multiple-level experimental design and optimisation approach was adopted, aiming to minimise the nickel contact resistance on graphene. The initial pH of the nickel bath was in the range 4.8 - 5. In practice, a pH increase of up to 7 was relatively easy to achieve and to maintain, but it was challenging to reach higher pH values. The pH is prone to drop, as 3 moles of H+ are produced for every mole of nickel ion deposited [416] and its concentration increases further with increasing temperature.

The nickel coating was continuous and uniform prior to the lift-off step for all samples, however the adhesion of metals onto graphene is problematic due to its inert

characteristic, addressed in section 2.7. Figure 6.11 reveals the defined nickel contacts for the selected bath conditions on single-layer graphene. Most of the samples, except for GC1, exhibited poor adhesion to the graphene surface with GC2 and GC3 demonstrating a discontinuous coating while on GC4 the deposited nickel film peeled to form scrolls.

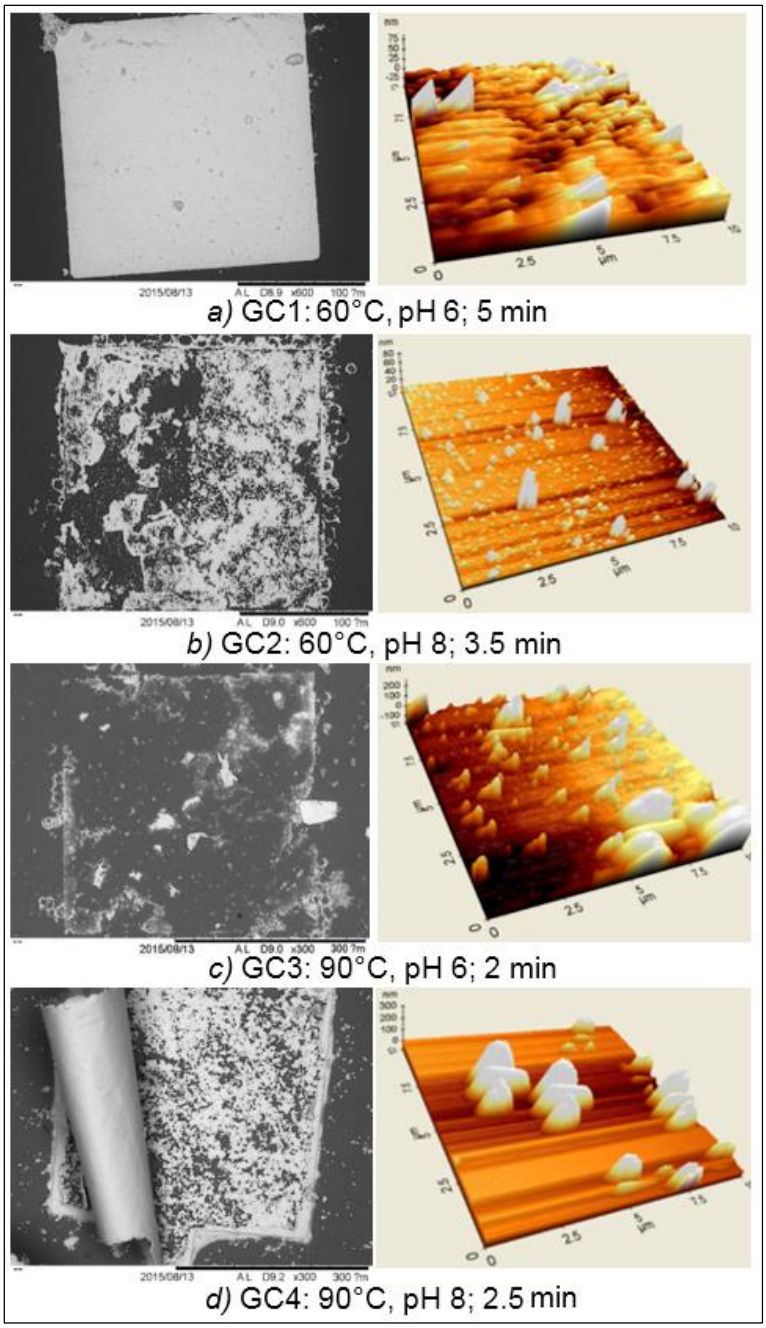


Figure 6.11. Electroless nickel deposition on CVD SLG in conditions of varied bath parameters and nickel bath immersion time (GC1-GC3). Left: SEM image of contact onto graphene (left); (a, b): 100 µm scale bar; (c, d): 300 µm scale bar; Right: AFM 3D surface image of the contact over 10 µm x 10 µm nickel area [424].

Moreover, the comparative Ni 2p XPS spectra of the four samples (GC1-GC4) is presented in Figure 6.12. The increase in the pH of the nickel bath caused an

increase in the oxide composition, at the cost of metal purity and adhesion. Similarities between the nickel peaks of the fitted spectra were noticed, with a slight variation in the nature and density of nickel chemical bonds, for example, sulphate bonds ($NiSO_4$) were observed for higher pH values.

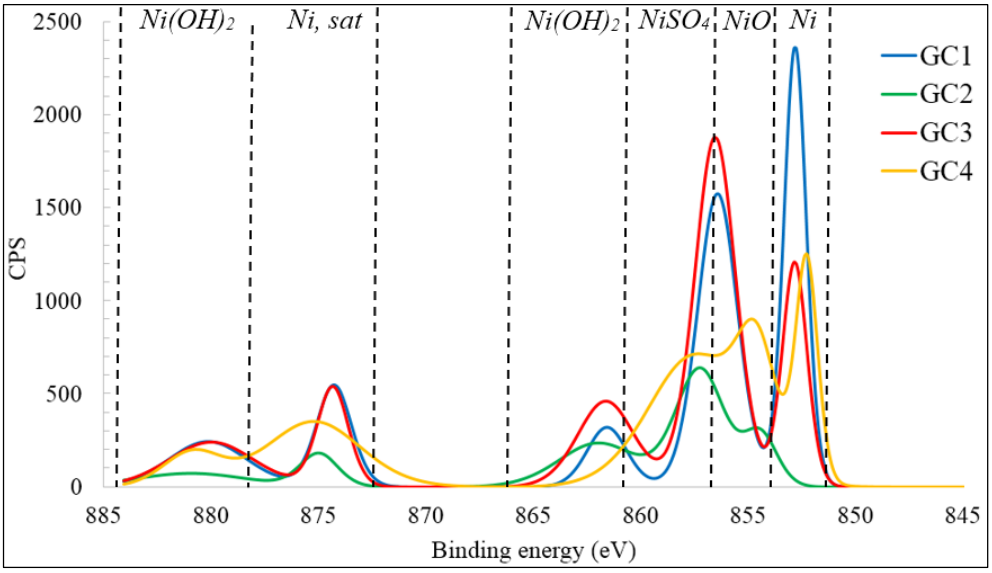


Figure 6.12. Ni 2p XPS spectra for samples GC1-GC4 with subtracted background signal and identified Ni-based regions [424].

Targeting a low contact resistance, the aspects of interest with regards to the nickel film are: metal purity, interface adhesion and surface smoothness. For MEMS applications, the thickness of the deposited layer must be controllable, which should be achievable based on the characteristic linearity of the electroless process once the nickel film continuity was achieved [416].

EDX and AFM measurements were used to quantify the atomic concentrations, coverage and surface roughness, presented in Table 6-3. In the case of poorly adhered contacts, the remaining nickel areas or film flakes were selected for analysis. The surface coverage was estimated by subtracting the atomic composition of the silicon due to the substrate and limited EDX resolution.

Table 6-3. EDX composition analysis for the electroless deposited nickel film composition on CVD SLG in various bath conditions (GC1-GC4 from top to bottom) [424].

| Temp [°C] | pH | Ni [at %] | P [at %] | Ni:P | C [at %] | Si [at %] | $O_2$ [at %] | rms [nm] | Coverage [%] |
|---|---|---|---|---|---|---|---|---|---|
| 60 | 6.0 | 73.5 | 14.9 | 4.9 | 3.3 | 5.6 | 2.4 | 5.1 | 94.4 |
| 60 | 8.0 | 2.6 | 0.3 | 8.9 | 0 | 63.2 | 33.9 | 2.3 | 36.8 |
| 90 | 6.0 | 85.4 | 12.6 | 6.8 | 0 | 0.5 | 0.1 | 52.5 | 99.5 |
| 90 | 8.0 | 32.2 | 5.2 | 6.2 | 8.2 | 39.6 | 14.8 | 17.5 | 60.5 |

Furthermore, the data was statistically analysed using a customized multiple response surface design in Minitab 17. The contour plots from Figure 6.13 indicate that the nickel film purity is highly dependent on the pH of the electroless nickel bath (Pearson correlation coefficient -0.897). The temperature is more critical for the nickel film surface roughness (Pearson correlation coefficient 0.669). The response surface methodology is a statistical optimization method that explores the relationships between the input variables and response(s) i.e. performance measures of interest. In order to do this, first or second-order models are used [425], depending on the level of interaction between variables. The response surface equations for each variable of interest are satisfactory, with $R^2$ - goodness of fit of the model - above 80%:

- $\text{Ni (at \%)} = 358 - 1.02 \cdot \text{Temp} - 51 \cdot \text{pH} + 0.225 \cdot \text{Temp} \cdot \text{pH}; R^2 = 85.92\%$
- $\text{rms (nm)} = -279 + 4.96 \cdot \text{Temp} + 31.8 \cdot \text{pH} - 0.570 \cdot \text{Temp} \cdot \text{pH}; R^2 = 88.98\%$
- $\text{Ni:P} = -38.1 + 0.507 \cdot \text{Temp} + 6.53 \cdot \text{pH} - 0.0736 \cdot \text{Temp} \cdot \text{pH}; R^2 = 80.35\%$
- $\text{Area cov (\%)} = 362 - 1.46 \cdot \text{Temp} - 46 \cdot \text{pH} + 0.263 \cdot \text{Temp} \cdot \text{pH}; R^2 = 88.95\%$

The pH and temperature were optimized for: maximum nickel purity, high nickel-to-phosphorous ratio, high area coverage and minimum surface roughness, with the statistical solution and predicted results displayed in Figure 6.14. The nickel bath conditions of 66°C and pH 6.6 were identified as statistically suitable for the CVD SLG surface.

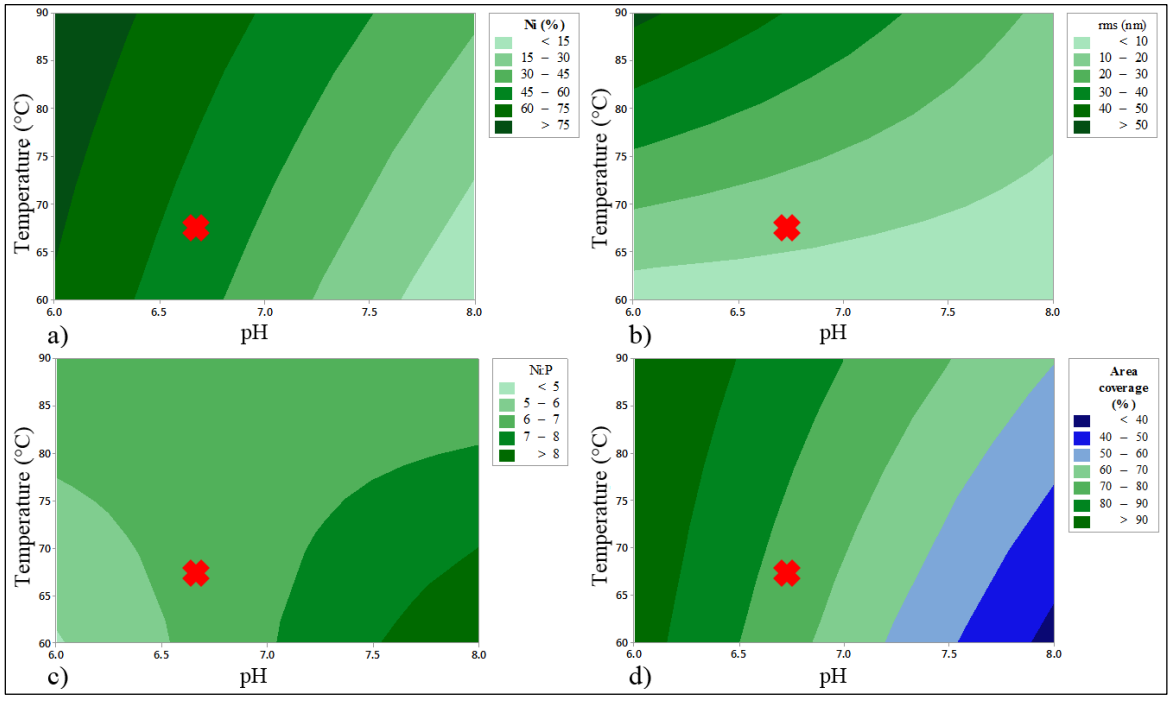


Figure 6.13. Contour plots showing the effect of pH and temperature on: (a) nickel composition; (b) surface roughness; (c) Ni:P ratio; (d) nickel surface coverage; the statistically determined optimum solution marked with a red cross [424].

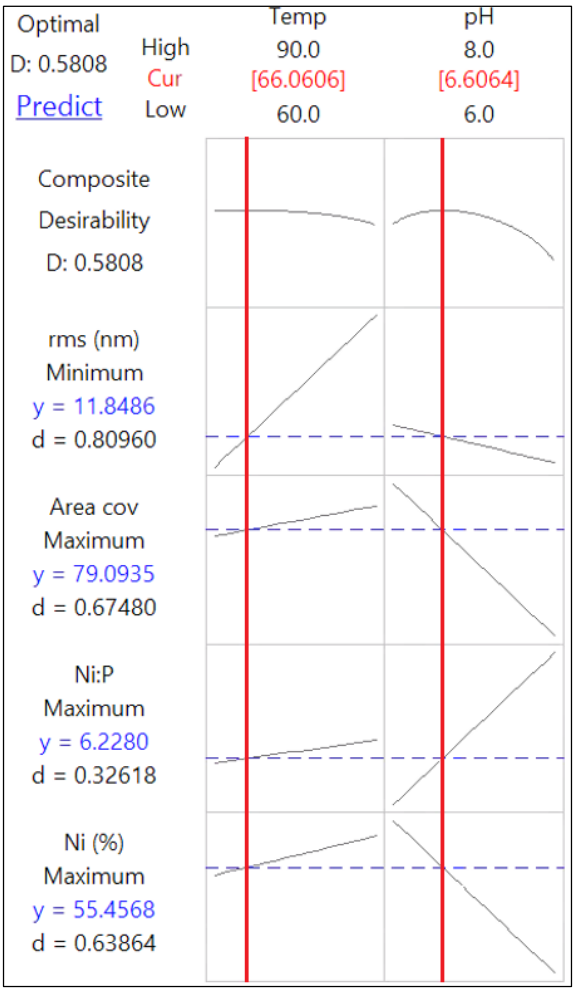


Figure 6.14. The response optimizer result (interactive plot with marked optimum identified solution) for electroless nickel bath parameters on CVD SLG.

## 6.4. Electroless nickel-CVD graphene: properties and interface

### 6.4.1 *Contact resistance of electroless nickel on CVD graphene*

The samples were prepared using the microfabrication protocol described in section 6.3.1.2. The electroless nickel bath was controlled at the optimum identified temperature of 66 ± 1°C and pH of 6.6 ± 0.1, requiring a nickel deposition time of approximately 4 minutes. Poor adhesion of the nickel film on the graphene layer was observed in certain areas under these optimum conditions, with a deposited layer thickness of between 0.4 µm and 0.7 µm. This can be explained by some level of local variability of the graphene surface, as well as the island-based nickel growth [416]. Graphene is known to be highly hydrophobic [426], however faster nickel deposition rates are highly likely on photoresist (observed in practice) and graphene defective areas which have improved chemical wettability [427]. In order to improve the graphene-nickel interface (via adhesion), the samples underwent a rapid annealing treatment at 400°C for 2 minutes.

The electrical properties of the contact i.e. $R_C$ and I-V were measured and extracted using the TLM method (see 2.7), with both linear (LTLM) and circular (CTLM) geometries. Figure 6.15 shows a representative I-V characteristic, confirming the ohmic nature of the contacts with a 32% increase in electrical current after the annealing treatment.

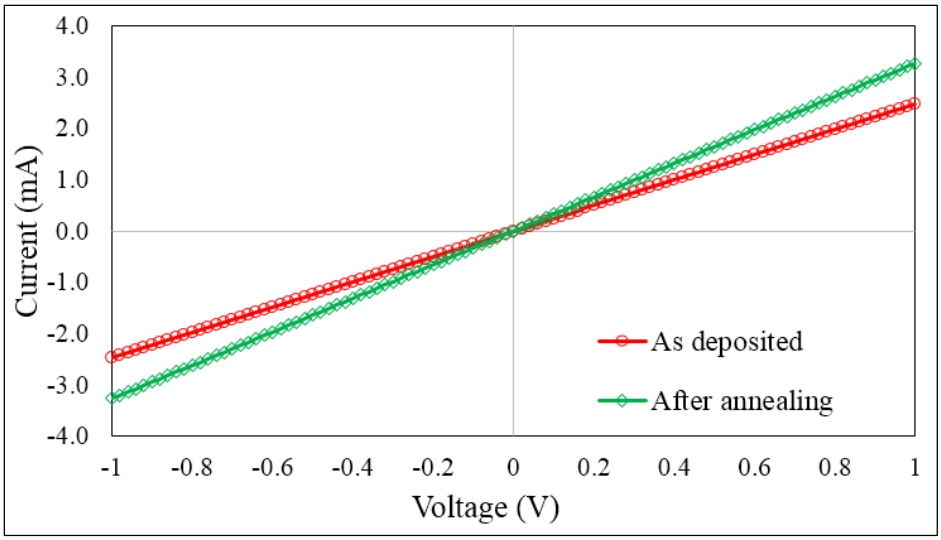


Figure 6.15. Representative I-V characteristic curve for two adjacent contacts before and after annealing [424].

Moreover, Figure 6.16 shows the resistance measurements across different LTLM structures before and after annealing. The average extracted contact resistance is 215 ± 23 Ω and it decreases to 107 ± 9 Ω after the rapid annealing treatment, but changes in the morphology of the nickel layer were observed. Air or gas bubbles cause circular blisters in the nickel film [428][429], especially in the poorly adhered regions (see Figure 6.16B).

The contact resistance can also be characterised by $R_C \cdot W$ as it provides a more accurate [430][256], while allowing for comparison with the literature. Assuming a uniform sheet resistance and using the equation 2-3, the as-deposited contact resistance is 43 ± 5 kΩ·µm and it decreases by just over 50% to 21 ± 2 kΩ·µm post-annealing. This can be attributed to the improvement of the interface between the metal and the graphene layer, associated with the formation of strong covalent bonds between the nickel surface and graphene layer [431], which leads to improved adhesion and lower contact resistance.

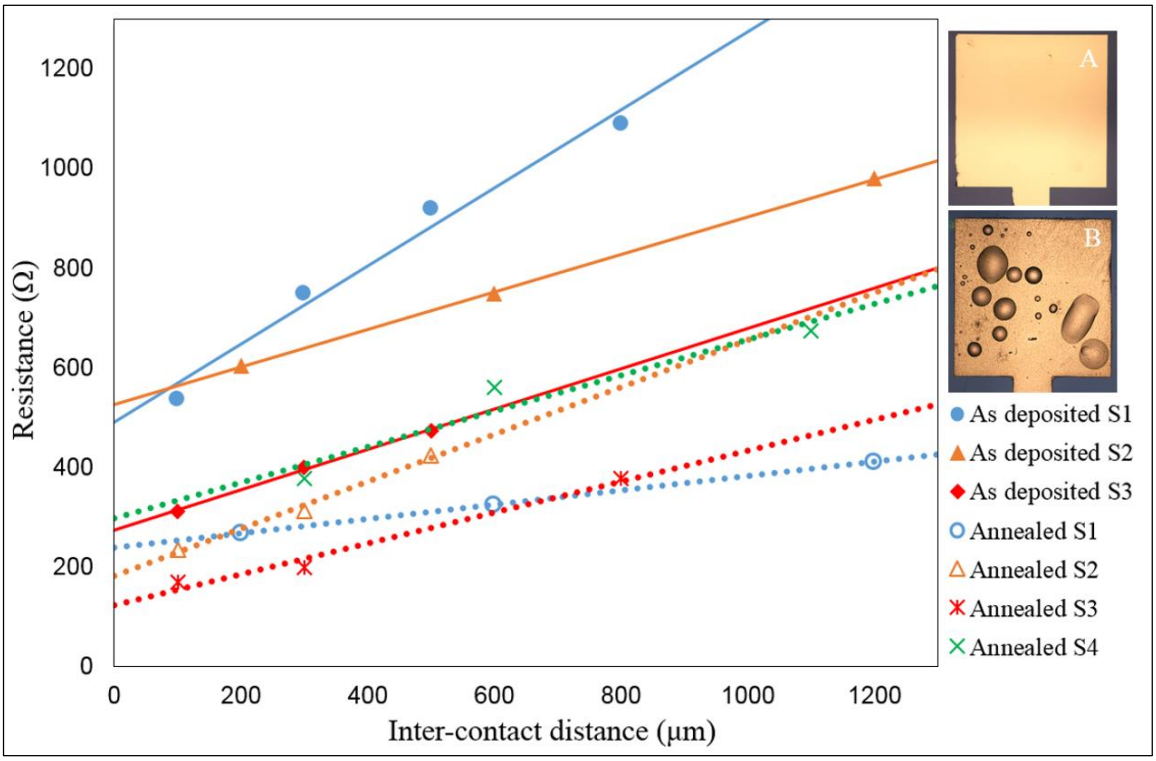


Figure 6.16. Resistance measurements for various inter-contact distances for electroless nickel on graphene [424].

### 6.4.2 *Electroless nickel growth on CVD graphene and annealing treatment effect*

It was observed that the electroless nickel deposition process evolved as discrete particles (nuclei), islands and coalesced islands to form a continuous layer, as presented in Figure 6.17, which is in agreement with the specialty literature [416].

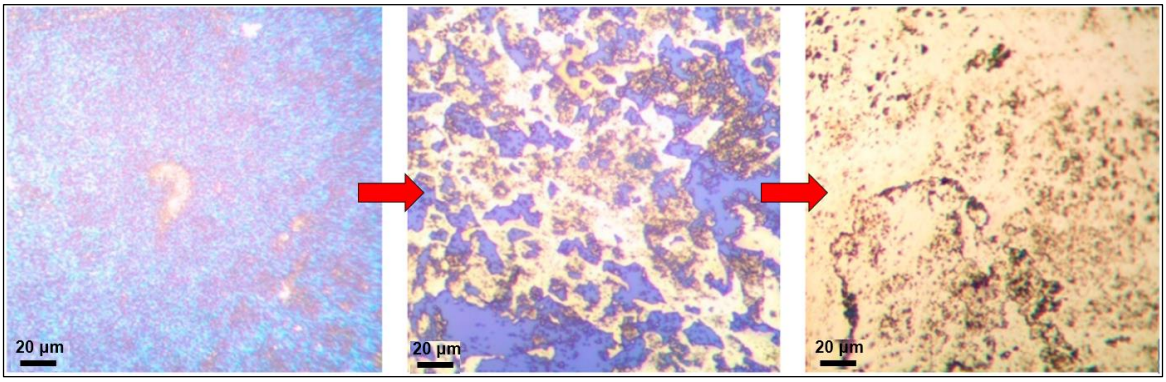


Figure 6.17. Optical images presenting the successive growth stages of electroless nickel growth on CVD SLG, x100 magnification, 20 μm scale bar.

Further studies were performed to investigate the variability in contact efficiency across several patterns. In order to understand the nickel film composition changes during its electroless growth, the process was interrupted at different deposition times and EDX analysis was performed (65-66°C, pH 6.6-6.7). Due to the nature of

electroless deposition process, this analysis had to be performed on different samples. Otherwise, it would have required re-activation (re-immersion in $PdCl_2$). A rectangular pattern was lithographically defined on the CVD single-layer graphene surface samples following the same protocol as described in section 6.2.3.1. The SEM images of the four samples are illustrated in Figure 6.18 and the corresponding EDX measurements are presented in Table 6-4.

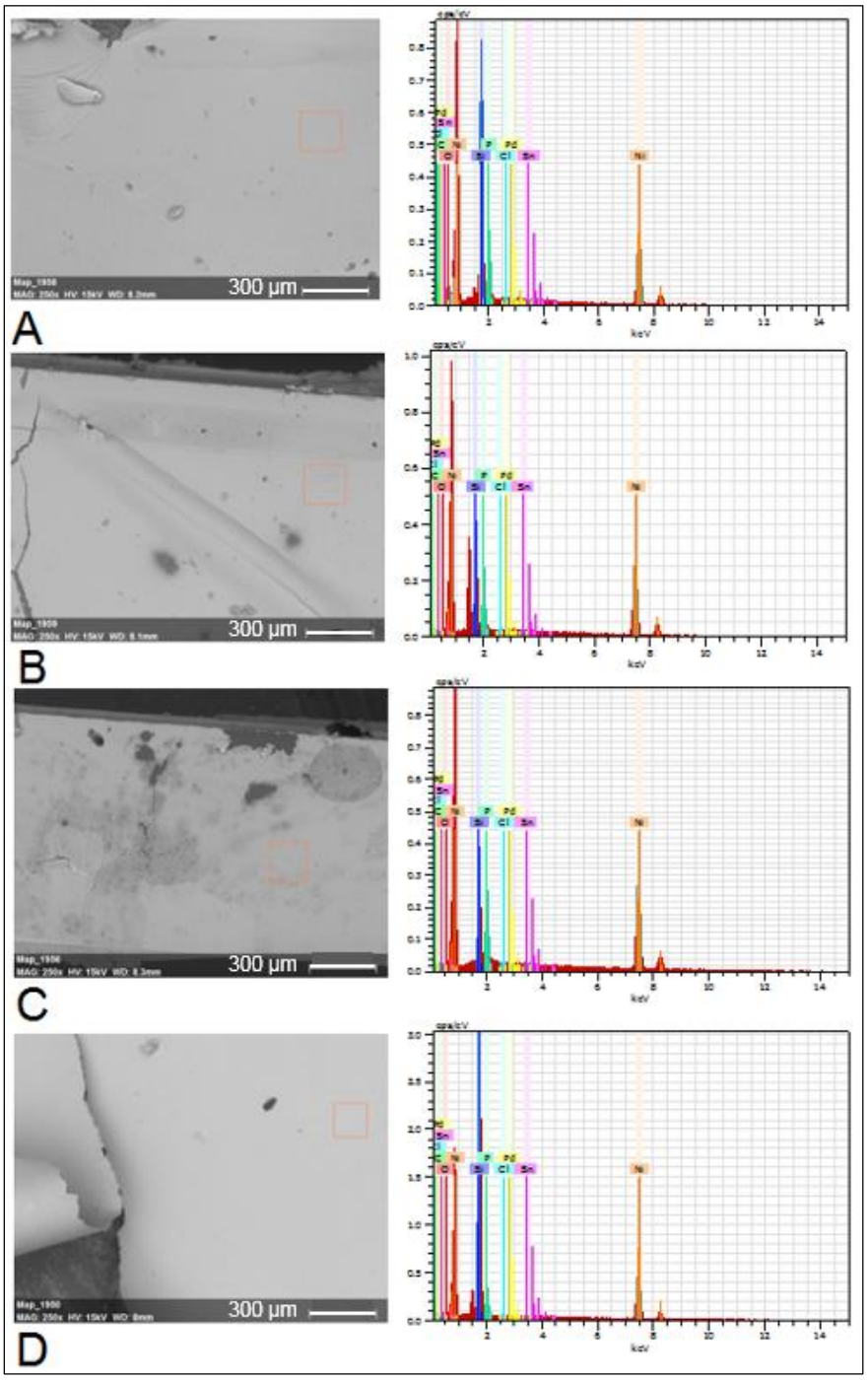


Figure 6.18.Top: SEM (x300 magnification, 300µm scale bar); Bottom: EDX spectra of nickel on CVD SLG (Ni element – orange colour) at different electroless deposition times: (A) 60 seconds; (B) 90 seconds; (C) 120 seconds; (D) 160 seconds.

Table 6-4. EDX composition analysis for the electroless nickel film composition as deposited on CVD SLG, function of the deposition time.

| Time [s] | Ni [at %] | P [at %] | Si+C+O [at %] |
|---|---|---|---|
| 60 | 43 | 8.8 | 47.2 |
| 90 | 44 | 8.9 | 46.5 |
| 120 | 58 | 9.5 | 32.2 |
| 160 | 79.7 | 15.4 | 4.4 |

The average deposition rate was found to be 4.1 ± 0.3 nm/s, with an overall linear behaviour, but interestingly, the deposition rate depended on the area of the surface-to-be-coated. Exponential film thickness growth was observed in the larger exposed graphene areas, confirming the variability in the nickel film thickness also observed for the TLM structures, due not only to local surface properties, but also due to photoresist presence.

Upon annealing, one would expect film stress relaxation and improvement of the nickel film adhesion, enhancing contact's electrical properties. Intrinsic stresses are introduced by the electroless deposition process, while extrinsic stresses are due to thermal effects i.e. film-substrate. Microcrystalline nickel and nickel phosphide ($Ni_3P$) are the common phases for the annealed metal-based composite film and sometimes can lead to some level of P atom diffusion [408].

Hence, XRD measurements were taken to evaluate the crystallinity of the Ni-P layer (see Figure 6.19). A sharp peak was identified at 44.5° for both as-deposited and annealed nickel, confirming that the annealing treatment drives the complete nickel crystallization with (111) texture. The peak of the heat treated nickel film on graphene was two orders of magnitude higher compared to the as-deposited nickel film, but it is broader, being suggestive of the presence of amorphous nickel such as $Ni_3P$, phase obtained after the complete crystallization of the alloy [432].

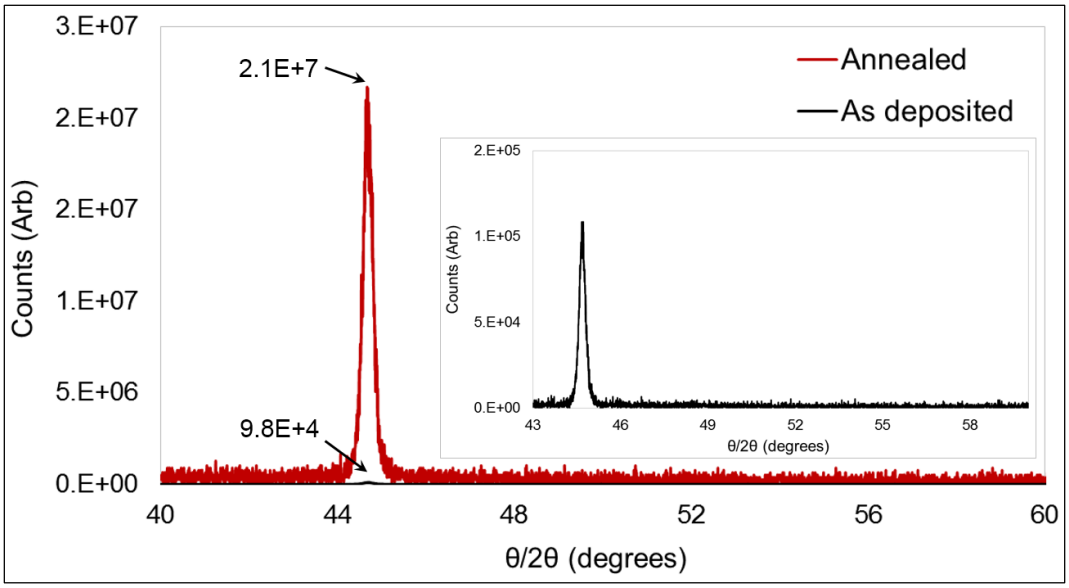


Figure 6.19. XRD for electroless nickel on CVD SLG: as-deposited and post-annealing; inset: as-deposited Ni-P on graphene.

Moreover, AFM also confirmed the growth of the grain size, by at least 10-fold i.e. rms increase from 1 nm to 42 nm, with the average grain size 900 nm after annealing [424], per ESEM images - see Figure 6.20. As a result of the annealing treatment, the phosphorous content in the nickel film decreased from 14 at% to 5 at% on average, with a corresponding increase nickel from 85 at % to 95 at%. Overall, the post-deposition annealing step facilitated the nickel crystallization process, in agreement with Mallory and Hajdu [405]. The annealed Ni-P films are expected to have a lower bulk resistivity due to larger, preferentially oriented grains with less electron scattering as opposed to rather randomly oriented grains in the as-deposited films [424].

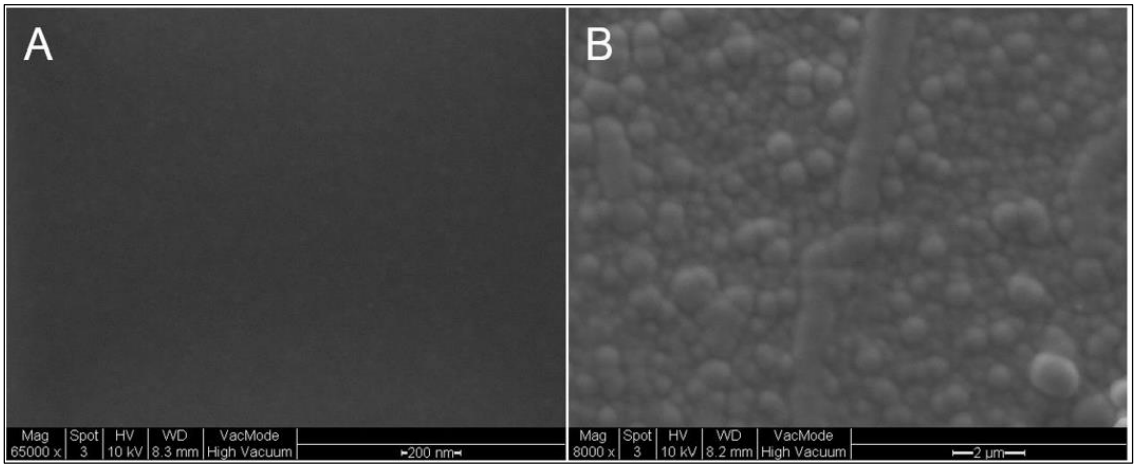


Figure 6.20. ESEM images of electroless nickel on CVD SLG: (A) as deposited, 65000x magnification, 200 nm scale bar; (B) after annealing treatment, 8000x magnification, 2 µm scale bar.

### 6.4.3 *Investigation of the limited nickel film adhesion and subsequent delamination from CVD graphene substrate*

A poor result repeatability was noticed among different samples, mainly due to the poor adhesion of the nickel on the CVD graphene substrates. Locally, the nickel film contact would delaminate from the CVD SLG. XPS and Raman measurements were performed to further investigate this issue, using various TLM structures. Figure 6.21 shows the quantified XPS spectra for C 1s, Si 2p and Ni 2p on a CTLM sample. The silicon signal is strong in areas with visible gaps in the nickel film, being indicative of the graphene layer delamination from the substrate. The XPS C 1s spectra supports this hypothesis, where in regions of delamination, little carbon was present.

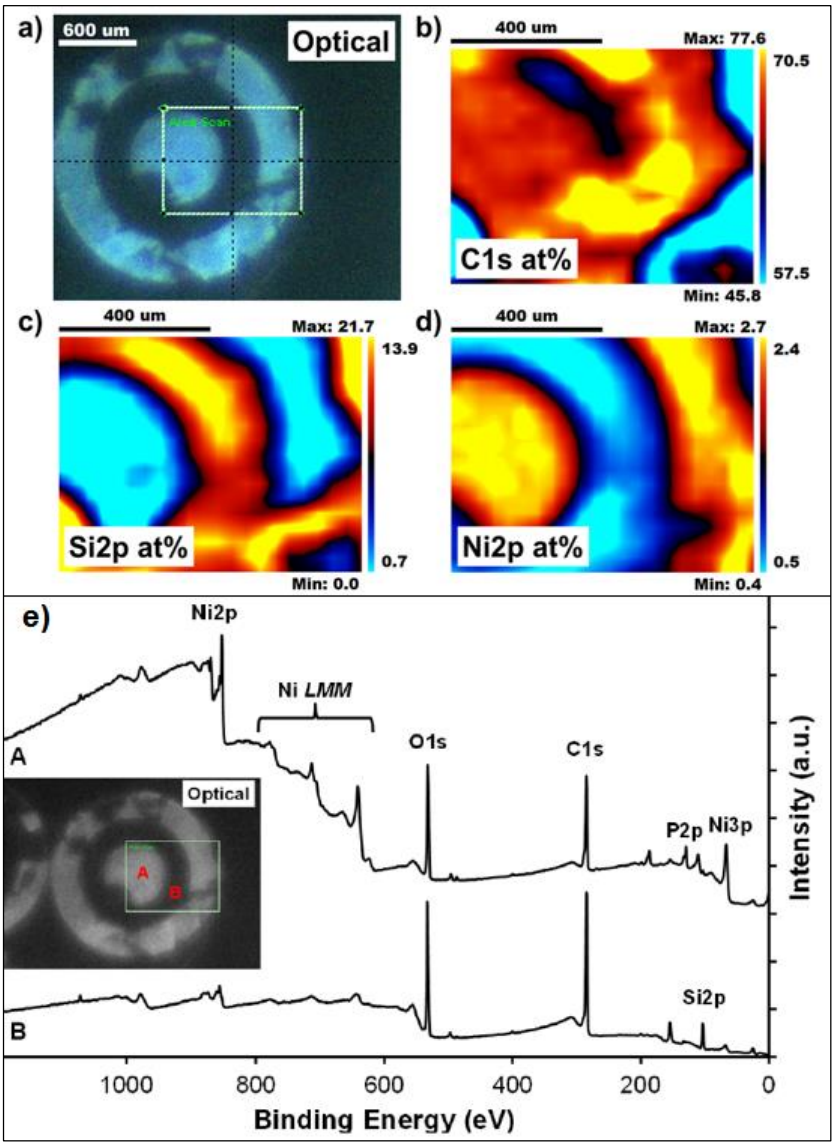


Figure 6.21. XPS maps of a patterned electroless nickel coated graphene structure: (a) optical image of the XPS map; data for: (b) carbon; (c) silicon; (d) nickel; (e) corresponding survey spectra.

The nickel map was used to define two survey analysis areas on and off the nickel pad as indicated by the markings A and B, with their corresponding survey spectra (e) [424].

Hence, it was essential to understand why metallization failed on certain graphene areas. The Raman spectra was acquired across two areas, as per Figure 6.22: A - where graphene was expected, as protected by photoresist during electroless deposition; B – gap in the electroless deposited nickel film. Defects and gaps in the graphene sheet were found in both cases, however, the graphene layer is likely to be missing in area B. Within area A, the graphene quality varied, as both single ($I_{2D}/I_G \approx 1.35$) and bilayer ($I_{2D}/I_G \approx 0.55$) graphene was identified, but also locally exposed silicon dioxide substrate [424].

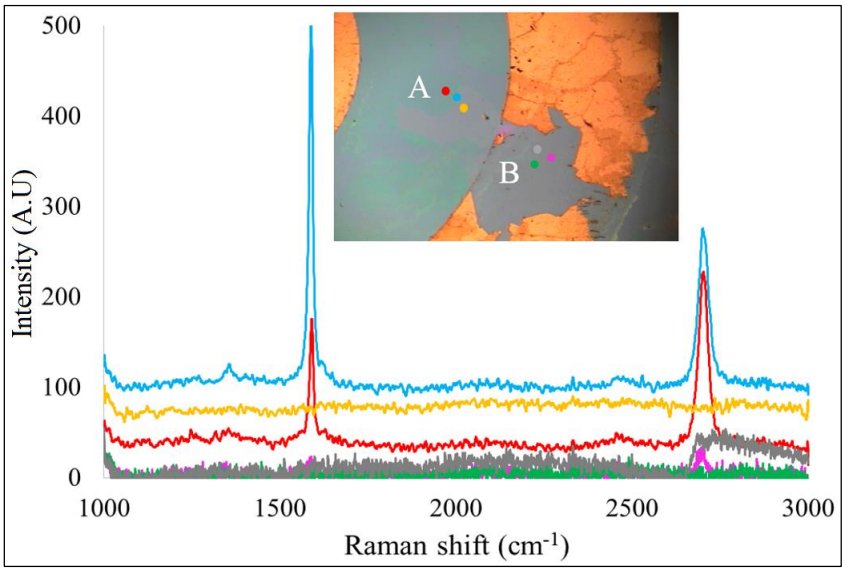


Figure 6.22. Raman spectrum for different graphene areas: (A) graphene substrate; (B) delaminated nickel as selectively exposed to electroless nickel deposition [424].

### 6.4.4 *Cleaning, patterning and electroless nickel deposition effect on CVD graphene*

Qualitative information on the graphene under the electroless deposited nickel film would clarify the strength of the graphene-nickel interface before and after annealing. Therefore, the electroless deposited nickel film was etched using a method similar to the one reported by Leong et al. [431]. The etching reaction was very fast and it was qualitatively controlled, however challenging due to non-uniform nickel etching. The etching method was carefully improved by aiming for a faster reaction and less damage to the graphene layer, and it was performed in heated Aqua regia solution (70°C) to give an etching time of 5-10 seconds [424]. This limited the graphene exposure time in the harsh chemical media. Figure 6.23 briefly presents the evolution of the nickel contact etching.

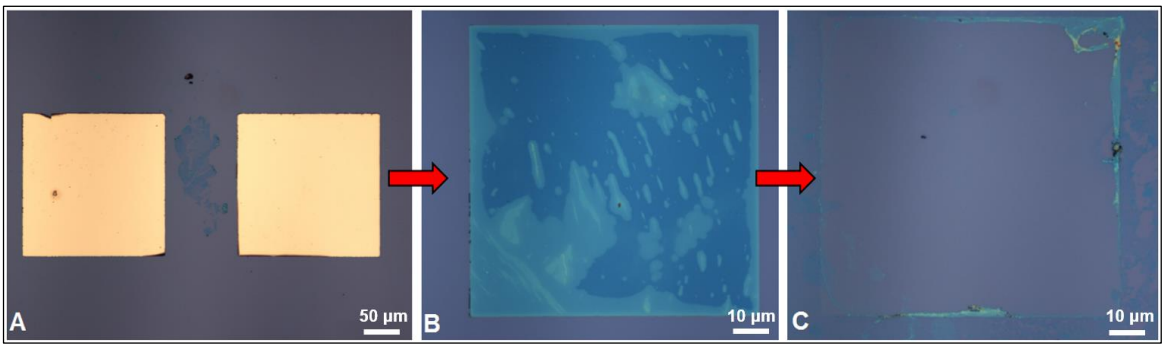


Figure 6.23. Optical microscope images showing the evolution of the etching process for as-deposited electroless nickel contact on CVD SLG: (A) initial surface, 100x; (B) after approximately 10 second immersion in $HNO_3$:HCl etchant, 200x; (C) after approximately 20 second etch, 200x magnification.

Three areas were targeted for further analysis, specifically: surface/central (location of the nickel-based film), at the edge (of deposited film) and outside the defined contacts (non-coated graphene). Raman mapping (see Figure 6.24) was employed to distinguish between the above-mentioned areas for as-deposited and annealed sample.

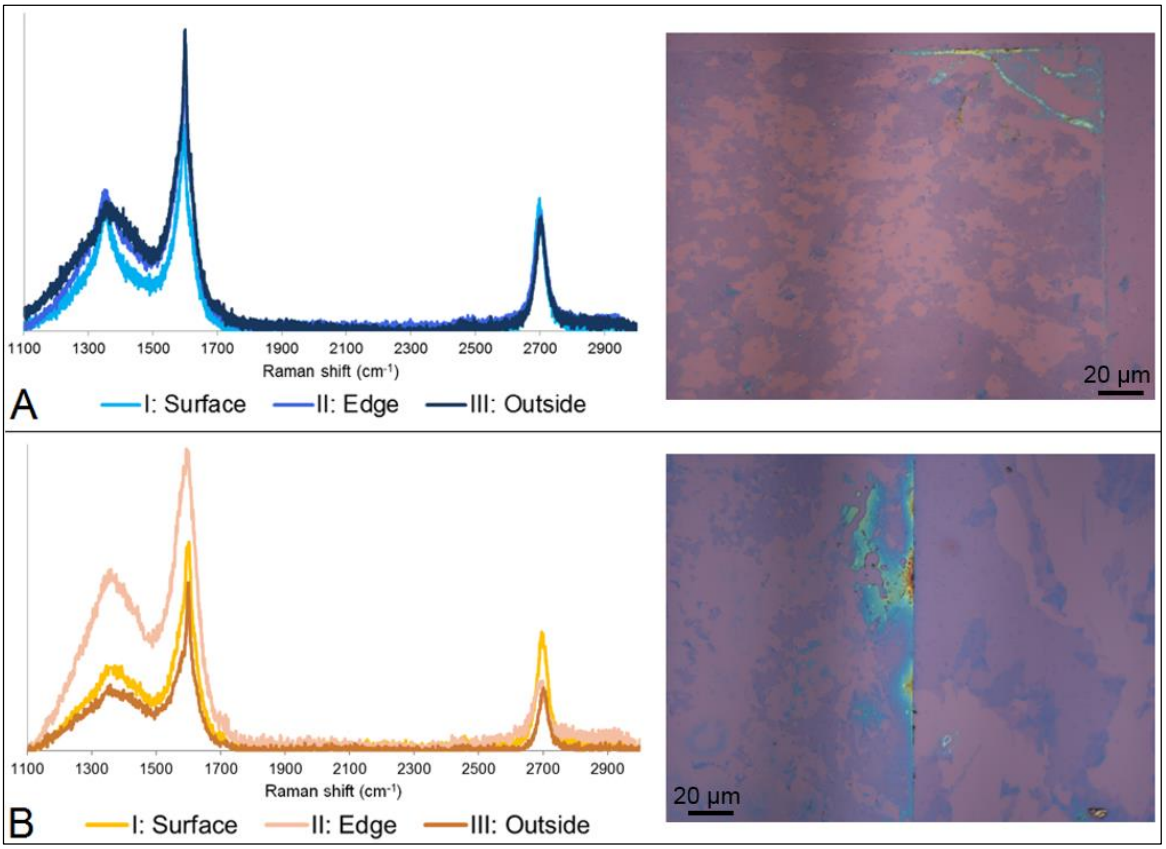


Figure 6.24. Representative Raman spectra of graphene after nickel etching for (A) as-deposited electroless nickel on SLG; (B) annealed sample for graphene-electroless nickel adhesion improvement, modified from [424].

The broadening of the D ≈ 1360 $cm^{-1}$ and G ≈ 1590 $cm^{-1}$ bands are characteristic for functionalized graphene [433]. Single-layer graphene is present in the mapped area, confirmed by the high and well-defined 2D peak at ≈ 2700 $cm^{-1}$. Upon annealing, a further broadening of the D (by 75 $cm^{-1}$) and G peaks (by 170 $cm^{-1}$) was observed at the contact edge. This is indicative of a higher defect density in this region. Outside the contacts, the Raman spectra was similar before and after annealing, however defective, with suppressed G and 2D peak intensities due to the longer exposure to Aqua regia during the etching procedure. After the annealing treatment, the contact resistance was significantly reduced by 50% due to the enhanced chemical reactivity of graphene via carbon dangling bonds and some level of Ni doping [424].

Last but not least, it is important to distinguish between the effects of different chemicals on CVD SLG, therefore the cleaning effect was also assessed using Raman spectroscopy, being presented in Figure 6.25. The graphene samples were mildly cleaned by dipping in acetone and isopropanol and finally blow dried with nitrogen (step 1 in 6.2.3.1). The peak intensity ratio $I_{2D}/I_G$ decreases dramatically from 4.3 to 0.6 after sample cleaning. Folds, creases and gaps towards the edges of the graphene were visible. Similar issues with the CVD grown graphene, transferred on silicon substrates have been previously acknowledged in the literature [434]. Moreover, the sheet resistance of the single-layer graphene doubled from 350 ± 72 Ω/sq to 696 ± 122 Ω/sq; these measurements were taken on three samples across an area of 49 $mm^2$.

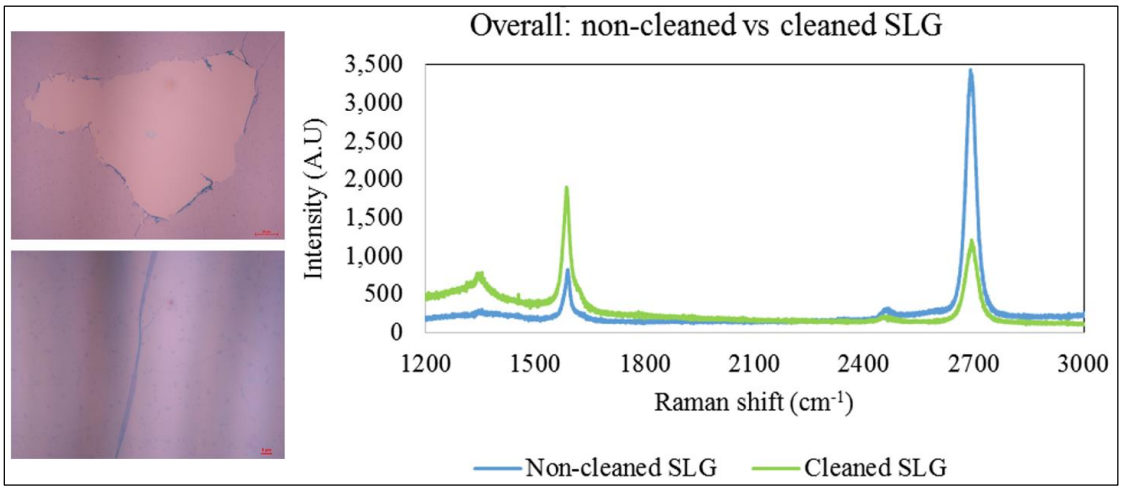


Figure 6.25. Left: Optical microscope image of defects identified on the transferred CVD SLG: folds (x200, 10 μm scale bar) and cracks (x500, 5 μm scale bar ); Right: Comparative Raman spectra for a non-cleaned and cleaned graphene sample [424].

As shown in Figure 6.26, layers and folds were visible on graphene after photolithography. The comparative Raman spectra highlights changes in the peaks of interests compared to the initial CVD SLG. $I_{2D}/I_G$ significantly dropped from 1.06 to

0.66, while the $I_D/I_G$ peak intensity ratio almost doubled as a results of the patterning steps. The broadening and intensity increase of the D peak can be attributed to graphene defects as wrinkles were visible, as well as possible photoresist residues. The Raman downshift in the 2D peak by approximately 17 $cm^{-1}$ can be explained by a combined presence of single and bilayer CVD grown graphene, while maintaining a single and sharp peak [377].

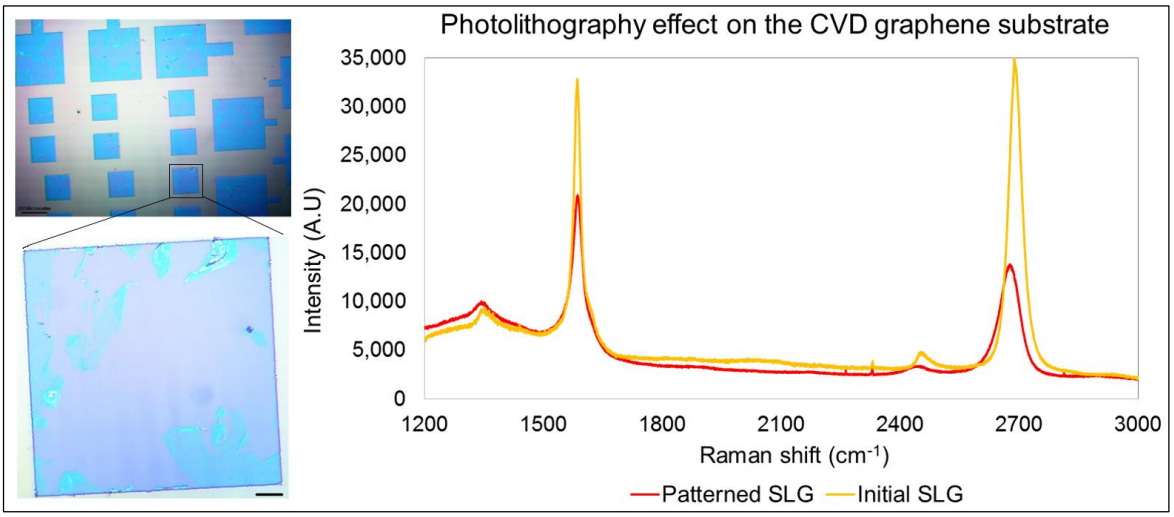


Figure 6.26. Left: Optical image of the patterned graphene windows, 100x and 500x magnification; Right: Comparative Raman spectra of the CVD SLG before and after photolithography patterning.

The evidence presented in this section suggest that the chemical cleaning procedure has a negative impact on CVD SLG, with local delamination of the graphene layer, as well as the presence of bilayer graphene due to folds.

### 6.4.5 *Electroless nickel deposition on rGO*

#### *6.4.5.1 The assessment of compatibility of rGO with microfabrication*

The electroless nickel metallization method was transferred to LightScribe rGO surfaces. It was initiatlly attempted to lithographycally define TLM structures, similarly to CVD graphene. However, during the experimental steps, some carbon-residue was observed delaminating from the top of the sample. As presented in Chapter 3, the Lightscribe produced rGO is laterally exfoliated. Using microfabrication techniques, the photoresist is adsorbed in the pores and expanded layers, with local discolorations visibile on the rGO substrate, as illustrated in Figure 6.27.

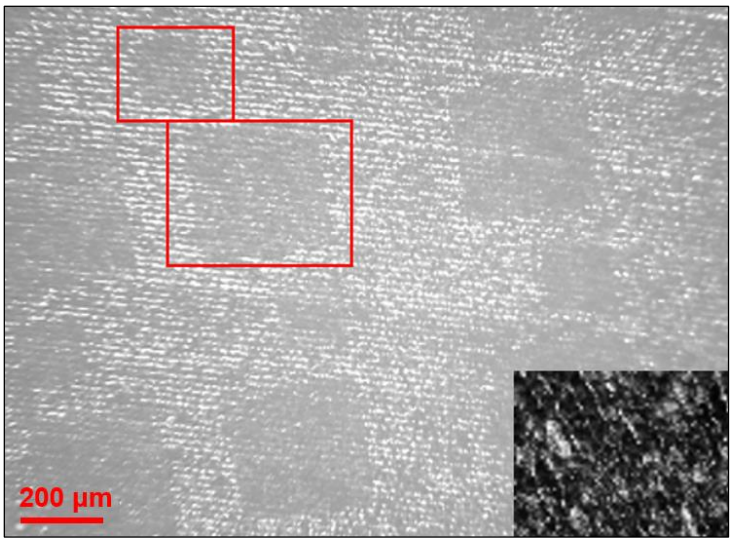


Figure 6.27. Optical image of the photolithography patterned rGO, 50x magnification, 200 µm scale bar. Inset: rGO tracks aspect before patterning, 100x magnification, 20 µm scale bar.

Little is known about the compatibility of microfabrication techniques with porous-based graphene materials, hence Raman spectroscopy was further performed in order to understand its impact on rGO (see Figure 6.28). Surprisingly, the graphene defect-specific D peak showed a significant reduction with a $I_D/I_G$ intensity ratio of 0.56. The G peak exhibited a right hand-side shoulder, representative of an additional hybridisation state [89]. These are characteristic for graphitic materials [377] and suggest a physical damage to the rGO pattern "tracks", locally revealing GO and partially reduced rGO.

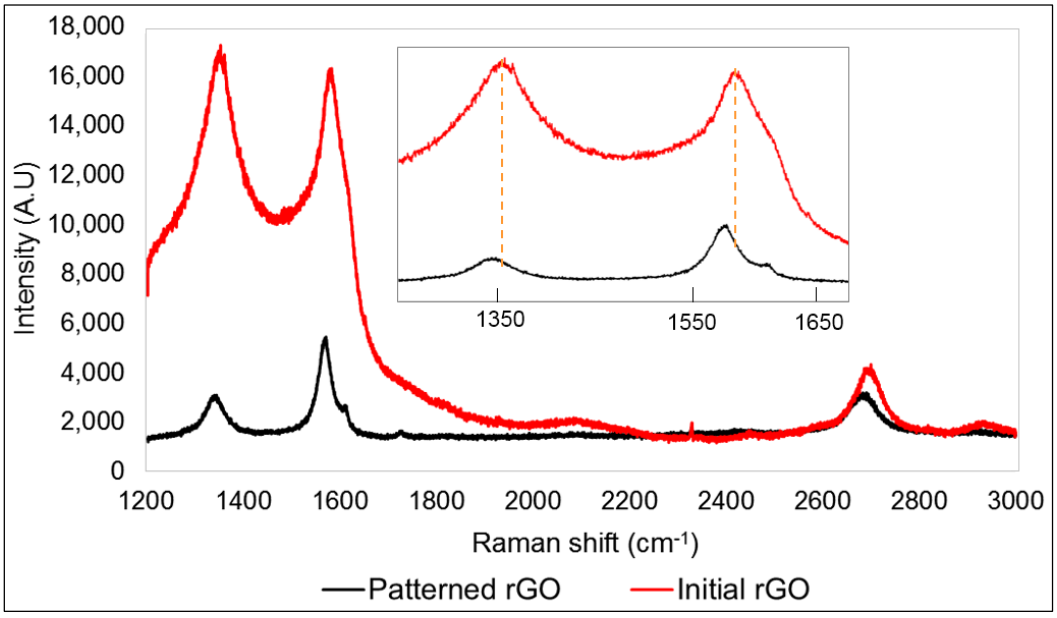


Figure 6.28. Comparative Raman spectra of the rGO substrate before and after photolithography.

### *6.4.5.2 Tuning the electroless nickel process for rGO surface*

The next step was to assess the transferability of the electroless nickel deposition process on rGO. In spite of varying the bath parameters (pH 6-7.5, 50-70°C) the electroless nickel deposition was unsuccessful on the rGO surface when following the conventional sensitization-activation-deposition sequence. Presented in Figure 6.29, the sensitization step was found to inhibit the electroless nickel deposition, while the electroless deposition for activated-only rGO showed a significant improvement.

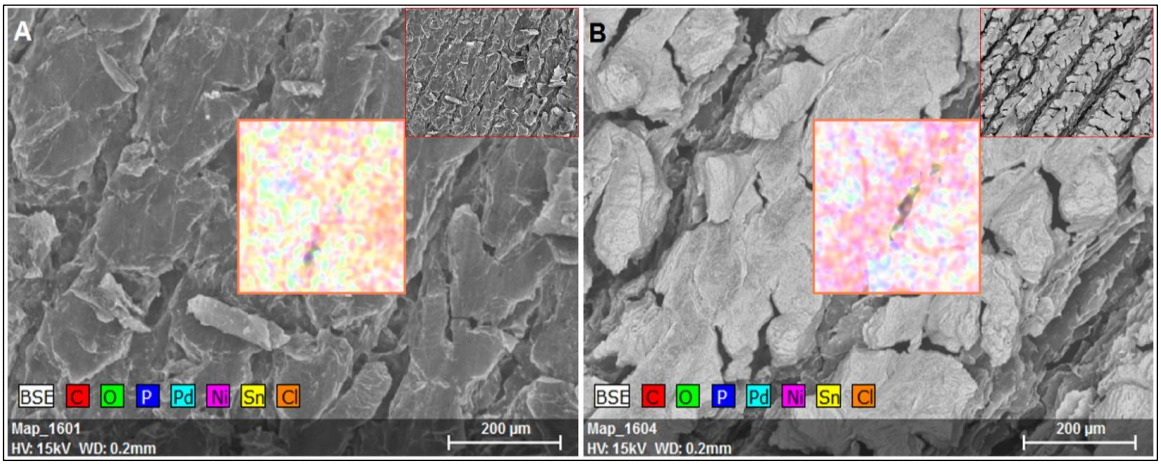


Figure 6.29. SEM / EDX map of rGO after the electroless nickel deposition on: (A) sensitized + activated sample; (B) activated-only sample. Inset: SEM image of the sample, x800 magnification.

It was believed that the tin sensitizer is too acidic for the rGO substrate, thus likely to have an etching effect, rendering the surface less hydrophilic and further limiting the adsorption of the palladium molecules during the activation step. Only brighter rGO track edges were observed for the sensitized-activated sample (A), while the activated-only sample (B) exhibited a uniform nickel coating (see Figure 6.29). Sample B (nickel deposited after activation step only) was uniformly metallized, with EDX revealing the coating composition as 14.1 at% P and 20% Ni. As expected, sample A (electroless nickel deposition after sensitization and activation) had a lower composition of Ni-P film, of 3.6 at% and 2.9 at% respectively.

Table 6-5. Corresponding EDX analysis for the samples shown in Figure 6.29: electroless nickel coating as deposited on rGO: (A) sensitized + activated substrate; (B) activated only substrate.

| Sample | Sn [at %] | Pd [at %] | Cl [at %] | Ni [at %] | P [at %] | C+O [at %] |
|---|---|---|---|---|---|---|
| A | 0.2 | 6.8 | 8.8 | 3.6 | 2.9 | 80 |
| B | - | 14.1 | 10.3 | 20 | 6.2 | 49.4 |

The electroless nickel deposition method failed to repeatedly coat the rGO samples. Moreover, the carbon debris originating from delaminated rGO fragments

quickly destabilized the electroless nickel bath. It was therefore essential to increase the deposition rate in order to minimize the immersion time of the rGO samples in the nickel bath. By using a small amount of silver conductive paint (RS Components) on the corner of the rGO sample, the electroless nickel was initiated at the silver point and successfully coated the rGO patterns. This represents an easier alternative to surface seeding, which is also used in electroplating [435]. Interestingly, this allows for selective deposition on patterns with attached conductive paint only, as shown in Figure 6.30. This result was obtained in electroless bath of pH 7.2 ± 0.2 at 73 ± 2°C. The activation time was 3 minutes, followed by a 2-minute immersion step in nickel solution, then reactivation for 10 seconds and further 3 minutes electroless deposition.

Finally, the favourable electroless nickel bath conditions for the rGO substrate were determined upon qualitative i.e. visual inspection as pH 7.4 ± 0.1, 68 ± 2°C. Outside this range, the nickel bath quickly decomposed or the coating failed to deposit on the rGO substrate. Brief and repeated activation and metallization steps, detailed in section 6.2.3.2, were adopted in order to maximise the deposition rate while growing a uniform nickel layer.

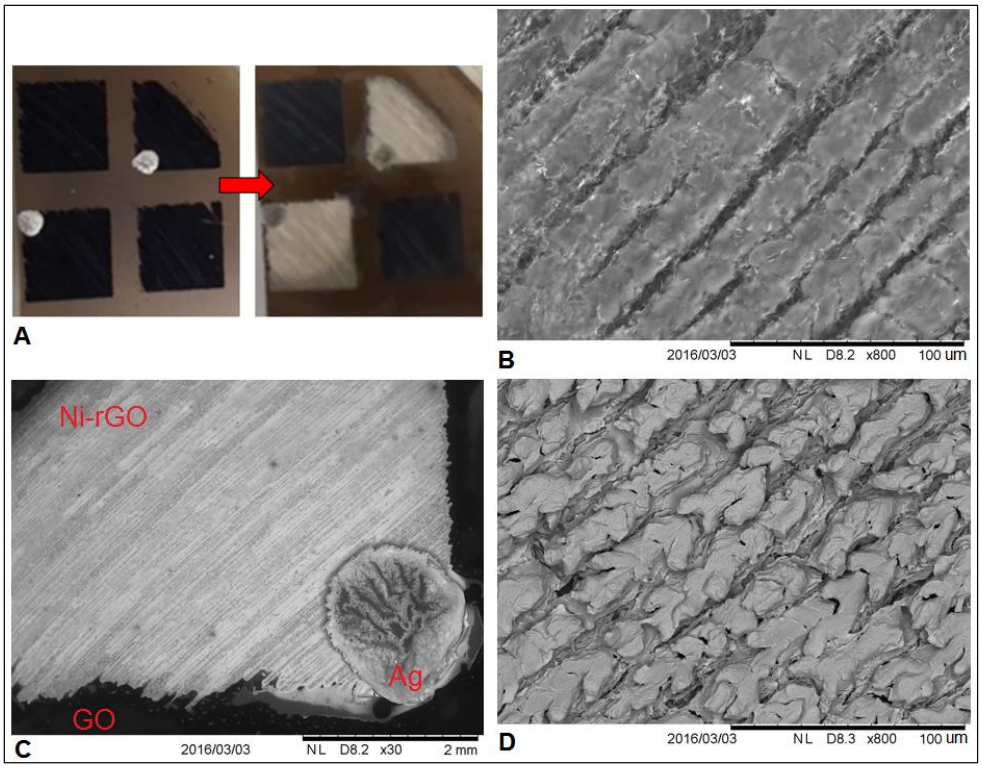


Figure 6.30. Electroless nickel on rGO: (A) selective rGO pattern coating based on conductive silver initiation point before-after; (B) SEM image of failed electroless coating (no Ag initiation point) on rGO, 800x, 100 µm scale bar; (C) SEM image of the nickel coated rGO with Ag initiation point, 300x, 2 mm scale bar; (D) SEM image of electroless nickel coating the rGO, 800x, 100 µm scale bar.

### 6.4.6 *Electroless nickel-rGO: properties*

#### *6.4.6.1 Contact resistance of electroless nickel on rGO*

As highlighted in section 6.4.5.1, the microfabrication techniques were found to be incompatible with the rGO sample and the patterning method had to be adjusted considering the substrate and rGO structural properties. In order to evaluate the contact resistance, structures of different lengths have been patterned using LightScribe (similar to TLM) and attached to an acetate substrate to control the level of immersion throughout the experiment. Matlab Image Viewer tool was used for pixel measurement (d1, d2, d3) using a ruler as baseline i.e. 1 mm (see Figure 6.31). The contact distance was calculated by adding the defined track distances.

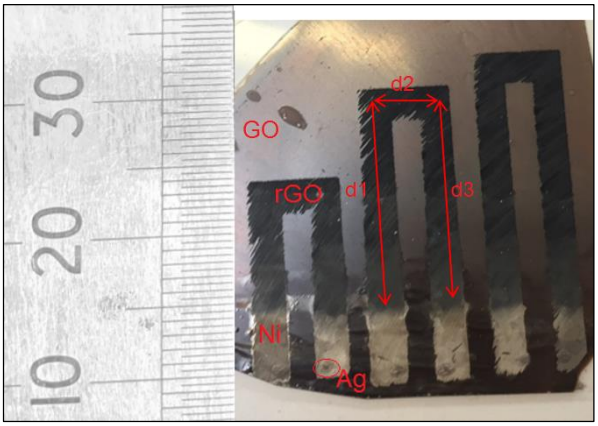


Figure 6.31. Optical image of the rGO patterns for contact resistance extraction.

Figure 6.32 presents the resistance measurements for three different rGO samples, with inter-contact distances varying between 1.5 mm and 42 mm. As the linearity of the measurements is highly limited, the contact resistance could not be extracted via TLM. The reproducibility is limited, apparent if comparing samples rGO1 and rGO2 as having similar inter-contact distances. For sample rGO3, the measured resistance at 40 mm was significantly close to its 20 mm value. This can be an effect of rGO properties variability due to disc location, as already discussed in section 3.2.4, but also due to measurement accuracy.

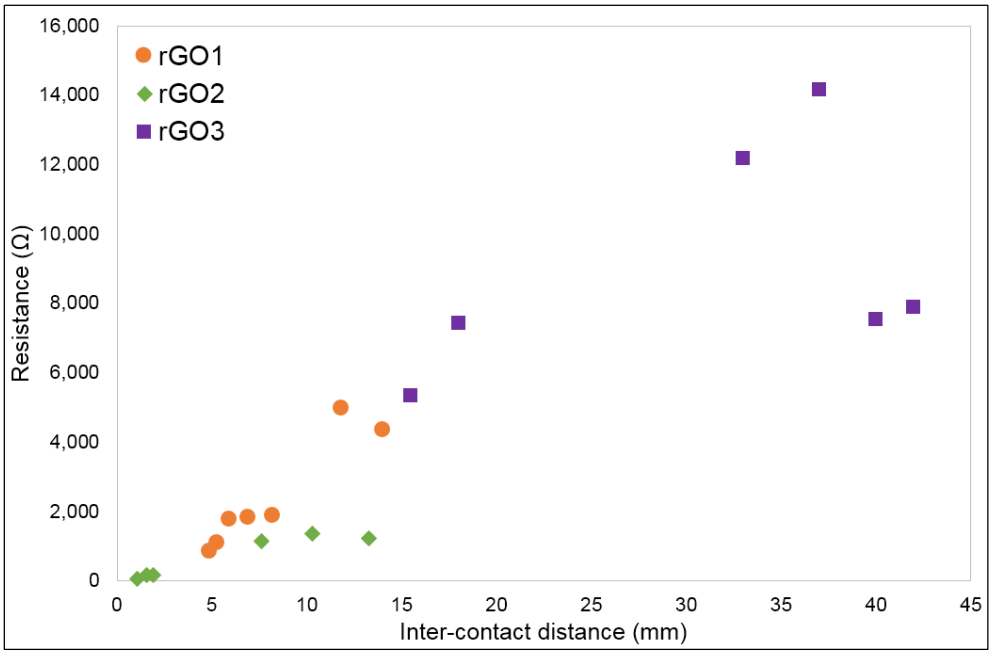


Figure 6.32. Resistance measurements for increasing inter-contact distances for electroless nickel on rGO.

#### *6.4.6.2 Electroless nickel growth on rGO*

Aiming to understand the electroless nickel growth on the rGO substrate, the process was interrupted at different stages on identical samples and conditions. SEM images of the samples and EDX data are presented in Figure 6.33 and Table 6-6. The palladium concentration at activation (1) and re-activation stages (3) was surprisingly low and the Ni:P ratio was found to increase with deposition time (step 4) from 1.5 for 20 second immersion time to 4 for 1 minute.

Table 6-6. EDX composition analysis for the electroless nickel film composition as deposited the rGO samples from Figure 6.33.

| Step no. | Ni [at %] | P [at %] | Pd [at %] | Cl [at %] | C+O [at %] |
|---|---|---|---|---|---|
| 1 (sample A) | 0.2 | 0.1 | 0.7 | 3 | 95 |
| 2 (sample B) | 1.4 | 0.9 | 0.4 | 4.6 | 92 |
| 3 (sample C) | 0.2 | 0.3 | 3.2 | 3.8 | 92 |
| 4,5 (sample D) | 43 | 10.6 | 3.6 | 12 | 31 |

Interestingly, in spite of the identified issues - i.e. bath decomposition, rGO delamination from the acetate substrate, the Ni-P alloy successfully coated the expanded layers of the rGO, visualised with HIM (see Figure 6.34).

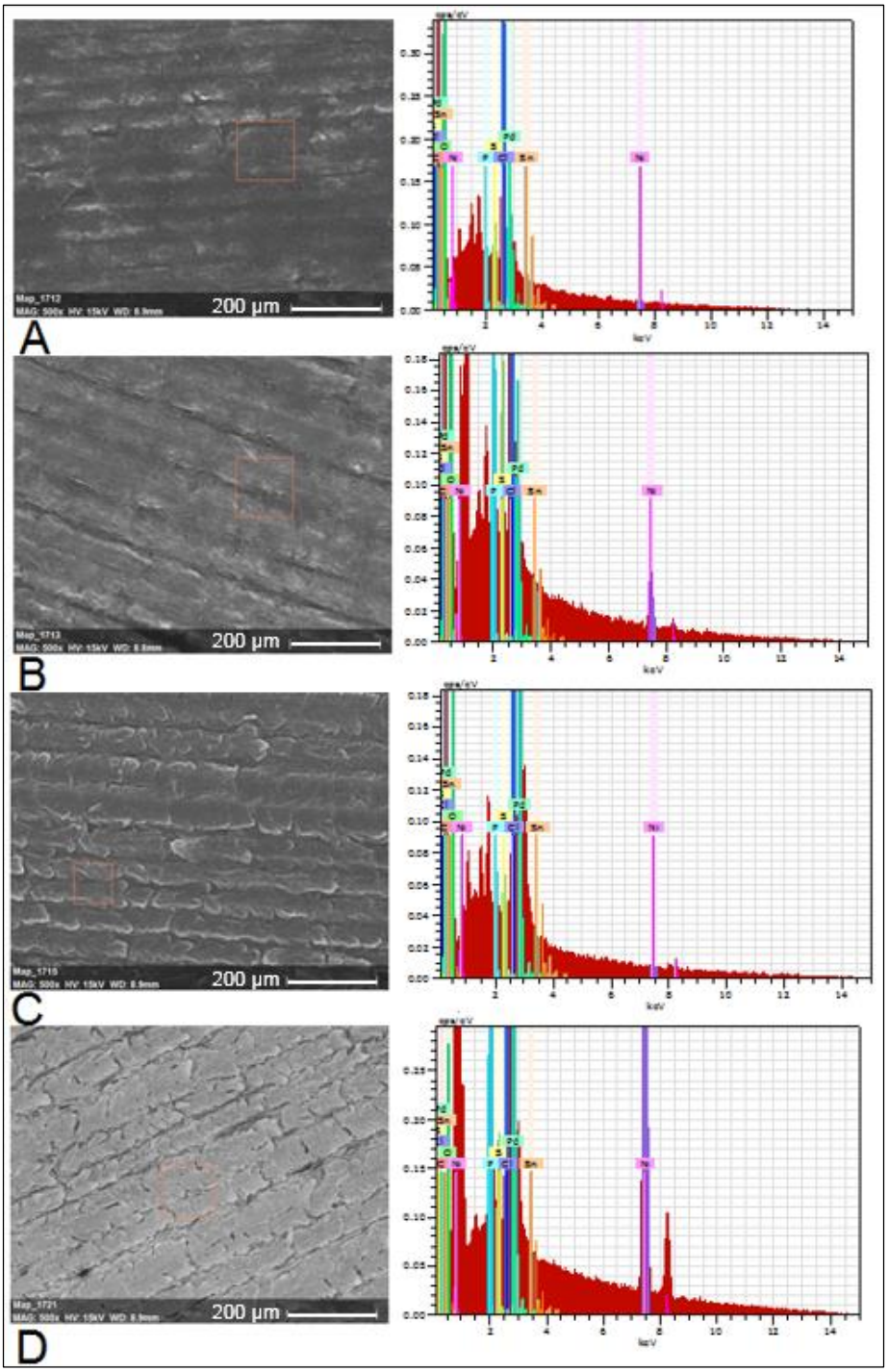


Figure 6.33. Top: SEM images (x500 magnification, 200 µm scale bar) showing the sequential electroless deposition on rGO; Bottom: EDX spectra of nickel (Ni element – purple colour) on rGO: (A) after 30 s activation; (B) after 20 s immersion in the nickel bath; (C) after 10 s re-activation step; (D) after 60 s immersion in the nickel bath.

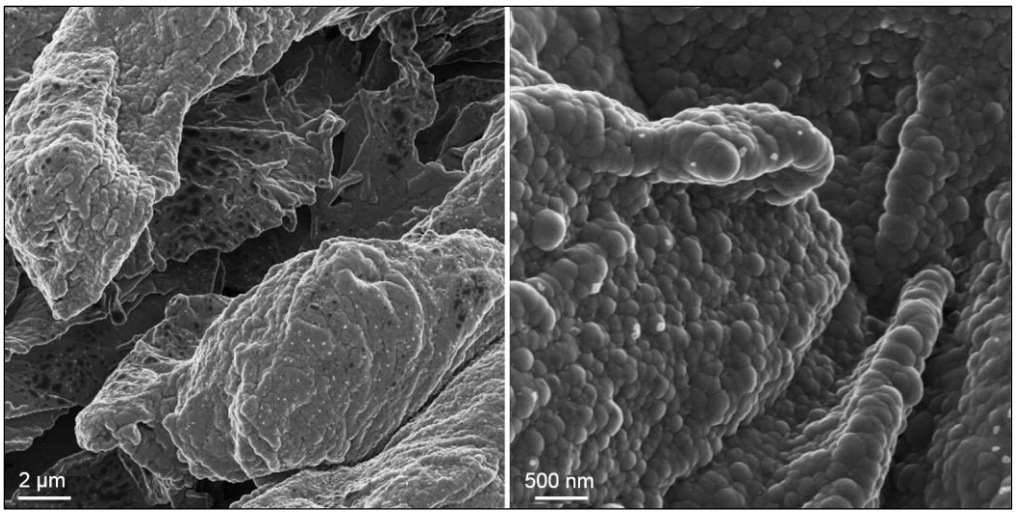


Figure 6.34. HIM image of the electroless Ni deposited on rGO substrate: 2 µm scale bar (left), 500 nm scale bar (right).

## 6.5. Conclusions

The work presented in this chapter shows that the electroless nickel deposition technique can be tuned for the successful metallization of graphene based materials in an attempt to overcome the limitations of conventional metallisation techniques.

Regarding the CVD transferred SLG, the obtained average contact resistance of the electroless nickel was 217 ± 64 Ω/sq. The graphene-nickel interface was significantly improved via a rapid annealing treatment at 400°C decreasing the contact resistance by 50%. With a final value of 108 ± 36 Ω/sq, the enhanced contact resistance corresponding to 21 ± 2 kΩ·µm is one order of magnitude higher compared to conventional deposition methods (see Table 2-6). The statistical model is satisfactory as the predicted Ni:P ratio is within 2.4% of the experimental results.

A main concern for the electroless nickel deposition on CVD SLG is its poor adhesion to the substrate. The surface analysis targeted the electroless nickel growth mechanism, while the nickel-graphene interfacial properties revealed some interesting aspects. At the edge with the electroless deposited contact, the graphene layer showed an enhanced chemical reactivity, as a result of sensitization and activation steps. Moreover, delaminated areas of the nickel film revealed discontinuities in the CVD transferred graphene. The observed poor adhesion after the lift-off step was caused by graphene delamination from the silicon substrate.

Moreover, a limited compatibility with the electroless nickel deposition technique was identified for rGO, which is a thick, 3D laterally expanded graphene based material. The delamination of the rGO layers (carbon debris) contaminates the nickel bath, leading to destabilization. To overcome this drawback, the deposition rate was

significantly increased by using a growth initiation point. Compared to CVD SLG, the reproducibility of the electroless nickel process on rGO was highly limited due to material's complex morphology.

Taken together, these results confirm the transferability of electroless nickel deposition method with different graphene based materials. The obtained electroless film is a Ni-P alloy and its electrical properties depend on the phosphorous content, as well as graphene substrate properties, patterning and annealing conditions. Prior to further experimental work for contacting CVD graphene, one should target a reliable graphene-substrate interface. An initial annealing treatment of the graphene samples, prior to lithographic patterning could eliminate residues and contaminants, while improving the adhesion of the CVD transferred graphene to the silicon substrate. This can eventually eliminate the need for chemical cleaning prior to patterning as this affected the quality of graphene (6.4.4), while focusing on lithography integration for electrical contact measurements.

# Chapter 7. Conclusions and recommendations

## 7.1. Conclusions

The main goal of this research project was to investigate the prospects of low-cost, accessible fabrication of fully functional graphene based biosensing platforms, with a proof of concept on the detection of prostate specific antigen (PSA). Throughout this thesis, four main subjects have been investigated:

- The synthesis and the application driven i.e. biosensing selection of graphene materials
- A comparative performance study of high-frequency antenna detection concept and conventional electrical impedance detection method for biosensing applications
- Graphene functionalization, integration in device prototypes and potential as electrochemical immunoassay
- A novel electroless nickel deposition technique on graphene was established for contacts' definition in an attempt to improve the metal-graphene interface.

With the variability and continuous expansion of the graphene nanomaterials' family, the characterisation work presented in Chapter 3 demonstrated the capability of current technologies to identify subtle surface and structural variations in graphene based nanomaterials: pristine graphene (SLG), bi-layer epitaxially grown graphene (EG), graphene oxide (GO), nano-graphene oxide (nGO) and reduced graphene oxide (rGO) obtained via different reduction methods (laser – Lightscribe and $CO_2$ laser, UV and l-ascorbic acid). It was shown that LightScribe reduced graphene oxide (rGO) and laser induced graphene (LIG) represent the best compromise in terms of graphene quality, resolution and electrical conductivity for electrochemical biosensing applications. The selected materials offer a series of advantages compared to expensive bottom-up fabricated graphene materials, among which the low cost and scalability opportunity, but also the presence of oxygen functional groups, which can be used as anchoring points for biomolecules immobilisation. The average chemical composition of rGO is, on average, 95% carbon and 5% oxygen, 98.5% carbon and 1.5% oxygen for LIG, respectively. LIG is a better electrical conductor than rGO having a 14-fold lower sheet resistance i.e. 36.6 Ω/sq. The rich morphologies of the two laser produced graphene materials were visualised with the aid of high-resolution microscopy (HIM): rGO has a laterally expanded structure, while LIG exhibits a vertical, but hierarchical layers arrangement. Generated by the photo-thermal reduction

process, these porous 3D reduced graphene materials are unlike the other analysed graphene materials, which exhibited a smooth, film-like aspect. However, some manufacturing limitations were identified for the simultaneous graphene production and patterning via laser. The rGO via LightScribe showed significant sample variability depending on disc location, while the delivered energy via $CO_2$ laser for LIG production was found to vary locally, as the available equipment was not fit for low power settings and soft film engraving.

The antenna-based capacitive sensing concept and the ease of patterning of the selected graphene materials (LightScribe and $CO_2$ laser) justified the investigation of a novel electrical detection method, as presented in Chapter 4. The overall aim of this section was to apply the impedance-matching concept on various biosensor designs e.g. capacitive, inductive, capacitive-inductive. This concept was initially analysed using NI Multisim (impedance response) and AWR Design Environment (RF domain). The simulations indicated a superior sensitivity for the impedance matching method, with detectable changes in the resonant peak based on 1-10% capacitive changes of the biosensors. By matching the impedance of the biosensor to 50 Ω i.e. input port, a resonant peak is introduced with a signal-to-noise ratio (SNR) amplified by five-fold from 15 dB to 76.9 dB. Furthermore, commercially available gold interdigitated electrode arrays (IDE) were employed in experimental work to test the hypothesis. The sensitivity of the impedance-matching RF concept was compared with conventional, low-frequency electrochemical impedance spectroscopy (EIS). The gold IDE devices were functionalized with PSA-10 antibody via DTSP crosslinking chemistry for PSA detection. The study revealed that the anticipated sensitivity of radio-frequency (MHz-GHz ranges) method and equipment (Vector Network Analyzer) is dramatically reflected in high noise levels, leading to a low SNR for non-conventional (non-RF) designs. The relationship between the biosensor impedance and PSA concentration was fitted by one-side binding curve, but the measurements recorded using the RF detection method did not show any clear correlation. Therefore, in conditions of exploring novel graphene based materials using an IDE geometry, the conventional EIS method was adopted for further feasibility studies.

A feasibility study of IDE biosensors based on the selected graphene materials (Lightscribe rGO and LIG) was presented in Chapter 5. The functionalization capability of rGO was initially assessed using amino-coated quantum dots (CdSe QD), which were successfully visualised with a fluorescence microscope. Moreover, XPS and Raman spectroscopy were performed at each chemical treatment step (EDC-NHS

functionalization, PSA-10 antibody, PSA) and they confirmed the presence of the protein on the chemically functionalized graphene surfaces (rGO, LIG) with an increase in both N at% and D-to-G Raman peak intensity ratio. The batch testing of the graphene based biosensors was extremely limited due to local variability and large porosity, quickly absorbing the buffer and drying off. Hence, the same surface was employed for PSA detection via successive analyte addition. In spite of their similar composition, the distinct morphologies of rGO and LIG led to significant differences in their EIS behaviour. Faradaic and non-faradaic EIS data of the graphene based biosensors was fitted by one side-binding curves in order to evaluate their sensitivity and performance. Due to biomolecules attachment to the expanded graphene layers, the capacitive reactance dominated the impedance changes for the rGO IDE sensors in both non-faradaic ($R^2 = 0.954 \pm 0.012$) and faradaic ($R^2 = 0.955 \pm 0.016$) conditions. However, the PSA molecular layers had a more complex effect on the faradaic impedance of the LIG IDE sensing structures, with combined resistive and capacitive changes. The goodness of fit for the one-side calibration curve for the LIG sensing structures was satisfactory for both non-faradaic ($R^2 = 0.988 \pm 0.006$) and faradaic impedance measurements ($R^2 = 0.991 \pm 0.006$). In addition, the successive protein testing was complemented by systematic tests in order to assess biosensors' performance i.e. porosity, protein desorption, drifting. These thorough studies revealed drift instability for the LIG biosensors and a significant adsorption effect on the rGO devices as well. Overall, the Lightscribe rGO is more suitable for electrochemical sensing applications. Interestingly, if compensating for the impedance variation due to drifting, both graphene biosensors show a decrease in $C_{dl}$. Based on the linear working range of the biosensor, $\Delta C_{dl}$ is estimated to 11% for rGO and 69% per mg/mL (of PSA) for LIG, respectively.

Lastly, the electroless deposition process was tuned for fast and low-cost nickel deposition on different graphene materials: 2D pristine graphene (CVD SLG) and 3D porous reduced graphene oxide (rGO) in Chapter 6. The experiments were conducted at different pH and temperatures of the electroless nickel bath, and a response surface design was used to statistically determine the suitable parameters for successful Ni-P film deposition on CVD SLG: 66ºC, pH 6.6. The electroless nickel deposition was integrated with a photolithographic patterning process for selective contact definition on the graphene surface. The contact resistance was reduced by just over 50% (to 21 ± 2 kΩ·µm) via a rapid post-annealing treatment at 400ºC. This treatment was found to also facilitate the nickel crystallization, increasing the nickel composition by

10 at% (to 95 at%) and reducing the phosphorous content to just 5 at%. A strong chemical bond is formed between the carbon-based substrate and the electrolessly deposited nickel, leading to defects introduction in the pristine graphene. Local metallic film delaminations and gaps were caused by the poor interface between the $Si/SiO_2$ substrate and the transferred CVD grown graphene, with SLG locally peeling off. In order to demonstrate the transferability of the electroless nickel deposition, the technique was then applied to LightScribe rGO. The method was qualitatively adapted to ensure the successful electroless coating on the rGO surfaces, by introducing an additional activation step ($PdCl_2$). The porous, expanded rGO layers facilitate the chemical species adsorption, with increasing composition of palladium and chloride throughout the chemical process and up to 53% Ni-P alloy. While delaminated carbon debris led to the destabilization of the electroless nickel chemical bath, limiting the duration of the process, EDX and high-resolution microscopy (HIM) show the effective and uniform coating of the expanded graphene layers.

In conclusion, this work provides valuable research insights for the production, characterisation, functionalization and contacting of graphene based materials, which is essential for the development of a new generation of low-cost, fully functional and highly sensitive generic biosensing platforms.

## 7.2. Future work recommendations

The synthesis and patterning of graphene based materials, either simultaneous or in separate processes, but without impacting graphene properties remain important issues for future research. A steady growth in laser-obtained graphene publications is anticipated for electrochemical supercapacitors and sensing i.e. chemical and biological applications. By controlling the pore size and material morphology, one could improve the biosensor performance. This could entail simplistic measures, such as the utilisation of easily tunable laser power. 3D and foam-like graphene based materials are of high interest and further studies could look into correlating the electrical resistance with material thickness, allowing for properties control. Also, the functionalization of graphene based materials and biosensor specificity can be explored to optimise the blocking layer. In spite of the strong adsorption mechanism which is problematic for long time immersions, the porous graphene based materials can be efficient as disposable, droplet-based biosensors.

Additional efforts are required to gain a thorough knowledge and understanding of the properties of various graphene based materials as induced by the production

method, especially in the case of reduced graphene oxide via hydrazine, laser or annealing reduction. In this respect, a graphene specific materials database would represent a solid starting point to further projects. This would enable graphene circuit modelling and design, including for high-frequency applications, where the 50 Ω source impedance matching is required e.g. microstrip, LC resonators. The current literature is limited even in terms of gold RF circuits, but this would provide essential evidence if graphene can actually outperform gold devices sensitivity at high frequencies.

Moreover, the selective electroless nickel coating on rGO can be further explored for contacting purposes. It would be interesting to understand if the electroless nickel deposition can be optimised for rGO substrates in a similar manner to the presented CVD SLG and also assess method compatibility with other types of reduced graphene e.g. thin films and graphene hybrid materials. Further work should target the careful optimization of the electroless nickel with controlled, uniform nickel film growth and improved result repeatability.

## References and bibliography


[1] A. St John and C. P. Price, “Existing and Emerging Technologies for Point-of-Care Testing,” *Clin. Biochem. Rev.*, vol. 35, no. 3, pp. 155–167, 2014.

[2] S. Borgmann, A. Schulte, S. Neugebauer, and W. Schuhmann, “Amperometric Biosensors,” pp. 1–83, 2012.

[3] C.-M. Tîlmaciu and M. C. Morris, “Carbon nanotube biosensors,” *Front. Chem.*, vol. 3, Oct. 2015.

[4] B. Derkus, “Applying the miniaturization technologies for biosensor design,” *Biosens. Bioelectron.*, vol. 79, pp. 901–913, 2016.

[5] K. Baryeh, S. Takalkar, M. Lund, and G. Liu, “Introduction to medical biosensors for point of care applications,” in *Medical Biosensors for Point of Care Applications*, R. J. Narayan, Woodhead Publishing, 2017.

[6] C. H. Ahn, J.-W. Choi, G. Beaucage, J. Nevin, J.-B. Lee, A. Puntambekar, and R. J. Y. Lee, “Disposable Smart Lab on a Chip for Point-of-Care Clinical Diagnostics,” *Proc. IEEE*, vol. 92, no. 1, pp. 154–173, 2004.

[7] K. J. Tietze, “Definitions and Concepts,” in *Basic Skills in Interpreting Laboratory Data*, M. Lee, American Society of Health-System Pharmacists, 2009.

[8] P. B. Luppa, C. Müller, A. Schlichtiger, and H. Schlebusch, “Point-of-care testing (POCT): Current techniques and future perspectives,” *TrAC Trends Anal. Chem.*, vol. 30, no. 6, pp. 887–898, 2011.

[9] R. McNerney, “Diagnostics for Developing Countries,” *Diagnostics*, vol. 5, no. 2, pp. 200–209, 2015 .

[10] W. Jung, J. Han, J.-W. Choi, and C. H. Ahn, “Point-of-care testing (POCT) diagnostic systems using microfluidic lab-on-a-chip technologies,” *Microelectron. Eng.*, vol. 132, pp. 46–57, 2015.

[11] D. R. Thévenot, K. Toth, R. A. Durst, and G. S. Wilson, “Electrochemical biosensors: recommended definitions and classification,” *Biosens. Bioelectron.*, vol. 16, no. 1–2, pp. 121–131, 2001.

[12] D. W. G. Morrison, M. R. Dokmeci, U. Demirci, and A. Khademhosseini, “Clinical Applications of Micro- and Nanoscale Biosensors,” in *Biomedical Nanostructures*, John Wiley & Sons, Inc., pp. 439–460, 2008.

[13] J. D. Newman and S. J. Setford, “Enzymatic Biosensors,” *Mol. Biotechnol.*, vol. 32, no. 3, pp. 249–268, 2006.

[14] E.-H. Yoo and S.-Y. Lee, “Glucose Biosensors: An Overview of Use in Clinical Practice,” *Sensors*, vol. 10, no. 5, pp. 4558–4576, 2010.

[15] W. ZHANG and G. LI, “Third-Generation Biosensors Based on the Direct Electron Transfer of Proteins,” *Anal. Sci.*, vol. 20, no. 4, pp. 603–609, 2004.

[16] G. Preda, O. Bizerea, and B. Vlad-Oros, “Sol-gel technology in enzymatic electrochemical biosensors for clinical analysis,” in *Biosensors for Health, Environment and Biosecurity*, InTech, 2011.

[17] M. A. Cooper, *Label-Free Biosensors Techniques and Applications*, 1st Ed. Cambridge University Press, 2009.

[18] N. Bhalla, P. Jolly, N. Formisano, and P. Estrela, “Introduction to biosensors,” *Essays Biochem.*, vol. 60, no. 1, pp. 1–8, 2016.

[19] D. A. Armbruster and T. Pry, “Limit of Blank, Limit of Detection and Limit of Quantitation,” *Clin. Biochem. Rev.*, vol. 29, no. Suppl 1, pp. S49–S52, 2008.

[20] N. J. Ronkainen, H. B. Halsall, and W. R. Heineman, “Electrochemical biosensors,” *Chem. Soc. Rev.*, vol. 39, no. 5, p. 1747, 2010.

[21] S. Prakash, M. Pinti, and B. Bhushan, “Theory, fabrication and applications of microfluidic and nanofluidic biosensors,” *Philos. Trans. R. Soc. A Math. Phys. Eng. Sci.*, vol. 370, no. 1967, pp. 2269–2303, 2012.

[22] D. G. Rackus, M. H. Shamsi, and A. R. Wheeler, “Electrochemistry, biosensors and microfluidics: a convergence of fields,” *Chem. Soc. Rev.*, vol. 44, no. 15, pp. 5320–5340, 2015.

[23] J. M. Montornes, M. S. Vreeke, and I. Katakis, “Glucose Biosensors,” in *Bioelectrochemistry: Fundamentals, Experimental Techniques and Applications*, P. N. Bartlett, John Wiley & Sons, Ltd, pp. 199–217, 2008.

[24] X.-E. Zhang, “Screen-printing methods for biosensor production,” in *Biosensors*, Second., J. Cooper and T. Cass, Eds. Oxford University Press, 2004.

[25] A. K. Geim, “Graphene: status and prospects,” *Science*, vol. 324, p. 1530, 2009.

[26] K. S. Novoselov, A. K. Geim, S. V Morozov, D. Jiang, Y. Zhang, S. V Dubonos, I. V Grigorieva, and A. A. Firsov, “Electric field effect in atomically thin carbon films.,” *Science*, vol. 306, no. 5696, pp. 666–669, 2004.

[27] A. K. Geim, “Graphene prehistory,” *Phys. Scr.*, vol. 2012, no. T146, p. 14003, 2012.

[28] D. R. Dreyer, R. S. Ruoff, and C. W. Bielawski, “From conception to realization: An historial account of graphene and some perspectives for its future,” *Angewandte Chemie - International Edition*, vol. 49, no. 49. pp. 9336–9344, 2010.

[29] X. Zhang, B. R. S. Rajaraman, H. Liu, and S. Ramakrishna, “Graphene’s potential in materials science and engineering,” *RSC Adv.*, vol. 4, no. 55, p. 28987, 2014.

[30] D. R. Cooper, B. D’Anjou, N. Ghattamaneni, B. Harack, M. Hilke, A. Horth, N. Majlis, M. Massicotte, L. Vandsburger, E. Whiteway, and V. Yu, “Experimental Review of Graphene,” *ISRN Condens. Matter Phys.*, vol. 2012, pp. 1–56, 2012.

[31] S. Stankovich, D. A. Dikin, G. H. B. Dommett, K. M. Kohlhaas, E. J. Zimney, E. A. Stach, R. D. Piner, S. T. Nguyen, and R. S. Ruoff, “Graphene-based composite materials.,” *Nature*, vol. 442, no. 7100, pp. 282–286, 2006.

[32] M. S. A. Bhuyan, M. N. Uddin, M. M. Islam, F. A. Bipasha, and S. S. Hossain, “Synthesis of graphene,” *Int. Nano Lett.*, vol. 6, no. 2, pp. 65–83, 2016.

[33] S. Kochmann, T. Hirsch, and O. S. Wolfbeis, “Graphenes in chemical sensors and biosensors,” *TrAC - Trends in Analytical Chemistry*, vol. 39. pp. 87–113, 2012.

[34] C. Zhu, S. Guo, Y. Fang, and S. Dong, “Reducing Sugar: New Functional Molecules for the Green Synthesis of Graphene Nanosheets,” *ACS Nano*, vol. 4, no. 4, pp. 2429–2437, 2010.

[35] M. F. Abdullah, R. Zakaria, and S. H. S. Zein, “Green tea polyphenol–reduced graphene oxide: derivatisation, reduction efficiency, reduction mechanism and cytotoxicity,” *RSC Adv.*, vol. 4, no. 65, p. 34510, 2014.

[36] M. F. El-Kady and R. B. Kaner, “Direct Laser Writing of Graphene Electronics,” *ACS Nano*, vol. 8, no. 9, pp. 8725–8729, 2014.

[37] E. E. Ghadim, N. Rashidi, S. Kimiagar, O. Akhavan, F. Manouchehri, and E. Ghaderi, “Pulsed laser irradiation for environment friendly reduction of graphene oxide suspensions,” *Appl. Surf. Sci.*, vol. 301, pp. 183–188, 2014.

[38] C. Sorensen, A. Nepal, and G. P. Singh, “Process for high-yield production of

graphene via detonation of carbon-containing material." Google Patents, 13-Sep-2016.

[39] K. S. Novoselov, V. I. Fal'ko, L. Colombo, P. R. Gellert, M. G. Schwab, and K. Kim, "A roadmap for graphene.," *Nature*, vol. 490, no. 7419, pp. 192–200, 2012.

[40] R. Rozada, J. I. Paredes, S. Villar-Rodil, A. Martínez-Alonso, and J. M. D. Tascón, "Towards full repair of defects in reduced graphene oxide films by two-step graphitization," *Nano Res.*, vol. 6, no. 3, pp. 216–233, 2013.

[41] S. Pei and H. M. Cheng, "The reduction of graphene oxide," *Carbon*, vol. 50, no. 9. pp. 3210–3228, 2012.

[42] D. R. Dreyer, S. Park, C. W. Bielawski, and R. S. Ruoff, "The chemistry of graphene oxide.," *Chem. Soc. Rev.*, vol. 39, no. 1, pp. 228–240, 2010.

[43] C. Soldano, A. Mahmood, and E. Dujardin, "Production, properties and potential of graphene," *Carbon N. Y.*, vol. 48, no. 8, pp. 2127–2150, 2010.

[44] S. Park, J. An, J. R. Potts, A. Velamakanni, S. Murali, and R. S. Ruoff, "Hydrazine-reduction of graphite- and graphene oxide," *Carbon N. Y.*, vol. 49, no. 9, pp. 3019–3023, 2011.

[45] G. Eda, G. Fanchini, and M. Chhowalla, "Large-area ultrathin films of reduced graphene oxide as a transparent and flexible electronic material.," *Nature nanotechnology*, vol. 3, no. 5. pp. 270–274, 2008.

[46] M. J. Fernández-Merino, L. Guardia, J. I. Paredes, S. Villar-Rodil, P. Solís-Fernández, A. Martínez-Alonso, and J. M. D. Tascón, "Vitamin C Is an Ideal Substitute for Hydrazine in the Reduction of Graphene Oxide Suspensions," *J. Phy. Chem. C*, vol. 114, p. 6426, 2010.

[47] C. Liu, K. Wang, S. Luo, Y. Tang, and L. Chen, "Direct Electrodeposition of Graphene Enabling the One-Step Synthesis of Graphene-Metal Nanocomposite Films," *Small*, vol. 7, no. 9, pp. 1203–1206, 2011.

[48] J. Yang and S. Gunasekaran, "Electrochemically reduced graphene oxide sheets for use in high performance supercapacitors," *Carbon N. Y.*, vol. 51, pp. 36–44, 2013.

[49] V. H. Pham, T. V. Cuong, S. H. Hur, E. W. Shin, J. S. Kim, J. S. Chung, and E. J. Kim, "Fast and simple fabrication of a large transparent chemically-converted graphene film by spray-coating," *Carbon N. Y.*, vol. 48, no. 7, pp. 1945–1951,

2010.

[50] X. Wang, L. Zhi, and K. Müllen, “Transparent, conductive graphene electrodes for dye-sensitized solar cells,” *Nano Lett.*, vol. 8, no. 1, pp. 323–327, 2008.

[51] X. Li, H. Wang, J. T. Robinson, H. Sanchez, G. Diankov, and H. Dai, “Simultaneous Nitrogen Doping and Reduction of Graphene Oxide,” *J. Am. Chem. Soc.*, vol. 131, no. 43, pp. 15939–15944, 2009.

[52] C. Vallés, J. David Núñez, A. M. Benito, and W. K. Maser, “Flexible conductive graphene paper obtained by direct and gentle annealing of graphene oxide paper,” *Carbon N. Y.*, vol. 50, no. 3, pp. 835–844, 2012.

[53] W. Xiong, Y. S. Zhou, W. J. Hou, L. J. Jiang, Y. Gao, L. S. Fan, L. Jiang, J. F. Silvain, and Y. F. Lu, “Direct writing of graphene patterns on insulating substrates under ambient conditions.,” *Sci. Rep.*, vol. 4, p. 4892, 2014.

[54] L. Guardia, S. Villar-Rodil, J. I. Paredes, R. Rozada, A. Martínez-Alonso, and J. M. D. Tascón, “UV light exposure of aqueous graphene oxide suspensions to promote their direct reduction, formation of graphene-metal nanoparticle hybrids and dye degradation,” *Carbon N. Y.*, vol. 50, pp. 1014–1024, 2012.

[55] G. Uses, “Graphene oxide,” 2017, webpage: http://www.graphene-uses.com/graphene-oxide/, accessed on 25-Apr-2017.

[56] D. Li, M. B. Müller, S. Gilje, R. B. Kaner, and G. G. Wallace, “Processable aqueous dispersions of graphene nanosheets,” *Nat. Nanotechnol.*, vol. 3, no. 2, pp. 101–105, 2008.

[57] M. F. El-Kady, V. Strong, S. Dubin, and R. B. Kaner, “Laser Scribing of High-Performance and Flexible Graphene-Based Electrochemical Capacitors,” *Science*, vol. 335. pp. 1326–1330, 2012.

[58] A. Bianco, H.-M. Cheng, T. Enoki, Y. Gogotsi, R. H. Hurt, N. Koratkar, T. Kyotani, M. Monthioux, C. R. Park, J. M. D. Tascon, and J. Zhang, “All in the graphene family – A recommended nomenclature for two-dimensional carbon materials,” *Carbon N. Y.*, vol. 65, pp. 1–6, 2013.

[59] P. Wick, A. E. Louw-Gaume, M. Kucki, H. F. Krug, K. Kostarelos, B. Fadeel, K. a Dawson, A. Salvati, E. Vázquez, L. Ballerini, M. Tretiach, F. Benfenati, E. Flahaut, L. Gauthier, M. Prato, and A. Bianco, “Classification framework for graphene-based materials,” *Angewandte Chemie - International Edition*, vol. 53, no. 30. pp. 7714–7718, 2014.

[60] V. C. Sanchez, A. Jachak, R. H. Hurt, and A. B. Kane, “Biological interactions of graphene-family nanomaterials: An interdisciplinary review,” *Chemical Research in Toxicology*, vol. 25, no. 1. pp. 15–34, 2012.

[61] X. Guo and N. Mei, “Assessment of the toxic potential of graphene family nanomaterials.,” *J. food drug Anal.*, vol. 22, no. 1, pp. 105–15, 2014.

[62] E. P. Randviir, D. A. C. Brownson, and C. E. Banks, “A decade of graphene research: production, applications and outlook,” *Mater. Today*, vol. 17, no. 9, pp. 426–432, 2014.

[63] N. Jing, Q. Xue, C. Ling, M. Shan, T. Zhang, X. Zhou, and Z. Jiao, “Effect of defects on Young’s modulus of graphene sheets: a molecular dynamics simulation,” *RSC Adv.*, vol. 2, no. 24, p. 9124, 2012.

[64] K. I. and M. K. and T. S. and Y. Awano, “Electrical Resistivity Measurements of Layer Number Determined Multilayer Graphene Wiring for Future Large Scale Integrated Circuit Interconnects,” *Jpn. J. Appl. Phys.*, vol. 52, no. 6S, 2013.

[65] Y. Y. Zhang and Y. T. Gu, “Mechanical properties of graphene: Effects of layer number, temperature and isotope,” *Comput. Mater. Sci.*, vol. 71, pp. 197–200, 2013.

[66] B. M. John, S. W. Mugo, N. S. Timonah, P. K. Ngumbi, and P. K. Ngumbi, “Correlation Of Optical Transmittance With Number Of Graphene Layers,” *IOSR J. Appl. Phys.*, vol. 8, no. 1, pp. 42–46, 2016.

[67] S.-J. P. and K.-S. Kim, “Surface Characterization of Carbon Materials by X-ray Photoelectron Spectroscopy,” *Microsc. Sci. Technol. Appl. Educ.*, 2010.

[68] D. Q. McNerny, B. Viswanath, D. Copic, F. R. Laye, C. Prohoda, A. C. Brieland-Shoultz, E. S. Polsen, N. T. Dee, V. S. Veerasamy, and a J. Hart, “Direct fabrication of graphene on SiO2 enabled by thin film stress engineering.,” *Sci. Rep.*, vol. 4, p. 5049, 2014.

[69] Thermo Fisher Scientific, “Lasurface com database.”, webpage: http://www.lasurface.com/database/elementxps.php, accessed on 20-Aug-2015.

[70] National Institute of Standards and Technology, “XPS database.", webpage: http://srdata.nist.gov/xps/EnergyTypeValSrch.aspx, accessed on 20-Aug-2015.

[71] J. E. Morris and K. Iniewski, “Direct graphene growth on dielectric substrates,”

in *Graphene Carbon Nanotubes and Nanostructures: Techniques and Applications*, CRC Press, 2013.

[72] R. Lv, Q. Li, A. R. Botello-Méndez, T. Hayashi, B. Wang, A. Berkdemir, Q. Hao, A. L. Elías, R. Cruz-Silva, H. R. Gutiérrez, Y. A. Kim, H. Muramatsu, J. Zhu, M. Endo, H. Terrones, J.-C. Charlier, M. Pan, and M. Terrones, "Nitrogen-doped graphene: beyond single substitution and enhanced molecular sensing," *Scientific Reports*, vol. 2. 2012.

[73] S. Kaciulis, "Spectroscopy of carbon: From diamond to nitride films," in *Surface and Interface Analysis*, vol. 44, no. 8, pp. 1155–1161, 2012.

[74] D. A. C. Brownson, S. A. Varey, F. Hussain, S. J. Haigh, and C. E. Banks, "Electrochemical properties of CVD grown pristine graphene: Monolayer- vs. quasi-graphene," *Nanoscale*, vol. 6, no. 3, pp. 1607–1621, 2014.

[75] X. Liang, B. A. Sperling, I. Calizo, G. Cheng, C. A. Hacker, Q. Zhang, Y. Obeng, K. Yan, H. Peng, Q. Li, X. Zhu, H. Yuan, A. R. Hight Walker, Z. Liu, L. Peng, and C. A. Richter, "Toward Clean and Crackless Transfer of Graphene," *ACS Nano*, vol. 5, no. 11, pp. 9144–9153, 2011.

[76] M. Boutchich, A. Jaffré, D. Alamarguy, J. Alvarez, A. Barras, Y. Tanizawa, R. Tero, H. Okada, T. V Thu, J. P. Kleider, and A. Sandhu, "Characterization of graphene oxide reduced through chemical and biological processes," *J. Phys. Conf. Ser.*, vol. 433, p. 12001, 2013.

[77] O. Akhavan, "The effect of heat treatment on formation of graphene thin films from graphene oxide nanosheets," *Carbon N. Y.*, vol. 48, p. 509, 2010.

[78] X. Dong, C.-Y. Su, W. Zhang, J. Zhao, Q. Ling, W. Huang, P. Chen, and L.-J. Li, "Ultra-large single-layer graphene obtained from solution chemical reduction and its electrical properties.," *Phys. Chem. Chem. Phys.*, vol. 12, no. 9, pp. 2164–2169, 2010.

[79] W. Chen, L. Yan, and P. R. Bangal, "Chemical reduction of graphene oxide to graphene by sulfur-containing compounds," *J. Phys. Chem. C*, vol. 114, no. 47, pp. 19885–19890, 2010.

[80] D. A. Sokolov, C. M. Rouleau, D. B. Geohegan, and T. M. Orlando, "Excimer laser reduction and patterning of graphite oxide," *Carbon N. Y.*, vol. 53, pp. 81–89, 2013.

[81] S. Vadahanambi, J.-H. Jung, and I.-K. Oh, "Microwave syntheses of graphene

and graphene decorated with metal nanoparticles," *Carbon N. Y.*, vol. 49, no. 13, pp. 4449–4457, 2011.

[82] F. T. Johra, J.-W. Lee, and W.-G. Jung, "Facile and safe graphene preparation on solution based platform," *J. Ind. Eng. Chem.*, vol. 20, no. 5, pp. 2883–2887, 2014.

[83] L. Y. Meng and S. J. Park, "Preparation and characterization of reduced graphene nanosheets via pre-exfoliation of graphite flakes," *Bull. Korean Chem. Soc.*, vol. 33, no. 1, pp. 209–214, 2012.

[84] B. Dai, L. Fu, L. Liao, N. Liu, K. Yan, Y. Chen, and Z. Liu, "High-quality single-layer graphene via reparative reduction of graphene oxide," *Nano Res.*, vol. 4, no. 5, pp. 434–439, 2011.

[85] D. Yang, A. Velamakanni, G. Bozoklu, S. Park, M. Stoller, R. D. Piner, S. Stankovich, I. Jung, D. A. Field, C. A. Ventrice, and R. S. Ruoff, "Chemical analysis of graphene oxide films after heat and chemical treatments by X-ray photoelectron and Micro-Raman spectroscopy," *Carbon N. Y.*, vol. 47, no. 1, pp. 145–152, 2009.

[86] A. C. Ferrari, J. C. Meyer, V. Scardaci, C. Casiraghi, M. Lazzeri, F. Mauri, S. Piscanec, D. Jiang, K. S. Novoselov, S. Roth, and A. K. Geim, "Raman spectrum of graphene and graphene layers," *Phys. Rev. Lett.*, vol. 97, no. 18, 2006.

[87] J. R. Gong, "Chapter 9: Graphene nanowalls," in *New Progress on Graphene Research*, InTech, 2013.

[88] M. Hulman, M. Haluška, G. Scalia, D. Obergfell, and S. Roth, "Effects of Charge Impurities and Laser Energy on Raman Spectra of Graphene," *Nano Lett.*, vol. 8, no. 11, pp. 3594–3597, 2008.

[89] A. Eckmann, A. Felten, A. Mishchenko, L. Britnell, R. Krupke, K. S. Novoselov, and C. Casiraghi, "Probing the nature of defects in graphene by Raman spectroscopy," *Nano Lett.*, vol. 12, no. 8, pp. 3925–3930, 2012.

[90] J. Hong, M. K. Park, E. J. Lee, D. Lee, D. S. Hwang, and S. Ryu, "Origin of New Broad Raman D and G Peaks in Annealed Graphene," *Sci. Rep.*, vol. 3, 2013.

[91] J. Robinson, X. Weng, K. Trumbull, R. Cavalero, M. Wetherington, E. Frantz, M. LaBella, Z. Hughes, M. Fanton, and D. Snyder, "Nucleation of epitaxial graphene on SiC(0001)," *ACS Nano*, vol. 4, no. 1, pp. 153–158, 2010.

[92] A. Umair and H. Raza, “Controlled synthesis of bilayer graphene on nickel,” *Nanoscale Research Letters*, vol. 7, no. 1. p. 437, 2012.

[93] D. Wei and X. Xu, “Laser direct growth of graphene on silicon substrate,” *Appl. Phys. Lett.*, vol. 100, no. 2, 2012.

[94] X. Huang, S. Li, Z. Qi, W. Zhang, W. Ye, and Y. Fang, “Low defect concentration few-layer graphene using a two-step electrochemical exfoliation,” *Nanotechnology*, vol. 26, no. 10, p. 105602, 2015.

[95] V. T. Nguyen, H. D. Le, V. C. Nguyen, T. T. Tam Ngo, D. Q. Le, X. N. Nguyen, and N. M. Phan, “Synthesis of multi-layer graphene films on copper tape by atmospheric pressure chemical vapor deposition method,” *Adv. Nat. Sci. Nanosci. Nanotechnol.*, vol. 4, no. 3, p. 35012, 2013.

[96] J. D. Fowler, M. J. Allen, V. C. Tung, Y. Yang, R. B. Kaner, and B. H. Weiller, “Practical Chemical Sensors from Chemically Derived Graphene,” *ACS Nano*, vol. 3, no. 2, pp. 301–306, 2009.

[97] D. Zhan, Z. Ni, W. Chen, L. Sun, Z. Luo, L. Lai, T. Yu, A. T. S. Wee, and Z. Shen, “Electronic structure of graphite oxide and thermally reduced graphite oxide,” *Carbon N. Y.*, vol. 49, no. 4, pp. 1362–1366, 2011.

[98] A. C. Ferrari and D. M. Basko, “Raman spectroscopy as a versatile tool for studying the properties of graphene,” *Nat. Nanotechnol.*, vol. 8, no. 4, pp. 235–246, 2013.

[99] L. M. Malard, M. A. Pimenta, G. Dresselhaus, and M. S. Dresselhaus, “Raman spectroscopy in graphene,” *Physics Reports*, vol. 473, no. 5–6. pp. 51–87, 2009.

[100] J. Lee, K. S. Novoselov, and H. S. Shin, “Interaction between metal and graphene: Dependence on the layer number of graphene,” *ACS Nano*, vol. 5, no. 1, pp. 608–612, 2011.

[101] S. Ryu, J. Maultzsch, M. Y. Han, P. Kim, and L. E. Brus, “Raman spectroscopy of lithographically patterned graphene nanoribbons,” *ACS Nano*, vol. 5, no. 5, pp. 4123–4130, 2011.

[102] S. Sahoo, G. Khurana, S. K. Barik, S. Dussan, D. Barrionuevo, and R. S. Katiyar, “In situ raman studies of electrically reduced graphene oxide and its field-emission properties,” *J. Phys. Chem. C*, vol. 117, no. 10, pp. 5485–5491, 2013.

[103] K. Ai, Y. Liu, L. Lu, X. Cheng, and L. Huo, “A novel strategy for making soluble

reduced graphene oxide sheets cheaply by adopting an endogenous reducing agent," *J. Mater. Chem.*, vol. 21, p. 3365, 2011.

[104] P. Cui, J. Lee, E. Hwang, and H. Lee, "One-pot reduction of graphene oxide at subzero temperatures," *Chemical Communications*, vol. 47, no. 45. p. 12370, 2011.

[105] H. C. and Y. P. C. Isaac Childres, Luis A. Jauregui, Wonjun Park, "Chapter 19 RAMAN SPECTROSCOPY OF GRAPHENE AND RELATED MATERIALS," in *New Developments in Photon and Materials Research*, 2013.

[106] Y. Y. Wang, Z. H. Ni, T. Yu, Z. X. Shen, H. M. Wang, Y. H. Wu, W. Chen, and A. T. S. Wee, "Raman studies of monolayer graphene: The substrate effect," *J. Phys. Chem. C*, vol. 112, no. 29, pp. 10637–10640, 2008.

[107] J. Song, C. Yang, H. Hu, X. Dai, C. Wang, and H. Zhang, "Penetration depth at various Raman excitation wavelengths and stress model for Raman spectrum in biaxially-strained Si," *Sci. China Physics, Mech. Astron.*, vol. 56, no. 11, pp. 2065–2070, 2013.

[108] C. Casiraghi, S. Pisana, K. S. Novoselov, A. K. Geim, and A. C. Ferrari, "Raman fingerprint of charged impurities in graphene," *Appl. Phys. Lett.*, vol. 91, no. 23, 2007.

[109] S. Berciaud, S. Ryu, L. E. Brus, and T. F. Heinz, "Probing the Intrinsic properties of exfoliated graphene: Raman spectroscopy of free-standing monolayers," *Nano Lett.*, vol. 9, no. 1, pp. 346–352, 2009.

[110] T. Kuila, S. Bose, P. Khanra, A. K. Mishra, N. H. Kim, and J. H. Lee, "Recent advances in graphene-based biosensors," *Biosensors and Bioelectronics*, vol. 26. pp. 4637–4648, 2011.

[111] Y. Liu, X. Dong, and P. Chen, "Biological and chemical sensors based on graphene materials," *Chem. Soc. Rev.*, vol. 41, no. 6, pp. 2283–2307, 2012.

[112] A. Y. Zhu, F. Yi, J. C. Reed, H. Zhu, and E. Cubukcu, "Optoelectromechanical Multimodal Biosensor with Graphene Active Region," *Nano Lett.*, vol. 14, no. 10, pp. 5641–5649, 2014.

[113] P. Labroo and Y. Cui, "Graphene nano-ink biosensor arrays on a microfluidic paper for multiplexed detection of metabolites.," *Anal. Chim. Acta*, vol. 813, pp. 90–6, 2014.

[114] N. Lei, P. Li, W. Xue, and J. Xu, “Simple graphene chemiresistors as pH sensors: fabrication and characterization,” *Meas. Sci. Technol.*, vol. 22, no. 10, p. 107002, 2011.

[115] Y. Ohno, K. Maehashi, Y. Yamashiro, and K. Matsumoto, “Electrolyte-Gated Graphene Field-Effect Transistors for Detecting pH and Protein Adsorption,” *Nano Lett.*, vol. 9, no. 9, pp. 3318–3322, 2009.

[116] M. Soikkeli, K. Kurppa, M. Kainlauri, S. Arpiainen, A. Paananen, D. Gunnarsson, J. J. Joensuu, P. Laaksonen, M. Prunnila, M. B. Linder, and J. Ahopelto, “Graphene Biosensor Programming with Genetically Engineered Fusion Protein Monolayers,” *ACS Appl. Mater. Interfaces*, vol. 8, no. 12, pp. 8257–8264, 2016.

[117] Y. Shao, J. Wang, H. Wu, J. Liu, I. A. Aksay, and Y. Lin, “Graphene Based Electrochemical Sensors and Biosensors: A Review,” *Electroanalysis*, vol. 22, no. 10, pp. 1027–1036, 2010.

[118] A. Bonanni, A. Ambrosi, and M. Pumera, “Nucleic Acid Functionalized Graphene for Biosensing,” *Chem. – A Eur. J.*, vol. 18, no. 6, pp. 1668–1673, 2012.

[119] M. Zhou, Y. Zhai, and S. Dong, “Electrochemical Sensing and Biosensing Platform Based on Chemically Reduced Graphene Oxide,” *Anal. Chem.*, vol. 81, no. 14, pp. 5603–5613, 2009.

[120] L. Yang, D. Liu, J. Huang, and T. You, “Simultaneous determination of dopamine, ascorbic acid and uric acid at electrochemically reduced graphene oxide modified electrode,” *Sensors Actuators B Chem.*, vol. 193, pp. 166–172, 2014.

[121] J. Lin, Z. Peng, Y. Liu, F. Ruiz-Zepeda, R. Ye, E. L. G. Samuel, M. J. Yacaman, B. I. Yakobson, and J. M. Tour, “Laser-induced porous graphene films from commercial polymers,” *Nat. Commun.*, vol. 5, p. 5714, 2014.

[122] F. Tehrani and B. Bavarian, “Facile and scalable disposable sensor based on laser engraved graphene for electrochemical detection of glucose,” *Sci. Rep.*, vol. 6, p. 27975, 2016.

[123] S. Kumar, S. Kumar, S. Srivastava, B. K. Yadav, S. H. Lee, J. G. Sharma, D. C. Doval, and B. D. Malhotra, “Reduced graphene oxide modified smart conducting paper for cancer biosensor,” *Biosens. Bioelectron.*, vol. 73, pp. 114–122, 2015.

[124] J. Ping, Y. Wang, K. Fan, J. Wu, and Y. Ying, “Direct electrochemical reduction of graphene oxide on ionic liquid doped screen-printed electrode and its

electrochemical biosensing application," *Biosens. Bioelectron.*, vol. 28, no. 1, pp. 204–209, 2011.

[125] A.-M. J. Haque, H. Park, D. Sung, S. Jon, S.-Y. Choi, and K. Kim, "An Electrochemically Reduced Graphene Oxide-Based Electrochemical Immunosensing Platform for Ultrasensitive Antigen Detection," *Anal. Chem.*, vol. 84, no. 4, pp. 1871–1878, 2012.

[126] B. Cai, S. Wang, L. Huang, Y. Ning, Z. Zhang, and G.-J. Zhang, "Ultrasensitive Label-Free Detection of PNA–DNA Hybridization by Reduced Graphene Oxide Field-Effect Transistor Biosensor," *ACS Nano*, vol. 8, no. 3, pp. 2632–2638, 2014.

[127] Q. He, H. G. Sudibya, Z. Yin, S. Wu, H. Li, F. Boey, W. Huang, P. Chen, and H. Zhang, "Centimeter-Long and Large-Scale Micropatterns of Reduced Graphene Oxide Films: Fabrication and Sensing Applications," *ACS Nano*, vol. 4, no. 6, pp. 3201–3208, 2010.

[128] C. Reiner-Rozman, C. Kotlowski, and W. Knoll, "Electronic Biosensing with Functionalized rGO FETs," *Biosensors*, vol. 6, no. 2, p. 17, 2016.

[129] C. Andronescu and W. Schuhmann, "Graphene-based field effect transistors as biosensors," *Curr. Opin. Electrochem.*, 2017.

[130] E. Morales-Narváez and A. Merkoçi, "Graphene Oxide as an Optical Biosensing Platform," *Adv. Mater.*, vol. 24, no. 25, pp. 3298–3308, 2012.

[131] Z. Wang, P. Huang, A. Bhirde, A. Jin, Y. Ma, G. Niu, N. Neamati, and X. Chen, "A nanoscale graphene oxide–peptide biosensor for real-time specific biomarker detection on the cell surface," *Chem. Commun.*, vol. 48, no. 78, p. 9768, 2012.

[132] E. Jenrette, S. K. Pradhan, G. Rutherford, J. Flowers, D. Ha, and A. K. Pradhan, "Quantum-dot-conjugated graphene oxide as an optical tool for biosensor," *Opt. Express*, vol. 23, no. 19, p. 25017, 2015.

[133] M. Li, X. Zhou, S. Guo, and N. Wu, "Detection of lead (II) with a 'turn-on' fluorescent biosensor based on energy transfer from CdSe/ZnS quantum dots to graphene oxide," *Biosens. Bioelectron.*, vol. 43, pp. 69–74, 2013.

[134] S. Roy, N. Soin, R. Bajpai, D. S. Misra, J. A. McLaughlin, and S. S. Roy, "Graphene oxide for electrochemical sensing applications," *J. Mater. Chem.*, vol. 21, no. 38, p. 14725, 2011.

[135] Y. V. Stebunov, O. A. Aftenieva, A. V. Arsenin, and V. S. Volkov, “Highly Sensitive and Selective Sensor Chips with Graphene-Oxide Linking Layer,” *ACS Appl. Mater. Interfaces*, vol. 7, no. 39, pp. 21727–21734, 2015.

[136] Moscow Institute of Physics and Technology, “Researchers design, patent graphene biosensors,” *Science Daily*, 2015, webpage: https://www.sciencedaily.com/releases/2015/11/151113112412.htm, accessed on 20-May-2016.

[137] M. F. C. and I. K. and M. D. B. and S. Russo, “Properties and applications of chemically functionalized graphene,” *J. Phys. Condens. Matter*, vol. 25, no. 42, p. 423201, 2013.

[138] H. Zhang, E. Bekyarova, J.-W. Huang, Z. Zhao, W. Bao, F. Wang, R. C. Haddon, and C. N. Lau, “Aryl Functionalization as a Route to Band Gap Engineering in Single Layer Graphene Devices,” *Nano Lett.*, vol. 11, no. 10, pp. 4047–4051, 2011.

[139] T. Kuila, S. Bose, A. K. Mishra, P. Khanra, N. H. Kim, and J. H. Lee, “Chemical functionalization of graphene and its applications,” *Prog. Mater. Sci.*, vol. 57, no. 7, pp. 1061–1105, 2012.

[140] Y. Guo, J. Li, and S. Dong, “Hemin functionalized graphene nanosheets-based dual biosensor platforms for hydrogen peroxide and glucose,” *Sensors Actuators B Chem.*, vol. 160, no. 1, pp. 295–300, 2011.

[141] I. Childres, L. A. Jauregui, J. Tian, and Y. P. Chen, “Effect of oxygen plasma etching on graphene studied using Raman spectroscopy and electronic transport measurements,” *New J. Phys.*, vol. 13, 2011.

[142] S. Trammell, S. Hernández, R. Myers-Ward, D. Zabetakis, D. Stenger, D. Gaskill, and S. Walton, “Plasma-Modified, Epitaxial Fabricated Graphene on SiC for the Electrochemical Detection of TNT,” *Sensors*, vol. 16, no. 8, p. 1281, 2016.

[143] N. Mohanty and V. Berry, “Graphene-Based Single-Bacterium Resolution Biodevice and DNA Transistor: Interfacing Graphene Derivatives with Nanoscale and Microscale Biocomponents,” *Nano Lett.*, vol. 8, no. 12, pp. 4469–4476, 2008.

[144] R. K. Srivastava, S. Srivastava, T. N. Narayanan, B. D. Mahlotra, R. Vajtai, P. M. Ajayan, and A. Srivastava, “Functionalized Multilayered Graphene Platform for Urea Sensor,” *ACS Nano*, vol. 6, no. 1, pp. 168–175, 2011.

[145] C. Shan, H. Yang, J. Song, D. Han, A. Ivaska, and L. Niu, “Direct Electrochemistry of Glucose Oxidase and Biosensing for Glucose Based on Graphene Direct Electrochemistry of Glucose Oxidase and Biosensing for Glucose Based on Graphene,” *Anal. Chem.*, 2009.

[146] D. Du, Z. Zou, Y. Shin, J. Wang, H. Wu, M. H. Engelhard, J. Liu, I. A. Aksay, and Y. Lin, “Sensitive Immunosensor for Cancer Biomarker Based on Dual Signal Amplification Strategy of Graphene Sheets and Multienzyme Functionalized Carbon Nanospheres,” *Anal. Chem.*, vol. 82, no. 7, pp. 2989–2995, 2010.

[147] H. V. Tran, B. Piro, S. Reisberg, L. Huy Nguyen, T. Dung Nguyen, H. T. Duc, and M. C. Pham, “An electrochemical ELISA-like immunosensor for miRNAs detection based on screen-printed gold electrodes modified with reduced graphene oxide and carbon nanotubes,” *Biosens. Bioelectron.*, vol. 62, pp. 25–30, 2014.

[148] J. Park and M. Yan, “Covalent functionalization of graphene with reactive intermediates,” *Acc. Chem. Res.*, vol. 46, pp. 181–189, 2013.

[149] S. Eissa, G. C. Jimenez, F. Mahvash, A. Guermoune, C. Tlili, T. Szkopek, M. Zourob, and M. Siaj, “Functionalized CVD monolayer graphene for label-free impedimetric biosensing,” *Nano Res.*, 2015.

[150] S. Eissa, C. Tlili, L. L’Hocine, and M. Zourob, “Electrochemical immunosensor for the milk allergen Beta-lactoglobulin based on electrografting of organic film on graphene modified screen-printed carbon electrodes,” *Biosens. Bioelectron.*, vol. 38, no. 1, pp. 308–313, 2012.

[151] L. Zhou, H. Mao, C. Wu, L. Tang, Z. Wu, H. Sun, H. Zhang, H. Zhou, C. Jia, Q. Jin, X. Chen, and J. Zhao, “Label-free graphene biosensor targeting cancer molecules based on non-covalent modification,” *Biosens. Bioelectron.*, vol. 87, pp. 701–707, 2017.

[152] V. K. Kodali, J. Scrimgeour, S. Kim, J. H. Hankinson, K. M. Carroll, W. A. de Heer, C. Berger, and J. E. Curtis, “Nonperturbative Chemical Modification of Graphene for Protein Micropatterning,” *Langmuir*, vol. 27, no. 3, pp. 863–865, 2011.

[153] R. Stine, J. T. Robinson, P. E. Sheehan, and C. R. Tamanaha, “Real-Time DNA Detection Using Reduced Graphene Oxide Field Effect Transistors,” *Adv. Mater.*, vol. 22, no. 46, pp. 5297–5300, 2010.

[154] X. Dong, Y. Shi, W. Huang, P. Chen, and L. J. Li, “Electrical detection of DNA hybridization with single-base specificity using transistors based on CVD-grown graphene sheets,” *Adv. Mater.*, vol. 22, no. 14, pp. 1649–1653, 2010.

[155] I. Shown and A. Ganguly, “Non-covalent functionalization of CVD-grown graphene with Au nanoparticles for electrochemical sensing application,” *J. Nanostructure Chem.*, vol. 6, no. 4, pp. 281–288, 2016.

[156] J. C. Claussen, A. Kumar, D. B. Jaroch, M. H. Khawaja, A. B. Hibbard, D. M. Porterfield, and T. S. Fisher, “Nanostructuring Platinum Nanoparticles on Multilayered Graphene Petal Nanosheets for Electrochemical Biosensing,” *Adv. Funct. Mater.*, vol. 22, no. 16, pp. 3399–3405, 2012.

[157] S. Mao, G. Lu, K. Yu, Z. Bo, and J. Chen, “Specific protein detection using thermally reduced graphene oxide sheet decorated with gold nanoparticle-antibody conjugates,” *Adv. Mater.*, vol. 22, no. 32, pp. 3521–3526, 2010.

[158] B. D. Ossonon and D. Bélanger, “Functionalization of graphene sheets by the diazonium chemistry during electrochemical exfoliation of graphite,” *Carbon N. Y.*, vol. 111, pp. 83–93, 2017.

[159] Y. Xu, H. Bai, G. Lu, C. Li, and G. Shi, “Flexible Graphene Films via the Filtration of Water-Soluble Noncovalent Functionalized Graphene Sheets,” *J. Am. Chem. Soc.*, vol. 130, no. 18, pp. 5856–5857, 2008.

[160] L.-H. Liu, M. M. Lerner, and M. Yan, “Derivitization of Pristine Graphene with Well-Defined Chemical Functionalities,” *Nano Lett.*, vol. 10, no. 9, pp. 3754–3756, 2010.

[161] J. Wang, Y. Zhao, F.-X. Ma, K. Wang, F.-B. Wang, and X.-H. Xia, “Synthesis of a hydrophilic poly-l-lysine/graphene hybrid through multiple non-covalent interactions for biosensors,” *J. Mater. Chem. B*, vol. 1, no. 10, p. 1406, 2013.

[162] V. F. Lvovich, “Chapter 1. Fundamentals of electrochemical impedance spectroscopy,” in *Impedance Spectroscopy: Applications to Electrochemical and Dielectric Phenomena*, Wiley, 2012, pp. 1–19.

[163] E. Barsoukov and J. R. Macdonald, “Chapter 1. Fundamentals of Impedance Spectroscopy,” in *Impedance Spectroscopy: Theory, Experiment, and Applications*, 2nd Ed., Wiley, 2005.

[164] Y. Barsukov and J. R. Macdonald, “Electrochemical Impedance Spectroscopy,” in *Characterization of Materials*, John Wiley & Sons, Inc., 2002.

[165] D. V Ribeiro and J. C. C. Abrantes, “Application of electrochemical impedance spectroscopy (EIS) to monitor the corrosion of reinforced concrete: A new approach,” *Constr. Build. Mater.*, vol. 111, pp. 98–104, 2016.

[166] M. Ates, “Review study of electrochemical impedance spectroscopy and equivalent electrical circuits of conducting polymers on carbon surfaces,” *Prog. Org. Coatings*, vol. 71, no. 1, pp. 1–10, 2011.

[167] G. Bierwagen, D. Tallman, J. Li, L. He, and C. Jeffcoate, “{EIS} studies of coated metals in accelerated exposure,” *Prog. Org. Coatings*, vol. 46, no. 2, pp. 149–158, 2003.

[168] S. S. Zhang, K. Xu, and T. R. Jow, “{EIS} study on the formation of solid electrolyte interface in Li-ion battery,” *Electrochim. Acta*, vol. 51, no. 8–9, pp. 1636–1640, 2006.

[169] U. Tröltzsch, O. Kanoun, and H.-R. Tränkler, “Characterizing aging effects of lithium ion batteries by impedance spectroscopy,” *Electrochim. Acta*, vol. 51, no. 8–9, pp. 1664–1672, 2006.

[170] B. Pejcic and R. De Marco, “Impedance spectroscopy: Over 35 years of electrochemical sensor optimization,” *Electrochim. Acta*, vol. 51, no. 28, pp. 6217–6229, 2006.

[171] A. Lasia, “Dispersion of Impedances at Solid Electrodes,” in *Electrochemical Impedance Spectroscopy and its Applications*, Springer, pp. 177–201, 2014.

[172] A. Lasia, “Impedance of the Faradaic Reactions in the Presence of Mass Transfer,” in *Electrochemical Impedance Spectroscopy and its Applications*, Springer, pp. 85–125, 2014.

[173] E. Katz and I. Willner, “Probing Biomolecular Interactions at Conductive and Semiconductive Surfaces by Impedance Spectroscopy: Routes to Impedimetric Immunosensors, DNA-Sensors, and Enzyme Biosensors,” *Electroanalysis*, vol. 15, no. 11, pp. 913–947, 2003.

[174] M. S. Chiriacò, F. de Feo, E. Primiceri, A. G. Monteduro, G. E. de Benedetto, A. Pennetta, R. Rinaldi, and G. Maruccio, “Portable gliadin-immunochip for contamination control on the food production chain,” *Talanta*, vol. 142, pp. 57–63, 2015.

[175] J. J. D. and P. R. Bueno, “Fundamentals and Applications of Impedimetric and Redox Capacitive Biosensors,” *Journal of Analytical & Bioanalytical Techniques*,

vol. 0, no. 0. OMICS Group Inc., 2014.

[176] M. Braiek, K. Rokbani, A. Chrouda, B. Mrabet, A. Bakhrouf, A. Maaref, and N. Jaffrezic-Renault, “An Electrochemical Immunosensor for Detection of Staphylococcus aureus Bacteria Based on Immobilization of Antibodies on Self-Assembled Monolayers-Functionalized Gold Electrode,” *Biosensors*, vol. 2, no. 4, pp. 417–426, 2012.

[177] A. Bogomolova, E. Komarova, K. Reber, T. Gerasimov, O. Yavuz, S. Bhatt, and M. Aldissi, “Challenges of Electrochemical Impedance Spectroscopy in Protein Biosensing,” *Anal. Chem.*, vol. 81, no. 10, pp. 3944–3949, 2009.

[178] I. I. Suni, “Impedance methods for electrochemical sensors using nanomaterials,” *TrAC Trends Anal. Chem.*, vol. 27, no. 7, pp. 604–611, 2008.

[179] X. Liu, Y. Li, J. Zheng, J. Zhang, and Q. Sheng, “Carbon nanotube-enhanced electrochemical aptasensor for the detection of thrombin,” *Talanta*, vol. 81, no. 4–5, pp. 1619–1624, 2010.

[180] J. Liu, M. M. Chisti, and X. Zeng, “General Signal Amplification Strategy for Nonfaradic Impedimetric Sensing: Trastuzumab Detection Employing a Peptide Immunosensor,” *Anal. Chem.*, vol. 89, no. 7, pp. 4013–4020, 2017.

[181] J. Wan, J. Ai, Y. Zhang, X. Geng, Q. Gao, and Z. Cheng, “Signal-off impedimetric immunosensor for the detection of Escherichia coli O157:H7,” *Sci. Rep.*, vol. 6, p. 19806, 2016.

[182] Franklin (Feng) Tao and S. L. Bernasek, “Chapter 13 Immobilization of Biomolecules at Semiconductor Interfaces,” in *Functionalization of Semiconductor Surfaces*, pp. 401–428, 2012.

[183] D. Berdat, A. C. Martin Rodríguez, F. Herrera, and M. A. M. Gijs, “Label-free detection of DNA with interdigitated micro-electrodes in a fluidic cell,” *Lab Chip*, vol. 8, no. 2, pp. 302–308, 2008.

[184] A. Qureshi, I. Roci, Y. Gurbuz, and J. H. Niazi, “An aptamer based competition assay for protein detection using CNT activated gold-interdigitated capacitor arrays,” *Biosens. Bioelectron.*, vol. 34, no. 1, pp. 165–170, 2012.

[185] H. Deniz and Z. Onur, “Chapter 8. Impedimetric Biosensors for Label-Free and Enzymless Detection,” in *State of the Art in Biosensors - General Aspects*, InTech, 2013.

[186] J. S. Daniels and N. Pourmand, “Label-free impedance biosensors: Opportunities and challenges,” *Electroanalysis*, vol. 19, no. 12. pp. 1239–1257, 2007.

[187] S. Patskovsky, V. Latendresse, A.-M. Dallaire, L. Doré-Mathieu, and M. Meunier, “Combined surface plasmon resonance and impedance spectroscopy systems for biosensing,” *Analyst*, vol. 139, no. 3, pp. 596–602, 2014.

[188] K.-C. Lin, V. Kunduru, M. Bothara, K. Rege, S. Prasad, and B. L. Ramakrishna, “Biogenic nanoporous silica-based sensor for enhanced electrochemical detection of cardiovascular biomarkers proteins,” *Biosens. Bioelectron.*, vol. 25, no. 10, pp. 2336–2342, 2010.

[189] A. K. Assaifan, J. S. Lloyd, S. Samavat, D. Deganello, R. J. Stanton, and K. S. Teng, “Nanotextured Surface on Flexographic Printed ZnO Thin Films for Low-Cost Non-Faradaic Biosensors,” *ACS Appl. Mater. Interfaces*, vol. 8, no. 49, pp. 33802–33810, 2016.

[190] G. Bacher, S. Pal, L. Kanungo, and S. Bhand, “A label-free silver wire based impedimetric immunosensor for detection of aflatoxin M1 in milk,” *Sensors Actuators B Chem.*, vol. 168, pp. 223–230, 2012.

[191] M. M. Barsan, C. T. Toledo, and C. M. A. Brett, “New electrode architectures based on poly(methylene green) and functionalized carbon nanotubes: Characterization and application to detection of acetaminophen and pyridoxine,” *J. Electroanal. Chem.*, vol. 736, pp. 8–15, 2015.

[192] R. D. Munje, M. Jacobs, S. Muthukumar, B. Quadri, N. R. Shanmugam, and S. Prasad, “A novel approach for electrical tuning of nano-textured zinc oxide surfaces for ultra-sensitive troponin-T detection,” *Anal. Methods*, vol. 7, no. 24, pp. 10136–10144, 2015.

[193] X. Luo, M. Xu, C. Freeman, T. James, and J. J. Davis, “Ultrasensitive Label Free Electrical Detection of Insulin in Neat Blood Serum,” *Anal. Chem.*, vol. 85, no. 8, pp. 4129–4134, 2013.

[194] E. Bernalte, C. Marín-Sánchez, E. Pinilla-Gil, and C. M. A. Brett, “Characterisation of screen-printed gold and gold nanoparticle-modified carbon sensors by electrochemical impedance spectroscopy,” *J. Electroanal. Chem.*, vol. 709, pp. 70–76, 2013.

[195] J.-Y. Park and S.-M. Park, “DNA Hybridization Sensors Based on

Electrochemical Impedance Spectroscopy as a Detection Tool," *Sensors*, vol. 9, no. 12, pp. 9513–9532, 2009.

[196] R. Sharma, S. E. Deacon, D. Nowak, S. E. George, M. P. Szymonik, A. A. S. Tang, D. C. Tomlinson, A. G. Davies, M. J. McPherson, and C. Wälti, "Label-free electrochemical impedance biosensor to detect human interleukin-8 in serum with sub-pg/ml sensitivity," *Biosens. Bioelectron.*, vol. 80, pp. 607–613, 2016.

[197] C. Brett, "Electrochemical Impedance Spectroscopy for Characterization of Electrochemical Sensors and Biosensors," in *ECS Transactions*, pp. 67–80, 2008.

[198] A. Bonanni, A. H. Loo, and M. Pumera, "Graphene for impedimetric biosensing," *TrAC Trends Anal. Chem.*, vol. 37, pp. 12–21, 2012.

[199] Y. Wang, J. Ping, Z. Ye, J. Wu, and Y. Ying, "Impedimetric immunosensor based on gold nanoparticles modified graphene paper for label-free detection of Escherichia coli O157:H7," *Biosens. Bioelectron.*, vol. 49, pp. 492–498, 2013.

[200] L. E. Delle, C. Huck, M. Bäcker, F. Müller, S. Grandthyll, K. Jacobs, R. Lilischkis, X. T. Vu, M. J. Schöning, P. Wagner, R. Thoelen, M. Weil, and S. Ingebrandt, "Impedimetric immunosensor for the detection of histamine based on reduced graphene oxide," *Phys. status solidi*, vol. 212, no. 6, pp. 1327–1334, 2015.

[201] A. Yagati, J. Park, and S. Cho, "Reduced Graphene Oxide Modified the Interdigitated Chain Electrode for an Insulin Sensor," *Sensors*, vol. 16, no. 1, p. 109, 2016.

[202] A. H. Loo, A. Bonanni, A. Ambrosi, H. L. Poh, and M. Pumera, "Impedimetric immunoglobulin G immunosensor based on chemically modified graphenes," *Nanoscale*, vol. 4, no. 3, pp. 921–925, 2012.

[203] S. H. Kazemi, E. Ghodsi, S. Abdollahi, and S. Nadri, "Porous graphene oxide nanostructure as an excellent scaffold for label-free electrochemical biosensor: Detection of cardiac troponin I," *Mater. Sci. Eng. C*, vol. 69, pp. 447–452, 2016.

[204] Q. Lian, Z. He, Q. He, A. Luo, K. Yan, D. Zhang, X. Lu, and X. Zhou, "Simultaneous determination of ascorbic acid, dopamine and uric acid based on tryptophan functionalized graphene," *Anal. Chim. Acta*, vol. 823, pp. 32–39, 2014.

[205] Q. Gong, Y. Wang, and H. Yang, "A sensitive impedimetric DNA biosensor for the determination of the HIV gene based on graphene-Nafion composite film,"

*Biosens. Bioelectron.*, 2016.

[206] W. Saleem, C. Salinas, B. Watkins, G. Garvey, A. C. Sharma, and R. Ghosh, “Antibody functionalized graphene biosensor for label-free electrochemical immunosensing of fibrinogen, an indicator of trauma induced coagulopathy,” *Biosens. Bioelectron.*, vol. 86, pp. 522–529, 2016.

[207] S. Teixeira, N. S. Ferreira, R. S. Conlan, O. J. Guy, and M. G. F. Sales, “Chitosan/AuNPs Modified Graphene Electrochemical Sensor for Label-Free Human Chorionic Gonadotropin Detection,” *Electroanalysis*, vol. 26, no. 12, pp. 2591–2598, 2014.

[208] A. K. Yagati, J.-C. Pyun, J. Min, and S. Cho, “Label-free and direct detection of C-reactive protein using reduced graphene oxide-nanoparticle hybrid impedimetric sensor,” *Bioelectrochemistry*, vol. 107, pp. 37–44, 2016.

[209] A. Gutés, B.-Y. Lee, C. Carraro, W. Mickelson, S.-W. Lee, and R. Maboudian, “Impedimetric graphene-based biosensors for the detection of polybrominated diphenyl ethers,” *Nanoscale*, vol. 5, no. 13, p. 6048, 2013.

[210] Z. Zhang, L. Luo, G. Chen, Y. Ding, D. Deng, and C. Fan, “Tryptamine functionalized reduced graphene oxide for label-free DNA impedimetric biosensing,” *Biosens. Bioelectron.*, vol. 60, pp. 161–166, 2014.

[211] Y. Zhu, S. Murali, W. Cai, X. Li, J. W. Suk, J. R. Potts, and R. S. Ruoff, “Graphene and Graphene Oxide: Synthesis, Properties, and Applications,” *Adv. Mater.*, vol. 22, no. 35, pp. 3906–3924, 2010.

[212] X. Huang, F. Liu, P. Jiang, and T. Tanaka, “Is graphene oxide an insulating material?,” in *2013 IEEE International Conference on Solid Dielectrics (ICSD)*, pp. 904–907, 2013.

[213] A. Erdem, E. Eksin, and M. Muti, “Chitosan–graphene oxide based aptasensor for the impedimetric detection of lysozyme,” *Colloids Surfaces B Biointerfaces*, vol. 115, pp. 205–211, 2014.

[214] V. K. Gupta, M. L. Yola, M. S. Qureshi, A. O. Solak, N. Atar, and Z. Üstündağ, “A novel impedimetric biosensor based on graphene oxide/gold nanoplatform for detection of DNA arrays,” *Sensors Actuators B Chem.*, vol. 188, pp. 1201–1211, 2013.

[215] S. Srivastava, M. A. Ali, S. Umrao, U. K. Parashar, A. Srivastava, G. Sumana, B. D. Malhotra, S. S. Pandey, and S. Hayase, “Graphene Oxide-Based

Biosensor for Food Toxin Detection," *Appl. Biochem. Biotechnol.*, vol. 174, no. 3, pp. 960–970, 2014.

[216] M. L. Yola, T. Eren, and N. Atar, "A novel and sensitive electrochemical DNA biosensor based on Fe@Au nanoparticles decorated graphene oxide," *Electrochim. Acta*, vol. 125, pp. 38–47, 2014.

[217] W. Sun, Y. Zhang, X. Ju, G. Li, H. Gao, and Z. Sun, "Electrochemical deoxyribonucleic acid biosensor based on carboxyl functionalized graphene oxide and poly-l-lysine modified electrode for the detection of tlh gene sequence related to vibrio parahaemolyticus," *Anal. Chim. Acta*, vol. 752, pp. 39–44, 2012.

[218] Gamry Instruments, "EIS of Organic Coatings and Paints.", webpage: https://www.gamry.com/application-notes/EIS/eis-of-organic-coatings-and-paints/, accessed on 08-Jun-2017.

[219] J. Fraden, "Impedance and its Corresponding Electrochemical Processes," in *Electrochemical Impedance Spectroscopy in PEM Fuel Cells: Fundamentals and Applications*, London: Springer London, pp. 95–138, 2010.

[220] D. V. Franco, L. M. Da Silva, W. F. Jardim, and J. F. C. Boodts, "Influence of the electrolyte composition on the kinetics of the oxygen evolution reaction and ozone production processes," *J. Braz. Chem. Soc.*, vol. 17, no. 4, pp. 446–757, 2006.

[221] A. Lasia, "Impedance of Porous Electrodes," in *Electrochemical Impedance Spectroscopy and its Applications*, Springer, 2014, pp. 203–250.

[222] A. Ehsani, F. Babaei, and H. Mostaanzadeh, "Electrochemical and Optical Investigation of Conductive Polymer and MWCNT Nanocomposite Film," *J. Braz. Chem. Soc.*, 2014.

[223] W. Wang, S. Guo, I. Lee, K. Ahmed, J. Zhong, Z. Favors, F. Zaera, M. Ozkan, and C. S. Ozkan, "Hydrous Ruthenium Oxide Nanoparticles Anchored to Graphene and Carbon Nanotube Hybrid Foam for Supercapacitors," *Sci. Rep.*, vol. 4, no. 1, p. 4452, 2015.

[224] S. Fletcher, V. J. Black, and I. Kirkpatrick, "A universal equivalent circuit for carbon-based supercapacitors," *J. Solid State Electrochem.*, vol. 18, no. 5, pp. 1377–1387, 2014.

[225] S. Liu and X. Qin, "Preparation of a Ag–MnO 2 /graphene composite for the oxygen reduction reaction in alkaline solution," *RSC Adv.*, vol. 5, no. 20, pp.

15627–15633, 2015.

[226] C. P. Fonseca, D. A. de L. Almeida, M. C. D. de Oliveira, M. R. Baldan, and N. G. Ferreira, “Influence of the polymeric coating thickness on the electrochemical performance of Carbon Fiber/PAni composites,” *Polímeros*, vol. 25, no. 5, pp. 425–432, 2015.

[227] X. Feng, J. Yang, Y. Bie, J. Wang, Y. Nuli, and W. Lu, “Nano/micro-structured Si/CNT/C composite from nano-SiO 2 for high power lithium ion batteries,” *Nanoscale*, vol. 6, no. 21, pp. 12532–12539, 2014.

[228] E. da Silva, “Smith charts and scattering parameters,” in *High Frequency and Microwave Engineering*, Elsevier, pp. 88–141, 2001.

[229] A. M. Niknejad, “Lecture notes: Scattering parameters (EECS 242),” *University of California, Berkeley*, webpage: http://rfic.eecs.berkeley.edu/~niknejad/ee242/pdf/eecs242_lect5_sparam.pdf., accessed on 15-Jun-2016.

[230] R. Schmitt, “Circuits as Guides for Waves and S-Parameters,” in *Electromagnetics Explained: A Handbook for Wireless/ RF, EMC, and High-Speed Electronics (EDN Series for Design Engineers)*, pp. 209–228, 2002.

[231] M. H. Jones, “Impedance matching,” in *A Practical Introduction to Electronic Circuits*, 3rd Ed., Cambridge University Press, 1995.

[232] W. Davis, “Impedance Matching,” in *Radio Frequency Circuit Design*, John Wiley & Sons, Inc., pp. 39–58, 2010.

[233] C. L. WADHWA, “Network Theorems,” in *Network Analysis and Synthesis*, Revised Se., New-Delhi: New Age International Limited, pp. 93–97, 2006.

[234] R. Sobot, “6.2 Maximum power transfer,” in *Wireless Communication Electronics Introduction to RF Circuits and Design Techniques*, Springer-Verlag, 2012.

[235] C. Bowick, *RF circuit design*, Newnes / Elsevier, 2008.

[236] C. Li, M.-R. Tofighi, D. Schreurs, and T.-S. Horng, “Chapter 1. Fundamentals of microwave engineering,” in *Principles and Applications of RF/Microwave in Healthcare and Biosensing*, 1st ed., Academic Press, 2016.

[237] J. L. Schepps and K. R. Foster, “The UHF and microwave dielectric properties of normal and tumour tissues: variation in dielectric properties with tissue water content.,” *Phys. Med. Biol.*, vol. 25, no. 6, pp. 1149–1159, 1980.

[238] P. Mehta, K. Chand, D. Narayanswamy, D. G. Beetner, R. Zoughi, and W. V. Stoecker, “Microwave Reflectometry as a Novel Diagnostic Tool for Detection of Skin Cancers,” *IEEE Trans. Instrum. Meas.*, vol. 55, no. 4, pp. 1309–1316, 2006.

[239] S. Afroz, S. W. Thomas, G. Mumcu, and S. E. Saddow, “Implantable SiC based RF antenna biosensor for continuous glucose monitoring,” in *IEEE SENSORS 2013 - Proceedings*, 2013.

[240] H. Park, H. Seo Yoon, U. Patil, R. Anoop, J. Lee, J. Lim, W. Lee, and S. Chan Jun, “Radio frequency based label-free detection of glucose,” *Biosens. Bioelectron.*, vol. 54, pp. 141–145, 2014.

[241] H. J. Lee, J. H. Lee, H. S. Moon, I. S. Jang, J. S. Choi, J. G. Yook, and H. Il Jung, “A planar split-ring resonator-based microwave biosensor for label-free detection of biomolecules,” *Sensors Actuators, B Chem.*, vol. 169, pp. 26–31, 2012.

[242] M. Salazar-Alvarez, O. Korostynska, A. Mason, A. Al-Shamma’a, J. C. Cooney, E. Magner, and S. a M. Tofail, “Label free detection of specific protein binding using a microwave sensor,” *Analyst*, vol. 139, no. 21, pp. 5335–8, 2014.

[243] E. Marquez-Segura, F. P. Casares-Miranda, P. Otero, C. Camacho-Penalosa, and J. E. Page, “Analytical model of the wire-bonded interdigital capacitor,” *IEEE Trans. Microw. Theory Tech.*, vol. 54, no. 2, pp. 748–754, 2006.

[244] H.-J. Lee, H.-S. Lee, K.-H. Yoo, and J.-G. Yook, “A Study on Biomaterial Detection Using Single-Walled Carbon Nanotube Based on Interdigital Capacitors,” *J. Korean Inst. Electromagn. Eng. Sci.*, vol. 19, no. 8, pp. 891–898, 2008.

[245] J. S. F. Chang, Y. Yin, C. Lin, “A Novel design of Antenna for biosensing applications,” in *14th International Meeting on Chemical Sensors - IMCS 2012*, 2012.

[246] N.-Y. Kim, K. K. Adhikari, R. Dhakal, Z. Chuluunbaatar, C. Wang, and E.-S. Kim, “Rapid, Sensitive, and Reusable Detection of Glucose by a Robust Radiofrequency Integrated Passive Device Biosensor Chip,” *Sci. Rep.*, vol. 5, p. 7807, 2015.

[247] V. V. S. S. Srikanth and K. C. J. Raju, “Graphene/Polymer Nanocomposites as Microwave Absorbers,” in *Graphene-Based Polymer Nanocomposites in Electronics*, Cham: Springer International Publishing, pp. 307–343, 2015.

[248] M. Yogeesh, K. Parrish, J. Lee, S. Park, L. Tao, and D. Akinwande, “Towards

the Realization of Graphene Based Flexible Radio Frequency Receiver," *Electronics*, vol. 4, no. 4, pp. 933–946, 2015.

[249] B. Park, H. Park, J. Ji, J. Cho, and S. Jun, "A Reduced Graphene Oxide Based Radio Frequency Glucose Sensing Device Using Multi-Dimensional Parameters," *Micromachines*, vol. 7, no. 8, p. 136, 2016.

[250] K.-A. Son, B. Yang, H.-C. Seo, D. Wong, J. S. Moon, and T. Hussain, "High-Speed Graphene Field Effect Transistors on Microbial Cellulose Biomembrane," *IEEE Trans. Nanotechnol.*, vol. 16, no. 2, pp. 239–244, 2017.

[251] W. Xuan, M. He, N. Meng, X. He, W. Wang, J. Chen, T. Shi, T. Hasan, Z. Xu, Y. Xu, and J. K. Luo, "Fast Response and High Sensitivity ZnO/glass Surface Acoustic Wave Humidity Sensors Using Graphene Oxide Sensing Layer," *Sci. Rep.*, vol. 4, p. 7206, 2014.

[252] M. S. Mannoor, H. Tao, J. D. Clayton, A. Sengupta, D. L. Kaplan, R. R. Naik, N. Verma, F. G. Omenetto, and M. C. McAlpine, "Graphene-based wireless bacteria detection on tooth enamel," *Nat. Commun.*, vol. 3, p. 763, 2012.

[253] K. Na, H. Ma, J. Park, J. Yeo, J.-U. Park, and F. Bien, "Graphene-Based Wireless Environmental Gas Sensor on PET Substrate," *IEEE Sens. J.*, vol. 16, no. 12, pp. 5003–5009, 2016.

[254] X. H. and T. L. and K. H. C. and J. C. C. and K. S. N. and Z. Hu, "Graphene radio frequency and microwave passive components for low cost wearable electronics," *2D Mater.*, vol. 3, no. 2, p. 25021, 2016.

[255] M. Deen and F. Pascal, "Electrical Characterization of Semiconductor Materials and Devices," in *Springer Handbook of Electronic and Photonic Materials*, Springer US, pp. 409–438, 2006.

[256] F. Xia, V. Perebeinos, Y. Lin, Y. Wu, and P. Avouris, "The origins and limits of metal–graphene junction resistance," *Nat. Nanotechnol.*, vol. 6, no. 3, pp. 179–184, 2011.

[257] A. Allain, J. Kang, K. Banerjee, and A. Kis, "Electrical contacts to two-dimensional semiconductors," *Nat. Mater.*, vol. 14, no. 12, pp. 1195–1205, 2015.

[258] M. Aliofkhazraei, N. Ali, W. I. Milne, C. S. Ozkan, S. Mitura, and J. L. Gervasoni, "Fabrication Considerations for Graphene Devices," in *Graphene Science Handbook Fabrication Methods*, CRC Press, 2016.

[259] T. J. Echtermeyer, L. Britnell, P. K. Jasnos, A. Lombardo, R. V. Gorbachev, A. N. Grigorenko, A. K. Geim, A. C. Ferrari, and K. S. Novoselov, “Strong plasmonic enhancement of photovoltage in graphene,” *Nat. Commun.*, vol. 2, p. 458, 2011.

[260] X. Tan, H.-J. Chuang, M.-W. Lin, Z. Zhou, and M. M.-C. Cheng, “Edge Effects on the pH Response of Graphene Nanoribbon Field Effect Transistors,” *J. Phys. Chem. C*, vol. 117, no. 51, pp. 27155–27160, 2013.

[261] K. Nagashio, T. Nishimura, K. Kita, and A. Toriumi, “Metal/graphene contact as a performance Killer of ultra-high mobility graphene analysis of intrinsic mobility and contact resistance,” in *2009 IEEE International Electron Devices Meeting (IEDM)*, pp. 1–4, 2009.

[262] S. Russo, M. F. Craciun, M. Yamamoto, A. F. Morpurgo, and S. Tarucha, “Contact resistance in graphene-based devices,” *Phys. E Low-dimensional Syst. Nanostructures*, vol. 42, no. 4, pp. 677–679, 2010.

[263] A. Hsu, H. Wang, K. K. Kim, J. Kong, and T. Palacios, “Impact of Graphene Interface Quality on Contact Resistance and RF Device Performance,” *IEEE Electron Device Lett.*, vol. 32, no. 8, pp. 1008–1010, 2011.

[264] R. Murali, “Graphene Transistors,” in *Graphene Nanoelectronics: From Materials to Circuits*, R. Murali, Springer US, pp. 51–91, 2012.

[265] S. Gahng, C. Ho Ra, Y. Jin Cho, J. Ah Kim, T. Kim, and W. Jong Yoo, “Reduction of metal contact resistance of graphene devices via CO2 cluster cleaning,” *Appl. Phys. Lett.*, vol. 104, no. 22, p. 223110, 2014.

[266] J. T. Smith, A. D. Franklin, D. B. Farmer, and C. D. Dimitrakopoulos, “Reducing contact resistance in graphene devices through contact area patterning,” *ACS Nano*, vol. 7, no. 4, pp. 3661–3667, 2013.

[267] T. Chu and Z. Chen, “Understanding the Electrical Impact of Edge Contacts in Few-Layer Graphene,” *ACS Nano*, vol. 8, no. 4, pp. 3584–3589, 2014.

[268] H. Zhong, Z. Zhang, B. Chen, H. Xu, D. Yu, L. Huang, and L. Peng, “Realization of low contact resistance close to theoretical limit in graphene transistors,” *Nano Res.*, vol. 8, no. 5, pp. 1669–1679, 2015.

[269] H.-Y. Park, W.-S. Jung, D.-H. Kang, J. Jeon, G. Yoo, Y. Park, J. Lee, Y. H. Jang, J. Lee, S. Park, H.-Y. Yu, B. Shin, S. Lee, and J.-H. Park, “Graphene: Extremely Low Contact Resistance on Graphene through n-Type Doping and Edge Contact Design (Adv. Mater. 5/2016),” *Adv. Mater.*, vol. 28, no. 5, pp. 975–975, 2016.

[270] B. Krishna Bharadwaj, D. Nath, R. Pratap, and S. Raghavan, “Making consistent contacts to graphene: effect of architecture and growth induced defects,” *Nanotechnology*, vol. 27, no. 20, p. 205705, 2016.

[271] W. S. Leong, H. Gong, and J. T. L. Thong, “Low-Contact-Resistance Graphene Devices with Nickel-Etched-Graphene Contacts,” *ACS Nano*, vol. 8, no. 1, pp. 994–1001, 2014.

[272] A. D. Franklin, S.-J. Han, A. A. Bol, and V. Perebeinos, “Double Contacts for Improved Performance of Graphene Transistors,” *IEEE Electron Device Lett.*, vol. 33, no. 1, pp. 17–19, 2012.

[273] S. K. Hong, S. M. Song, O. Sul, and B. J. Cho, “Reduction of metal-graphene contact resistance by direct growth of graphene over metal,” *Carbon Lett.*, vol. 14, no. 3, pp. 171–174, 2013.

[274] V. Tsouti, C. Boutopoulos, I. Zergioti, and S. Chatzandroulis, “Capacitive microsystems for biological sensing,” *Biosens. Bioelectron.*, vol. 27, no. 1, pp. 1–11, 2011.

[275] J. Z. Chen, A. a Darhuber, S. M. Troian, and S. Wagner, “Capacitive sensing of droplets for microfluidic devices based on thermocapillary actuation.,” *Lab Chip*, vol. 4, pp. 473–480, 2004.

[276] M. Kitsara, D. Goustouridis, S. Chatzandroulis, M. Chatzichristidi, I. Raptis, T. Ganetsos, R. Igreja, and C. J. Dias, “Single chip interdigitated electrode capacitive chemical sensor arrays,” *Sensors Actuators, B Chem.*, vol. 127, no. 1, pp. 186–192, 2007.

[277] A. V. Mamishev, K. Sundara-Rajan, Fumin Yang, Yanqing Du, and M. Zahn, “Interdigital sensors and transducers,” *Proc. IEEE*, vol. 92, no. 5, pp. 808–845, 2004.

[278] M. W. Den Otter, “Approximate expressions for the capacitance and electrostatic potential of interdigitated electrode,” *Sensors Actuators, A Phys.*, vol. 96, pp. 140–144, 2002.

[279] R. Igreja and C. J. Dias, “Analytical evaluation of the interdigital electrodes capacitance for a multi-layered structure,” *Sensors Actuators A Phys.*, vol. 112, no. 2–3, pp. 291–301, 2004.

[280] T. J. G. and J. PHILIP, “An Inter-digital Capacitive Electrode Modified as a Pressure Sensor,” *Sensors Transducers J.*, vol. 99, no. 12, pp. 25–32, 2008.

[281] M. Vakilian and B. Y. Majlis, “Study of interdigitated electrode sensor for lab-on-chip applications,” in *2014 IEEE International Conference on Semiconductor Electronics (ICSE2014)*, pp. 201–204, 2014.

[282] N. Couniot, D. Flandre, L. A. Francis, and A. Afzalian, “Bacteria Detection with Interdigitated Microelectrodes: Noise Consideration and Design Optimization,” *Procedia Eng.*, vol. 47, pp. 188–191, 2012.

[283] M. Ibrahim, J. Claudel, D. Kourtiche, and M. Nadi, “Geometric parameters optimization of planar interdigitated electrodes for bioimpedance spectroscopy,” *J. Electr. Bioimpedance*, vol. 4, no. 1, pp. 13–22, 2013.

[284] S. MacKay, P. Hermansen, D. Wishart, W. Hiebert, and J. Chen, “Simulating electrical properties of interdigitated electrode designs for impedance-based biosensing applications,” in *2015 IEEE 28th Canadian Conference on Electrical and Computer Engineering (CCECE)*, pp. 370–375, 2015.

[285] A. Cohen and R. Kunz, “Large-area interdigitated array microelectrodes for electrochemical sensing,” *Sensors Actuators B Chem.*, pp. 23–29, 2000.

[286] M. Li, Y.-T. Li, D.-W. Li, and Y.-T. Long, “Recent developments and applications of screen-printed electrodes in environmental assays—A review,” *Anal. Chim. Acta*, vol. 734, pp. 31–44, 2012.

[287] C. Cugnet, O. Zaouak, A. René, C. Pécheyran, M. Potin-Gautier, and L. Authier, “A novel microelectrode array combining screen-printing and femtosecond laser ablation technologies: Development, characterization and application to cadmium detection,” *Sensors Actuators B Chem.*, vol. 143, no. 1, pp. 158–163, 2009.

[288] M. Brischwein, S. Herrmann, W. Vonau, F. Berthold, H. Grothe, E. R. Motrescu, and B. Wolf, “Electric cell-substrate impedance sensing with screen printed electrode structures,” *Lab Chip*, vol. 6, no. 6, p. 819, 2006.

[289] Y. Liu, D. Zhang, E. C. Alocilja, and S. Chakrabartty, “Biomolecules Detection Using a Silver-Enhanced Gold Nanoparticle-Based Biochip,” *Nanoscale Res. Lett.*, vol. 5, no. 3, pp. 533–538, 2010.

[290] D. Lee, J. Ondrake, and T. Cui, “A Conductometric Indium Oxide Semiconducting Nanoparticle Enzymatic Biosensor Array,” *Sensors*, vol. 11, no. 12, pp. 9300–9312,.2011.

[291] B. Y. Park, R. Zaouk, and M. J. Madou, “Fabrication of Microelectrodes Using

the Lift-Off Technique," in *Microfluidic Techniques*, New Jersey: Humana Press, pp. 23–26, 2006.

[292] M. Dimaki, M. Vergani, A. Heiskanen, D. Kwasny, L. Sasso, M. Carminati, J. Gerrard, J. Emneus, and W. Svendsen, "A Compact Microelectrode Array Chip with Multiple Measuring Sites for Electrochemical Applications," *Sensors*, vol. 14, no. 6, pp. 9505–9521, 2014.

[293] P. Van Gerwen, W. Laureyn, W. Laureys, G. Huyberechts, M. Op De Beeck, K. Baert, J. Suls, W. Sansen, P. Jacobs, L. Hermans, and R. Mertens, "Nanoscaled interdigitated electrode arrays for biochemical sensors," *Sensors Actuators, B Chem.*, vol. 49, no. 1–2, pp. 73–80, 1998.

[294] K. Hayashi, J. Takahashi, T. Horiuchi, Y. Iwasaki, and T. Haga, "Development of Nanoscale Interdigitated Array Electrode as Electrochemical Sensor Platform for Highly Sensitive Detection of Biomolecules," *J. Electrochem. Soc.*, vol. 155, no. 9, p. J240, 2008.

[295] S. Partel, S. Kasemann, P. Choleva, C. Dincer, J. Kieninger, and G. A. Urban, "Novel fabrication process for sub-micron interdigitated electrode arrays for highly sensitive electrochemical detection," *Sensors Actuators B Chem.*, vol. 205, pp. 193–198, 2014.

[296] S. Nadzirah, N. Azizah, U. Hashim, S. C. B. Gopinath, and M. Kashif, "Titanium Dioxide Nanoparticle-Based Interdigitated Electrodes: A Novel Current to Voltage DNA Biosensor Recognizes E. coli O157:H7," *PLoS One*, vol. 10, no. 10, p. e0139766, 2015.

[297] P. B. Bhushan, *Springer Handbook of Nanotechnology*. Berlin, Heidelberg: Springer Berlin Heidelberg, 2010.

[298] A. Jayaraman, "Electrical impedance characterization of microporous films at elevated temperatures with interdigitated design," Michigan State University, 2008.

[299] K.-S. Chou and C.-H. Lee, "Fabrication of Silver Interdigitated Electrode by a Stamp Method," *Adv. Mater. Sci. Eng.*, vol. 2014, pp. 1–5, 2014.

[300] Li Xie, Geng Yang, M. Mantysalo, F. Jonsson, and Li-Rong Zheng, "A system-on-chip and paper-based inkjet printed electrodes for a hybrid wearable bio-sensing system," in *2012 Annual International Conference of the IEEE Engineering in Medicine and Biology Society*, pp. 5026–5029, 2012.

[301] P. Ihalainen, F. Pettersson, M. Pesonen, T. Viitala, A. Määttänen, R. Österbacka, and J. Peltonen, “An impedimetric study of DNA hybridization on paper-supported inkjet-printed gold electrodes.,” *Nanotechnology*, vol. 25, no. 9, p. 94009, 2014.

[302] Z. Li, Y. Fu, W. Fang, and Y. Li, “Electrochemical Impedance Immunosensor Based on Self-Assembled Monolayers for Rapid Detection of Escherichia coli O157:H7 with Signal Amplification Using Lectin,” *Sensors*, vol. 15, no. 8, pp. 19212–19224, 2015.

[303] L. H. D. Skjolding, C. Spegel, A. Ribayrol, J. Emnéus, and L. Montelius, “Characterisation of nano-interdigitated electrodes,” *Journal of Physics: Conference Series*, vol. 100, no. 5. p. 52045, 2008.

[304] V. Van Thu, P. T. Dung, L. T. Tam, and P. D. Tam, “Biosensor based on nanocomposite material for pathogenic virus detection,” *Colloids Surfaces B Biointerfaces*, vol. 115, pp. 176–181, 2014.

[305] A. K. Samarao, M. J. Rust, and C. H. Ahn, “Rapid Fabrication of a Nano Interdigitated Array Electrode and its Amperometric Characterization as an Electrochemical Sensor,” in *2007 IEEE Sensors*, pp. 644–647, 2007.

[306] Z. Zou, J. Kai, M. J. Rust, J. Han, and C. H. Ahn, “Functionalized nano interdigitated electrodes arrays on polymer with integrated microfluidics for direct bio-affinity sensing using impedimetric measurement,” *Sensors Actuators, A Phys.*, vol. 136, no. 2, pp. 518–526, 2007.

[307] R. Ohno, H. Ohnuki, H. Wang, T. Yokoyama, H. Endo, D. Tsuya, and M. Izumi, “Electrochemical impedance spectroscopy biosensor with interdigitated electrode for detection of human immunoglobulin A,” *Biosens. Bioelectron.*, vol. 40, no. 1, pp. 422–426, 2013.

[308] S. K. Arya, G. Chornokur, M. Venugopal, and S. Bhansali, “Antibody functionalized interdigitated μ-electrode (IDμE) based impedimetric cortisol biosensor,” *Analyst*, vol. 135, no. 8, p. 1941, 2010.

[309] S. Kim, G. Yu, T. Kim, K. Shin, and J. Yoon, “Rapid bacterial detection with an interdigitated array electrode by electrochemical impedance spectroscopy,” *Electrochim. Acta*, vol. 82, pp. 126–131, 2012.

[310] A. Quershi, Y. Gurbuz, W. P. Kang, and J. L. Davidson, “A novel interdigitated capacitor based biosensor for detection of cardiovascular risk marker,” *Biosens.*

*Bioelectron.*, vol. 25, pp. 877–882, 2009.

[311] D. A. Healy, C. J. Hayes, P. Leonard, L. McKenna, and R. O'Kennedy, "Biosensor developments: application to prostate-specific antigen detection," *Trends Biotechnol.*, vol. 25, no. 3, pp. 125–131, 2007.

[312] C. Fernández-Sánchez, A. M. Gallardo-Soto, K. Rawson, O. Nilsson, and C. J. McNeil, "Quantitative impedimetric immunosensor for free and total prostate specific antigen based on a lateral flow assay format," *Electrochem. commun.*, vol. 6, no. 2, pp. 138–143, 2004.

[313] C. T.-S. Ching, T.-R. Chou, T.-P. Sun, and H.-L. Shieh, "Impedimetric PSA Immunosensor: Prostate Specific Antigen Biosensor," in *2012 International Conference on Biomedical Engineering and Biotechnology*, pp. 329–331, 2012.

[314] G. Chornokur, S. K. Arya, C. Phelan, R. Tanner, and S. Bhansali, "Impedance-Based Miniaturized Biosensor for Ultrasensitive and Fast Prostate-Specific Antigen Detection," *J. Sensors*, vol. 2011, pp. 1–7, 2011.

[315] S. K. Arya and S. Bhansali, "Anti-Prostate Specific Antigen (Anti-PSA) Modified Interdigitated Microelectrode-Based Impedimetric Biosensor for PSA Detection," *Biosensors Journal*, vol. 1. pp. 1–7, 2012.

[316] M. S. Chiriacò, E. Primiceri, A. Montanaro, F. de Feo, L. Leone, R. Rinaldi, and G. Maruccio, "On-chip screening for prostate cancer: an EIS microfluidic platform for contemporary detection of free and total PSA," *Analyst*, vol. 138, no. 18, p. 5404, 2013.

[317] P. Jolly, N. Formisano, J. Tkáč, P. Kasák, C. G. Frost, and P. Estrela, "Label-free impedimetric aptasensor with antifouling surface chemistry: A prostate specific antigen case study," *Sensors Actuators B Chem.*, vol. 209, pp. 306–312, 2015.

[318] J. Wang, G. Liu, H. Wu, and Y. Lin, "Quantum-Dot-Based Electrochemical Immunoassay for High-Throughput Screening of the Prostate-Specific Antigen," *Small*, vol. 4, no. 1, pp. 82–86, 2008.

[319] G. Ertürk, M. Hedström, M. A. Tümer, A. Denizli, and B. Mattiasson, "Real-time prostate-specific antigen detection with prostate-specific antigen imprinted capacitive biosensors," *Anal. Chim. Acta*, vol. 891, pp. 120–129, 2015.

[320] H.-J. Lee, J.-H. Lee, and H.-I. Jung, "A symmetric metamaterial element-based RF biosensor for rapid and label-free detection," *Appl. Phys. Lett.*, vol. 99, no.

16, p. 163703, 2011.

[321] Y. Ueno, K. Furukawa, K. Matsuo, S. Inoue, K. Hayashi, and H. Hibino, “On-chip graphene oxide aptasensor for multiple protein detection,” *Anal. Chim. Acta*, vol. 866, pp. 1–9, 2015.

[322] D.-J. Kim, I. Y. Sohn, J.-H. Jung, O. J. Yoon, N.-E. Lee, and J.-S. Park, “Reduced graphene oxide field-effect transistor for label-free femtomolar protein detection,” *Biosens. Bioelectron.*, vol. 41, pp. 621–626, 2013.

[323] Y. Wang, Y. Qu, G. Liu, X. Hou, Y. Huang, W. Wu, K. Wu, and C. Li, “Electrochemical immunoassay for the prostate specific antigen using a reduced graphene oxide functionalized with a high molecular-weight silk peptide,” *Microchim. Acta*, vol. 182, no. 11–12, pp. 2061–2067, 2015.

[324] C. D. Chin, V. Linder, and S. K. Sia, “Commercialization of microfluidic point-of-care diagnostic devices,” *Lab Chip*, vol. 12, no. 12, p. 2118, 2012.

[325] I. E. Tothill, “Biosensors for cancer markers diagnosis,” *Semin. Cell Dev. Biol.*, vol. 20, no. 1, pp. 55–62, 2009.

[326] J. Li, S. Li, and C. F. Yang, “Electrochemical Biosensors for Cancer Biomarker Detection,” *Electroanalysis*, vol. 24, no. 12, pp. 2213–2229, 2012.

[327] E. Ghafar-Zadeh, “Wireless Integrated Biosensors for Point-of-Care Diagnostic Applications,” *Sensors*, vol. 15, no. 2, pp. 3236–3261, 2015.

[328] S. Vigneshvar, C. C. Sudhakumari, B. Senthilkumaran, and H. Prakash, “Recent Advances in Biosensor Technology for Potential Applications – An Overview,” *Front. Bioeng. Biotechnol.*, vol. 4, 2016.

[329] M. Ngoepe, Y. Choonara, C. Tyagi, L. Tomar, L. du Toit, P. Kumar, V. Ndesendo, and V. Pillay, “Integration of Biosensors and Drug Delivery Technologies for Early Detection and Chronic Management of Illness,” *Sensors*, vol. 13, no. 6, pp. 7680–7713, 2013.

[330] Z. Liu, S. Tabakman, K. Welsher, and H. Dai, “Carbon nanotubes in biology and medicine: In vitro and in vivo detection, imaging and drug delivery,” *Nano Res.*, vol. 2, no. 2, pp. 85–120, 2009.

[331] Phys.Org, “Wearable graphene-based biomedical device to monitor and combat diabetes,” 2016, webpage: https://phys.org/news/2016-03-wearable-graphene-based-biomedical-device-combat.html, accessed on 23-Apr-2017.

[332] P. Preechaburana, M. C. Gonzalez, A. Suska, and D. Filippini, “Surface Plasmon Resonance Chemical Sensing on Cell Phones,” *Angew. Chemie Int. Ed.*, vol. 51, no. 46, pp. 11585–11588, 2012.

[333] A. Sun, T. Wambach, A. G. Venkatesh, and D. A. Hall, “A low-cost smartphone-based electrochemical biosensor for point-of-care diagnostics,” in *2014 IEEE Biomedical Circuits and Systems Conference (BioCAS) Proceedings*, pp. 312–315, 2014.

[334] C. Desmet, C. A. Marquette, L. J. Blum, and B. Doumèche, “Paper electrodes for bioelectrochemistry: Biosensors and biofuel cells,” *Biosens. Bioelectron.*, vol. 76, pp. 145–163, 2016.

[335] C. Silveira, T. Monteiro, and M. Almeida, “Biosensing with Paper-Based Miniaturized Printed Electrodes–A Modern Trend,” *Biosensors*, vol. 6, no. 4, p. 51, 2016.

[336] M. Holzinger, A. Le Goff, and S. Cosnier, “Nanomaterials for biosensing applications: a review,” *Front. Chem.*, vol. 2, 2014.

[337] S. Deng and V. Berry, “Wrinkled, rippled and crumpled graphene: an overview of formation mechanism, electronic properties, and applications,” *Mater. Today*, vol. 19, no. 4, pp. 197–212, 2016.

[338] Q. Mei and Z. Zhang, “Photoluminescent Graphene Oxide Ink to Print Sensors onto Microporous Membranes for Versatile Visualization Bioassays,” *Angew. Chemie Int. Ed.*, vol. 51, no. 23, pp. 5602–5606, 2012.

[339] K. Griffiths, C. Dale, J. Hedley, M. D. Kowal, R. B. Kaner, and N. Keegan, “Laser-scribed graphene presents an opportunity to print a new generation of disposable electrochemical sensors,” *Nanoscale*, vol. 6, no. 22, pp. 13613–13622, 2014.

[340] Y. Song, Y. Luo, C. Zhu, H. Li, D. Du, and Y. Lin, “Recent advances in electrochemical biosensors based on graphene two-dimensional nanomaterials,” *Biosens. Bioelectron.*, vol. 76, pp. 195–212, 2016.

[341] Y. Bo, H. Yang, Y. Hu, T. Yao, and S. Huang, “A novel electrochemical DNA biosensor based on graphene and polyaniline nanowires,” *Electrochim. Acta*, vol. 56, no. 6, pp. 2676–2681, 2011.

[342] A. Bonanni, I. Fernández-Cuesta, X. Borrisé, F. Pérez-Murano, S. Alegret, and M. del Valle, “DNA hybridization detection by electrochemical impedance

spectroscopy using interdigitated gold nanoelectrodes," *Microchim. Acta*, vol. 170, no. 3–4, pp. 275–281, 2010.

[343] Y. Ueno, K. Furukawa, K. Hayashi, M. Takamura, H. Hibino, and E. Tamechika, "Graphene-modified interdigitated array electrode: fabrication, characterization, and electrochemical immunoassay application.," *Anal. Sci.*, vol. 29, no. January, pp. 55–60, 2013.

[344] V. Strong, S. Dubin, M. F. El-Kady, A. Lech, Y. Wang, B. H. Weiller, and R. B. Kaner, "Patterning and electronic tuning of laser scribed graphene for flexible all-carbon devices," *ACS Nano*, vol. 6, no. 2, pp. 1395–1403, 2012.

[345] Y. Zhang, L. Guo, S. Wei, Y. He, H. Xia, Q. Chen, H. B. Sun, and F. S. Xiao, "Direct imprinting of microcircuits on graphene oxides film by femtosecond laser reduction," *Nano Today*, vol. 5, no. 1, pp. 15–20, 2010.

[346] A. Qureshi, Y. Gurbuz, and J. H. Niazi, "Biosensors for cardiac biomarkers detection: A review," *Sensors Actuators B Chem.*, vol. 171–172, pp. 62–76, 2012.

[347] Q. Xu and J. J. Davis, "The Diagnostic Utility of Electrochemical Impedance," *Electroanalysis*, vol. 26, no. 6, pp. 1249–1258, 2014.

[348] S. Vogt, Q. Su, C. Gutiérrez-Sánchez, and G. Nöll, "Critical View on Electrochemical Impedance Spectroscopy Using the Ferri/Ferrocyanide Redox Couple at Gold Electrodes," *Anal. Chem.*, vol. 88, no. 8, pp. 4383–4390, 2016.

[349] X. Luo and J. J. Davis, "Electrical biosensors and the label free detection of protein disease biomarkers," *Chem. Soc. Rev.*, vol. 42, no. 13, p. 5944, 2013.

[350] X. Muñoz-Berbel, N. Godino, O. Laczka, E. Baldrich, F. M. Xavier, and F. J. D. C. D, "Chapter 15. Impedance-based biosensors for pathogen detection," in *Principles of Bacterial Detection: Biosensors, Recognition Receptors and Microsystems*, M. Zourob, S. Elwary, and A. Turner, Springer, 2008.

[351] I. David and W. Robert M., "Dielectric Detection Using Biochemical Assays," in *[Point-of-Care Diagnostics on a Chip*, Springer-Verlag Berlin Heidelberg, pp. 97–100, 2013.

[352] J. Wang, S. Yang, D. Guo, P. Yu, D. Li, J. Ye, and L. Mao, "Comparative studies on electrochemical activity of graphene nanosheets and carbon nanotubes," *Electrochem. commun.*, vol. 11, no. 10, pp. 1892–1895, 2009.

[353] A. A. K. King, B. R. Davies, N. Noorbehesht, P. Newman, T. L. Church, A. T. Harris, J. M. Razal, and A. I. Minett, “A New Raman Metric for the Characterisation of Graphene oxide and its Derivatives,” *Sci. Rep.*, vol. 6, no. 1, p. 19491, 2016.

[354] R. R. Kamath and M. J. Madou, “Three-Dimensional Carbon Interdigitated Electrode Arrays for Redox-Amplification,” *Anal. Chem.*, vol. 86, no. 6, pp. 2963–2971, 2014.

[355] A. Sai Sarathi Vasan, “Point-of-care biosensor system,” *Front. Biosci.*, vol. S5, no. 1, p. 39, 2013.

[356] P. Dak, A. Ebrahimi, V. Swaminathan, C. Duarte-Guevara, R. Bashir, and M. Alam, “Droplet-based Biosensing for Lab-on-a-Chip, Open Microfluidics Platforms,” *Biosensors*, vol. 6, no. 2, p. 14, 2016.

[357] K. Kiilerich-Pedersen, C. R. Poulsen, T. Jain, and N. Rozlosnik, “Polymer based biosensor for rapid electrochemical detection of virus infection of human cells,” *Biosens. Bioelectron.*, vol. 28, no. 1, pp. 386–392, 2011.

[358] I. Ida, J. Takada, T. Toda, and Y. Oishi, “An adaptive impedance matching system and considerations for a better performance,” in *APCC/MDMC ’04. The 2004 Joint Conference of the 10th Asia-Pacific Conference on Communications and the 5th International Symposium on Multi-Dimensional Mobile Communications Proceeding*, vol. 2, pp. 563–567, 2004.

[359] T. Duong and J.-W. Lee, “A Dynamically Adaptable Impedance-Matching System for Midrange Wireless Power Transfer with Misalignment,” *Energies*, vol. 8, no. 8, pp. 7593–7617, 2015.

[360] S.-J. Han, A. V. Garcia, S. Oida, K. a Jenkins, and W. Haensch, “Graphene radio frequency receiver integrated circuit,” *Nat. Commun.*, vol. 5, p. 3086, 2014.

[361] M. Dragoman, D. Neculoiu, A.-C. Bunea, G. Deligeorgis, M. Aldrigo, D. Vasilache, A. Dinescu, G. Konstantinidis, D. Mencarelli, L. Pierantoni, and M. Modreanu, “A tunable microwave slot antenna based on graphene,” *Appl. Phys. Lett.*, vol. 106, no. 15, p. 153101, 2015.

[362] X. Huang, T. Leng, X. Zhang, J. C. Chen, K. H. Chang, A. K. Geim, K. S. Novoselov, and Z. Hu, “Binder-free highly conductive graphene laminate for low cost printed radio frequency applications,” *Appl. Phys. Lett.*, vol. 106, no. 20, p. 203105, 2015.

[363] H. Wang, A. Hsu, and T. Palacios, “Graphene Electronics for RF Applications,” *IEEE Microw. Mag.*, vol. 13, no. 4, pp. 114–125, 2012.

[364] H.-J. Lee and J.-G. Yook, “Recent research trends of radio-frequency biosensors for biomolecular detection.,” *Biosens. Bioelectron.*, vol. 61, pp. 448–59, 2014.

[365] Y. L. Kong, M. S. Mannoor, and M. C. McAlpine, “Chapter 9. Bionic graphene biosensors,” in *Carbon Nanomaterials for Biomedical Applications*, M. Zhang, R. R. Naik, and L. Dai, Eds. Springer International Publishing, pp. 277–279, 2016.

[366] F. W. Scheller, A. Yarman, T. Bachmann, T. Hirsch, S. Kubick, R. Renneberg, S. Schumacher, U. Wollenberger, C. Teller, and F. F. Bier, “Future of Biosensors: A Personal View,” in *Biosensors Based on Aptamers and Enzymes*, pp. 1–28, 2013.

[367] S. Cui, H. Pu, E. C. Mattson, Z. Wen, J. Chang, Y. Hou, C. J. Hirschmugl, and J. Chen, “Ultrasensitive Chemical Sensing through Facile Tuning Defects and Functional Groups in Reduced Graphene Oxide,” *Anal. Chem.*, vol. 86, no. 15, pp. 7516–7522, 2014.

[368] J. T. Robinson, F. K. Perkins, E. S. Snow, Z. Wei, and P. E. Sheehan, “Reduced Graphene Oxide Molecular Sensors,” *Nano Lett.*, vol. 8, no. 10, pp. 3137–3140, 2008.

[369] T. K. Das and S. Prusty, “Graphene-Based Polymer Composites and Their Applications,” *Polym. Plast. Technol. Eng.*, vol. 52, no. 4, pp. 319–331, 2013.

[370] D. Berman, A. Erdemir, and A. V. Sumant, “Graphene: a new emerging lubricant,” *Mater. Today*, vol. 17, no. 1, pp. 31–42, 2014.

[371] S. C. Youn, J. Geng, B. S. Son, S. B. Yang, D. W. Kim, H. M. Cho, and H.-T. Jung, “Effect of the Exposure Time of Hydrazine Vapor on the Reduction of Graphene Oxide Films,” *J. Nanosci. Nanotechnol.*, vol. 11, no. 7, pp. 5959–5964, 2011.

[372] A. Pirkle, J. Chan, A. Venugopal, D. Hinojos, C. W. Magnuson, S. McDonnell, L. Colombo, E. M. Vogel, R. S. Ruoff, and R. M. Wallace, “The effect of chemical residues on the physical and electrical properties of chemical vapor deposited graphene transferred to SiO 2,” *Appl. Phys. Lett.*, vol. 99, no. 12, p. 122108, 2011.

[373] A. J. Barlow, S. Popescu, K. Artyushkova, O. Scott, N. Sano, J. Hedley, and P. J. Cumpson, “Chemically specific identification of carbon in XPS imaging using

Multivariate Auger Feature Imaging (MAFI)," *Carbon,* vol. 107, 2016.

[374] D. Li and R. B. Kaner, "MATERIALS SCIENCE: Graphene-Based Materials," *Science (80-. ).*, vol. 320, no. 5880, pp. 1170–1171, 2008.

[375] NEXUS, "D-Parameter and MAFI Imaging.", webpage, http://www.ncl.ac.uk/nexus/xps/applications/d-parameter.htm., accessed on 20-Aug-2015.

[376] B. Mednikarov, G. Spasov, T. Babeva, J. Pirov, M. Sahatchieva, C. Popov, and W. Kulisch, "OPTICAL PROPERTIES OF DIAMOND-LIKE CARBON AND NANOCRYSTALLINE DIAMOND FILMS," *J. Optoelectron. Adv. Mater.*, vol. 7, no. 3, pp. 1407–1413, 2005.

[377] A. C. Ferrari, "Raman spectroscopy of graphene and graphite: Disorder, electron–phonon coupling, doping and nonadiabatic effects," *Solid State Commun.*, vol. 143, no. 1–2, pp. 47–57, 2007.

[378] L. Bokobza, J.-L. Bruneel, and M. Couzi, "Raman Spectra of Carbon-Based Materials (from Graphite to Carbon Black) and of Some Silicone Composites," *C*, vol. 1, no. 1, pp. 77–94, 2015.

[379] S. Liu, T. H. Zeng, M. Hofmann, E. Burcombe, J. Wei, R. Jiang, J. Kong, and Y. Chen, "Antibacterial Activity of Graphite, Graphite Oxide, Graphene Oxide, and Reduced Graphene Oxide: Membrane and Oxidative Stress," *ACS Nano*, vol. 5, no. 9, pp. 6971–6980, 2011.

[380] V. Iberi, I. Vlassiouk, X.-G. Zhang, B. Matola, A. Linn, D. C. Joy, and A. J. Rondinone, "Maskless Lithography and in situ Visualization of Conductivity of Graphene using Helium Ion Microscopy," *Sci. Rep.*, vol. 5, p. 11952, 2015.

[381] J. Lilloja, E. Kibena-Põldsepp, M. Merisalu, P. Rauwel, L. Matisen, A. Niilisk, E. Cardoso, G. Maia, V. Sammelselg, and K. Tammeveski, "An Oxygen Reduction Study of Graphene-Based Nanomaterials of Different Origin," *Catalysts*, vol. 6, no. 8, p. 108, 2016.

[382] H. Tian, M. A. Mohammad, W.-T. Mi, Y. Yang, and T.-L. Ren, "Laser-Scribing Technology for Wafer-Scale Graphene Devices," in *Advances in Carbon Nanostructures*, InTech, 2016.

[383] J. Cai, C. Lv, and A. Watanabe, "Cost-effective fabrication of high-performance flexible all-solid-state carbon micro-supercapacitors by blue-violet laser direct writing and further surface treatment," *J. Mater. Chem. A*, vol. 4, no. 5, pp. 1671–

1679, 2016.

[384] H. Tian, Y. Yang, D. Xie, Y.-L. Cui, W.-T. Mi, Y. Zhang, and T.-L. Ren, “Wafer-scale integration of graphene-based electronic, optoelectronic and electroacoustic devices.,” *Sci. Rep.*, vol. 4, p. 3598, 2014.

[385] P. Simon and Y. Gogotsi, “Materials for electrochemical capacitors,” *Nat. Mater.*, vol. 7, no. 11, pp. 845–854, 2008.

[386] L. Liu, Q. Yang, and J. Shen, “Correlation between Porosity and Electrical-Mechanical Properties of Carbon Nanotube Buckypaper with Various Porosities,” *J. Nanomater.*, vol. 2015, pp. 1–9, 2015.

[387] I. DUFOUR, “Chapter 3. Microcantilever Transduction,” in *Chemical Sensors and Biosensors*, R. Lalauze, Wiley, 2012.

[388] S. Rana, R. H. Page, and C. J. McNeil, “Comparison of Planar and 3-D Interdigitated Electrodes as Electrochemical Impedance Biosensors,” *Electroanalysis*, vol. 23, no. 10, pp. 2485–2490, 2011.

[389] X. T. Guo, Z. Hua Ni, C. Yan Liao, H. Yan Nan, Y. Zhang, W. Wei Zhao, and W. Hui Wang, “Fluorescence quenching of CdSe quantum dots on graphene,” *Appl. Phys. Lett.*, vol. 103, no. 20, 2013.

[390] K. P. Loh, Q. Bao, G. Eda, and M. Chhowalla, “Graphene oxide as a chemically tunable platform for optical applications,” *Nat. Chem.*, vol. 2, no. 12, pp. 1015–1024, 2010.

[391] F. A. Permatasari, A. H. Aimon, F. Iskandar, T. Ogi, and K. Okuyama, “Role of C–N Configurations in the Photoluminescence of Graphene Quantum Dots Synthesized by a Hydrothermal Route,” *Sci. Rep.*, vol. 6, no. 1, p. 21042, 2016.

[392] V. Ratta, “CRYSTALLIZATION, MORPHOLOGY, THERMAL STABILITY AND ADHESIVE PROPERTIES OF NOVEL HIGH PERFORMANCE SEMICRYSTALLINE POLYIMIDES,” Faculty of Virginia Polytechnic Institute and State University, 1999.

[393] A. Lamberti, F. Perrucci, M. Caprioli, M. Serrapede, M. Fontana, S. Bianco, S. Ferrero, and E. Tresso, “New insights on laser induced graphene electrodes for flexible supercapacitors: tunable morphology and physical properties,” *Nanotechnology*, 2017.

[394] J. Ederer, P. Janoš, P. Ecorchard, J. Tolasz, V. Štengl, H. Beneš, M. Perchacz,

and O. Pop-Georgievski, “Determination of amino groups on functionalized graphene oxide for polyurethane nanomaterials: XPS quantitation vs. functional speciation,” *RSC Adv.*, vol. 7, no. 21, pp. 12464–12473, 2017.

[395] H. Kim, I.-S. Bae, S.-J. Cho, J.-H. Boo, B.-C. Lee, J. Heo, I. Chung, and B. Hong, “Synthesis and characteristics of NH2-functionalized polymer films to align and immobilize DNA molecules,” *Nanoscale Res. Lett.*, vol. 7, no. 1, p. 30, 2012.

[396] Y. Gao and I. Kyratzis, “Covalent Immobilization of Proteins on Carbon Nanotubes Using the Cross-Linker 1-Ethyl-3-(3-dimethylaminopropyl)carbodiimide—a Critical Assessment,” *Bioconjug. Chem.*, vol. 19, no. 10, pp. 1945–1950, 2008.

[397] T. Kondo, D. Guo, T. Shikano, T. Suzuki, M. Sakurai, S. Okada, and J. Nakamura, “Observation of Landau levels on nitrogen-doped flat graphite surfaces without external magnetic fields,” *Sci. Rep.*, vol. 5, p. 16412, 2015.

[398] A. Lasia, “Conditions for Obtaining Good Impedances,” in *Electrochemical Impedance Spectroscopy and its Applications*, Springer, pp. 271–300, 2014

[399] B. Ratner, A. Hoffman, F. Schoen, and J. Lemons, “Applications of Biomaterials,” in *Biomaterials Science An Introduction to Materials in Medicine*, 3rd Ed., Elsevier Inc., pp. 957–959, 2013.

[400] P. A. Basnayaka, M. K. Ram, L. Stefanakos, and A. Kumar, “Graphene/Polypyrrole Nanocomposite as Electrochemical Supercapacitor Electrode: Electrochemical Impedance Studies,” *Graphene*, vol. 2, no. 2, pp. 81–87, 2013.

[401] P. Gupta and R. N. Goyal, “Graphene and Co-polymer composite based molecularly imprinted sensor for ultratrace determination of melatonin in human biological fluids,” *RSC Adv.*, vol. 5, no. 50, pp. 40444–40454, 2015.

[402] A. Mahadhy, E. Ståhl-Wernersson, B. Mattiasson, and M. Hedström, “Use of a capacitive affinity biosensor for sensitive and selective detection and quantification of DNA—A model study,” *Biotechnol. Reports*, vol. 3, pp. 42–48, 2014.

[403] V. Kamakoti, A. Panneer Selvam, N. Radha Shanmugam, S. Muthukumar, and S. Prasad, “Flexible Molybdenum Electrodes towards Designing Affinity Based Protein Biosensors,” *Biosensors*, vol. 6, no. 3, p. 36, 2016.

[404] D. T. E. Such, J. K, *Nickel and chromium plating*. London, Newnes-Butterworth,

1972.

[405] G. O. Mallory and J. B. Hajdu, *Electroless Plating: Fundamentals and Applications*. William Andrew Publishing/Noyes, 1990.

[406] B.-H. Lin, “Investigation of electroless deposition for thin films in integrated circuits, MSc Report,” 1960.

[407] B. Ghosh, “Electrical contacts for II–VI semiconducting devices,” *Microelectron. Eng.*, vol. 86, no. 11, pp. 2187–2206, 2009.

[408] S. Kundu, S. K. Das, and P. Sahoo, “Properties of electroless Nickel at elevated temperature - A review,” *Procedia Eng.*, vol. 97, pp. 1698–1706, 2014.

[409] M. Liebau, E. Unger, G. S. Duesberg, A. P. Graham, R. Seidel, F. Kreupl, and W. Hoenlein, “Contact improvement of carbon nanotubes via electroless nickel deposition,” *Appl. Phys. A*, vol. 77, no. 6, pp. 731–734, 2003.

[410] K. P. Yung, J. Wei, and B. K. Tay, “Electroless plating of nickel on carbon nanotubes film,” *Electronic Packaging Technology Conference, 2005. EPTC 2005. Proceedings of 7th*, vol. 2. p. 3 pp., 2005.

[411] Q. L. and S. F. and W. H. and C. S. and Wenjie Liang, “Coating of Carbon Nanotube with Nickel by Electroless Plating Method,” *Jpn. J. Appl. Phys.*, vol. 36, no. 4B, p. L501, 1997.

[412] S.-S. Tzeng and F.-Y. Chang, “Electrical resistivity of electroless nickel coated carbon fibers,” *Thin Solid Films*, vol. 388, no. 1–2, pp. 143–149, 2001.

[413] L. M. Ang, T. S. A. Hor, G. Q. Xu, C. H. Tung, S. P. Zhao, and J. L. S. Wang, “Decoration of activated carbon nanotubes with copper and nickel,” *Carbon N. Y.*, vol. 38, no. 3, pp. 363–372, 2000.

[414] L.-M. Ang, T. S. A. Hor, G.-Q. Xu, C. Tung, S. Zhao, and J. L. S. Wang, “Electroless Plating of Metals onto Carbon Nanotubes Activated by a Single-Step Activation Method,” *Chem. Mater.*, vol. 11, no. 8, pp. 2115–2118, 1999.

[415] P. Sahoo and S. K. Das, “Tribology of electroless nickel coatings - A review,” *Mater. Des.*, vol. 32, no. 4, pp. 1760–1775, 2011.

[416] M. Schlesinger, “Electroless Deposition of Nickel,” in *Modern Electroplating*, John Wiley & Sons, Inc., pp. 447–458, 2011.

[417] P. Gadhari and P. Sahoo, “Optimization of Electroless Ni–P–Al2O3 Composite Coatings based on Multiple Surface Roughness Characteristics,” *Procedia*

*Mater. Sci.*, vol. 5, pp. 21–30, 2014.

[418] R. Muraliraja and R. Elansezhian, “ME-306 International Conference on Advances in Manufacturing and Materials Engineering Optimization of Reducing Agent and Key Parameters Effect on Efficiencies Electroless Ni-P plating by taguchi method,” vol. 5, pp. 2478–2486, 2014.

[419] X. Wei and D. K. Roper, “Tin Sensitization for Electroless Plating Review,” *J. Electrochem. Soc.* , vol. 161, no. 5, pp. D235–D242, 2014.

[420] C. M. Polley, W. R. Clarke, and M. Y. Simmons, “Comparison of nickel silicide and aluminium ohmic contact metallizations for low-temperature quantum transport measurements,” *Nanoscale Res. Lett.*, vol. 6, no. 1, p. 538, 2011.

[421] S. M. Song, J. K. Park, O. J. Sul, and B. J. Cho, “Determination of Work Function of Graphene under a Metal Electrode and Its Role in Contact Resistance,” *Nano Lett.*, vol. 12, no. 8, pp. 3887–3892, 2012.

[422] B. Ghosh, C. Dale, R. Dewanto, N. Keegan, and J. Hedley, “A Novel Electrical Contacting Technology To Graphene,” *Nanotech*, vol. 1, pp. 196–199, 2012.

[423] M. J. Aleksinas, “Chapter 3 Troubleshooting Electroless Nickel Plating Solutions,” *Electroless Plat. - Fundmentals Appl.*, pp. 101–109, 1990.

[424] S. M. Popescu, A. J. Barlow, S. Ramadan, S. Ganti, B. Ghosh, and J. Hedley, “Electroless Nickel Deposition: An Alternative for Graphene Contacting,” *ACS Appl. Mater. Interfaces*, p. acsami.6b08290, 2016.

[425] R. H. Myers, D. C. Montgomery, and C. M. Anderson-Cook, “Response Surface Methodology,” in *Response Surface Methodology: Process and Product Optimization Using Designed Experiments*, 4th ed., John Wiley & Sons, Inc., 2016.

[426] L. G. P. Martins, Y. Song, T. Zeng, M. S. Dresselhaus, J. Kong, and P. T. Araujo, “Direct transfer of graphene onto flexible substrates,” *Proc. Natl. Acad. Sci.*, vol. 110, no. 44, pp. 17762–17767, 2013.

[427] Z. Li, Y. Wang, A. Kozbial, G. Shenoy, F. Zhou, R. McGinley, P. Ireland, B. Morganstein, A. Kunkel, S. P. Surwade, L. Li, and H. Liu, “Effect of airborne contaminants on the wettability of supported graphene and graphite,” *Nat. Mater.*, vol. 12, no. 10, pp. 925–931, 2013.

[428] G. A. Di Bari, “Electrodeposition of Nickel,” in *Modern Electroplating*, John Wiley

& Sons, Inc., pp. 79–114, 2011.

[429] P. Gadkari, “Effect of Annealing on Copper Thin Films: the Classical Size Effect and Agglomeration,” University of Central Florida Orlando, 2005.

[430] K. Nagashio, T. Nishimura, K. Kita, and A. Toriumi, “Contact resistivity and current flow path at metal/graphene contact,” *Appl. Phys. Lett.*, vol. 97, no. 14, p. 143514, 2010.

[431] W. S. Leong, C. T. Nai, and J. T. L. Thong, “What Does Annealing Do to Metal–Graphene Contacts?,” *Nano Lett.*, vol. 14, no. 7, pp. 3840–3847, 2014.

[432] R. C. Agarwala and V. Agarwala, “Electroless alloy / composite coatings,” in *Frontiers in Materials Science*, B. Raj and S. B. Rao, Eds. Universities Press (India) Private Limited, 2005.

[433] J. M. Englert, C. Dotzer, G. Yang, M. Schmid, C. Papp, J. M. Gottfried, H.-P. Steinrück, E. Spiecker, F. Hauke, and A. Hirsch, “Covalent bulk functionalization of graphene.,” *Nat. Chem.*, vol. 3, no. 4, pp. 279–286, 2011.

[434] S. Kumar, N. Peltekis, K. Lee, H.-Y. Kim, and G. Duesberg, “Reliable processing of graphene using metal etchmasks,” *Nanoscale Res. Lett.*, vol. 6, no. 1, p. 390, 2011.

[435] M. Schlesinger, “Deposition on Nonconductors,” in *Modern Electroplating*, John Wiley & Sons, Inc., pp. 413–420, 2011.